The Pennsylvania State University
The Graduate School
Graduate Program in Acoustics

ESTIMATING AND MODELING THE BUBBLE POPULATION RESULTING FROM AN UNDERWATER EXPLOSION BY INVERSION OF ACOUSTIC ATTENUATION MEASUREMENTS

A Thesis in
Acoustics
by
Fred Dryden Holt IV

Submitted in Partial Fulfillment
of the Requirements
for the Degree of

Master of Science

December 2010

The thesis of Fred Dryden Holt IV was reviewed and approved* by the following:

R. Lee Culver
Associate Professor of Acoustics
Thesis Advisor

Russell C. Burkhardt
Assistant Professor of Acoustics

Anthony P. Lyons
Associate Professor of Acoustics

Victor W. Sparrow
Professor of Acoustics
Interim Chair of the Intercollege Graduate Program in Acoustics

*Signatures are on file in the Graduate School.

Abstract

Underwater explosions have been studied intensively in the United States since 1941 [e.g., Cole (1945)]. Research to date primarily focuses on the initial shock and subsequent pressure waves caused by the oscillations of a "gas-globe" that is the result of a charge detonation. These phenomena have relatively short timescales (typically less than 2 [s]). However, as the gas globe rises in the water column and breaks the surface, it leaves behind a residual bubble cloud which has been markedly less studied. A recent experiment measured the spatial and temporal acoustic response of the bubble cloud resulting from a charge detonated at 15.2 [m] (50 [ft.]) depth. A directional projector was used to propagate a 40 kHz continuous-waveform (CW) pulse and a linear FM ($5 - 65$ kHz) pulse through the bubble cloud to two hydrophone arrays in order to measure the energy lost in propagating through the bubble cloud as well as backscattered to the vicinity of the acoustic projector. This thesis focuses on estimating and modeling the bubble population resulting from an underwater explosion (UNDEX). The resulting model is used to predict attenuation through, and backscatter from an UNDEX bubble cloud, and is compared to measured data.

Table of Contents

List of Figures

List of Tables

List of Symbols

Scalars and Vectors

$\alpha_b(\omega)$ Attenuation, in $\left[\frac{\text{Np}}{\text{m}}\right]$ unless otherwise specified.

$\alpha_w(f)$ Frequency dependent attenuation due to water, in $\left[\frac{\text{Np}}{\text{m}}\right]$.

$A(f)$ Attenuation, in $\left[\frac{\text{dB}}{\text{m}}\right]$ unless otherwise specified.

a Bubble radius, in [m] unless otherwise noted.

a_R A resonant bubble, in [m] unless otherwise noted.

c Sound speed, in $\left[\frac{\text{m}}{\text{s}}\right]$ unless otherwise specified.

$\mathbf{c}$ column vector c (bold non-italicized lower-case letters).

δ, δ_R Bubble damping constant, subscript R denotes resonance approximation.

D_{max} Maximum depth of the UNDEX bubble cloud in [m].

f Frequency, in Hertz.

f_R Resonance frequency of a bubble.

f'_R First order approximation of f_R.

k Acoustic wavenumber, $k = \frac{\omega}{c}$ $\left[\frac{1}{s}\right]$,

where k_R is wavenumber of a bubble at resonance,
k'_R is the first order approximation of k_R.

$\mathbf{M}$ matrix 'M'.

p_i Location of acoustic transducer in model geometry, (x_i, y_i, z_i) in [m].

$\mathbf{P}_i$ An ensemble of points along a path between the acoustic transducer and the ith hydrophone, in [m].

ψ Number of bubbles, in $\left[\frac{\#}{\text{m}^3} \text{ in a 1m bin}\right]$, unless otherwise specified.

R	Reference distance, 1 [m] unless otherwise specified.
σ	Denotes standard deviation (without subscript).
σ_a	The **a**bsorption cross section of a bubble, in $\left[\mathrm{m}^2\right]$.
σ_{bs}	The **b**ack**s**cattering cross section of a bubble, in $\left[\mathrm{m}^2\right]$.
σ_e	The **e**xtinction cross section of a bubble, in $\left[\mathrm{m}^2\right]$.
σ_s	The **s**cattering cross section of a bubble, in $\left[\mathrm{m}^2\right]$.
ω	Angular frequency, in radians per second. $\omega = 2\pi f$.
z	Water column depth, in [m].

Functions

$FT(\cdot)$	Formal theory of attenuation by a given bubble population, applied as an operator.
$\log(\cdot)$	Log base e, unless otherwise specified.
$\psi(\cdot)$	Bubble population, in $\left[\frac{\#}{\mathrm{m}^3} \text{ in a } 1\mu\mathrm{m} \text{ bin}\right]$ unless otherwise stated.
$\psi_U(\cdot)$	Bubble population due to an UNDEX, in $\left[\frac{\#}{\mathrm{m}^3} \text{ in a } 1\mu\mathrm{m} \text{ bin}\right]$ unless otherwise stated.
$RBA(\cdot)$	Resonant Bubble Approximation, applied as an operator.

Relations

$\approx$	Approximately equal to.
$\triangleq$	Defined as.
$\propto$	Proportional to.

Acknowledgments

I would like to thank my adviser Dr. Lee Culver for his support and guidance throughout my graduate career. His dedication, encouragement and patience has been fundamental to my success.

I would like to think my committee, Dr. Russ Burkhardt and Dr. Tony Lyons for their careful review and feedback. Also, Bob Jones and Ken Hillsley provided valuable feedback during my graduate career.

I want to thank Dr. Helen Czerski for sharing her time and expertise, and also for allowing me to reprint figures from her Portland, Oregon Acoustical Society of America talk in May 2009. NSWC Carderock and NSWC Indian Head were very helpful with the tests. Also, helpful suggestions were made by Tim Leighton and Preston Wilson,

I would like to thank my friends and fellow graduate students, specifically Chris Applegate, Brett Bissinger, Colin Jemmott, and Alex Sell for their advice, suggestions and camaraderie over the last few years. Each of these sources have been a positive influence throughout my academic and personal life, and have provided a unique, diverse and challenging perspective.

Lastly, this thesis would not have been possible without the financial support of the Office of Naval Research.

Chapter 1

Introduction

1.1 Motivation

Bubble populations for various underwater phenomena have been studied exhaustively since before World War II. A copious body of work exists describing the bubble populations present under wind-generated breaking waves [1, 2, 3]. There are also a few studies of bubble populations present in ship wakes [4, 5]. Bubble assemblages generated by underwater explosions are, however, largely unrepresented in this field. Underwater explosions have been studied in two respects: 1) the initial shock wave generated by detonation of the explosive material; and 2) the subsequent pressure waves generated by the oscillation of the resulting gas globe [6, 7].

To date, very few studies have been made of the bubble populations present around the explosion depth, or in the water column, after the gas globe has ejected from the surface. Cole, in 1941 stated that "the region near the explosion appears to remain nearly opaque for up to several minutes after explosion" [6]. The present work is a contribution to the body of research pertaining to underwater explosions, specifically, by estimating and modeling the bubble population within the vicinity of the underwater explosion by inversion of acoustic attenuation measurements.

1.2 Objective

This thesis concentrates on inverting attenuation measurements to estimate and model the bubble population in the vicinity of an underwater explosion (hereafter referred to as UNDEX) in a freshwater quarry in southern Virginia. This is accomplished using measured attenuation of acoustic energy propagating through the UNDEX bubble cloud. Results from the bubble population inversion methods are compared to other published in-water bubble populations. The bubble population model is used to predict attenuation through, and backscatter from, the bubble cloud which is compared to the measured data in order to verify the model.

1.3 Thesis Overview and Organization

In Chapter 2, the theory of acoustic interaction with bubbles is discussed. Topics such as resonance, scattering and attenuation due to clouds of bubbles are presented as a theoretical framework for the remainder of the thesis.

In Chapter 3, the acoustic inversion methods are presented. In no particular order these methods are that of Commander & McDonald [8], Caruthers *et. al.* [9], and Czerski & Farmer [10]. All of these methods are based upon the acoustical theory developed in Ch. 2. Each method is illustrated by example along with a detailing of important factors to consider during its application.

Chapter 4 presents experimental data from a 2008 test in which acoustic attenuation through a bubble cloud generated by an underwater explosion (UNDEX) was measured for a series of in-water detonations performed by the Naval Surface Warfare Center (NSWC). The results discussed in this thesis were obtained from the analysis of two 30 [lb.] PBXN-111 charges detonated at 15.2 [m] depth in the water column. A test signal was transmitted through the region of the bubble cloud left behind after detonation, and received by an array of hydrophones in order to estimate the energy lost by propagation through the UNDEX cloud. Another array of hydrophones was used to measure the energy scattered back to the region around the acoustic source. Received signals and a discussion of the processing techniques applied to obtain an estimate of attenuation due to the UNDEX bubble cloud are presented.

In Chapter 5, the bubble population inversion techniques presented in Ch. 3 are applied to the attenuation measurements made in the 2008 Quarry experiment presented in Ch. 4 to estimate the bubble population in the UNDEX cloud. A statistical analysis is performed to determine which inversion technique most consistently reproduces the measured attenuation. Finally, an estimate of the bubble population vs. time is presented for the second of the two detonations.

In Chapter 6, the spatial, temporal and bubble size characteristics present in the bubble population estimates are used to develop a model of the UNDEX bubble cloud. The bubble size spectrum is compared to other bubble size spectra from published in-water phenomena (*e.g.* under wind-generated breaking waves). Results computed using the model are then compared to the measured attenuation and backscatter to verify the model's accuracy.

In Chapter 7, general conclusions are made and possible future continuation of this work is discussed.

Chapter 2

Bubbles in Sound Fields

This chapter presents a brief overview of acoustic theory which is necessary to understand the remainder of the thesis. The reader is assumed to have at least a basic background in acoustics and mathematics. These concepts are well documented in many sources [4][7][11], and unless otherwise noted the majority of this material is adapted from Clay & Medwin (1977) [11].

First, a note about convention used in this thesis. All quantities used in equations are understood to be in MKS units, unless explicitly stated otherwise. For clarity, some figures and tables are presented with a in [μm] (instead of [m]), and frequency in kHz (instead of Hz). In these instances, units will be explicitly stated.

2.1 Initial Assumptions

This derivation begins by assuming that a mono-frequency, spherically spreading acoustic wave is propagating within an unbounded homogeneous medium. A wave propagating in any direction from the source is subject to range dependent transmission loss defined as

$$TL(R,f) = 20\log_{10}\left(\frac{R}{R_1}\right) + \alpha_w(f)R \qquad \text{in } \left[\frac{\text{dB}}{\text{m}}\right], \tag{2.1}$$

where R is the distance of propagation in meters, the reference distance, R_1, is traditionally 1 [m] and $\alpha_w(f)$ is the frequency-dependent absorption of sound in water. Absorption in water is ignored in this thesis since $\alpha_w R$ (where $\alpha_w \approx 1.2 \times 10^{-2}$ $\left[\frac{\text{dB}}{\text{m}}\right]$ for f $\leq$100 kHz in freshwater) is negligible in comparison to $20\log_{10}(R)$, for a propagation distance of approximately 100 [m] (which results in about 40 dB of transmission loss) [11].

For sound that travels long distances in the ocean, the acoustic ray path curves due to gradients in the sound velocity profile (SVP). Since we have assumed a homogeneous medium, ray path curvature due to varying SVP is ignored. This assumption is justified because the path length difference between curved and straight-line propagation for distances less than 100 [m] results in a negligible travel time difference. This assumption is discussed further in Ch. 4).

The sound speed in water, c, depends on temperature, salinity and ambient pressure. For freshwater at 22° C, the sound speed is about 1408 $\left[\frac{\text{m}}{\text{s}}\right]$ at 1 [m] depth, and 1466 $\left[\frac{\text{m}}{\text{s}}\right]$ at 15 [m] depth.

2.2 Bubbles at Resonance

2.2.1 Bubble Resonance Frequency Estimate

Small gas bubbles in water absorb and scatter sound in a frequency dependent fashion, and can resonate at a frequency which is inversely proportional to their radius, a (in [m] unless otherwise specified). Bubbles at resonance can effectively absorb and scatter energy at up to 10^3 times their physical cross section, and are the dominant source of acoustic scattering and absorption within a bubbly liquid provided that geometric scattering from large bubbles is not occurring (discussed in Sec. 5.2.3). The resonant frequency of a bubble can be derived by accounting for the compressibility of the enclosed gas and the liquid mass entrained by the bubble's surface as it oscillates about an equilibrium radius. Minnaert was the first to derive an expression for the resonance frequency of an air bubble in water[12], but Clay & Medwin [13] present a simplified approximation as

$$f'_R(a,z) \simeq \frac{3.25\sqrt{1+0.1z}}{a(\text{meters})}, \tag{2.2}$$

where a is the radius, and z is the depth of the air bubble. If a and z are in [m], then $f'_R(a,z)$ is in Hz. The prime indicates this is a first order approximation. Table 2.1 presents a few bubble radii and their resonance frequencies at 1 [m] and 15 [m] depths (significance of these depths is discussed in Ch. 4).

a [μm]	${f_R}'\big\vert_{z=1[\text{m}]}$ kHz	${f_R}'\big\vert_{z=15[\text{m}]}$ kHz
10	341	398
100	34.1	39.8
1000	3.41	3.98

Table 2.1. Approximate bubble resonance frequencies for bubbles with a=10 [μm], 100 [μm] and 1000 [μm]. Calculated using Eqn. 2.2.

2.2.2 Bubble Damping at Resonance

The mechanisms that govern how much energy is absorbed and attenuated by a single ensonified bubble are thermal conductivity, shear viscosity and reradiated sound. These loss mechanisms occur primarily at the air-water interface of the bubble wall, and can be accounted for by adding a damping element to a resonant oscillator (the bubble). The bubble damping factor at resonance, δ_R, is defined as

$$\delta_R = \delta_{Rr} + \delta_{Rt} + \delta_{Rv}, \tag{2.3}$$

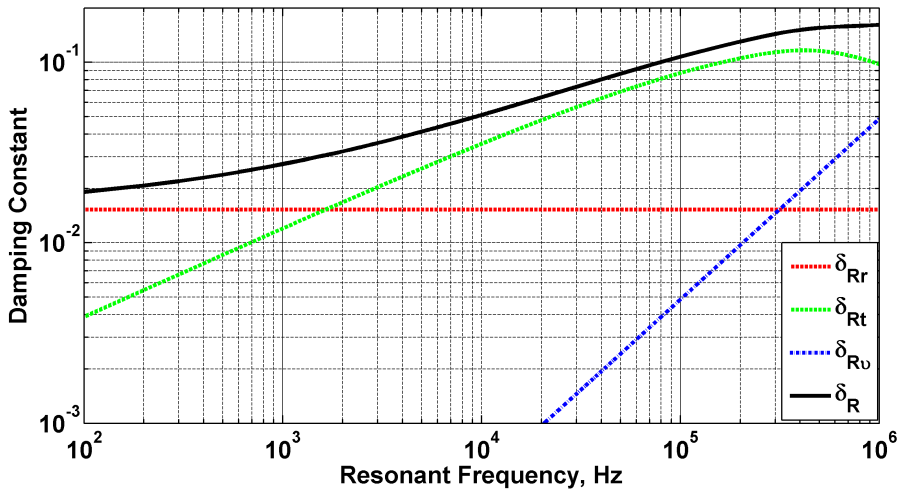

Fig. 2.1. Bubble damping constant at resonance: δ_R and contributions from δ_{Rr}, δ_{Rt} and $\delta_{R\upsilon}$. Calculated for bubbles at 1 [m] depth.

where $\delta_{Rr} = k'_R a_R = 0.0136$ is the contribution due to reradiation (see following assumption)
$\delta_{Rt} = \left(\frac{d}{b}\right)\Big|_{f=f_R}$ is the contribution due to thermal conductivity
$\delta_{R\upsilon} = \frac{4\mu}{\rho_A \omega_R a_R^2}$ is the contribution due to viscosity

The constants used in this calculation and a definition for $\frac{d}{b}$ will be given in Sec. 2.3.

Figure 2.1 shows the total and component bubble damping constants at resonance for a bubble located at 1 [m] depth. The reradiation term (δ_{Rr}) is not frequency dependent since the bubble's resonant frequency (Eqn. 2.2) can be re-written in terms of the resonant wavenumber, $k'_R(a) = \frac{2\pi f'_R(a)}{c}$ (since $\omega'_R = 2\pi f'_R = ck'_R$), which results in a constant δ_{Rr}. The reradiation term is the primary cause of damping below about 1 kHz. At frequencies above 1 kHz energy lost to thermal processes is the primary cause of damping. Viscous losses are important for bubbles with resonant frequencies greater than 500 kHz ($a_R \leq 7$ [μm]).

2.3 Off-Resonance Effects

While bubbles at resonance dominate the acoustic response of a bubble cloud, it is also important to determine the scattering and radiation characteristics of bubbles excited off-resonance.

A derivation of the full bubble damping constant is presented in Clay & Medwin Appendix 6 investigates the mechanical response of a bubble based upon gaseous and material constants [11]. The formulation requires that we know the bubble resonance frequency more precisely than f'_R given in Eqn. 2.2, which did not include the effects of surface tension and viscosity. The complete expression for the bubble resonance frequency can be calculated using Eqn. 2.4 with the physical properties given in Table 2.2. The difference between f'_R and f_R can be substantial

for bubbles with radii smaller than 600 [μm] (up to 20% difference in resonance frequency for small bubbles).

$$f_R(a) = \frac{1}{2\pi a}\sqrt{\frac{3\gamma P_A b\beta}{\rho_a}}, \tag{2.4}$$

where $\beta = \frac{P_{iA}}{P_A} = 1 + \frac{2\tau}{P_A a}\left(1 - \frac{1}{3\gamma b}\right)$

$$b = \left[1 + \left(\frac{d}{b}\right)^2\right]^{-1}\left[1 + \frac{3\gamma-1}{X}\frac{\sinh X - \sin X}{\cosh X - \cos X}\right]^{-1}$$

$$\frac{d}{b} = 3\left(\gamma - 1\right)\left[\frac{X(\sinh X + \sin X) - 2(\cosh X - \cos X)}{X^2(\cosh X - \cos X) + 3(\gamma-1)X(\sinh X - \sin X)}\right],$$

$$X = a\sqrt{\frac{2\omega\rho_g C_{pg}}{K_g}},$$

where b and d account for the magnitude and phase of the polytropic coefficient, γ. The angular frequency is defined as $\omega = 2\pi f$ $\left[\frac{\text{radians}}{\text{sec}}\right]$. The term $\frac{d}{b}$ is calculated in addition to b as these two forms are required separately to calculate of the bubble damping constant and resonance frequency of a bubble, respectively.

Including frequency dependence, the full form of the damping constant is

$$\delta = ka + \frac{d}{b}\left(\frac{f}{f_R}\right)^2 + \frac{4\mu}{\rho_A \omega a^2}, \tag{2.5}$$

where the terms correspond to contributions from reradiation (δ_r), thermal conductivity (δ_t), and viscosity (δ_ν), respectively. The definitions of $\frac{d}{b}$ and the physical constants are the same as the full resonance equation, Eqn. 2.4. Figure 2.2 presents the full bubble damping constant for a monofrequency sonar at 1 kHz and 100 kHz. Note that the abscissa for the plot of resonant

Constant:	Symbol:	Value or Formula:
Thermal Conductivity of Air	K_g	0.025 $\left[\frac{\text{w}}{\text{m}\cdot\text{K}}\right]$
Density, Air @ Std. Temp. & Pres.	ρ_{gA}	1.29 $\left[\frac{\text{kg}}{\text{m}^3}\right]$
Density, Air	ρ_g	$\rho_{gA}[1 + \frac{2\tau}{P_A a}](1 + 0.1z)$ $\left[\frac{\text{kg}}{\text{m}^3}\right]$
Surface Tension	τ	0.075 $\left[\frac{\text{N}}{\text{cm}}\right]$
Ambient Pressure @ Water Depth z	P_A	$101.3(1 + 0.1z)$ [kPa]
Avg. Interior Pressure (incl. surf. ten. effect)	P_{iA}	$P_{iA} = \beta P_A$ in [Pa]
Specific Heat at Constant Pressure, Air	C_{pg}	1.012 $\left[\frac{\text{J}}{\text{g}\cdot\text{K}}\right]$
Viscosity of Water	μ	$1E^{-3}$ $\left[\frac{\text{kg}}{\text{m}\cdot\text{s}}\right]$
Ratio of Specific Heats, Air	γ	1.4

Table 2.2. Physical relationships and constants used for bubble resonance frequency (2.4), and damping constant (Eqn. 2.5) calculations.

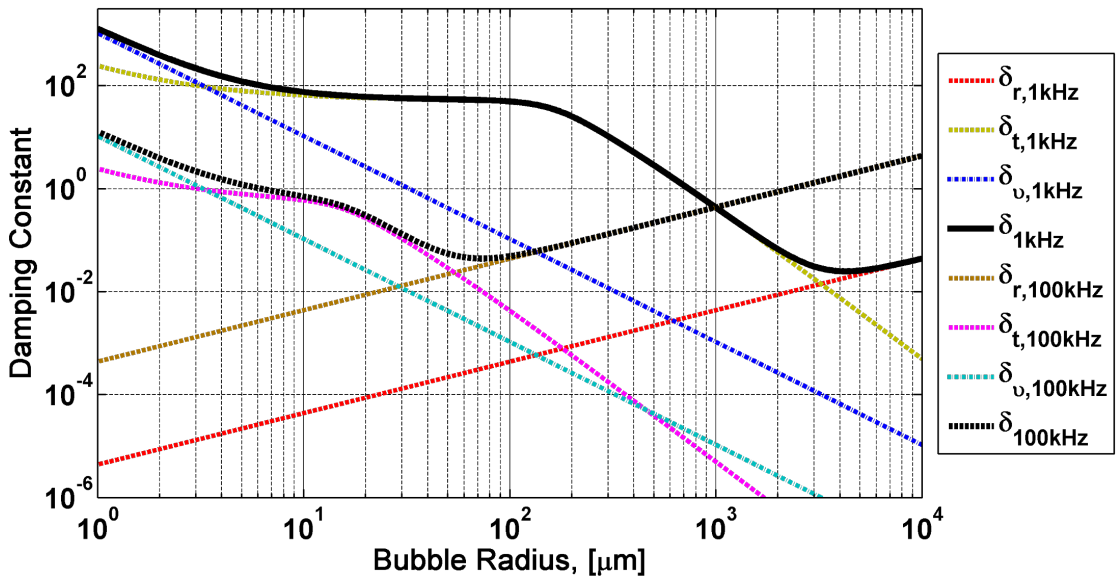

Fig. 2.2. Bubble damping constant, full calculation for bubbles resonant at 1 kHz, and 100 kHz. Calculated using Eqn. 2.5 for 1 [m] depth.

bubble damping (Fig. 2.1) is frequency, whereas the abscissa for Fig. 2.2 (the full bubble damping const., δ) is bubble radius, a in [μm].

The resonance frequency occurs near the lowest point in the bubble damping curve (δ_{1kHz} and δ_{100kHz}), thus bubbles not ensonified near resonance are more highly damped. Losses related to thermal conduction are less important at high frequencies (for $\delta_{100\text{kHz}}$), whereas they are a dominant factor at 1 kHz over the majority of bubble sizes. Viscosity is the dominant loss mechanism for small bubbles at both frequencies, and reradiation becomes more important with increasing bubble radius.

2.4 The Acoustic Cross Section of a Bubble

Water is generally not a homogeneous medium; bubbles and particulate often exist in various amounts dispersed throughout the medium, and will often have an affect on a propagating acoustic wave. The frequency dependent scattering properties of an object depend on its size, relative shape, compressibility and density.

The acoustic wavelength, λ [m], can be calculated from $\lambda = \frac{c}{f}$, where c is the sound speed in $\left[\frac{\text{m}}{\text{s}}\right]$, and f is frequency in Hz (*e.g.* $\lambda(5\text{ kHz}) \approx 0.28$ [m] in freshwater). If a small spherical object is located in the far-field relative to the sound source, an assumption can be made that the spherical wave emanating from the source is acting locally (*i.e.* at the object) like a plane wave. The far-field assumption is valid for distances greater than the critical distance (R_c), which is defined as

$$R_c \triangleq \frac{W^2}{\lambda}, \tag{2.6}$$

where R_c (in [m]) is the distance away from the source that corresponds to the approximate boundary between the near-field and far-field radiation patterns. W is the dimension of the source [11]. For the purposes of this thesis, we are always operating in the far-field.

When an acoustic plane wave interacts with a body, the effect is frequency dependent. A non-dimensional measure of the size of an object in the presence of a given frequency is commonly known as ka, where k $\left(= \frac{2\pi f}{c}\ [\mathrm{m}^{-1}]\right)$ is the wavenumber, and a [m] is the radius of the object. An object whose dimensions are much smaller than the acoustic wavelength generally does not adversely affect acoustic propagation and the object will scatter little energy. Scattering in this region ($ka \ll 1$) is known as Rayleigh scattering. For a body much larger than a wavelength, *i.e.* $ka \gg 1$, the acoustic wave is scattered in a geometric fashion, which is discussed shortly. When $ka \approx 1$, it is within a transition region that exhibits characteristics of both Rayleigh and geometric scattering.

When an object scatters energy, its physical cross-section may be insufficient to fully describe its impact on the incident plane-wave. The effective area over which the scattering body interacts with the incident wave is the acoustic cross section, which is defined as the ratio of the acoustic power scattered by the body, Π_s [W], to the incident intensity of the acoustic plane wave, I_p $[\frac{\mathrm{W}}{\mathrm{m}^2}]$, or

$$\sigma_s \equiv \frac{\Pi_s}{I_p} = \frac{\int_0^{4\pi} I_s R^2\, d\Omega}{I_p} = \int_0^{4\pi} \zeta(k,a,\theta)\mathrm{A} d\Omega \qquad \text{in } [\mathrm{m}^2], \tag{2.7}$$

where R is the distance between the scatterer and receiver in [m]. The scattered power is the integral of the scattered intensity over all angles. A scattering function $\zeta(k,a,\theta)$ $(= \frac{I_s R^2}{I_p A})$ incorporates I_p and I_s. $\zeta(k,a,\theta)$ is also divided by a factor of $\mathrm{A} = \pi a^2$ [m^2], the physical cross section of the object.

If the scatterer is omnidirectional, the integration over all angles yields a factor of 4π and the scattering cross section becomes

$$\sigma_s = \frac{4\pi R^2 I_s}{I_p} \qquad \text{in } \left[\mathrm{m}^2\right]. \tag{2.8}$$

Eqn. 2.8 applies when the scatter is omnidirectional, which is not the case for most most non-resonant objects. The mechanism that causes this effect is discussed in further detail later.

The same object may absorb energy from the incident sound wave, and the absorption cross section can be defined similar to the scattering cross section. The absorption cross section is defined as

$$\sigma_a \triangleq \frac{\Pi_a}{I_p} \qquad \text{in } \left[\mathrm{m}^2\right], \tag{2.9}$$

where Π_a [W] is the power absorbed by the object.

The total amount of power lost (or extinguished) is the sum of the scattered and absorbed power. This loss can be characterized using an effective cross-section over which the object

extinguishes energy. The extinction cross section, σ_e, is defined as

$$\sigma_e = \sigma_s + \sigma_a \qquad \text{in } \left[\mathrm{m}^2\right]. \tag{2.10}$$

If the body is sufficiently small ($ka \ll 1$), the Rayleigh scattering function, ζ, can be used to describe the angular dependence of energy scattered at any angle with respect to the incident direction:

$$\zeta(k, a, \theta) = \frac{(ka)^4}{\pi}\left[\frac{e-1}{3e} - \left(\frac{g-1}{2g+1}\right)\cos\theta\right]^2, \qquad ka \ll 1. \tag{2.11}$$

where a is the radius of the object (or approximate radius of a non-spherical object) in [m]
$k = \frac{2\pi}{\lambda}$, wavenumber [m^{-1}],
$e = \frac{E_1}{E_0}$, ratio of elasticities of the sphere to the medium
$g = \frac{\rho_1}{\rho_0}$, ratio of densities of the sphere to the medium
θ is the angle between incident and scattered rays, 0° is the forward scattering direction

In this function, the elasticities (Young's moduli) are usually derived from the density and sound speed as $E = c^2\rho_A \left[\frac{\mathrm{N}}{\mathrm{m}^2}\right]$, where ρ_A is the ambient density. The subscript 0 denotes the propagation medium, and 1 is the scattering object. "When the sound wavelength is much greater than the sphere's circumference, there are two effects that can cause scatter[ing]. (a) If the sphere elasticity E_1 (=compressibility^{-1}) is less than that of the water E_0, incident condensations and rarefactions compress and expand the sphere, and a spherical wave is reradiated. This monopole radiation occurs also if $E_1 > E_0$ but the phase is different. (b) If the sphere density ρ_1 is much greater than that of the medium ρ_0, the sphere's inertia will cause it to lag behind as the plane wave in the fluid swishes back and forth. The motion is equivalent to the medium being at rest and the sphere being in oscillation. This action generates a dipole type of reradiation. When $\rho_1 < \rho_0$, the effect is the same but the phase is different. In either event when $\rho_1 \neq \rho_0$ the scattered pressure is proportional to $\cos(\theta)$ where θ is the angle between the scattered direction and the incident direction" [11].

Figure 2.3 shows the effective scattering directivity (ζ) of three objects: a grain of sand, a non-resonant bubble and a rigid sphere, with corresponding values of e and g presented in Table 2.3. In these plots, 0° is the forward scattering direction (pointing to the right). The grain of sand (left) is more elastic and has a slightly higher density than the water, thus the scattered energy is nearly omnidirectional, however it scatters slightly less energy in the forward direction (0°) due to a slight phase shift introduced by the density difference. The non-resonant bubble (center) is much more elastic than water and has a much lower density, thus shows no preferential scattering direction. The rigid sphere (right) has a considerably higher density than the water, thus a phase shift is introduced and results in the dipole-like radiation pattern.

Eqn. 2.11 is only valid where $ka \ll 1$, and within this region the scattering function is $(ka)^4$ multiplied by a term depending only on material properties and θ. For $ka \gg 1$, the high frequency approximation can be assumed. This is called the geometric scattering region, in which

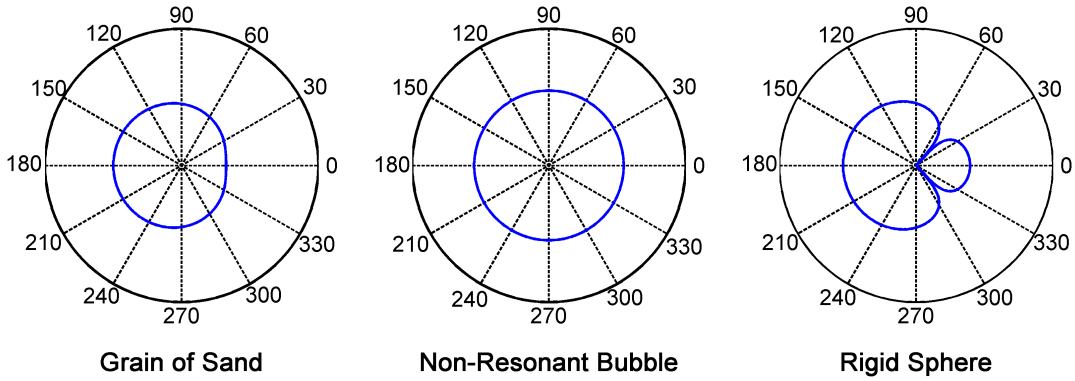

Fig. 2.3. Scattering directionality for several objects with $a = 10$ [μm]: grain of sand (left), non-resonant bubble (center), and rigid sphere (right). 0 is the forward scattering direction (pointing to the right), and all cases assume $ka \ll 1$.

	e	g
Grain of Sand	21.4	2.4
Non-Resonant Air Bubble	4.7×10^{-5}	9.6×10^{-4}
Rigid Sphere	20	10

Table 2.3. Ratios of elasticity and density for the scattering objects in Figure 2.3

traditional ray acoustics is used to estimate the scattered field. If a ray encounters a perfectly rigid sphere at angle θ relative to the surface normal, the scattered ray is reflected in-phase at angle 2θ relative to the surface normal. If the surface is not perfectly rigid, the appropriate reflection and transmission coefficients provide the proper phase and magnitude of the reflected wave.

Figure 2.4 shows relative levels of scattered energy for a rigid body for values of ka: 0.1, 1, 8, respectively [11]. The relative amplitude of energy scattered in the forward direction increases as ka increases, which is visible in the figure as the relative magnitude of the main scattering lobes. For small ka (object is smaller than an acoustic wavelength), the object scatters considerably less energy than if it were larger than the acoustic wavelength. (Note, for values of $ka \geq 1$, Eqn. 2.11 no longer applies, the high-frequency approximation must be used. *see:* Sec. 6.2.2 of [11]).

Rayleigh's scattering function (Eqn. 2.11) can be substituted into the original definition of the scattering cross section, Eqn. 2.7. Performing the integration over the solid angle, the scattering cross section becomes

$$\sigma_s(k,a) = \pi a^2 \int_0^{4\pi} \zeta d\Omega = 4\pi a^2 (ka)^4 \left[\left(\frac{e-1}{3e} \right)^2 + \frac{1}{3} \left(\frac{g-1}{2g+1} \right)^2 \right] \qquad ka \ll 1, \tag{2.12}$$

which describes the directivity pattern for small scatterers.

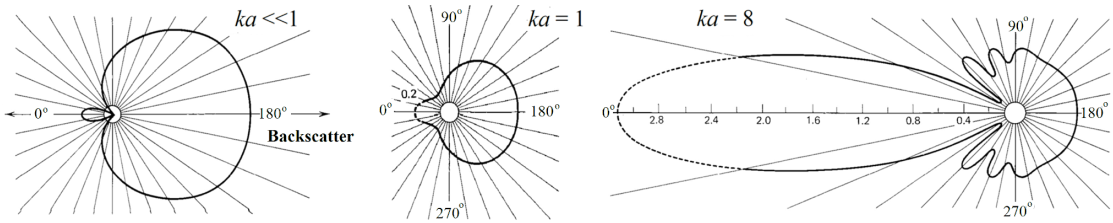

Fig. 2.4. Relative magnitude of the scattering function for a rigid body where $ka \ll 1$ (left), $ka = 1$ (middle), and $ka = 8$ (right). 0° is the forward scattering direction (pointing to the left), and the relative magnitude is shown by labels in the figure, as well as the relative proportion of the curves. (Reprinted with permission from Fig 6.2.6 of [11])

For the rest of this derivation, the focus will be on small bubbles filled with air. The gas inside of the bubble is much less dense, and much more elastic than the surrounding water ($e \gg 1$ and $g \ll 1$ in Eqn. 2.11). Clay & Medwin present an alternative method using a mechanical domain representation of the radial oscillation of a bubble (*see* Appendix A6.1 of [11]) to describe the scattering cross section,

$$\sigma_s(f,a) = 4\pi R_1^2 \frac{|P_s|^2}{|P_p|^2} = \frac{4\pi a^2}{\left[\left(\frac{f_R}{f}\right)^2 - 1\right]^2 + \delta^2} \qquad \text{in } \left[\mathrm{m}^2\right], \tag{2.13}$$

which is derived from the ratio of the scattered pressure, P_s, to the incident plane-wave pressure P_p. Eqn. 2.13 is used when the ensonifying field is near the bubble's resonant frequency since resonance effects can result in scattering cross sections several orders larger than that predicted by Eqn. 2.12. Eqn. 2.13 can be used to compute the scattering cross section of an air bubble at all frequencies since the damping constant can be appropriately computed for all frequencies [4].

After combining σ_a (Eqn. 2.9) and σ_s (Eqn: 2.13), the extinction cross section is calculated from

$$\sigma_e(f,a) = \frac{4\pi a^2 \frac{\delta}{\delta_r}}{\left[\left(\frac{f_R}{f}\right)^2 - 1\right]^2 + \delta^2} \qquad \text{in } \left[\mathrm{m}^2\right]. \tag{2.14}$$

Figure 2.5 shows the acoustic cross sections for 5 kHz and 50 kHz for a range of bubbles between [10 10000] [μm]. The extinction cross section is shown in black, and the scattering and absorption cross sections are shown as colored lines. The extinction cross section shows a sharp peak at the resonant bubble radius, a_R, and rapidly decreases for nearby radii. For radii larger than a_R, the extinction cross section reaches a minimum (*e.g.* at 50 kHz, this occurs at about 150 [μm]), then begins to increase monotonically. For large bubbles present at a given frequency, the magnitude of σ_e can be larger than that of the resonance peak (*e.g.,* for 50 kHz, this occurs for $a_R \geq 2 \times 10^3$ [μm]). The total extinguished acoustic energy, or attenuation from multiple bubbles of the same size, or of different sizes is discussed in the next section.

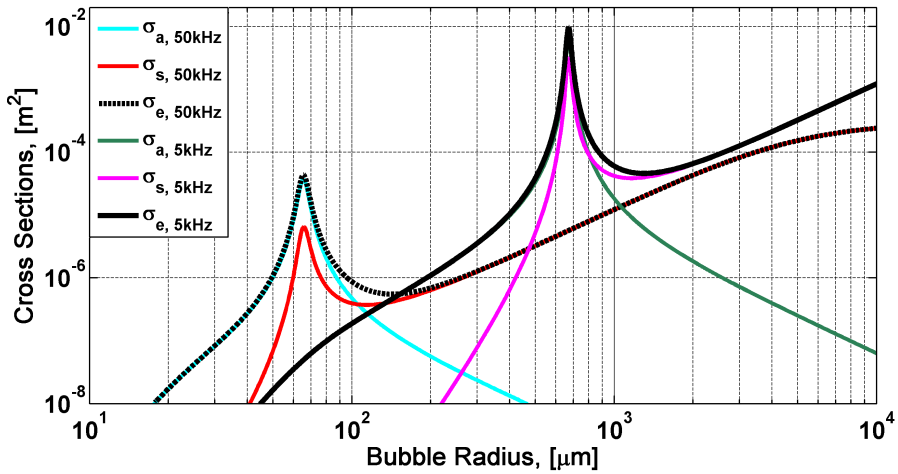

Fig. 2.5. Acoustic cross section of air bubbles ensonified at 5 kHz, and 50 kHz. The black lines indicate the extinction cross section, σ_e, which is a sum of the scattering and absorption cross sections, σ_s and σ_a respectively

2.5 Attenuation due to Bubbles

2.5.1 Bubbles of a Single Size

If N_a denotes the number of bubbles with radius a dispersed within a unit volume, their cumulative effect on an acoustic plane wave can be determined using the extinction cross section. If individual bubbles are separated by a distance greater than $\sqrt{\sigma_e}$, their effects are additive [11]. If the bubbles are closer together ($\leq \sqrt{\sigma_e}$ apart), their effects may not be linearly additive, and this case is called multiple scattering since an acoustic wave will interact with each bubble individually, and the scattered wave will also interact with surrounding bubbles. If the bubble population is sufficiently dense, the phase speed of propagation can be altered[14]. However, this effect is ignored in this thesis for reasons further discussed in Ch. 3.

If the intensity of the incident plane wave is I_p, is known, the change in intensity over a small distance dx can be expressed as

$$dI(x) = -I_p\ \sigma_e(f,a)\ N_a\ dx \qquad \text{in} \left[\frac{\text{W}}{\text{m}^2}\right]. \tag{2.15}$$

The change in intensity is always negative since this is a dissipative process. Then, integrating over the acoustic path yields the intensity at x,

$$I(x) = I_p e^{-\sigma_e(f,a)N_a x} \ \text{ in} \left[\frac{\text{W}}{\text{m}^2}\right]. \tag{2.16}$$

As the number of bubbles in the acoustic path increases, the transmitted intensity decreases exponentially. Intensity is proportional to the square of acoustic pressure ($I_p \propto p_p^2$), which affects

the sound pressure level (SPL) as

$$\Delta\text{SPL} = 20\log_{10}\frac{P(x)}{P_p} = -10\ \sigma_e(f,a)\ N_a\ x\ \log_{10}(e) \qquad \text{in dB.} \tag{2.17}$$

Then, the attenuation per unit distance traveled due to a small region of uniformly distributed resonant bubbles (N_a in $\left[\frac{\#\text{ of bubbles}}{\text{m}^3}\right]$) can be evaluated from Eqn. 2.17, as

$$A_b(f) = -\frac{\Delta\text{SPL}}{x} = 4.34\ \sigma_e(f,a)\ N_a \qquad \text{in } \left[\frac{\text{dB}}{\text{m}}\right], \tag{2.18}$$

where x is a unit distance, in this case 1 [m]. This expression for attenuation is true for all frequencies.

2.5.2 Bubbles of Many Sizes

Attenuation due to a population containing many sizes of bubbles can be calculated in a similar fashion. The number of bubbles of each radius must be known, and defined in terms of an incremental radius da (typically 1 [m]), which specifies the bin width between two adjacent radii. This bubble population has the form

$$\psi(a)da = \frac{\#\text{ of bubbles between (a) and (a + da)}}{\text{unit volume}}, \tag{2.19}$$

where the unit volume is traditionally 1 $\left[\text{m}^3\right]$, and the units of $\psi(a)$ are traditionally $\left[\frac{\#\text{ of bubbles}}{1\text{ m}^3}\right.$ in a 1 m bin] if da in [m]. Integrating $\sigma_e(f,a)$ (Eqn. 2.14) times Eqn. 2.19 over the entire bubble spectrum yields the total extinction cross section,

$$S_e(f) = \textstyle\int_0^\infty \sigma_e(f,a)\psi(a)\ da = \displaystyle\int_0^\infty \frac{4\pi a^2 \frac{\delta}{\delta_r}\ \psi(a)\ da}{\left[\left(\frac{f_R}{f}\right)^2 - 1\right]^2 + \delta^2} \qquad \text{in } \left[\frac{1}{\text{m}}\right]. \tag{2.20}$$

$S_e(f)$ quantifies the total extinction cross section due to the known bubble population over a specified volume. It assumes plane wave ensonification at a single frequency.

To calculate the attenuation per distance traveled through a bubble population in terms of $S_e(f)$, integrate Eqn. 2.18 times the bubble population. Utilizing Eqns. 2.14 and 2.20, we can write

$$A_b(f) = 4.34 S_e(f) \quad \text{in } \left[\frac{\text{dB}}{\text{m}}\right]. \tag{2.21}$$

Equation 2.21 provides the frequency dependent attenuation for a known bubble population. This is the primary focus of Ch. 2, and the remainder of this thesis is comprised of various methods to estimate this quantity as a forward problem, and as an inverse problem.

2.5.3 Example Bubble Populations

This section presents two example bubble populations used by Commander & McDonald [8] to evaluate their inversion techniques (detailed further in Ch. 3).

The left panel of Figure 2.6 contains a triangular bubble distribution, ψ_{tri}, dubbed for its visual shape, and the right panel shows a power-law type distribution, ψ_{PL}, with the form:

$$\psi(a) = Ca^{-m}, \tag{2.22}$$

where C is a scaling constant, and $m = 3.7$ defines the slope of the bubble population on a log-log plot.

ψ_{tri} is defined for bubbles with radii between [1 300] [μm], while ψ_{PL} was truncated with a lower-limit of 20 [μm] to avoid extremely large numbers of small bubbles. The triangular population was chosen to show that $\psi(a)$ may be a peaked function of radius, and the ψ_{PL} is similar to published in-water bubble population models [2] [15].

Figure 2.7 shows the result of employing Eqn. 2.21 to calculate the attenuation associated with the example populations in the water at shallow depth. At high frequencies ($\geq$ 50 kHz) the attenuation is much different for these populations because the small bubbles are much more numerous for the ψ_{PL}. The attenuation is very similar at low frequencies since both distributions have few bubbles with larger radii. Attenuation for the triangular population (ψ_{tri}) has a peak near 15 kHz since the majority of the bubbles are between [100 200] [μm] (f_R of a 200 [μm] radius bubble is 16.6 kHz). Attenuation for the power-law population (ψ_{PL}) is relatively flat over a broad span of higher frequencies because ψ_{PL} contains many small bubbles.

Figure 2.7 shows the application of the theory developed in this chapter to calculate the frequency dependent attenuation due to a known bubble population containing many different sizes of bubbles. The next chapter discusses methods to estimate the bubble population from attenuation data (like that presented in Fig. 2.7).

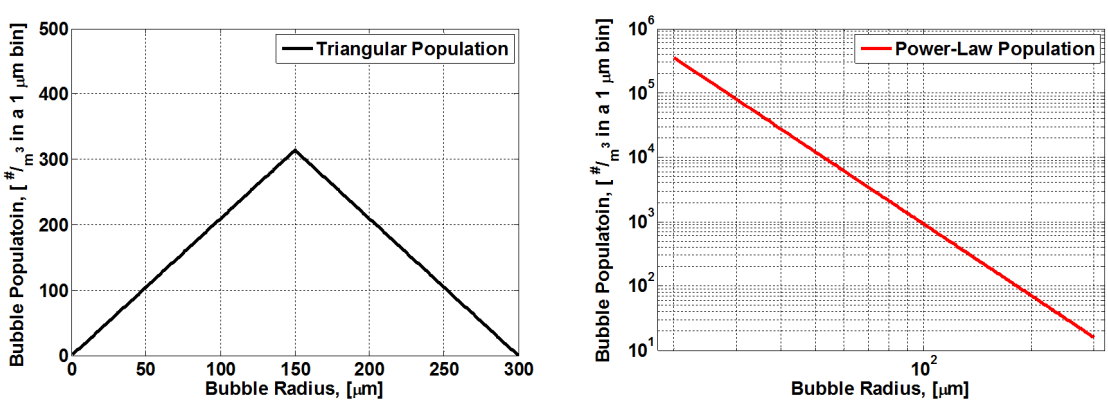

Fig. 2.6. Example populations: (a) triangular shaped bubble population, $\psi_{tri}(a)$. (b) power-Law type population, $\psi_{PL}(a)$. Bubble populations plotted in this figure are shown in $\left[\frac{\#}{\mathrm{m}^3}\ in\ a\ \mathbf{1}\ \mu\mathbf{m\ bin}\right]$.

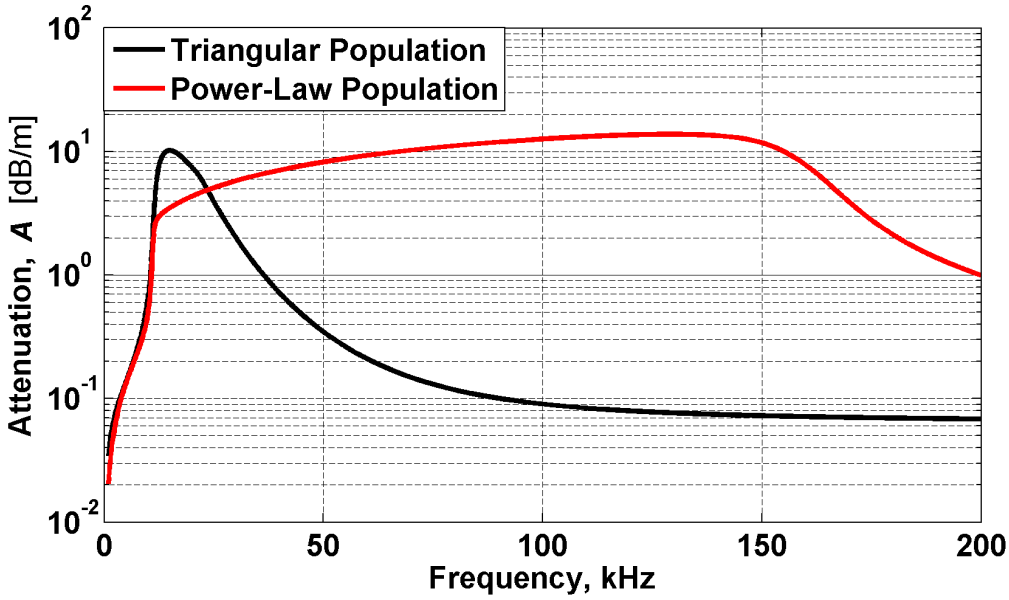

Fig. 2.7. Attenuation calculated for the two sample bubble populations in Fig. 2.6

.

Chapter 3

Bubble Population Inversion Methods

This chapter presents three methods that can be used to invert measurements of acoustic attenuation in order to estimate the bubble population. These methods stem from the fundamental acoustic theory presented in Ch. 2. Each of these methods is illustrated using the attenuation computed using the example bubble populations defined in Fig. 2.6.

3.1 Commander & McDonald Method

Interest in obtaining high-resolution bubble spectra from attenuation measurements led K. Commander and R. McDonald to seek a finite-element method (FEM) solution of the inverse bubble problem in the form of a Fredholm integral of the first kind [8].

The method developed in this section is slightly different than the presentation in [8]. These differences will addressed as they become important.

3.1.1 Method:

As developed in Ch. 2, the attenuation for a given bubble population can be calculated using Eqns. 2.20 and 2.21. Commander & McDonald present a similar equation for attenuation in $\left[\frac{\mathrm{Np}}{\mathrm{m}}\right]$:

$$\alpha_b(f) = \int_{a_{\min}}^{a_{\max}} \sigma_e(f,a)\psi(a)da \qquad \text{in } \left[\frac{\mathrm{Np}}{\mathrm{m}}\right]. \tag{3.1}$$

Note that the units of $\sigma_e(f,a)$ are $\left[\frac{\mathrm{m}^2}{\mathrm{bubble}}\right]$, and those of $\psi(a)da$ are $\left[\frac{\mathrm{bubbles}}{\mathrm{m}^3} \text{ in a 1 m bin}\right]$, so the units of $\sigma_e(f,a)\psi(a)da$ are $\left[\frac{1}{\mathrm{m}}\right]$. The conversion between $\left[\frac{\mathrm{Np}}{\mathrm{m}}\right]$ and $\left[\frac{\mathrm{dB}}{\mathrm{m}}\right]$ is: $1\left[\frac{\mathrm{Np}}{\mathrm{m}}\right] =$

$10\log_{10}(e)\left[\frac{\text{dB}}{\text{m}}\right] = 4.34\left[\frac{\text{dB}}{\text{m}}\right]$. This equation assumes that the bubble population $\psi(a)$ attenuates an acoustic plane-wave propagating through a deterministic volume.

Equation 3.1 can be recognized as a generalized Fredholm integral of the first kind:

$$g(x) = \int_a^b K(x,y)\phi(y)dy, \tag{3.2}$$

where $K(x,y)$ is the kernel ($\sigma_e(f,a)$ in Eqn. 3.2), $g(x)$ is the data ($\alpha_b(f)$ in Eqn. 3.2), and $\phi(y)$ is the unknown (bubble population, $\psi(a)$). The kernel is always positive for the inverse bubble problem, thus the only solution to the homogeneous form of Eqn. 3.2 (where $g(x) = 0$) is the trivial solution ($\phi(y) = 0$), which implies that solutions to Eqn. 3.1 are unique [8].

Commander & McDonald approximate the solution to Eqn. 3.1 by discretizing the terms and implementing a linear system of equations. Bubble populations likely contain a large variety of bubble sizes, whose resonant frequencies, f_R, are roughly inversely proportional to the bubble radius, a_R (per Eqn. 2.2). $\alpha_b(f)$ is a column vector containing a measurement of attenuation at each frequency spanning the range of resonant radii (a_R) likely to be present in the bubble population.

A finite sum of linear basis functions are used to approximate the bubble population, as

$$\psi(a) = \sum_{j=1}^{N} \psi_j B_j(a), \qquad \text{in } \left[\frac{\text{bubbles}}{\text{m}^3} \text{ in a 1 m bin}\right] \tag{3.3}$$

where a series of linear B-splines, $B_j(a_j)$ are used to decompose the bubble population into small subsets ($\mathbf{a}_j = [a_{j-1}, a_{j+1}]$) that account for the scattering and attenuation properties of bubbles local to a_j for which the population (ψ_j) is to be estimated. The radius central to each range of radii ($\mathbf{a}_j$) is dubbed the *knot* radius, a_j. The total bubble population is $\psi(a)$.

The knot radii can theoretically be chosen arbitrarily; however, in practice, difficulty in the inversion is minimized when the knot radii are chosen to correspond to frequencies at which the attenuation was measured, resulting in a square $\mathbf{K}$. A more detailed discussion of how the knot radii are determined is presented in Sec. 5.2.1.

The attenuation at a given frequency, Eqn. 3.1, can then be expressed as a summation:

$$\alpha_b(f_i) = \sum_{j=1}^{N} K_{ij}(f_i, a_j)\psi_j(a_j) \qquad \text{in } \left[\frac{\text{Np}}{\text{m}}\right], \tag{3.4}$$

where i is an index over frequency, and K_{ij} is defined as

$$K_{ij}(f_i, a_j) = \int_{a_{\min}}^{a_{\max}} \sigma_e(f_i, a_j) B_j(a_j) da \qquad \text{in } \left[\frac{\text{m}^2}{\text{bubbles}}\right]. \tag{3.5}$$

The method utilized in this thesis differs from Commander & McDonald in that the use of B-splines has been replaced by an integration over a range of radii that span half-way between a_j and its neighboring knot radii (*e.g.* $\frac{a_{j-1}+a_j}{2} < a_j < \frac{a_{j+1}+a_j}{2}$). This substitution is justified

because only bubbles very near resonance account for the vast majority of attenuation, and because other off-resonant effects are also accounted for in the kernel (discussed shortly). The K_{ij}s are computed for each frequency and bubble radius. This results in an effective measure of how a certain (small) range of bubble radii attenuate at a single frequency.

Eqn. 3.4 can be expressed in matrix form, where

$$\boldsymbol{\alpha}_b = \mathbf{K}\,\boldsymbol{\psi}, \quad \text{or,} \tag{3.6}$$

$$\begin{array}{c} \text{(low frequency)} \\ \\ \\ \text{(high frequency)} \end{array} \begin{pmatrix} \alpha_{b,1} \\ \alpha_{b,2} \\ \vdots \\ \alpha_{b,M} \end{pmatrix} = \begin{pmatrix} K_{11} & K_{12} & \cdots & K_{1N} \\ K_{21} & K_{22} & \cdots & K_{2N} \\ \vdots & \vdots & \ddots & \vdots \\ K_{M1} & K_{M2} & \cdots & K_{MN} \end{pmatrix} \begin{pmatrix} \psi_1 \\ \psi_2 \\ \vdots \\ \psi_N \end{pmatrix} \begin{array}{c} \text{(small bubbles)} \\ \\ \\ \text{(large bubbles)} \end{array} . \tag{3.7}$$

The goal of inversion is to solve Eqn. 3.6 for $\boldsymbol{\psi}$ given $\boldsymbol{\alpha}_b$ and $\mathbf{K}$. Values for the measured attenuation at a discrete frequencies, $\boldsymbol{\alpha}_b$, form a column vector on the left side of this matrix equation (where $f_{R,2} > f_{R,1}$). $\mathbf{K}$ is a 2-dimensional representation of $\sigma_e(f, a)$ that has been quantized over an appropriate range of bubble radii centered about the knot radii (a_j). The column vector $\boldsymbol{\psi}$ contains the number of bubbles for each knot radius (the a_j's) (where $a_2 > a_1$).

If large bubbles are numerous and the acoustic frequencies are high, the lower off-antidiagonal terms (lower right in $\mathbf{K}$) may be comparable to or larger in magnitude than the antidiagonal, indicating that geometric scattering may be an important contributor to the total power extinguished (Π_e) by the bubble population. The assumption that only resonant bubbles are responsible for attenuating sound may lead to a misrepresentation of the bubble populations of both small and large bubbles due to this effect. This is discussed further in Sec. 3.3 [16].

The inverse problem in bubble acoustics is often ill-posed since it involves attenuation measurements that span large frequency ranges, resulting in a large range of knot radii. $\mathbf{K}$ is said to be ill-conditioned if the singular values of the matrix span a large range of magnitude. For an ill-conditioned $\mathbf{K}$, inversion of the matrix can become unstable, meaning that small fluctuation in the measured attenuation vector can cause large changes in the estimated bubble population. Such sensitivity may cause severe misrepresentation (under- or over-estimation) of the bubble population for a particular range of radii. Conventional methods of inverting an ill-conditioned $\mathbf{K}$ are likely to fail (*e.g.*, Gaussian elimination) [8].

Singular value decomposition (SVD) is one method used to obtain a generalized inversion of an ill-conditioned matrix. SVD is our method of choice since 1) SVD can be used on square and non-square matricies (discussed further shortly) 2) SVD allows regularization of the singular values which can improve the condition number of the matrix, and 3) it results in a least-squares type solution, whereas the MatLab / or *inv* operations utilize Gaussian-elimination[14]. The

SVD used here is of the form

$$\mathbf{K} = \mathbf{U}\mathbf{W}\mathbf{V}^T, \tag{3.8}$$

where $\mathbf{K}$ is the K-matrix, $\mathbf{U}^T$ denotes the conjugate transpose of $\mathbf{U}$, and $\mathbf{U}$ and $\mathbf{V}$ are unitary matricies (where $\mathbf{U}\mathbf{U}^T = \mathbf{U}^T\mathbf{U} = \mathbf{I}$). $\mathbf{W}$ is a diagonal matrix containing the singular values of $\mathbf{K}$. The singular values of matrix $\mathbf{K}$ are the positive square roots of the eigenvalues of $\mathbf{K}^T\mathbf{K}$[14].

The generalized inverse of $\mathbf{K}$ is defined as

$$\mathbf{K}^+ = \mathbf{V}\left(\frac{1}{\mathbf{W}}\right)\mathbf{U}^T. \tag{3.9}$$

The bubble population estimate is then obtained by

$$\boldsymbol{\psi} = \mathbf{K}^+\boldsymbol{\alpha}. \tag{3.10}$$

If $\mathbf{K}$ is not too ill-conditioned, the resulting estimate of the bubble population should be a reasonably accurate representation of the true bubble population. An example of this procedure is shown in Sec 3.1.4. Large amounts of variability at the smaller bubble radii is a common issue with this type of inversion [10], partially resulting from the discrepancy between f_R and f'_R. This variability can be alleviated to a certain degree with regularization, truncation of singular values, and extrapolation of the attenuation boundaries in some cases. The first two techniques are now discussed.

3.1.2 Regularization

The method detailed in the previous sections is viable so long as the $\mathbf{K}$ is not too ill-conditioned such that inversion does not result in a reasonable bubble population estimate. For cases where $\mathbf{K}$ is too ill-conditioned, one or more regularization techniques may be required in order to stabilize the solution. Commander & McDonald suggest subjecting the solution ($\psi(a)$) to a minimum curvature constraint, which forces the solution to vary more slowly with bubble radius. This regularization takes the form

$$(\mathbf{K}^T\mathbf{K} + \xi\mathbf{D}^T\mathbf{D})\psi(a) = \mathbf{K}^T\alpha(\omega), \tag{3.11}$$

where $\mathbf{D}$ is the second difference operator [17], and $\mathbf{D}^T$ is its transpose, and Eqn. 3.11 can only be applied to non-square $\mathbf{K}$. Here, ξ is the parameter used to constrain the solution, also called the regularization parameter. The singular values of $\mathbf{K}$ are the positive square roots of the eigenvalues of $\mathbf{K}^T\mathbf{K}$ [8], thus this method essentially adds an arbitrary value to the singular values of $\mathbf{K}$ in order to decrease the span of the magnitude of the eigenvalues of $\mathbf{K}$. Equation 3.11 is utilized in place of Eqn. 3.10.

For $\xi = 0$, the solution is unconstrained. For large values of ξ the bubble population is forced to be a straight line (in log-log space). The difficulty of using this method is finding an appropriate value for ξ. Commander & McDonald state that initially, the smallest singular

value is usually chosen for ξ, and this value is iteratively increased by a small amount until the largest singular values become affected, or the solution is sufficiently stabilized. This process effectively makes the system less sensitive to measurement noise, and therefore should provide a more stable solution than inverting $\mathbf{K}$ without regularization. While regularization results in a smoother bubble population, it may also remove important characteristics from the bubble population estimate.

3.1.3 Truncation

The singular values of the $\mathbf{K}$ matrix can span several orders of magnitude, resulting in a system that is difficult to invert. As the spread in singular values increases, inversion becomes more sensitive to noise, and is less likely to result in a reasonable bubble population estimate. As mentioned previously, one or more singular values can be 'zeroed'[1] to remove their contribution to the bubble population estimate in an effort to minimize the ill-conditioning of $\mathbf{K}$ and stabilize the inversion. However, 'zeroing' one or more SVs results in the loss of information, decreasing the ability of the estimated bubble population to reproduce the measured attenuation. This method of eliminating a particular radius' contribution to $\mathbf{K}$ and $\mathbf{K}^+$ is called truncation.

3.1.4 Example Result

Figure 3.1 shows $\mathbf{K}$ as formed from the knot radii needed to span the range of a_R for ψ_{tri} (the triangular distribution in Fig. 2.6). The ordinate is frequency (or wavelength) and the color scale has been compressed by $\log_{10}(\mathbf{K})$ (where $\mathbf{K}$ is always positive). Note that $f_R \propto \frac{1}{a_R}$, whereas $\lambda_R \propto a_R$, and the plot axes were chosen so that the peaks of $\mathbf{K}$ fall along the antidiagonal of $\mathbf{K}$.

Previous discussion assumed that $\mathbf{K}$ is non-square. However, the $\mathbf{K}$ shown in the left panel of Fig. 3.1 was formed using frequencies corresponding to the knot radii, thus is a square matrix.

As stated previously, the $\mathbf{K}$-matrix is essentially a 2-D representation of the extinction cross section. It is possible to observe the characteristic curve of σ_e in the rows of the left panel of Fig. 3.1. For a particular frequency, a row of the $\mathbf{K}$-matrix (or the band across all bubble radii) is the extinction cross section. Since the extinction cross section peaks at resonance, the highest value along this row of the matrix will occur at a_R. For example, at 50 kHz, a bubble with a radius 65 [μm] is resonant (at 1 [m] depth), and the peak for this row is near 65 [μm] (σ_e for 50 kHz is shown in Fig. 2.5). Also, as in Fig 2.5, the cross section at surrounding radii drops off quite rapidly. The antidiagonal of the $\mathbf{K}$-matrix marks the maxima in the extinction cross-section. It should be noted that off-resonance effects are not dominant compared to the antidiagonal in Fig. 3.1, but their effect can be seen increasing in the lower right corner of $\mathbf{K}$.

For a square $\mathbf{K}$, some of the procedures presented previously in this section require adaptation. For example, the singular value decomposition (SVD) of a square matrix is known as the eigenvalue decomposition (EVD), which has the property $\mathbf{U} = \mathbf{V}$ in Eqn. 3.8. Further, if $\mathbf{K}$ is

[1] In this case, 'zeroing' means removing (some of) the smallest SVs from $\mathbf{W}$, and removing the corresponding row(s) and column(s) from $\mathbf{U}$ & $\mathbf{V}$. The inner dimensions of the matrix multiplication change, the outer dimensions do not.

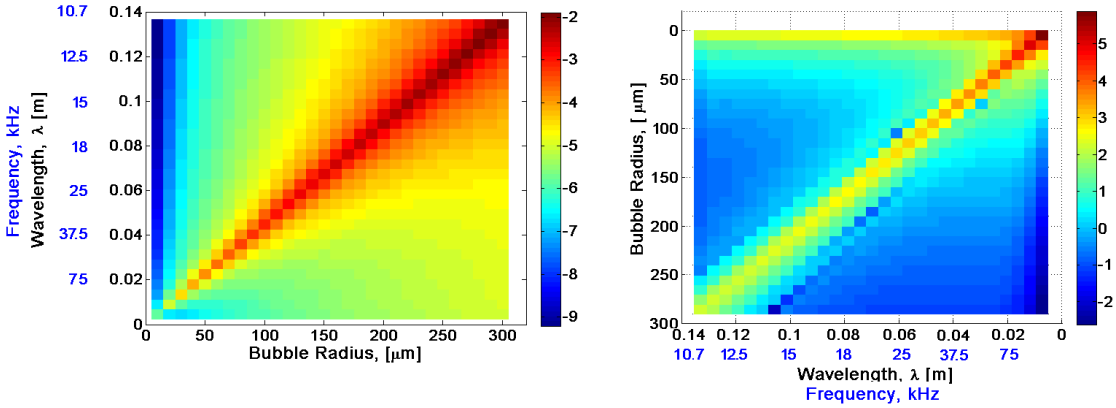

Fig. 3.1. Left: $\log_{10}(\mathbf{K})$, a 2-D representation of the extinction cross section computed for the range of bubble radii present in ψ_{tri}. Right: $\log_{10}(|\ \mathbf{K}^{-1}\ |)$ This figure is shown with frequency in kHz, and bubble radius in [μm]. This figure shows frequency in kHz, and bubble radius in [μm].

square and invertible, its inverse is denoted by $\mathbf{K}^{-1}$ (instead of $\mathbf{K}^{+}$ in Eqns. 3.9 and 3.10), and is found by the same procedure as $\mathbf{K}^{+}$.

While this particular example is relatively easy to invert using MatLab's built-in functions (*e.g. inv* or \ (matrix left division operator)), many cases involving real data arise that require some form of regularization in order to obtain a suitable inversion. Techniques similar that presented in Sec. 3.1.2 may be applied to the eigenvalues of a square $\mathbf{K}$ [8, 17, 18]. The methods of 'zeroing' or truncating the eigenvalues of $\mathbf{K}$ may be used to obtain a more stable solution, but still remove pertinent information from the resulting bubble population estimate.

The right panel of Figure 3.1 shows $\log_{10}$ of the magnitude of $\mathbf{K}^{-1}$ (as computed from $\mathbf{K}$ shown in Fig. 3.1). The antidiagonal contains large values for small radii and higher frequencies, and decreases with larger radii and lower frequencies. The antidiagonal in the inverted matrix is proportional to the bubble population at the respective knot radii. The right panel of Fig. 3.1 also shows that the attenuation at all frequencies is comprised of contributions from each range of radii present in the $\mathbf{K}$-matrix, especially for small bubbles (top row).

Figure 3.2 presents the result of applying Eqn. 3.10 (with $\mathbf{K^{-1}}$ instead of $\mathbf{K}^{+}$) to the attenuation curves presented in Fig. 2.6. The blue lines are the example bubble populations shown in Fig. 2.7. The red circles are the estimated population from Eqn. 3.10. The estimated population at the interior radii (between about 30 [μm] and 290 [μm]) matches the example bubble population (ψ_{tri} and ψ_{PL}) with very little error. Deviation at the smaller bubble radii are common with this type of inversion [10], partially resulting from the discrepancy between f_R and f'_R.

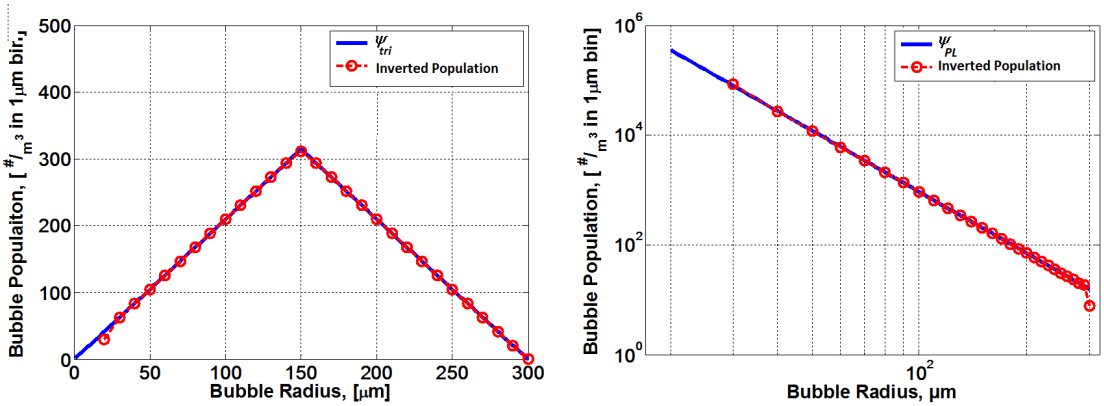

Fig. 3.2. Comparison between known and estimated bubble populations by applying the Commander & McDonald inversion method. Blue lines indicate the *a priori* populations (Left: ψ_{tri}, Right: ψ_{PL}), red dots indicate the population estimate. Bubble populations in this figure are shown in $\left[\frac{\#}{\mathrm{m}^3}\right.$ in a **1** μ**m bin**$\left.\right]$.

3.2 Caruthers *et al.* Method

A method for iteratively estimating $\psi(a)$ was presented by Caruthers *et al.* in [9], hereafter referred to as the Caruthers method. This procedure relies on an initial approximation that assumes attenuation is predominantly due to bubbles near resonance. After estimating the bubble population, the full theory (Eqns. 2.20 and 2.21) is applied to calculate attenuation due to the estimated bubble population, which is then compared to the measured attenuation. A correction is made to the estimated bubble population based on the difference between the measured and estimated attenuation. These steps may be repeated until the bubble population estimate sufficiently reproduces the measured attenuation.

3.2.1 Mathematical Derivation

Caruthers begins with an equation for the attenuation coefficient for a known population of bubbles,

$$\alpha_b(\omega) = \frac{2\pi c_o}{\omega} \int_0^\infty \frac{a\delta\ \psi(a)\ da}{\left[\left(\frac{\omega_R(a)}{\omega}\right)^2 - 1\right]^2 + \delta^2} \qquad \text{in } \left[\frac{\mathrm{Np}}{\mathrm{m}}\right], \tag{3.12}$$

where all variables are consistent with the previous presentations. Eqn. 3.12 is equivalent to Eqn. 2.20, with $\delta_{Rr} = ka_R$, with the exception that Eqn. 3.12 has a coefficient of 2 instead of 4. The origin of this discrepancy is unclear, however it leads to a different result than that reported in [9], [4] and [13], thus a coefficient of 4 is assumed in the remainder of this derivation.

A number of assumptions are applied to Eqn. 3.12 based on a generic in-water environment in order to eliminate its dependence on several factors. The goal is to find a simple equation for bubble population in terms of measured attenuation. First, assume that only bubbles very near resonance contribute significantly to the attenuation, which is generally true given the peaked

nature of the extinction cross-section (see Fig. 2.5). This assumption has been made for the case of attenuation due to ship wakes [4]. The assumption fails for larger bubbles and high frequencies, in which geometric scattering can dominate. The Czerski & Farmer method detailed in the next section does not make this assumption and thus better accounts for the effects of geometric scattering. Second, assume that the bubble population changes slowly about the resonant radius, which effectively means that the bubble population is smooth. This also guards against discontinuities in the bubble population estimate. Third, assume the effects of surface tension can be neglected. Surface tension becomes important for bubbles smaller than 10 [μm] [4], which are resonant above 300 kHz and are not of interest to us in the data presented in Ch. 4. Fourth, assume that bubble damping remains constant. Since the extinction cross section is largest in magnitude at resonance, the damping is at a minimum (approximately where δ_r and δ_t cross in Fig 2.2), we assume $\delta \simeq \delta_{Rr}$ ($= 1.36 \times 10^{-2}$, *see:* Ch 28 of [4]).

By making these assumptions, starting with Eqn. 2.20 (6.4.2 from Clay & Medwin [11]), and observing only bubbles with radii of, and slightly larger or smaller than a_R by some amount ϵ, the bracketed term in the denominator of Eqn. 2.20 is approximated as

$$\left[\left(\frac{a_R}{a}\right)^2 - 1\right]^2 \approx \frac{4\epsilon^2}{a_R^2}, \tag{3.13}$$

recognizing that $\frac{f_R}{f} \approxeq \frac{a_R}{a}$.

Then, Eqn. 3.13 can be substituted into Eqn. 2.20, and a trigonometric identity yields

$$\int_0^\infty \frac{da}{\left[\left(\frac{a_R}{a}\right)^2 - 1\right]^2 + \delta^2} \approx \frac{\pi a_R}{2\delta_R}. \tag{3.14}$$

For further details regarding the approximations in Eqns. 3.13 and 3.14, see Appendix A.

Thus, Eqn. 3.12 simplifies to

$$\alpha_b(\omega) = \frac{4\,\pi^2\,a_R^3\,\psi(a_R),}{\delta_{Rr}} \qquad \text{in} \left[\frac{\text{Np}}{\text{m}}\right], \tag{3.15}$$

and by employing Eqn. 2.21, and recalling $\delta_{Rr} = ka_R = \frac{2\pi f a_R}{c}$, the attenuation per unit distance becomes

$$A_b(f) \approx \frac{4.34\,\pi\,c\,a_R^2\,\psi(a_R)}{f} \qquad \text{in} \left[\frac{\text{dB}}{\text{m}}\right]. \tag{3.16}$$

To complete this derivation, substitute $a_R = \frac{3.25\sqrt{1+0.1z}}{f}$ (from Eqn. 2.2) into Eqn. 3.16

$$A_b(f) \approx \frac{144\,c\,\psi(a_R)\;[1+0.1z]}{f^3} \qquad \text{in} \left[\frac{\text{dB}}{\text{m}}\right], \tag{3.17}$$

where $c \approx 1500\ \left[\frac{\text{m}}{\text{s}}\right]$. Since the goal is to estimate the number of resonant bubbles causing attenuation at a given frequency, simple algebraic manipulation yields

$$\psi(a) \approx \frac{4.6 \times 10^{-6}\, f^3\, A_b(f)}{(1+0.1z)} \qquad \text{in} \left[\frac{\#}{\text{m}^3} \text{in a 1m bin}\right] \tag{3.18}$$

where $\psi(a)$ is an estimate of the number of resonant bubbles within a specified volume. f is the frequency (in Hz) at which the attenuation, $A_b(f)$ $\left[\frac{\text{dB}}{\text{m}}\right]$, is known. For the remainder of this thesis Eqn. 3.18 will be referred to as the resonant bubble approximation, or RBA.

Caruthers states that the body of experimental results indicate that many underwater bubble populations are in the form of power-laws, and that the RBA can successfully be applied to these distributions. Also, recall that we made the assumption that the bubble population is a smooth function of bubble radius. For this reason only the power-law example population will be illustrated. Also, Medwin states that assuming a constant damping factor at resonance leads to underestimating the attenuation when the order of the power-law is ≤ -4 [13]. Commander & Moritz discuss overestimations in the population due to neglecting off-resonance scattering, which includes both near resonance scattering and geometric effects [16]. Note that the approximate solution (RBA) is still based upon a solution to the Fredholm integral similar to Eqn. 3.4.

3.2.2 Implementation

Caruthers *et al.* developed an iterative method for finding the bubble population from attenuation measurements at discrete frequencies. The RBA was shown to produce bubble populations that inadequately reproduced the measured attenuation, but successive approximations of the bubble populations allows for corrections that significantly increase the ability to reproduce the measured attenuation.

We now define a set of operators in order to clearly describe the method. The attenuation due to a bubble population is found by applying the formal theory (FT) from Eqn. 3.1. Assuming that the "true" bubble population is known (in theory), then the "true" attenuation ($A_t(f)$) can be calculated by applying the formal theory to the "true" bubble population ($\psi_{\mathbf{t}}$), or,

$$A_t(f) = FT(\psi_t(a)) \qquad \text{in} \left[\frac{\text{dB}}{\text{m}}\right]. \tag{3.19}$$

Note that $A_t(f)$ in Eqn. 3.19 is the same as $A_b(f)$ in Eqn. 2.21. In practice, ψ_t is unknown, and the method is applied to a set of frequency-dependent attenuation measurements ($A_{measured}(f)$). However, for the following illustration, we assume that ψ_{PL} is the bubble population in order to directly compare the resulting bubble population estimate with ψ_{PL}.

The resonant bubble approximation is used to estimate the "true" bubble population from measurements of attenuation; it is an approximation to FT^{-1}. By employing the RBA as an operator, this is expressed symbolically as

$$\psi_{RBA}(a) = RBA(A_t(f)) \approx FT^{-1}(A_t(f)) = \psi_t, \tag{3.20}$$

where ψ_{RBA} is the resulting population estimate from applying RBA to the measured attenuation.

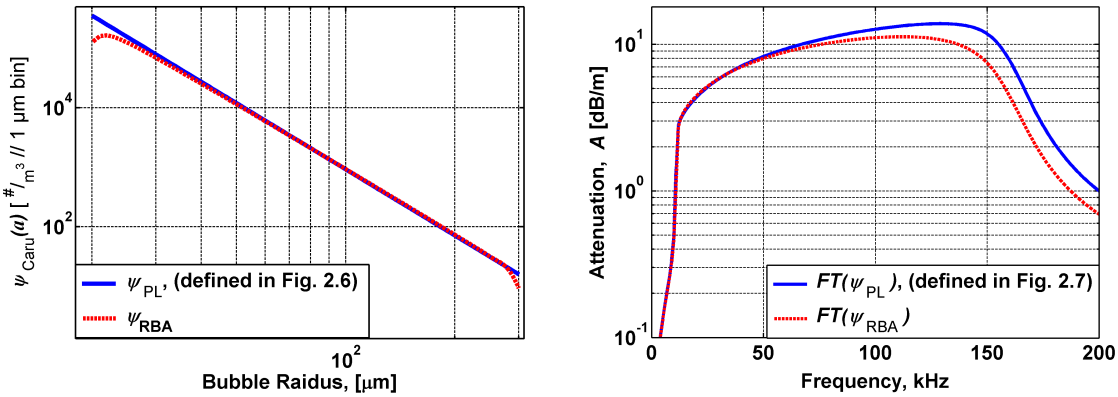

Fig. 3.3. Power-Law Bubble Population and Attenuation from the First Iteration via RBA using Caruthers *et al.* Method. This estimate of the bubble population (ψ_{RBA}) agrees well with the majority of the ψ_{PL} bubble population, but underestimates the boundaries of ψ_{PL}, and is unable to precisely recreate the attenuation curve above 100 kHz. Bubble populations plotted in this figure are shown in $\left[\frac{\#}{\mathrm{m}^3}\ in\ a\ \mathbf{1}\ \mu\mathbf{m\ bin}\right]$.

For the remainder of this thesis, $A_x(f)$ and $FT(\psi_x(a))$ will be used interchangeably.

Since this derivation neglects the effects of surface tension and viscosity, applying the RBA to very small bubbles ($\leq 20[\mu\mathrm{m}]$) consistently misrepresents their populations. The Caruthers method works best on power-law type bubble populations, thus the following example will utilize only the power-law bubble population (ψ_{PL} in Fig. 2.6), that has been truncated below 20 [μm].

The attenuation used in this example was calculated using $FT(\psi_{PL}) = A_{PL}(f)$, which was presented in Fig. 2.7. The left panel of Figure 3.3 compares ψ_{PL} to the results of applying the RBA to $FT(\psi_{PL})$. The bubble population estimate, ψ_{RBA}, is consistent with ψ_{PL} between 40 and 270 [μm], but is not a good match at the bounds of ψ_{PL}. There is a very slight departure for radii below 40 [μm], and a more prominent divergence for radii below 25 [μm]. Bubbles larger than 270 [μm] also suffer from boundary underestimation.

The right panel of Fig. 3.3 shows the attenuation estimate calculated using $FT(\psi_{RBA})$ ($=A_{RBA}(f)$, in red) as well as the attenuation calculated from the example bubble population (Fig. 2.6, or, A_{PL}) Attenuation for the lower frequencies (corresponding to bubbles with $a \approx 300$ [μm]) is almost indistinguishable between $FT(\psi_{PL})$ and $FT(\psi_{RBA})$.

The degree to which $FT(\psi_{PL})$ and $FT(\psi_{RBA})$ differ at higher frequencies is a visual indication of the shortcomings of the resonant bubble approximation. Since the RBA assumes that only resonant bubbles are contributing to attenuation, the discrepancy between the attenuation curves is due to a mis-estimation of the bubble population resonant at that frequency. For example, underestimating the number of small bubbles leads to an underestimation of attenuation at high frequencies. This estimated bubble population differs from the *true* population, ψ_{PL}, by some amount, which is defined as the error population, ψ_ϵ, as

$$\psi_\epsilon = \psi_{PL} - \psi_{RBA}. \tag{3.21}$$

Since FT is a linear operator, we can claim that

$$FT(\psi_{RBA}) = A_{RBA}(f) = FT\left[\psi_{PL} - \psi_\epsilon\right] = A_{PL} - FT\left[\psi_\epsilon\right], \tag{3.22}$$

By slight algebraic manipulation and the approximation that $RBA[A_x] \approx FT^{-1}[\psi_x]$, the error population is found to be the difference between the measured attenuation and $FT[\psi_{RBA}]$, which results in an approximation of the error population by

$$\psi_\epsilon = FT^{-1}\left[A_{PL} - A_{RBA}\right] \approx RBA\left[A_{PL} - A_{RBA}\right] \triangleq \psi_\epsilon\prime \tag{3.23}$$

Since the true error between ψ_{PL} and ψ_{RBA} cannot be calculated, the error is approximated as ψ'_ϵ. This error population is added to ψ_{RBA} in an effort to correct the estimated population in the direction of the true population (which is unknown in applying the Caruthers method to measured attenuation). Figure 3.4 presents an estimate of ψ'_ϵ obtained by applying Eqn. 3.23 to $A_{RBA}(f) = FT(\psi_{RBA}$ and $A_{PL}(f) = FT(\psi_{PL})$. The portion of the plot in black indicates an underestimation in the RBA population ($+\psi'_\epsilon$), and the red indicates overestimation ($-\psi'_\epsilon$). The red portion of the curve will be subtracted off of ψ_0, and black will be added. The resultant population is

$$\psi'_t = \psi_0 + \psi'_\epsilon. \tag{3.24}$$

where ψ'_t indicates a better estimate of the true bubble population.

The result of correcting the bubble population to first order is shown in the left panel of Fig. 3.5, where ψ'_t is indicated by the green line. The correction clearly improves upon ψ_{RBA} for small radii, and while less visible, it also improves ψ_{RBA} for the large radii. The bounds

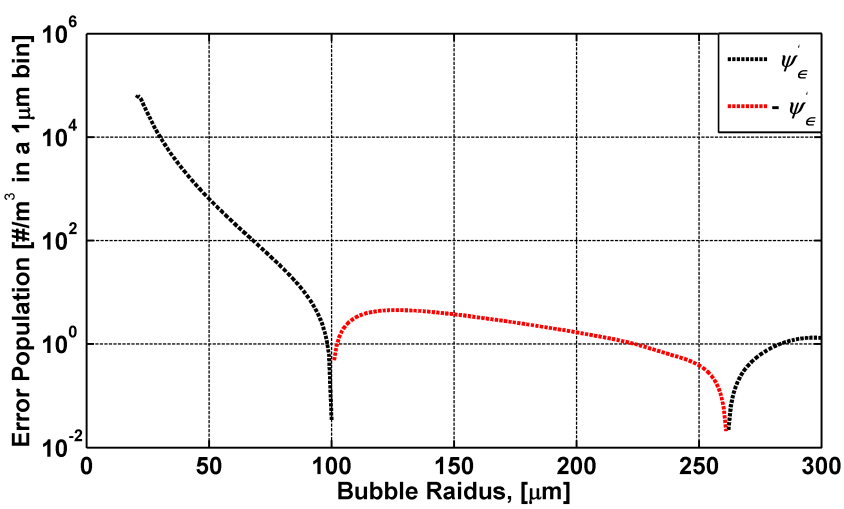

Fig. 3.4. Estimate of error population, $\psi'_\epsilon(a)$. Bubble populations plotted in this figure are shown in $\left[\frac{\#}{\mathrm{m}^3}\ in\ a\ \mathbf{1}\ \mu\mathbf{m\ bin}\right]$.

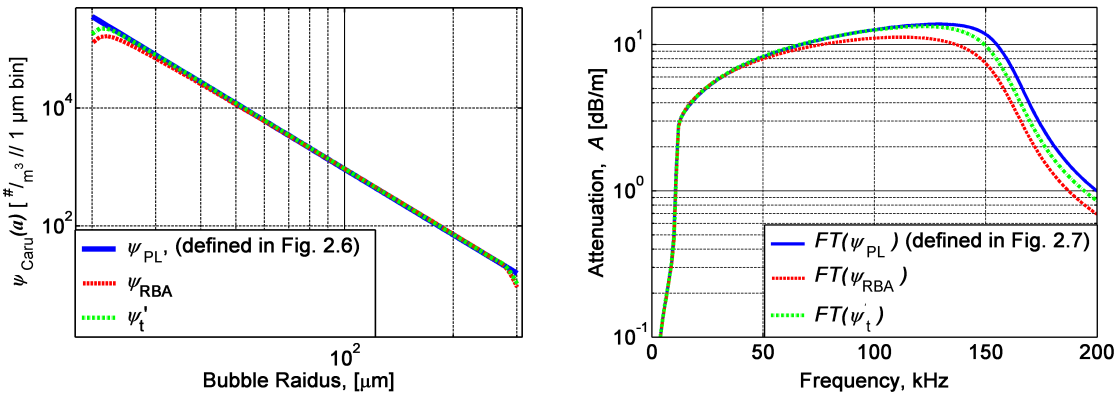

Fig. 3.5. Bubble population estimate (left) and attenuation (right) after iteration using Caruthers *et al.* method for the power-law population presented in Fig. 2.6. Improvement in estimating the bounds of the bubble population is visible, and the resulting attenuation shows an improvement at higher frequencies. Bubble populations plotted in this figure are shown in $\left[\frac{\#}{\mathrm{m}^3}\ in\ a\ \mathbf{1}\ \mu\mathbf{m\ bin}\right]$.

of the population are the most affected by this correction. Improvement is also visible in the attenuation shown in the right panel of Fig. 3.5. The increase in small bubbles causes an increase in attenuation at high frequencies, resulting in better agreement with $FT(\psi_{PL})$.

If $FT(\psi_t')$ matches A_{PL} sufficiently well, there is no need to further iterate this process. If, however, a better match is desired, then the procedure presented in Eqn. 3.20 through Eqn. 3.23 can be utilized to find a second-order bubble density correction, ψ_ϵ''. This process can be repeated until either the measured attenuation is reproduced, or the process fails to yield further correction.

3.2.3 Caveats

3.2.3.1 Boundary Error

Caruthers states that in order to achieve a reasonable estimate at the boundaries of the measured attenuation, a quasi-continuous attenuation curve that extends beyond the boundaries of the measurement is needed. This is due to the resonant bubble-only assumption, in which off-resonance effects result in an underestimation at the bounds of both bubble population and attenuation estimates. For this reason, extrapolating the attenuation measurements to higher and lower frequencies is necessary. The particular method used to extrapolate the attenuation data is a user preference. An example utilizing this type of extrapolation is used in the data presented in Sec. 5.1.

3.2.3.2 Spacing in a-domain

If the difference between two adjacent knot radii, da, is too large, the resulting bubble population may be insufficient to reproduce the measured attenuation. This is due to not having dense enough knot radii (for definition of knot radius, see Section 3.1.1) to represent the entire frequency

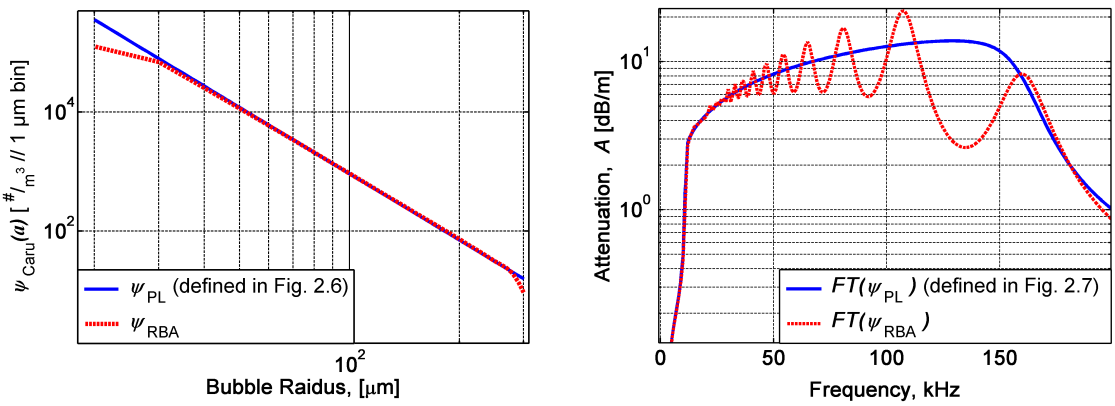

Fig. 3.6. Coarse spacing in the small radius region of the a-domain results in severe ringing in the calculated attenuation. This example uses linear spacing in the a-domain (represented on a logarithmic scale). Bubble populations plotted in this figure are shown in $\left[\frac{\#}{\mathrm{m}^3}\ in\ a\ \mathbf{1}\ \mu\mathbf{m\ bin}\right]$.

spectrum of interest, resulting in variability and ringing in the attenuation estimate. Figure 3.6 shows an exaggeration of this effect. The left panel shows bubble population as estimated by the RBA (ψ_{RBA}); where knot radii are indicated by red circles. For this example, $da = 10$ [μm]. The right panel shows the attenuation calculated by the formal theory. The striking feature in Fig. 3.6 is that the attenuation due to small bubbles is poorly estimated. There are visible oscillations in the A_{RBA} (red curve) relative to the measured attenuation (A_{PL}), and large differences in magnitude of attenuation at frequencies corresponding to the knot radii. This is an effect of the selection of the bin size for the smaller radii. Bubbles near resonance absorb and scatter energy, and when da becomes too large, the span between resonant frequencies become large.

One possible solution is to vary da in the a-domain. While it is convenient to maintain a constant da (equal spacing for entire range of knot radii), a suitable solution is to generate a bubble radius spectrum with two sections: one where bubbles less than a chosen size are not spaced equally (generally dictated by resonant frequencies at which attenuation was measured), and above which knot radii are spaced equally. With an appropriate choice of da and the threshold knot radius, this compromise is sufficient to reproduce the desired attenuation smoothly without over- or under-representing one particular region of the knot radius spectrum. For the example in Fig. 3.6, $da = 10$ [μm] is sufficient to match the measured attenuation ($FT(\psi_{PL})$) for frequencies less than 30 kHz (which corresponds to $a \geq 100$ [μm]), using a da of less than 10 [μm] may be necessary to appropriately reproduce $A_{PL}(f)$ above 30 kHz. This is discussed further in 5.2.1.

3.3 Czerski & Farmer Method

The Czerski & Farmer or 'sequence' method was developed with the goal of better estimating the number of small bubbles (≤ 20 [μm]) under breaking waves or otherwise in the upper ocean [10]. A consideration that has not been addressed in Caruthers' method is that attenuation at high frequencies may not be due entirely to small resonant bubbles, but also to large bubbles

scattering geometrically.

3.3.1 Assumptions

The Czerski method accounts for the effect of geometric scattering on bubble population estimates. Geometric scattering occurs when large bubbles are present and high frequencies are used. Large bubbles are capable of geometric reflection of high frequencies (where $ka \gg 1$), leading to ambiguity as to whether scattering was caused by small resonant bubbles or geometrically scattering large bubbles. By observing the effect of large bubbles on the measured attenuation first, this method seeks to more accurately evaluate the bubble population by reducing contamination from geometric scattering.

The resonant bubble approximation developed in Sec. 3.2 is based upon a series of assumptions that neglected surface tension and thermal conductivity, which resulted in underestimating the number of small resonant bubbles. However, perhaps the principle cause of misrepresentation of small bubble populations can be geometric scattering by large bubbles. The acoustic cross section demonstrates this effect very clearly. Figure 3.7 shows the acoustic cross section for bubbles with radii between [1 1000] [μm] in the presence of a 1.1 MHz sonar (left panel). The extinction cross section is represented by the black line, which is proportional to attenuation due to a single bubble. While the resonant peak is at 3 [μm], if bubbles larger than $a \geq 100$ [μm] are present within the same volume, attenuation and scattering caused by the 3 [μm] bubble can be dominated by bubbles with larger radii. The right panel of this figure shows a comparison of the extinction cross section for a single bubble with a radius of 3 [μm] and 300 [μm], for frequencies between [1 3000] kHz. The extinction cross section for a 3 [μm] bubble is several orders of magnitude below that of the 300 [μm] bubble, even at resonance. Even if the number of larger bubbles is several orders of magnitude less than the number of smaller bubbles, geometric and off-resonance scattering can dominate the cumulative attenuation from all bubble sizes present in the water.

Since the Czerski method attempts to better estimates the number of bubbles with very small radii, a slightly different bubble population will be used to illustrate this method. Figure 3.8 shows the bubble population used for this example, and how it compares to the power law distribution used in the previous examples. The left pane shows that the slope and density of bubbles are unchanged, however the lower bound is now 3 [μm], where for the previous population it was at 20 [μm]. The right panel compares the attenuation calculated for the two bubble populations. The population which contains radii between [3 20] [μm] causes significant attenuation out to approximately 1 MHz, instead of dropping off at about 140 kHz. A bubble with $a = 3$ [μm] resonates at approximately 1.16 MHz (via Eqm. 2.4). The population is unchanged between [20 300] [μm], and similarly attenuation between [10 140] kHz is largely unchanged. Slightly higher attenuation seen around 140 kHz is due to bubbles slightly smaller than 20 [μm].

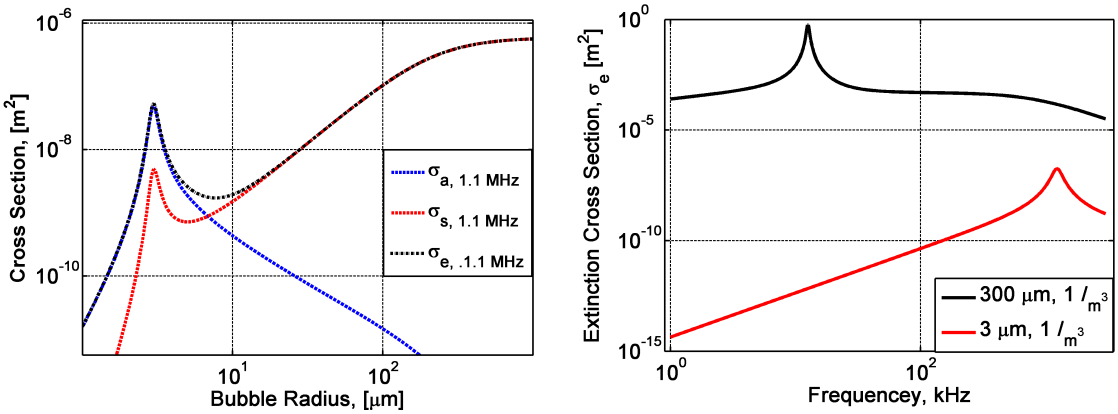

Fig. 3.7. Acoustic cross sections for a 1.1 MHz (left, where σ_a, σ_s, and σ_e are the **a**bsoption, **s**cattering, and **e**xtinction cross sections, respectively). Comparison of the extinction cross sections of single bubbles with radii of 3 [μm] and 300 [μm] over a range of [1 10^6] Hz (right). In this figure, bubble radius is shown in [μm], and frequency in kHz.

3.3.2 Method

Execution of the Czerski method is similar to the first approximation of the Caruthers Method. The RBA is used to estimate the number of bubbles for a single resonant radius at a time, then its contribution is subtracted from the total attenuation.

Attenuation measurements spaced evenly in frequency are suggested for this method, which may require interpolation of the attenuation measurements.[2] The relationship between f_R and a_R is essentially an inverse (with a correction for radii < 600 [μm], see Eqn. 2.4), thus it necessitates a significantly larger number of knot radii for the inversion. This increase in the number of knot

[2]Interpolation of the attenuation measurements requires assuming the attenuation is a smooth function of frequency, which was also assumed for the Commander & McDonald and Caruthers *et al.* methods.

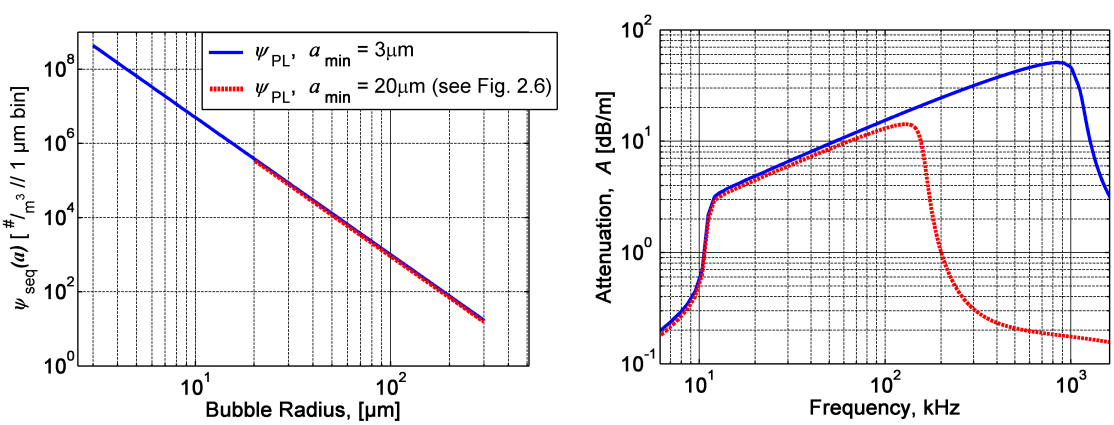

Fig. 3.8. Bubble population and corresponding attenuation used to illustrate the Czerski method. This population is very similar to the power-law type population used in previous examples, however extends to lower radii thus has a void fraction of 5×10^{-6} compared to 1×10^{-6} for the previous examples. Bubble populations shown in this figure are in $\left[\frac{\#}{\mathrm{m}^3}\ \textit{in a}\ \mathbf{1}\ \mu\mathbf{m\ bin}\right]$.

radii is primarily to avoid excessive ringing as demonstrated for the Caruthers method in Fig. 3.6.

The RBA is invoked for only one frequency at a time, first at the lowest (measured) frequency ($f_i|_{i=1}$, which corresponds to the largest knot (resonant) radius ($a_i|_{i=1}$)) in order to obtain an estimate for the population at the largest knot radius bin, or

$$\psi(a_i) = RBA(A_{i-1}(f))|_{f=f_i}, \quad \text{where} \quad i = 1 \tag{3.25}$$

where ψ_i is the bubble population at a_i, and $A_{i-1}|_{i=1} = A_0$ is the measured (or interpolated) attenuation, $A_0 = A_{PL}$ in this case. Next we calculate attenuation over the entire frequency band due to only bubbles of size a_i via the formal theory, $A_{a_i}(f) = FT(\psi(a_i))$ (see Eqn. 3.19). Then we can define a new attenuation,

$$A_i = A_{i-1} - A_{a_i}, \quad \text{where} \quad i = 1. \tag{3.26}$$

where the remaining attenuation, A_i, contains information about the bubble population at all bubble sizes *other* than at radius $a_{R,i}$. Figure 3.9 shows this process visually. For this example, $i = 3$ will be used to demonstrate the process. First, RBA is applied to the attenuation measurement using Eqn. 3.26 (for $i = 3$):

$$\psi(a_3) = RBA(A_2(f))|_{f=f_3=12.6kHz} = 28.3 \times 10^6. \tag{3.27}$$

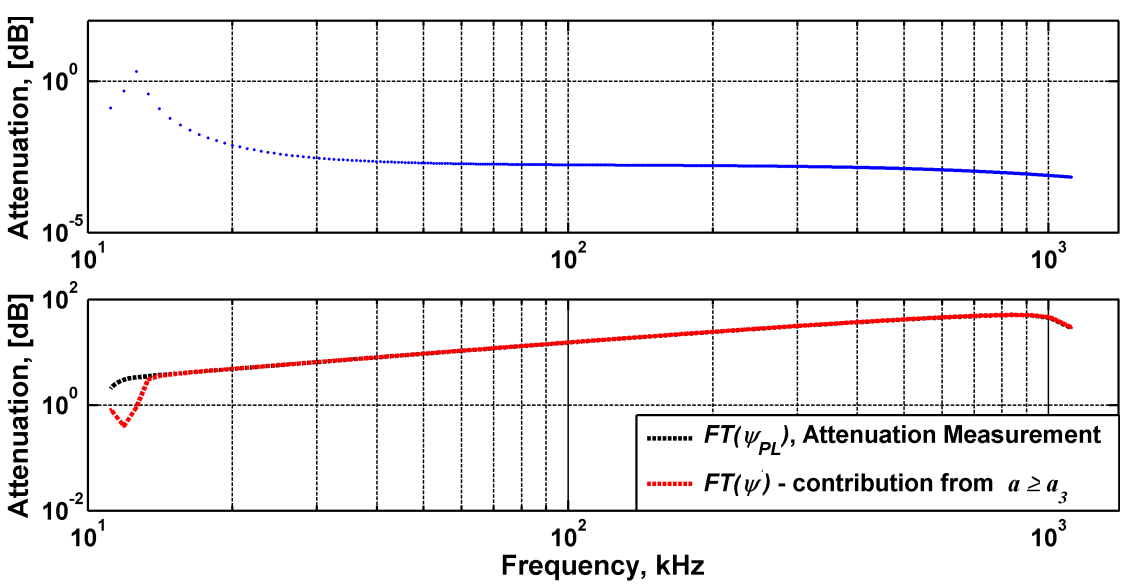

Fig. 3.9. Illustration of Czerski method by using the largest bubble size. The upper panel shows the attenuation due to bubbles of $a = 267$ [μm], as predicted by RBA followed by FT. The lower panel shows the attenuation measurement (black dashed line), and the attenuation after removing the contribution due to bubbles larger than $a = 267$ [μm] (red dashed line).

Here the attenuation at 12.6 kHz is 3.3 $\left[\frac{\text{dB}}{\text{m}}\right]$, and the resulting $\psi(a_3) \approx 28.3 \times 10^6$ $\left[\frac{\text{bubbles}}{\text{m}^3}\right.$ in a 1 m bin]. Using the formal theory (Eqn. 2.21), attenuation is calculated over the entire frequency span of the attenuation measurement, and is shown in the top panel of Figure 3.9. This curve shows the contribution of a single bubble size over a large range of frequencies (meaning that it exhibits the peaked nature of Fig. 3.7, with a sharp drop-off to either side of the peak). While the attenuation at higher frequencies ($f \approx 1$ MHz) due to bubbles resonant at or near 12.6 kHz may not be very significant, contributions from all bubble sizes can be cumulatively significant.

The next step is to remove the attenuation due to $\psi(a_3)$) from the measured attenuation over the entire frequency range. This procedure is shown in the lower panel of Figure 3.9. Here, the black line represents the measured attenuation, while the red line is attenuation after subtracting $FT(\psi(a_3))$ (in the top panel). The result is $A_3(f)$.

Once the remaining attenuation ($A_3(f)$) is calculated, the index i is increased by one, and then the process is repeated (Eqns. 3.25 through 3.26) for the next smallest bin size. This iterative process is repeated until the smallest bin size has been accounted for. The total bubble population estimate, $\psi_{seq}(a)$ is the combination of each individual population (the $\psi(a_i)$s).

The resulting bubble population estimate, ψ_{seq}, from this method should be a reasonably accurate reproduction of ψ_{PL} (which is being estimated from $FT(\psi_{PL})$. Again, the formal theory can be used to estimate the attenuation caused by this population. Figure 3.10 presents this comparison. The left panel compares ψ_{PL} (blue) and ψ_{seq} (red), and the right panel compares the attenuation with corresponding colors. A small departure at the upper and lower bounds of the bubble population occurs, resulting in a slight overestimation of the attenuation at low frequencies, and underestimation at high frequencies. This departure, in part is due to the very high resolution of knot radii used for the inversion. For this example, a very high resolution in bubble radius is feasible. However, for real attenuation measurements, the resolution is limited by factors discussed in Chapter 4. Another contributor to the mis-estimation of attenuation is that this bubble population contains a large range of radii, including very small bubbles, which means that some geometric scattering is present. Overall, the Czerski method produces a population estimate (ψ_{seq}) that agrees well with the bubble population to within a desired tolerance for a population containing very small bubbles.

3.3.3 Comments

Again, only the power law example population was used to illustrate the Czerski method. A better illustration would utilize a bubble population that exploits the geometric scattering effect, as in [10]. Figure 3.11 (reproduced form [10]) shows the results of applying these three inversion methods to a bubble population that contains small bubbles, and exploits the possibility of geometric scattering. Each panel in Fig. 3.11 has the same three known bubble populations, which are shown as solid lines, and inverted results are shown with correspondingly colored circles. The vertical axes are bubble density (n here is bubble population), followed by the method used to obtain the results in the plot. The top panel shows the results of the Caruthers *et al.* method.

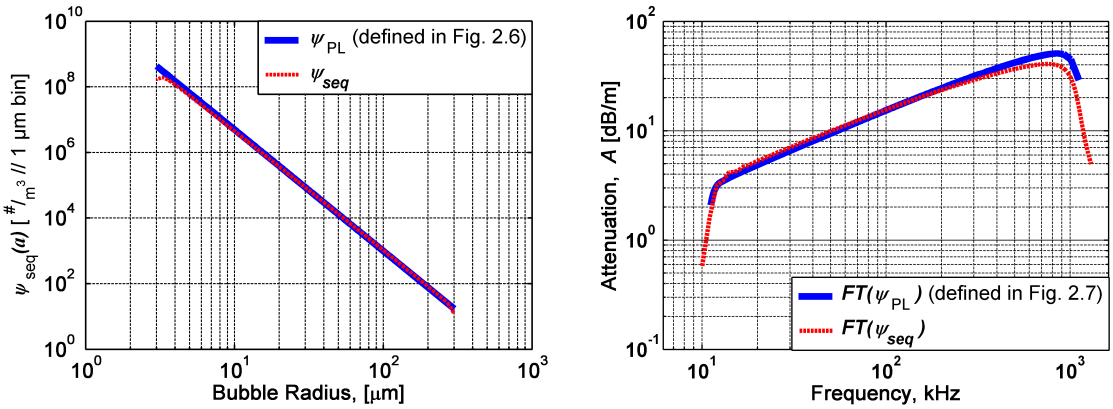

Fig. 3.10. Result of the Czerski method. Left: bubble population estimate (ψ_{seq}, red) compared to ψ_{PL} (blue). Right: attenuation calculated from the population estimate (ψ_{seq}, red), and from ψ_{PL}(blue). Bubble populations in this figure are shown in $\left[\frac{\#}{\mathrm{m}^3}\ in\ a\ \mathbf{1}\ \mu\mathbf{m\ bin}\right]$.

The middle plot shows results from the Czerski method (labeled 'n,sequence'), and the bottom plot is the Commander & McDonald (or SVD) method.

The results from the Commander & McDonald method (or SVD, bottom panel) are obviously inferior to the other two, and are only able to track the blue and red populations for a very narrow region between [30 50] [μm] with suitable resemblance to the ground-truth distribution. This estimate could probably be improved with further regularization of $\mathbf{K}$.

Results from the Caruthers method (top panel) show greater agreement between the *a priori* (ψ_{PL}) and inverted distributions, although there are varying degrees of success with different population slopes. It appears that the steeper the slope (more negative), the better the performance. The red line, which has a positive slope up to 50 [μm] does not invert properly below 25 [μm], and the no-slope case (in blue) shows a strong and variable departure for bubbles smaller than 6 [μm] (likely due to f'_R vs. f_R). However they are consistent for larger bubbles. The black line has the steepest slope (most negative), and performs the best of the three trial populations.

The Czerski method (middle panel, 'n,sequence') shows better consistency at larger bubble radii for all cases, but still departs from the ground truth populations for the blue and red lines near the same points that the Caruthers method failed. The Czerski method does improve on the stability of the solution for small bubbles in the blue population, since the result is consistent and remains positive. Czerski also provides a vertical blue dashed line indicating the cutoff for valid population inversion. This occurs at approximately 8 [μm], at which point 90% of the attenuation occurring above the resonant frequency of an 8 [μm] bubble is due to geometric scattering, thus invalidating the population results for smaller radii.

The Czerski method provides advantages over the Commander & McDonald and Caruthers methods. The Caruthers method does not account for the possibility of geometric scatter during its iterative process, however geometric scatter is accounted for when applying the formal theory to compare the attenuation data with that caused by the inverted population. The Commander & McDonald method performs poorly for these populations, only reproducing a very small range

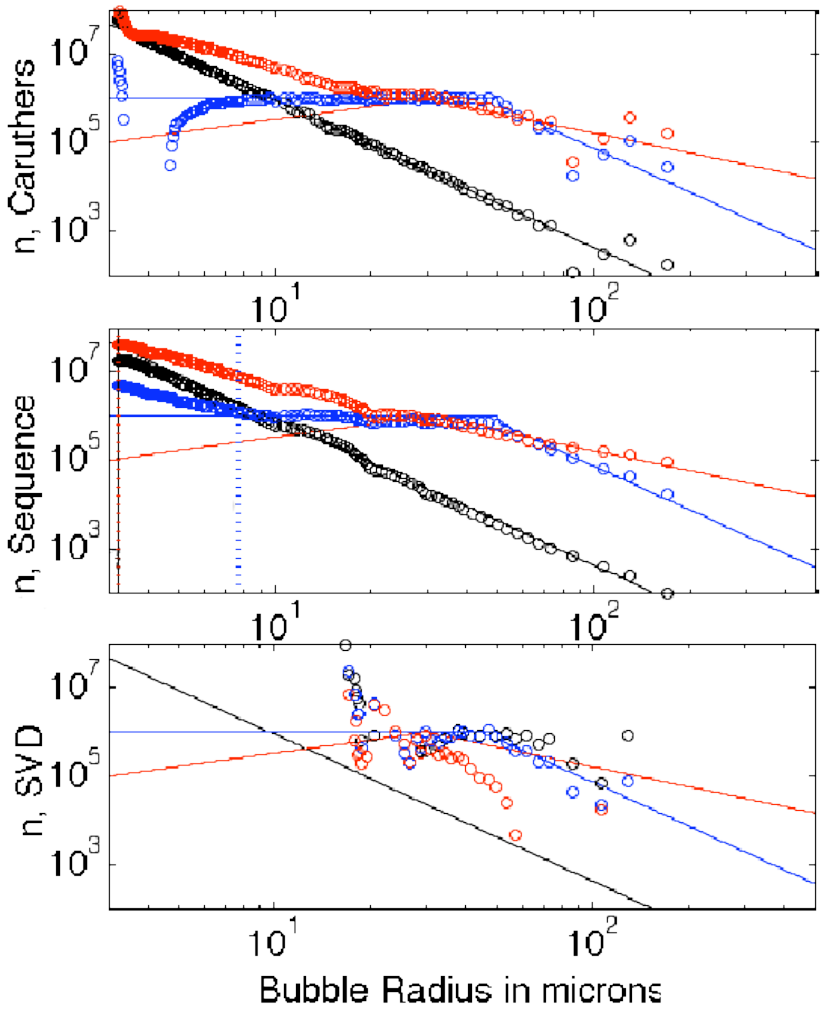

Fig. 3.11. Comparison of three population inversion methods for three different inversion methods. Bubble populations shown in this figure are in $\left[\frac{\#}{\mathrm{m}^3}\ \textit{in a}\ \mathbf{1}\ \mu\mathbf{m\ bin}\right]$. (Reproduced from [10] with permission of the author.)

of the populations correctly.

Czerski claims that her method "allows the calculation of the attenuation limits," and while it more accurately reproduces the bounds of the data than the Commander & McDonald and Caruthers methods, some fall-off is still present [10]. Reproducing the bounds of the data still requires some extrapolation [10]. The slope of the resulting bubble population can be an indicator of the presence of geometric scatter. Geometric scatter is proportional to a^2, so if the slope of the bubble population is steeper than -2 then geometric scatter is likely not a problem [10] [11].

3.4 Summary of Inversion Methods

The methods presented in this chapter all provide estimates of the bubble population from a measurement of attenuation through bubbly water. Each method has advantages and limitations. They are each able to yield a bubble population that sufficiently reproduces the sample populations presented in Ch. 2.

The Czerski & Farmer and Caruthers *et al.* methods are more stable than the Commander & McDonald method since they do not require the inversion of a likely ill-conditioned matrix. For the SVD method, regularization is required to varying degrees depending on the error tolerance for a given application.

Each method assumes the attenuation is due largely to resonant or near-resonant bubbles. This poses limits upon the validity of the results as it can ignore important scattering properties of large bubbles. The Czerski method attempts to remove the effects of geometric scattering to minimize the contamination of the estimated bubble population inherent in a RBA-only approach for very small bubbles. The Czerski method also makes it easier to track which bubbles are responsible for the largest contribution to the total attenuation at a given frequency.

Also, it should be noted that even though only the Commander & McDonald method technically requires inversion of a system of matrix equations, all of these methods are referred to as *inversion* methods (or *inversions*) in that they all seek solutions to the inverse bubble acoustic problem. This means that each method to attempts to *invert* the formal theory (FT) in order to obtain a bubble populations from a set of acoustic attenuation measurements.

Chapter 4

Measurement of Acoustic Attenuation Through, and Backscatter from, a Bubble Cloud Generated by an Underwater Explosion

4.1 Introduction

In May 2008 a series of measurements were made in a freshwater-filled quarry in central Virginia to investigate the bubble cloud produced by an underwater explosion. This is accomplished by exploiting measurements of the acoustic attenuation through, and backscatter from, the bubble and particulate cloud left behind at or near the charge location after an UNDEX event. Two charges consisting of approximately 13.6 [kg] of PBXN-111 explosive compound were detonated. These detonations, referred to as events 1 and 2, occurred at 2008 May 6 at 1631 and May 7 at 1219 (local time, EST), respectively. The data and analysis presented in this thesis pertain to the forward-loss attenuation and backscatter measurements for events 1 and 2.

After estimating attenuation due to the bubble cloud, the techniques presented in Ch. 3 are used to obtain an estimate for the bubble population present in the UNDEX cloud in Ch. 5. Characteristics of the UNDEX bubble population are then used to develop a temporally and spatially evolving model of the UNDEX bubble cloud (Ch. 6). This model is then used to predict the energy backscattered by the bubbles, which is compared with backscatter measurements.

4.2 2008 Quarry Test Geometry

The quarry is an instrumented facility operated by NTS corporation [19], where underwater explosive tests are regularly performed. Figure 4.1 is an overhead view of the quarry taken from Google Earth^{TM}. The quarry is approximately 450 [m] long by 100 [m] wide. The explosive charge was suspended at 15.2 [m] (50 [ft.]) depth, about 30 [m] from the end of a dock, as pictured in Figs. 4.1 and 4.5.

The test geometry is shown in Figure 4.2. The upper panel shows an overhead of the charge location (labeled UNDEX) and acoustic transducers. An acoustic projector, and an array of nine backscatter hydrophones are located approximately 38.1 [m] (125 [ft.]) southwest of the charge location. The backscatter hydrophones are arranged in three vertical arrays, each consisting of three elements. Seven forward-loss hydrophones are located opposite the charge location, also 38.1 [m] from the charge location. A cylindrical metal object was present in the water during this series of tests. Its position varied from test to test, but only one location is shown. Also, a multibeam sonar placed at the charge depth (hung off of the end of the dock), was used to image the region of UNDEX from approximately 33 [m] (100 [ft.]) away from the charge location. The depth separation for the hydrophones is detailed in the lower panel of Figure 4.2.

Two types of hydrophones were used to record in-water acoustic levels during this test; thirteen Reson TC4032s, and three International Transducer Inc. (ITC) 6080Cs. The two hydrophone types required different pre-amplification and signal isolation systems, but data from both were recorded using the same digital-to-analog converter and recording system. Signals from the Reson hydrophones were passed through a 100 Hz to 100 kHz band-pass filter, which also applied a 16× gain, and the ITC hydrophones were passed through a separate but similar

Fig. 4.1. Satellite image of the water-filled quarry with coordinate overlay. Arrows indicate the relative direction and the location of the dock, which is discussed in the measurement geometry in Fig. 4.2. (Image from Google Earth^{TM} on Feb 1, 2007)

filter. A 16-bit National Instruments analog-to-digital converter (ADC) with an input range of $\pm$ 5 [V] was used to record voltage levels from all 16 hydrophones at 250 $\frac{\text{kSamples}}{\text{s}}$.

In Figure 4.3 the forward loss and backscatter hydrophone configurations are shown. The forward loss vertical array consists of five elements equally spaced between 7.9 [m] (26 [ft.]) and 15.2 [m] (50 [ft.]) depth. One element was located 3.7 [m] (12 [ft.]) on either side of the vertical array at 11.6 [m] (38 [ft.]) depth to make up a three element horizontal array. This configuration was chosen to measure attenuation over different paths in a vertical plane containing the UNDEX.

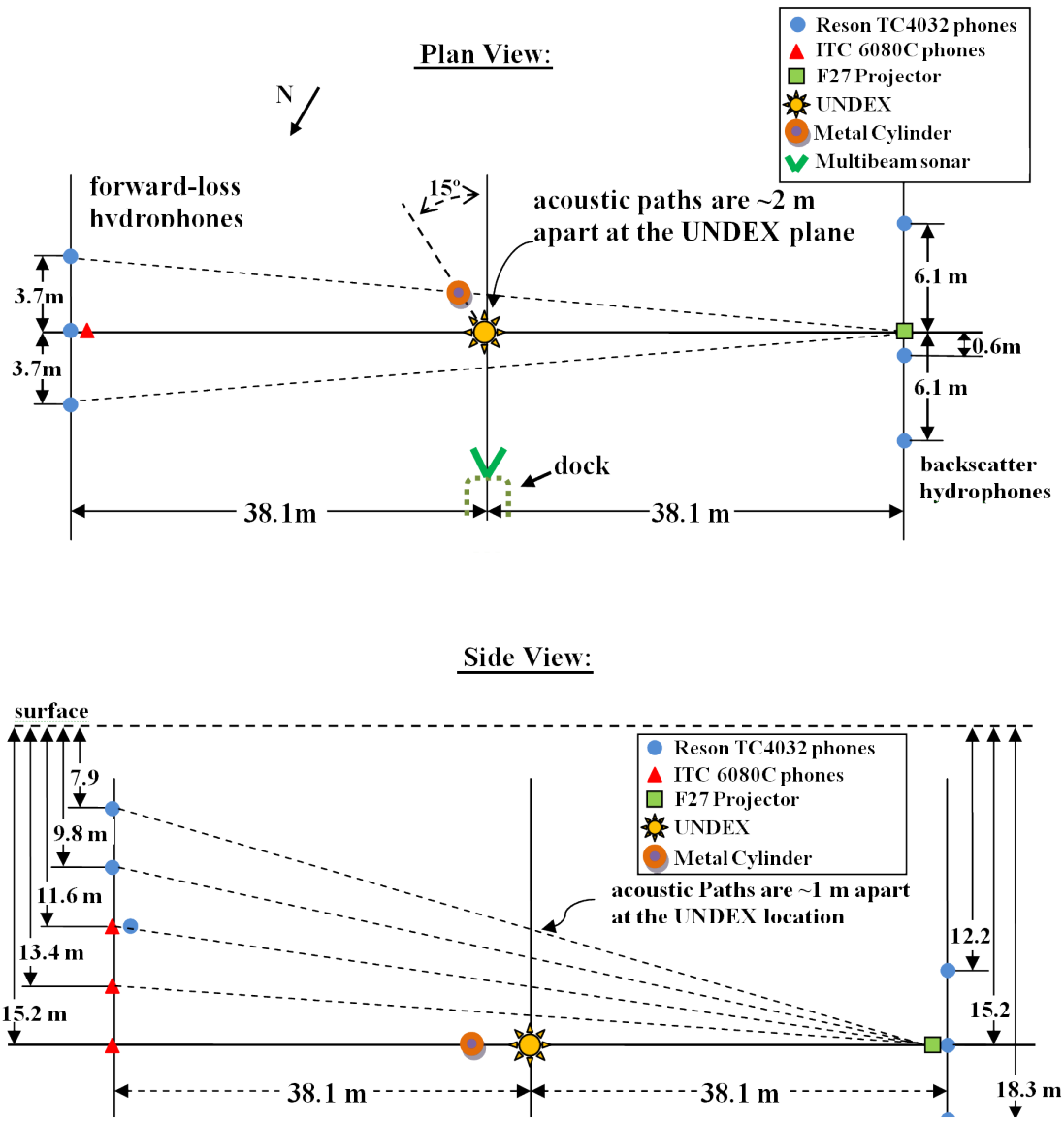

Fig. 4.2. Geometry for the May 2008 Quarry Test. Plan view (upper) showing the horizontal spacing of transducers with respect to the UNDEX location. Side view (lower) showing the vertical distribution of sensors.

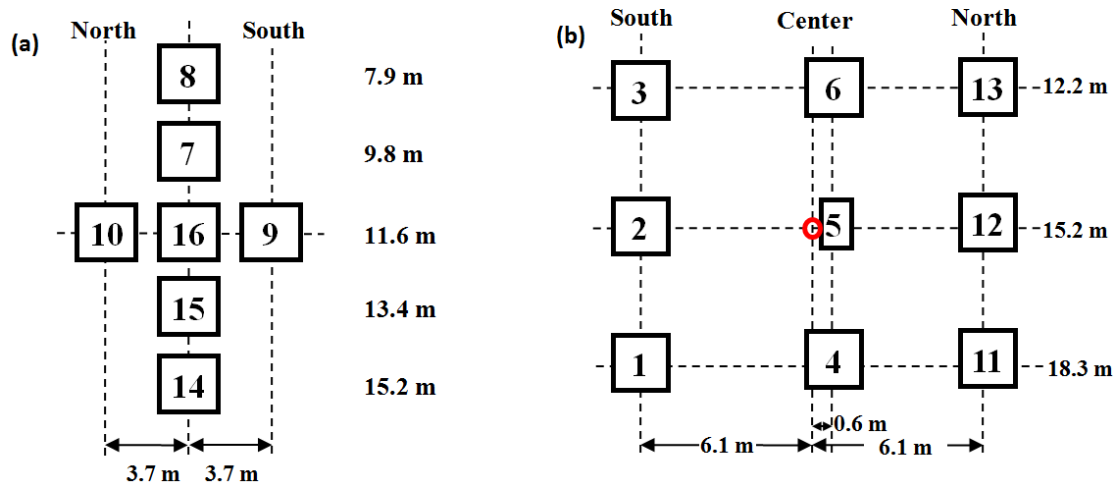

Fig. 4.3. Forward loss (a) and backscatter (b) hydrophone configurations. The hydrophone numbers (*i.e.* data channel) is noted by the number inside of the boxes. Their arrangement and relative location corresponds to the layout in Fig. 4.2. The red circle indicates the projector location.

The direct acoustic ray-path from the projector to the forward loss hydrophones is approximately 76.2 [m] (250 [ft.]). The sound speed for this environment is approximately 1485 $\left[\frac{\text{m}}{\text{s}}\right]$, which leads to a one-way (straight-line) propagation time of about 51 [ms]/footnoteThe assumption of homogeneous propagation media is applied to this data since a sound-velocity profile was not obtained for these measurements. Sound speed is estimated using a surface temperature measurement of 21°C on 2008 May 7 at 12:19 local time. $\left(\approx \frac{76.2\,[\text{m}]}{1485\left[\frac{\text{m}}{\text{s}}\right]}\right)$.

The backscatter array consists of three vertical arrays, each with three hydrophones. They are spaced 6.1 [m] (20 [ft.]) apart, and span between 12.2 [m] (40 [ft.]) and 18.3 [m] (60 [ft.]) depth. The acoustic projector is at 15.2 [m] (50 [ft.]) depth in the center of the backscatter array. Due to the location of the projector, the central vertical array was displaced 0.6 [m] (2 [ft.]) to the north. All UNDEX events occurred at 15.2 [m] (50 [ft.]) depth.

Figure 4.4 shows the relative size and location of the gas cavity in the moments following detonation of the explosive [7]. The lower panel of the figure will be explained first. When detonation occurs, a pressure shock wave travels through the explosive medium and propagates into the surrounding water. At the moment of detonation, one can assume that the entire charge is transformed into a high-temperature, high-pressure gas cavity, called the "gas-globe'[1]. The pressure inside of the gas-globe is much greater than the surrounding water, causing the globe to rapidly expand outward. The momentum of the water will cause the gas-globe to extend beyond the pressure-equilibrium with the water. The globe will reach a maximum diameter and subsequently collapse. When the gas-globe reaches a minimum volume, the drag force is minimum and the gas-globe rises at its fastest rate; also, a positive pressure pulse is generated as the gas-globe rebounds and rapidly expands outward [7]. The gas-globe will continue to oscillate and migrate upward until it breaks the surface of the water. The pressure diagram (Fig. 4.4

[1]Helen Czerski, personal correspondence.

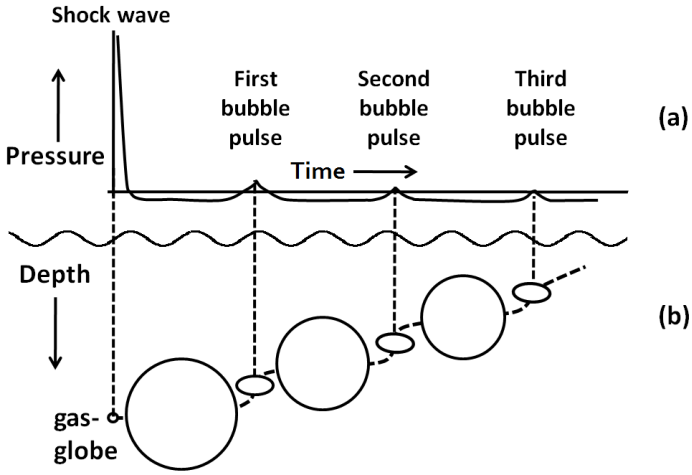

Fig. 4.4. Diagram of the size and position of the gas-globe moments after UNDEX. (a) Initial shock wave from UNDEX, and subsequent pressure waves due to the oscillation of the gas globe. (b) Pulsations and migration of the gas-globe. (After [20].)

(a)), can be summarized as a large shock wave from the initial detonation followed by a series of gas-globe generated pressure pulses that decrease in magnitude as the globe migrates to the surface. The period of oscillation (determined by the period between pressure waves) is a function of charge size and depth.

Figure 4.5 shows the surface of the water before and after an UNDEX as seen from the shore. The left panel is an image taken immediately before UNDEX. The dock, labeled (a) in this image, protrudes about 30 [m] from the shore. A segmented network of 10 [cm]-diameter PVC piping, labeled (b), can be seen in the left panel of Figure 4.5. The purpose of this structure is to suspend concentric semi-circular arrays of pressure sensors at the charge depth to measure the yield of the charge detonation (not pictured here, though visible in multibeam sonar data, Sec.

Fig. 4.5. Image the quarry immediately prior to (left) and approximately 2.5 seconds after the UNDEX (right). (Photo by author.)

4.3.3). The PVC structure is designed to separate after an explosion. Several white buoys (c) to the left of the PVC network are attached to a metal cylinder hanging vertically in the water. A small platform (visually indiscernible) floating immediately to the left of the PVC structure suspends the charge at 15.2 [m] depth.

The right panel of Figure 4.5 is an image taken approximately 2.5 seconds after UNDEX, when the gas-globe is seen breaching the surface of the water. The gaseous mixture begins to breach the surface within 2 seconds of the UNDEX, and reaches a maximum at about 2.5 seconds after UNDEX. The main globe ejection lasts for approximately one second, during which time the PVC structure and the white buoys are masked by the white cloud. After the cloud reaches a maximum, it falls quickly and the surface of the water remains visibly darkened due to bubbles and debris for several minutes after UNDEX.

4.3 Received Signals & Processing

The transducer arrays were comprised of sixteen hydrophones and one acoustic projector present in the water during the UNDEX events. A Navy standard F27 [21] projector was used to transmit a signal containing a linear frequency-modulated (LFM) and continuous waveform (CW) pulse before and after each UNDEX. Figure 4.6 shows the transmit pulse used in the quarry test. The top panel is a time-domain representation, and the lower panel is a spectrogram of the transmit waveform. The first signal is a 30 millisecond long LFM pulse, sweeping from 5 kHz to 65 kHz (at 2 $\frac{\text{kHz}}{[\text{ms}]}$). The LFM pulse is followed by 200 [ms] of no transmit, then by a 30 millisecond long 40 kHz CW pulse. Transmission of the 260 [ms] long signal will be referred to as a 'ping.' Each element of the measurement system is uniquely frequency dependent, having an amplitude-dependent frequency response. An *in-situ* measurement of the system allowed the transmit waveform to be amplitude shaded in a frequency dependent fashion as to maximize the drive level of the acoustic projector without distortion of the transmit waveform. Both the LFM and CW signals were amplitude-shaded in the frequency domain to control side lobes.

The signal was transmitted with a repetition rate of 0.75 [s] before and after each UNDEX event. Acoustic received signal levels were recorded for approximately three minutes before, and several minutes after each UNDEX. However, due to interference between the acoustic pulses and the pressure sensor measurement system, transmission of the acoustic signal was stopped for about two minutes leading up to charge detonation. Several cycles of the test waveform were transmitted between T-3 and T-2 minutes to obtain acoustic pressure levels prior to the introduction of bubbles debris due to UNDEX. During the no-transmit period, ambient acoustic background and the pressure waves from charge detonation were recorded. Transmission of the signal was typically re-established less than one second after detonation.

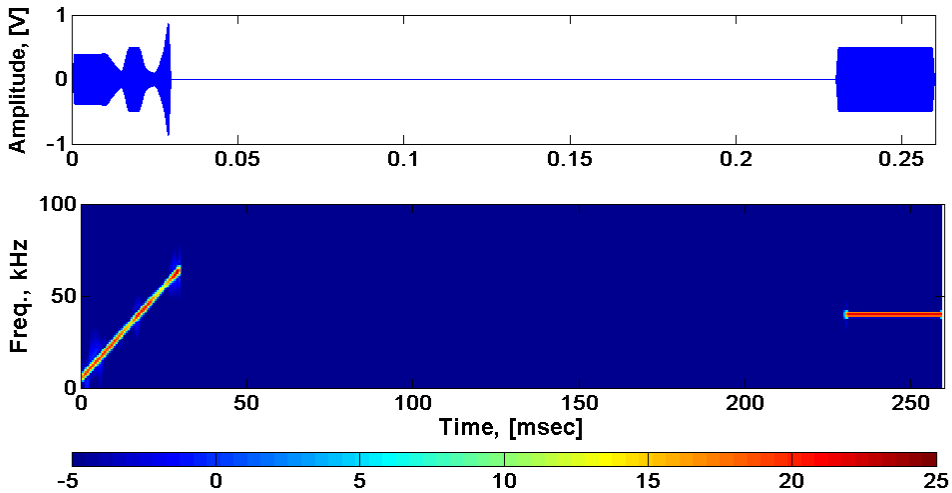

Fig. 4.6. Test waveform used in May 2008 quarry test. 30 [ms] long LFM pulse ranging from 5 kHz to 65 kHz, followed by 200 [ms] of no transmit, then a 30 [ms] 40 kHz continuous wave (CW) pulse.

4.3.1 Received Signals from Forward Loss Array

The left panel of Figure 4.7 shows a 0.55 second time record of the received signal from the forward-loss hydrophones. This ping was transmitted prior to event 2. Each of the five plots are labeled with the hydrophone make (Res for Reson, or ITC) and the corresponding depth of the hydrophone in meters. Received level is plotted in volts.

The first large amplitude signal of this received time series, labeled (a), is due to electrical contamination between the signal transmission and Reson hydrophone receive systems. The two Reson phones in the vertical array show a significant amount of transmit signal contamination, while the three ITC phones lack this feature as a result of their independent isolation system. A signal trigger was also recorded to indicate the duration of signal transmission, shown in red, is 'high' or approximately 5 [V] during the 260 millisecond signal transmission. This confirms that signal transmit and received signal contamination occur coincidentally. The LFM pulse is transmitted during the first 30 [ms] of when the trigger is 'high,' and the CW pulse occurs during the last 30 [ms].

The level of recorded contamination varies with hydrophone make and location, and in some cases is clipped at $\pm$ 5 [V]. This clipping is not an issue for the vast majority of the recorded data. However, the level is so high during some instances of the contamination that the precision filter and gain unit becomes overloaded and the recorded signal experiences a few milliseconds of drop-out, during which no acoustic signal is detected. Periods of dropout are usually less than 10 [ms] and generally do not interfere with reception of acoustic signals of interest. The drop-out becomes slightly more significant in the backscatter data, and will be discussed later.

The direct path received signal is expected to arrive about 54 [ms] after the start of signal transmission, which is seen in the region labeled (b). This agrees well with the prediction made

above, since the trigger goes 'high' at t=0 [s], and the direct path arrival begins at about 0.054 seconds. Due to the vertical span of the phones in the forward loss array, the direct path arrival is slightly delayed for shallower phones (compared to deeper phones). However, this path length difference only amounts to about one third of a millisecond difference in arrival time between the 15.2 [m] and 7.9 [m] hydrophones.

The signal amplitude variation across the phones is a function of the frequency dependent beam pattern of the acoustic projector and the hydrophone's response. As frequency increases during the LFM pulse, the beam-width becomes more narrow. At high frequencies, the main lobe of the projector's beam-pattern is not wide enough to span all of the vertical array phones, causing a visible dip in the received level in the shallowest hydrophone for a certain range of frequencies. At the highest frequencies ($\geq$60 kHz), the received level is a minimum at the 11.6 [m] phone, indicating the presence of a null in the transmit beam pattern in the direction of that hydrophone.

Since the UNDEX does not occur in a free field, but rather a very reflective stone quarry, a lengthy period of reverberation is seen following the LFM pulse, labeled (c) in Fig. 4.7, which is likely a combination of arrivals scattered from the surface of the water, bottom and side walls the quarry. The 30 [ms] CW transmit contamination can be seen in (d) starting at 0.23 [s], again most prominently for the Reson hydrophones. The direct path arrival for the CW pulse is shown in (e). The amplitude of the signal varies from being the highest, at about 2 [V] for the 15.2 [m] deep phone, to the lowest at about 0.75 [V] for the 7.9 [m] phone. It is important to note that the two hydrophone types have different sensitivities to the in-water pressure level. The lower 3 hydrophones are all ITCs, and thus have approximately the same sensitivity. The signal level increases with depth, indicating that the projector is pointed at the deepest receive hydrophone. A period of reverberation caused by the CW pulse can be seen in the region marked (f). While the quarry is very reverberant, the direct-path and scattered signals can be easily discriminated.

The right panel of Fig. 4.7 presents the received signal from the forward loss horizontal array of phones. These phones are all at 11.6 [m] depth and are labeled according to their relative cardinal position (*i.e.* North, Center, and South, see also Figure 4.3). These data show similar characteristics as the vertical array.

One particularly interesting point within the LFM arrival is the hydrophone response at higher frequencies ($\geq$60 kHz). The ITC transducer sensitivity begins to roll-off at about 45 kHz (-155 dB), and by about 60 kHz falls to -160 dB (re $\left[\frac{1\text{V}}{\mu\text{Pa}}\right]$) [22]. The Reson hydrophones do not begin to roll off until around 80 kHz [23]. This decreasing sensitivity is partially responsible for the decrease in received level at the late-end of the LFM arrival in the ITC phone (in comparison to the Reson phones). Acoustic pressure levels can be determined by applying hydrophone sensitivities to the received signals. The pressure level in dB (re: 1μPa, not shown) is higher at the center hydrophone than at either the north or south phones, indicating that the projector was aimed primarily at the center element of the horizontal array.

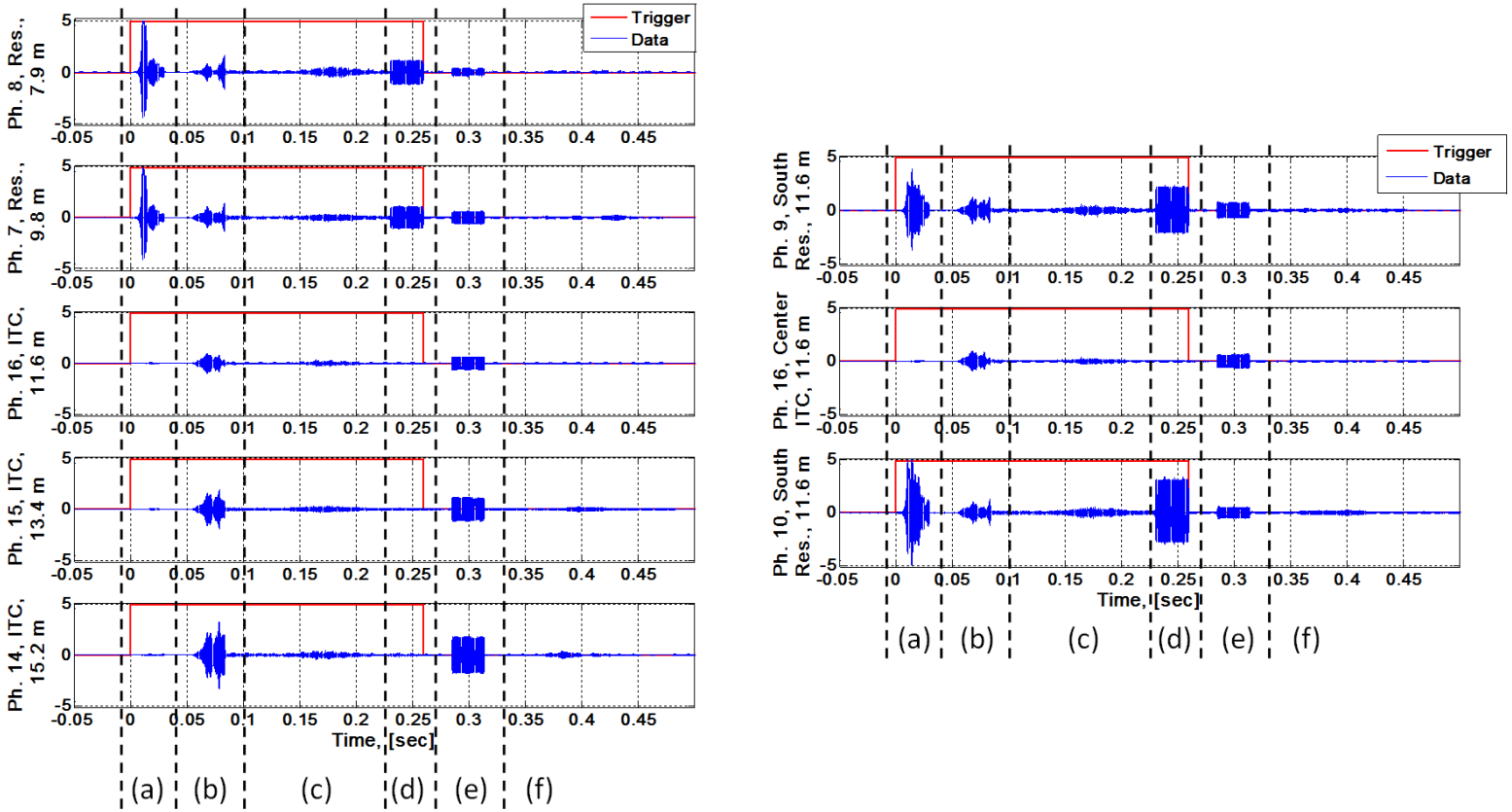

Fig. 4.7. Time series of signal received at the forward loss array of hydrophones. Left: Vertical Array. The shallowest two phones are Reson phones, lower 3 are ITCs. Right: Horizontal Array. The general regions of signal, signal contamination, and reverberation are segregated by vertical dashed lines though these figure. The red line indicates the time during which transmit occurred.

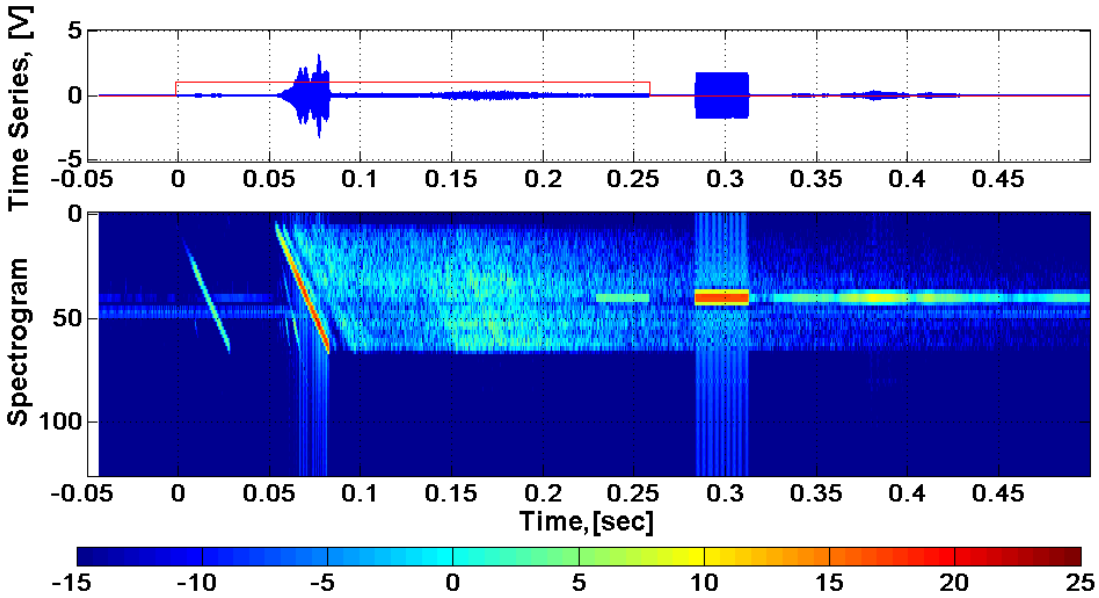

Fig. 4.8. Received signal time series (upper) and spectrogram (lower) for a pre-UNDEX ping, recorded by hydrophone 14, ITC, 15.2 [m] depth.

Figure 4.8 shows a time-series and spectrogram of a pre-UNDEX ping as recorded by the 15.2 [m] deep ITC phone. The data in these plots is the same as the lower left panel in Fig: 4.7. The spectrogram better visualizes the level of electronic contamination in the ITC phones for the direct-path and the reverberant arrivals. Significant background noise is present around 50 kHz throughout this time record. This is likely due to electronic noise within the measurement system, as it appears throughout time record, even during periods without signal transmission. Reverberation from the previous ping's 40 kHz CW pulse is intermittently visible in the first 100 [ms] of this time series. A particularly strong region of reverberation from the LFM pulse occurs between 0.15 and 0.2 seconds in the spectrogram, and can also be identified in the time series plot. Reverberation from the LFM pulse is present during the CW pulse direct-path arrival.

Discussion of the LFM and CW pulses will be separated for the remainder of this thesis, since the two types of signals require different processing techniques. The following sections detail the methods used to obtain received pressure level estimates for these received signals.

4.3.1.1 CW Received Level

After correcting for the sensitivity of the hydrophones, the RMS level of the direct path 30 [ms] CW pulse was tabulated for each ping. Figure 4.9 shows the RMS received level for the CW pulse for the vertical array in dB//1μPa for events 1 and 2. In order to conserve space and to ease comparison, plots for events 1 and 2 are presented side-by-side. The left half of this figure shows the vertical array measurement during event 1, and the right half during event 2. Detonation of the charge occurs near time 0 in these plots. Received level is only processed for times when the acoustic projector was transmitting, the void for approximately 2 minutes before

detonation ($-150 \geq t \leq 0$ seconds) is due to no transmit. The measurement system operator began transmitting the signal manually after detonation, so $t = 0$ of these plots occurs during the first ping, not the actual detonation of the charge, though transmission of the signal was restarted between 0.3 and 1 second after UNDEX.

The pre-UNDEX levels occurring between [-170 -150] seconds show only slight variability since the projector and hydrophones were stationary in the water. The shallowest hydrophone (at 7.9 [m]) is plotted in the top panel, and the deepest phone (at 15.2 [m]) in the lowest panel.

For both events, the first few of pings after UNDEX show much lower signal level at all depths. The 15.2 [m] deep phone shows approximately a 20 dB drop in level, and the 7.9 m phone shows approximately 60 dB loss for only one or two pings. The hydrophones are affected by the shock wave caused by the explosion, and comparison with Fig. 4.31 (hydrophone response to UNDEX, discussed in Sec. 4.3.4) indicates that these pings are likely not representative of the loss introduced by the bubble cloud, but rather the loss introduced by the hydrophone's (or other electronics') response to UNDEX, or possibly refraction of the sound wave due to large void fraction (discussed shortly).

For event 1, the deepest hydrophone (15.2 [m]) shows little to no drop in signal receive level after UNDEX, whereas during event 2 a drop of up to 5 dB lasts up to 25 seconds after UNDEX. The most shallow hydrophone (7.9 [m]) shows a more severe signal loss in both events. During event 1, the signal loss remains in excess of 10 dB for up to 30 seconds, then returns slowly to pre-UNDEX levels. Although the post-UNDEX level eventually stabilizes at approximately the pre-UNDEX value, there is markedly increased variability in level at the shallower phones, which indicates a persistent presence of bubbles and debris in the water in excess of 3 minutes post-detonation. This is a reasonable duration of level variability, since it takes approximately 3 minutes for a 250 [μm] bubble ($f_R \approx 18.8$ kHz) to rise from depth of UNDEX to pass through the field of view for the 7.9 [m] deep hydrophone [24].

The 7.9 [m] phone for event 2 shows a similar, but more substantial response to UNDEX, where consistent signal loss of up to 15 dB lasts for up to 50 seconds after UNDEX, and the approximate return to pre-UNDEX levels occurs after about 3 minutes. Received levels for all hydrophones during event 2 showed more variability, and took considerably longer ($\approx 2\times$) to return to pre-UNDEX values in comparison to event 1. It should be noted that events 1 and 2 were the same charge size. The reason for this is unknown, but will be discussed in some detail later.

There are several general trends that can be seen in the received level of the vertical array: Event 2 seems to have more of an effect at all hydrophones than event 1. The deepest hydrophone, which is at the same depth as the charge and the acoustic projector, sees the least change in signal level before and after the UNDEX for both events. The signal loss tends to increase in magnitude inversely with hydrophone depth. For event 1, the shallowest hydrophone (# 8, 7.9 [m]) shows the largest loss of received level due to UNDEX, with each subsequent hydrophone experiencing a lower level of signal loss. During event 2, the 11.6 [m] deep phone (# 16) shows the largest drop in received signal level, with decreasing levels of signal loss for shallower and

deeper hydrophones. This effect could be due to the two UNDEX events occurring at different times of day (event 1 at about 1630 EST, event 2 at about 1230 EST), resulting in a change in the sound velocity profile (SVP, not measured) between detonations, causing downward refraction of the acoustic energy.

Figure 4.10 presents the RMS level of the CW pulse for the horizontal array during events 1 (left) and 2 (right), in the same format as Fig. 4.9. The center panel, hydrophone 16, is the same data as plotted in Fig. 4.9. All three of these phones are located at 11.6 m depth. For both events, the south hydrophone (9) shows a very slight drop in received level for only a few seconds after UNDEX. The received levels post-UNDEX are considerably more variable than prior to UNDEX.

The north phone (10) experiences a drop in level during event 1, but appears to have a higher receive level after UNDEX. Phone 10 during event 2 shows about 12 dB of loss after UNDEX. The received level in this phone does not return to the pre-UNDEX value (for either event), which indicates that there is either: a) a large amount of debris and bubbles in the water attenuating the sound in excess of 200 seconds, or b) the projector-hydrophone geometry changed slightly as a result of UNDEX, causing a slight drop in the maximum possible receive level.

The center hydrophone (16) shows the most significant amount of loss due to UNDEX for both events. For event 1, received level drops by about 10 dB for about 20 seconds. For event 2, level drops in excess of 20 dB for the first few seconds after UNDEX. The phone returns to a near pre-UNDEX level within 40 seconds.

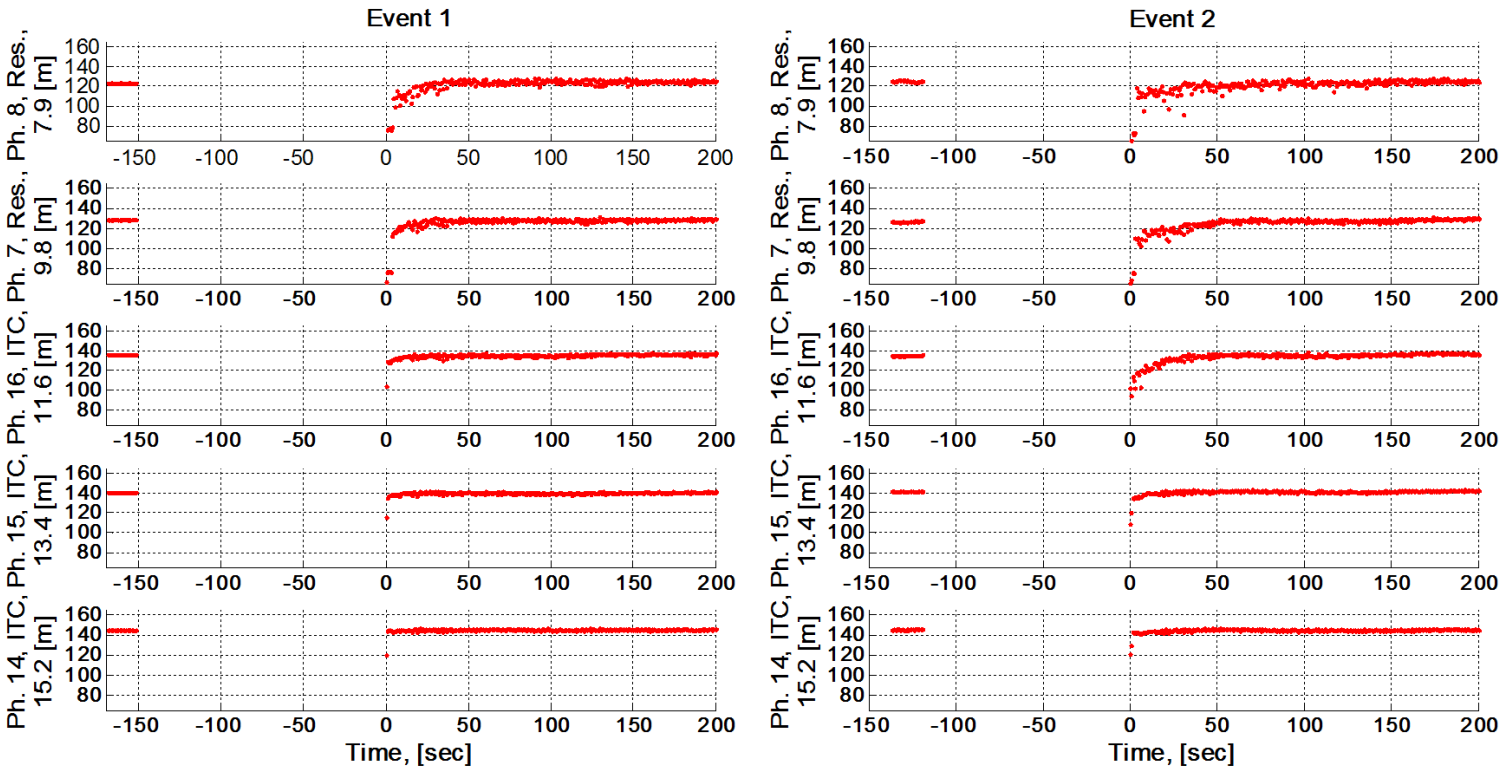

Fig. 4.9. RMS received level of the CW pulse (40kHz) at the vertical array during events 1 (left) and 2 (right).

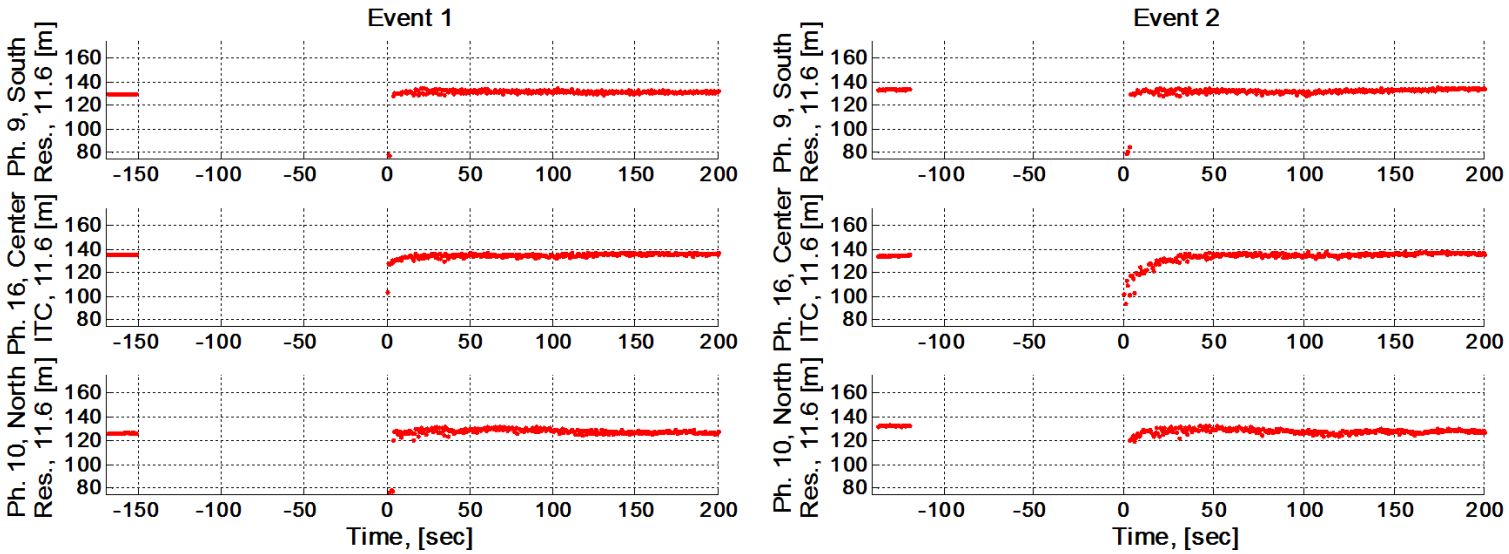

Fig. 4.10. RMS received level of the CW pulse (40kHz) at the horizontal array during events 1 (left) and 2 (right).

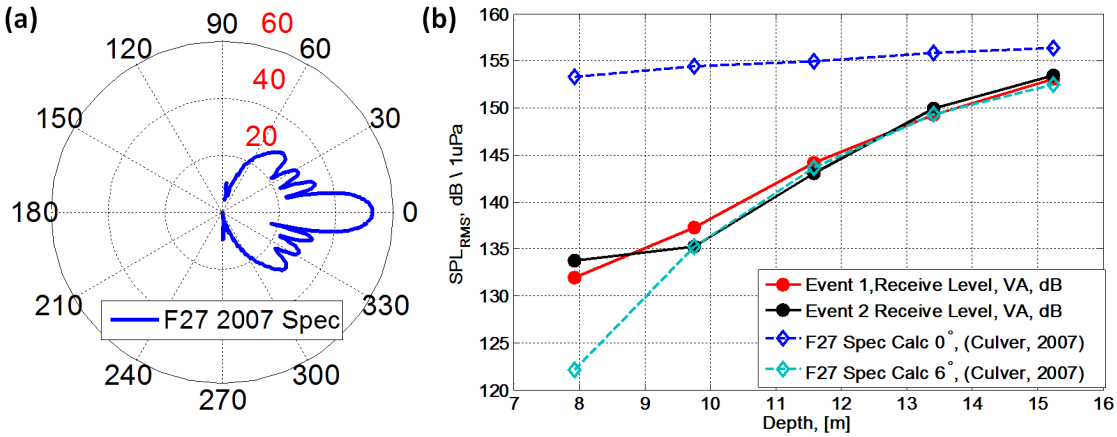

Fig. 4.11. a) F27 acoustic projector beam pattern at 40 kHz, 2007 ARL Penn. State measurement [25]. b) Measured and predicted RMS received levels at the vertical array (VA) of hydrophones. Measured RMS level vs receiver depth (prior to UNDEX) for event 1 (red) and event 2 (black). Predicted received level for the VA of hydrophones if projector aimed directly at 15.2 [m] hydrophone (0°, blue), and if the projector was pointed 6° below the horizontal (cyan).

As discussed for Fig 4.7, the pre-UNDEX receive levels for the vertical array are a function of the position and 'aiming' of the acoustic projector. The left panel of Figure 4.11 shows the calibrated beam pattern for the F27 projector at 40 kHz. The right panel of Fig. 4.11 shows SPL_{RMS} at the hydrophone locations, and two predictions of the received level. The red line indicate the SPL_{RMS} of the 30 [ms] CW pulse for the hydrophones at each receiver depth during event 1, black for event 2. The F27 transducer has a 3 dB beam width of about 11° at 40 kHz[2]. The blue curve is a prediction of the received level using the calibrated beam pattern for this projector assuming it was pointed directly at the 15.2 [m] deep hydrophone. The cyan line is the predicted received level if the projector was aimed ≈ 6° below the horizontal. This downward angle causes the received level at the 15.2 [m] hydrophone to be approximately 3 dB less than the anticipated on-axis received level (based on the transmit beam pattern). Consequently, the level at each of the shallower hydrophones was several dB lower than if the projector had been positioned directly on-axis with the lowest receive hydrophone. The the received level of the 7.9 [m] deep hydrophone is higher than predicted for both on-axis and pointing 6° downward. This discrepancy is likely due to an upward refracting sound speed profile, and not an ambient noise limitation. As stated in the beginning of this chapter, sound speed gradients are ignored due to lack of SVP data.

4.3.1.2 LFM Received Level

Obtaining received levels from the LFM pulse requires the application of signal processing techniques. This section demonstrates the matched filter technique used, and presents the received levels at 30 discrete frequencies between 5 kHz and 65 kHz. The attenuation is then estimated

[2]The calibration of the F27 transducer was verified by The Penn. State Applied Research Laboratory in 2007 [25].

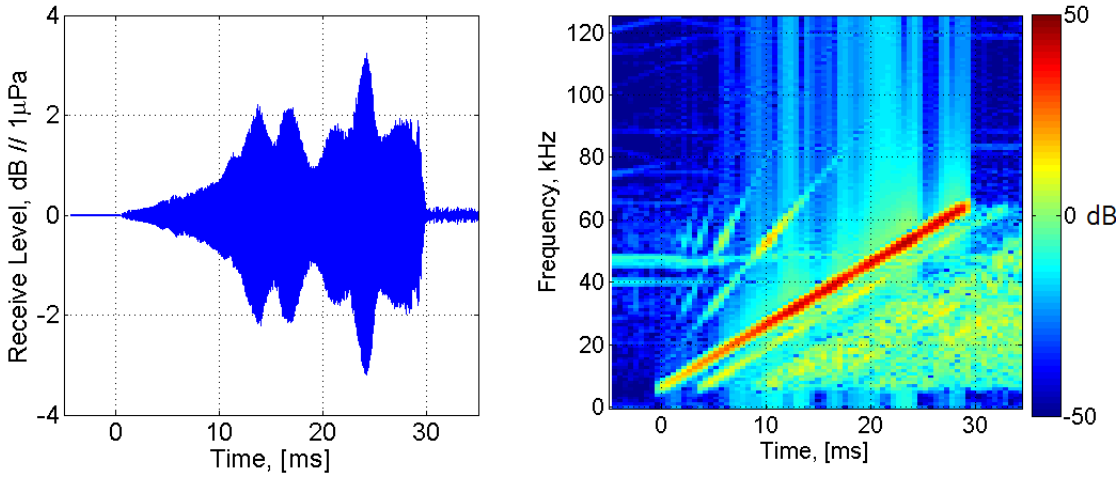

Fig. 4.12. Time series and spectrogram of the LFM pulse as recorded by the 15.2 [m] deep hydrophone (Ph # 14, ITC). $t = 0$ [ms] in this figure denotes the beginning of the direct path received signal (which occurs at approximately $t = 0.054$ [ms] in Fig. 4.8).

from the received levels similarly to the method used for the CW pulse.

Figure 4.12 shows the time series and spectrogram of the LFM pulse as recorded by the 15.2 [m] deep forward loss phone (Ph. 14) for event 2, shown in volts. Arrival of the direct path received signal begins at 5 [ms], and concludes at about 35 [ms], after which reverberation is present. The spectrogram shows an arrival approximately 4 [ms] after the direct path, which is a reflection from the surface of the water (path length difference of about $\frac{6.1[\mathrm{m}]}{1485\left[\frac{\mathrm{m}}{\mathrm{s}}\right]} = 4$ [ms]). Several higher order harmonics are visible during the direct path arrival, however they are within specification of the F27 transducer, which has a total harmonic distortion (THD) $\leq 2\%$[3].

The amplifier used to transmit the signal had a monitor channel that allowed monitoring of the voltage level used to drive the acoustic projector, but unfortunately this signal from the monitor channel is unusable due to two issues: 1) the signal was recorded during a test-run of the measurement system and the amplitude-shading of the test signal may have been modified between the recording of the monitor channel and the UNDEX events. 2) the monitor channel was not properly filtered before being passed to the analog-to-digital recorder, and thus is contaminated with higher order harmonics that aliased into the frequency range of interest. For these reasons, a mathematically generated replica of the transmitted LFM pulse was used in the signal cross-correlation process. This mathematical replica is shown in the left panel of Figure 4.13, and is a linear phase frequency domain signal that mimics the frequency-dependent amplitude of the acoustic signal that was transmitted by the acoustic projector[4].

[3]The underwater connector of the F27 malfunctioned some time between events 1 and 2, and had to be dried out, re-sealed prior to event 2. As a result, the projector was re-positioned prior to event 2. This short could have resulted in additional signal distortion during the data measured during event 1.

[4]This accounts for the F27 projector Transmission Voltage Response (TVR), and amplitude shading in the frequency domain with respect to the actual monitor channel signal [25]. We were, however, unable to correct for the projector's downward pointing angle in this replica, as it would affect each hydrophone differently. The correction made is an on-axis prediction of the projector's acoustic response.

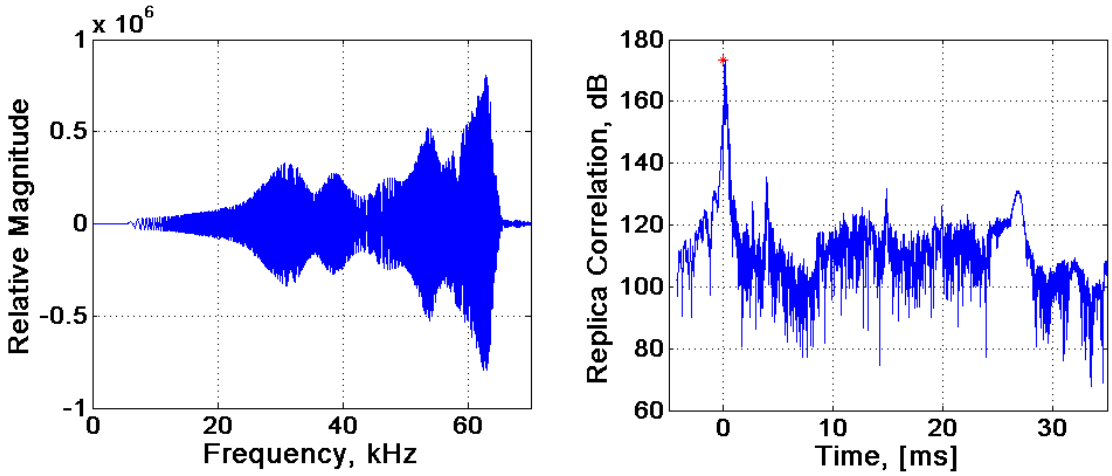

Fig. 4.13. Mathematical Replica shown in the left panel, this is used to cross-correlate the received signal to find the near exact time of direct path arrival. The right panel shows the cross-correlation of the mathematical replica & the LFM received signal for hydrophone # 14 (15.2 [m]) during event 2.

The right panel of Fig. 4.13 shows the result of cross-correlating the mathematical replica and the received LFM pulse for a pre-UNDEX ping recorded by hydrophone 14 during event 2. The red star indicates the maximum correlation during the direct path signal, which is used to find the near-exact time of arrival of the LFM signal for the receive hydrophone. The second peak, approximately 4 ms after the direct path, is due to the surface bounce, after which reverberation dominates the remainder of the cross-correlation output.

The replica was then split up into 30 'sweeplets,' which are 4 kHz wide subsections of the frequency domain replica, where signal contributions more than ± 2 kHz of the center frequency are zeroed, and the half power width of each sweeplet is ± 1 kHz from the center frequency. The sweeplets are shown in the left panel of Figure 4.14, where each color represents a different center frequency sweeplet, ranging from 6 kHz to 64 kHz in 2 kHz increments. Adjacent sweeplets overlap by 50%, and the combined envelope in the frequency domain is the same as the total mathematical replica.

The sweeplets are then normalized to yield a gain of 1 at the center frequency, and cross-correlated with the received LFM signal. The right panel of Figure 4.14 shows the result of correlating the sweeplet centered at 62 kHz with the received LFM pulse, where the red star indicates the direct-path received level for the 62 kHz sweeplet.

Figure 4.15 shows the result of matched filtering using all sweeplets for a pre-UNDEX (a, $t = -136.7$ [s]) and post-UNDEX and (b), $t = +5.25$ [s]) ping for hydrophone 14 during event 2. These are sweeplet center frequency vs. time plots, with received level is in dB (//1μPa). Correlating with the sweeplets results in the peak occurring at $t = 0$ [ms], so the high received level at $t = 0$ [ms] indicates the strength of the direct path arrival for each sweeplet. For the pre-UNDEX ping (a), the surface and bottom reflections can also be seen at 4 [ms] and 6 [ms], respectively, occurring across all frequency bins. The end of the time record occurs at about 30

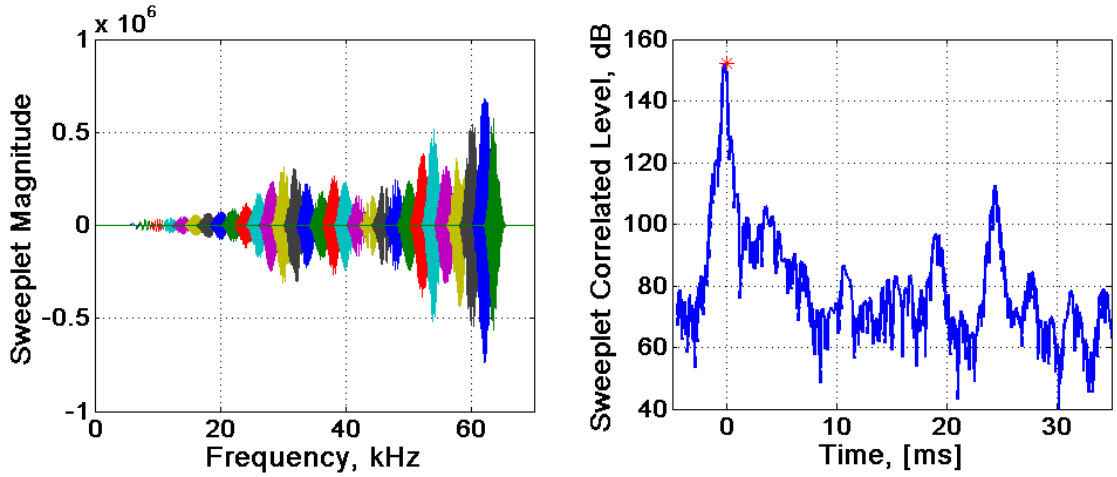

Fig. 4.14. Left: 4 kHz wide 'sweeplets,' generated from the mathematical replica in Fig. 4.13. Right: Time Domain of the cross-correlation output for the sweeplet centered at 62 kHz. The red star indicates the correlation peak of the 62 kHz sweeplet with the received signal. The red star at $t = 0$ [ms] indicates the received level at 62 kHz in dB.

[ms] in Fig. 4.12, however as a result of correlating with sweeplets and using MatLab's circular FFT routine, the time record is 'wrapped' around $t = 0$ [ms], appearing as a nearly diagonal drop in received level in the left panel of Fig. 4.15, from 60 kHz at 7 [ms] to 5 kHz at 37 [ms]. This effect causes the higher order harmonics to 'wrap' around, and appear to arrive later than the direct-path signal.

The matched filtered output for the post-UNDEX ping (b, $t = 5.25$ [s]) shows similar characteristics as the pre-UNEX ping, but with a higher level of noise both before and after the direct-path arrival of the LFM pulse. The surface and bottom bounce signals are not visible after UNDEX due to reverberation from the UNDEX, the presence of the UNDEX cloud, transducer motion, and/or breakup of the surface (due to gas-globe ejection).

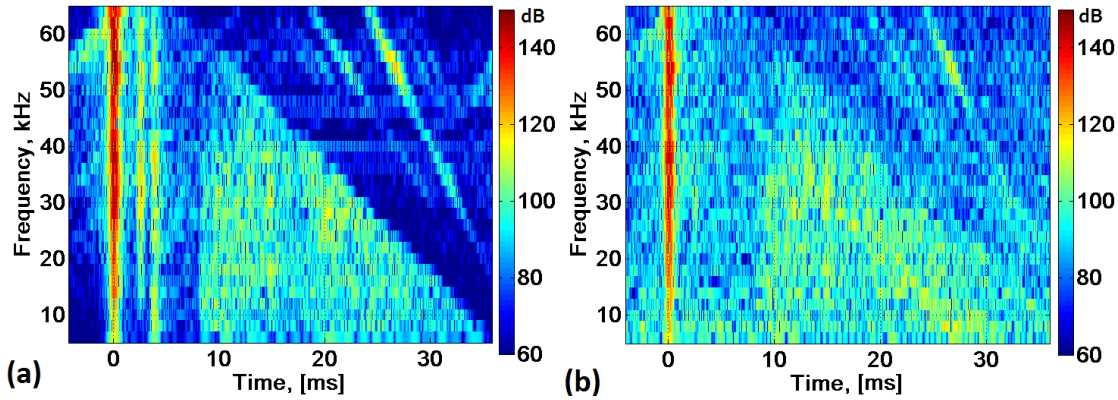

Fig. 4.15. Matched filter output for a pre-UNDEX (a) and 5.25 [s] after UNDEX (b) ping after applying all of the sweeplets to the LFM pulse as recorded by hydrophone # 14 (15.2 [m]) during Event 2. The direct-path arrival at each frequency band has been shifted to $t = 0$ [ms].

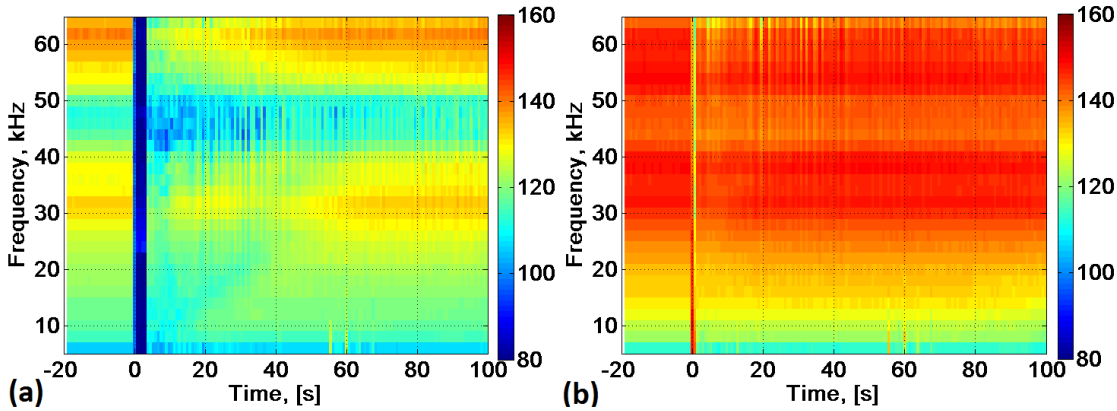

Fig. 4.16. Received level for the LFM pulse vs time since UNDEX in seconds for hydrophone 8 at 7.6 [m] depth (a), and, and hydrophone 14 at 15.2 [m] depth (b). UNDEX occurs at $t = 0$ [s].

For each ping, the received level of the direct path for each frequency bin is recorded from $t = 0$ [ms] in Fig. 4.15. Figure 4.16 presents the level of the direct path arrival recorded by hydrophones 8 (a, 7.9 [m]) and 14 (b, 15.2 [m]) during event 2[5]. These are frequency vs time plots, where the abscissa is in seconds, with $t = 0$ [s] corresponding to UNDEX. Hydrophone 8 (a, 7.9 [m]) is insensitive to acoustic signals for about 5 seconds after UNDEX, which is the reason for the low received level (dropout) immediately following $t = 0$ [s]. After hydrophone sensitivity returns to normal, the received signal level is lower as a result of the UNDEX bubble cloud and debris, with a strong frequency-dependent variability. The low frequency received levels return to the pre-UNDEX level within about 25 seconds, and in particular the 25-65 kHz band takes approximately 50 seconds to return.

The received level for hydrophone 14 (b, 15.2 [m]) differs from phone 8 (a, 7.9 [m]) in several ways. The received level at all frequencies is higher in phone 14 since it is at the same depth as the acoustic projector, and is nearly on-axis for the projector (*see:* F27 beam pattern and received level, Fig. 4.11). Also, phone 14 also shows a shorter duration and lower level of received signal loss after the UNDEX.

Fig. 4.16 also shows a time-dependent variability in level that is introduced by the UNDEX, as the effect is not present prior to $t = 0$ [s]. The cause of this effect is likely motion of the acoustic transducers, but most predominantly the acoustic projector. As the projector moves, the beam pattern shifts and the acoustic levels vary by several dB over the range of the forward-loss hydrophones (see: Fig. 4.11). This effect could also be related to surface movement due to gas-globe ejection. It appears to decrease in magnitude and frequency with time since UNDEX.

[5]Previously, hydrophone 14 was discussed since it experiences the highest level of received signal (Figs. 4.12 - 4.14). Here phone 8 (a, 7.9 [m]) is also shown in Fig. 4.16 since it experiences a larger effect due to UNDEX.

4.3.2 Signals Received at the Backscatter Array

A set of nine backscatter hydrophones present in the quarry during these tests recorded the level of backscattered energy from the UNDEX cloud during all five events. All nine backscatter hydrophones were Reson TC4032s, and signals were recorded with the same electronics used for the forward loss hydrophone signals. A limited set of backscatter data is presented now.

Figure 4.17 shows a time-series and spectrogram of the received backscattered signal from hydrophone 5 for event 1 prior to UNDEX. The electronic contamination is a striking feature in the time series (upper). The contamination is so strong that it clips at the ± 5 [V] rails of the analog-to-digital converter. At approximately 0.05 seconds the LFM pulse backscattered by the charge shell or metal cylinder can be seen as a slightly elevated received level, followed by a few milliseconds of quiet then by a diffuse reverberation that varies in amplitude. The CW pulse transmit contamination is present beginning at about 0.23 seconds, and the corresponding backscattered signal follows. The spectrogram (lower) shows many of the same characteristics as the spectrogram from the forward loss data (Fig. 4.12). Reverberation from the previous ping's 40 kHz pure tone is faintly present for $t \leq 0$ [ms]. Strong harmonics are present during transmission of both the LFM and CW pulses as a result of the electronic contamination. The backscattered signal is received starting at approximately 0.03 seconds, which corresponds to a surface bounce. The signal backscattered by the charge and/or metal cylinder is received at approximately 0.05 seconds after transmit, which can be 'picked' out of the reverberation as a slightly stronger arrival with the same slope as the LFM transmit contamination. Reverberation is present through the remainder of the time record at high frequencies, and diminishes earlier

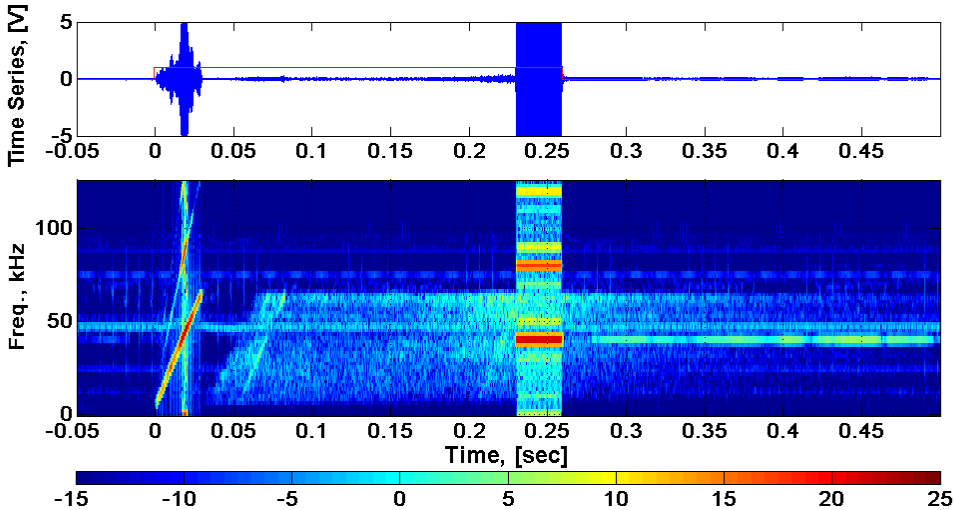

Fig. 4.17. The backscattered received signal from hydrophone 5 prior to UNDEX, event 1. Electrical contamination is the only visibly significant signal in the time series data, though received levels well above background noise are visible in the spectrogram. The red line in the upper panel indicates the trigger channel. Duration of the transmitted signal is 260 [ms], repeated every 0.75 [s]. Color scale for bottom plot is dB //1 [V].

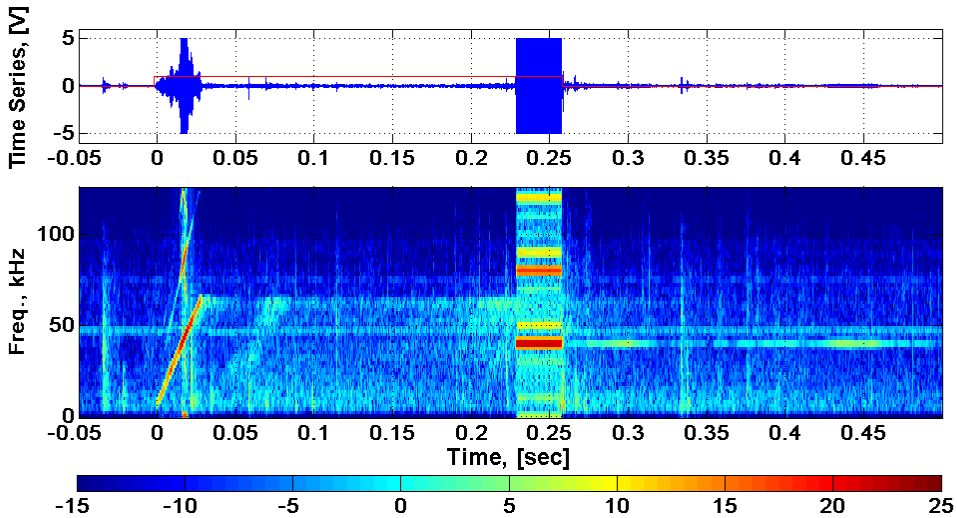

Fig. 4.18. The backscattered received signal from hydrophone 5 during event 1, approximately 5 seconds post-UNDEX. Electrical contamination is present, as well as echos from reverberation and other UNDEX induced noise. The spectrogram shows significant broadband noise induced by the UNDEX. Color scale for bottom plot is dB //1 [V].

at lower frequencies. For a few 10s of milliseconds before the CW pulse transmit, reverberation from the LFM pulse increases in magnitude. This may be the result of a specular reflection off of a vertical wall in the quarry that is normal to the projector axis (as seen north-east of the dock in Fig. 4.1). The reverberation from the LFM backscatter is still present during reception of the CW backscatter signal, but the receive level for the CW pulse is easily detected.

Figure 4.18 shows a time series and spectrogram for hydrophone 5 approximately 8 seconds after UNDEX. The received signal is largely the same as before UNDEX, but with a higher level of broadband noise apparent in both the time-series and spectrogram. This noise is the result of reflections and reverberation from the shock and pressure waves of the charge detonation. Short time broadband signals (*e.g.* $t \approx -.035$ and $t \approx 0.34$ [s]) are reflections, and the more diffuse received level (between 2 kHz and 100 kHz) is reverberation. This effect can be seen for many 10s of seconds after UNDEX (not visible in Fig. 4.18), during which, some discrete backscatter arrivals from the metal cylinder, pressure sensors and/or bubbles near UNDEX location are masked. This is discussed further in Sec. 4.3.2.2.

4.3.2.1 Backscatter from the CW Pulse

Similar to the forward loss data, the energy scattered from the CW pulse requires the least processing, so it will be discussed first. The received signal is band-pass filtered with 3 dB-down points of approximately 32 and 48 kHz in order to retain only signals near 40 kHz. The RMS signal level is then calculated over one millisecond intervals. Figure 4.19 shows backscattered energy from the CW pulse as recorded by hydrophone 5 during event 1. The received level (color) is dB //1 $\mu\text{Pa}_{\text{RMS}}$. The horizontal axis is time since signal transmit in milliseconds, where $t = 0$

[ms] corresponds to the leading edge of the CW pulse transmission. The vertical axis is time in seconds since UNDEX (which occurred at $T = 0$ [ms]). Recall that the signal was not transmitted for approximately two minutes prior to the UNDEX, and in Figs. 4.19 thru 4.27, the received signal displayed for $T < 0$ [ms] actually occurs approximately two minutes prior to their reference position in the figure.

The top portion of the plot, where $T \leq 0$ (labeled (a) in the figure) is the region prior to UNDEX. The received levels in this region are relatively constant. The left portion of the plot, prior to $t = 0$ (b in the figure), is due to the reflection of the LFM pulse from the far wall (see Fig. 4.17). The intense swath of energy between $0 \geq t \leq 30$ [ms] is transmit signal contamination ((c) in the figure), and this region masks any received signal that could be otherwise seen at the hydrophone. The echo from the charge location begins at about 50 milliseconds. A reflection from the charge shell is not resolved in this image prior to UNDEX because the range resolution of this pulse is 22 [m] (69 [ft.] $= \frac{ct}{2} = \frac{1485\left[\frac{\mathrm{m}}{\mathrm{s}}\right] \times 0.03[\mathrm{s}]}{2}$). Elevated levels around 50 [ms] ((d) in the figure) are likely due to the combined reflections of the charge shell, the pressure sensors surrounding the charge and the metal cylinder hanging in the water approximately 5 [m] northeast of the charge location. For approximately 5 seconds after UNDEX ($0 \geq T \leq 5$ [s]) no reliable signal is recorded. Received signal level after UNDEX is notably more variable than before detonation. Reverberation from the LFM transmit ($t \leq 0$ [ms], b in the figure) is still present for a short period of time after the transmit contamination stops, though diminished in level. Reverberation from the charge detonation (shock and pressure waves seen as vertical lines in the spectrogram of Fig. 4.18) can be seen as horizontal long-duration strata of higher received level following the UNDEX intermittently for up to 15 seconds after UNDEX, labeled (e).

The level of the 30 millisecond pulse received between approximately 40 and 80 [ms] (labeled (f)) is dependent on a number of factors, and becomes visible only after the 15 second period of reverberation due to UNDEX. The variable level of the signal suggests that it is subject to interference that is either mostly constructive, or mostly destructive, and not often in-between. The surface of the water is moving due to the gas globe being ejected from the surface, which causes the suspension floats and PVC structure to move and perturb the pressure sensor locations.

The reason for the 40 [ms] swath of reverberation (for a 30 [ms] pulse) could, in part, be due to movement of the pressure sensors and metal cylinder away from the UNDEX location as well as backscatter from the UNDEX bubble cloud extending some distance away from the (former) charge location. While this cannot be easily resolved by analysis of the CW pulse, the subsequent analysis of the LFM backscatter more clearly shows this effect.

Figures 4.20 and 4.21 show backscatter levels for the CW pulse for all 9 backscatter hydrophones for events 1 and 2, arranged according to their location during the quarry testing (see geometry in Fig. 4.3). Phone 5 is 0.6 [m] from the acoustic projector, and the three vertical arrays are spaced 6.1 m apart, with hydrophones at 12.2, 15.2, and 18.2 [m] depth. All plots within an event have the same color scale, in dB //1 $\mu\mathrm{Pa}_{\mathrm{RMS}}$, and same axes as Fig. 4.19.

First, looking at Fig. 4.20, a few trends are immediately visible. Each of the outer hydrophones experience a direct-path received signal that is visible for approximately four millisec-

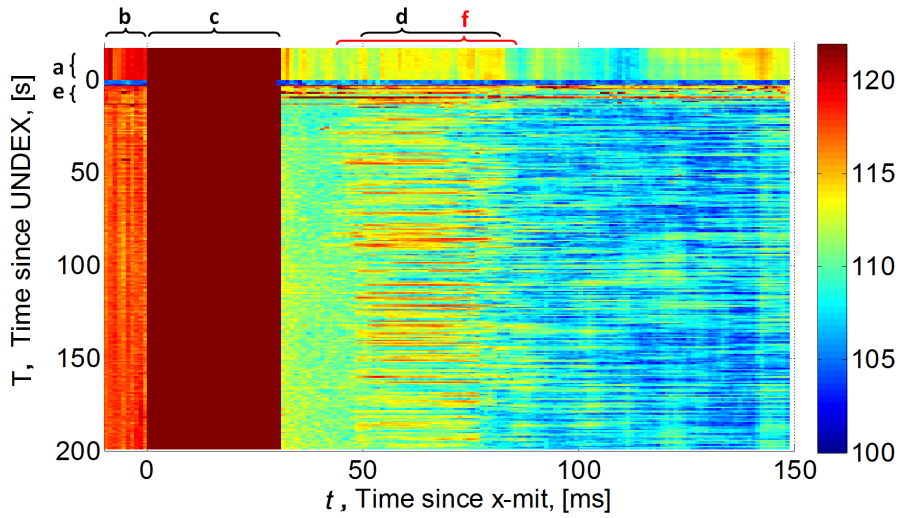

Fig. 4.19. Backscattered energy from the CW pulse during event 1, recorded by hydrophone 5. The CW pulse is transmitted at $t = 0$, and UNDEX occurs at $T = 0$. Color scale indicates received level in dB //1 [$\mu\text{Pa}_{\text{RMS}}$].

onds following the transmit contamination. Hydrophone 5 does not exhibit this signal since it is masked by transmit contamination. The backscattered signal is higher in level at the lowest hydrophones, and lower in level at the top right phones. For the lowest three hydrophones, the pre-UNDEX backscatter from the metal cylinder or charge is more prominent and temporally stable than for phone 5. The reason for the bias in the pre-UNDEX received level is not fully understood, but could, in part, be due to he beamwidth of the acoustic projector, and/or its downward pointing orientation.

The received signal does not appear to have an obvious correlation between hydrophones, however for a given hydrophone the signal does seem to be somewhat correlated - meaning that while the signal is present sometimes, and not present at others, there are instances where the signal is either present for several consecutive pings, or is not. This could allude to the period of which the geometry is oscillating.

For event 2 (Fig. 4.21), many of the characteristics are the same as for event 1. Arrivals prior to UNDEX are slightly less consistent for all hydrophones during this event, however a consistent pattern of arrivals after UNDEX is still not apparent. The duration of hydrophone insensitivity immediately following UNDEX is shorter for event 2, however clipping at the preamplifier immediately following the CW transmit contamination for phone 6 prevents the recording of acoustic signal for about 10 [ms] ($30 \geq t \leq 40$ [ms]). In general, the level of reverberation in the quarry is higher for event 2 (for each phone, in comparison to event 1). Backscattered levels from the UNDEX region (cloud or metal cylinder) appear to be less consistent, and it is difficult to see scattering from that region for long periods of time, *e.g.* $50 \geq T \leq 100$ [s] for phone 5. Also, there appears to be a large amplitude transient signal apparent at approximately $T = 75$ seconds, which is likely due to human activity, and not related to the UNDEX.

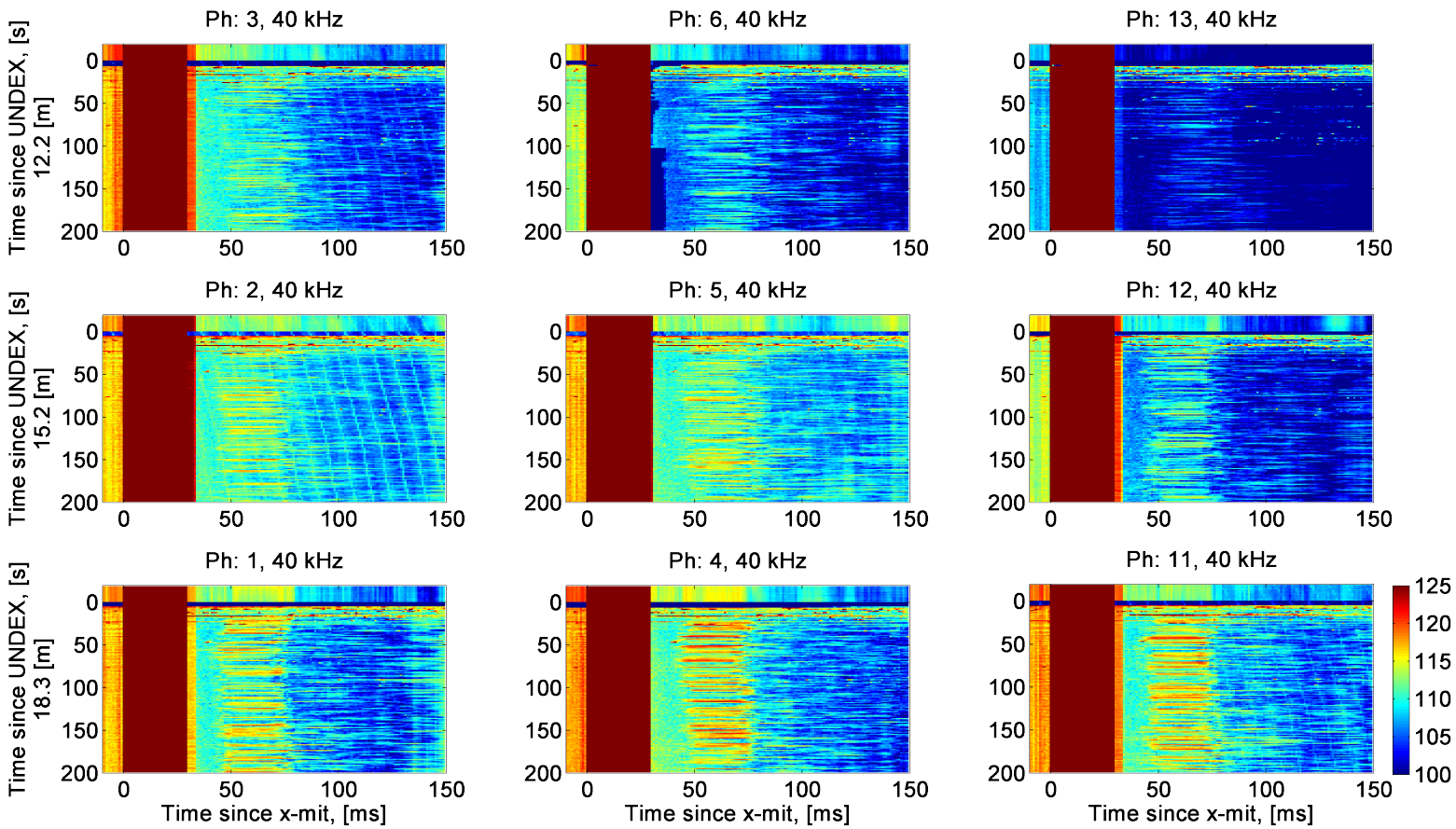

Fig. 4.20. Backscattered energy from the CW pulse for Event 1, showing all backscatter receive hydrophones arranged according to their physical position in the water (see Fig. 4.3). Color scale indicates received level in dB //1 [$\mu\mathrm{Pa}_{\mathrm{RMS}}$].

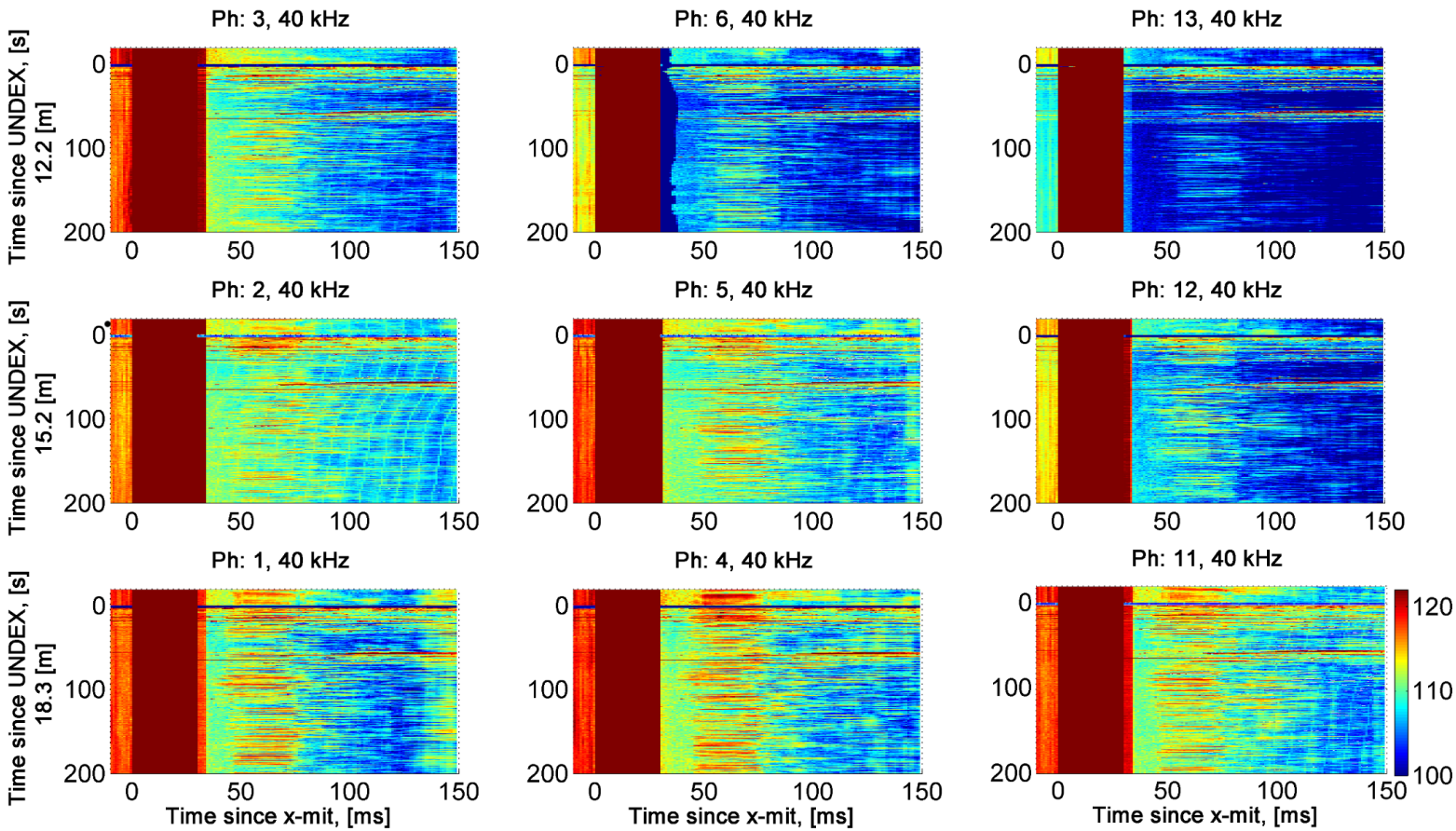

Fig. 4.21. Backscattered energy from the CW pulse for Event 2, showing all backscatter receive hydrophones arranged according to their physical position in the water (see Fig. 4.3). Color scale indicates received level in dB //1 [$\mu\mathrm{Pa}_{\mathrm{RMS}}$].

Backscatter from the metal cylinder and bubble cloud can be more easily picked out of the reverberation for event 1 (Fig. 4.20), which makes the divergence of the cylinder echo and otherwise UNDEX-related backscatter more visible. This is particularly visible in phone 4 where the received level abruptly drops at about $t = 100$ [ms]. The level of reverberation due to the CW pulse is spatially dependent for both events. The left most column (phones 1-3) shows similar noise levels, with the middle phones having a higher background than either phones 1 or 3.

4.3.2.2 Backscatter from the LFM Pulse

The LFM backscatter signals require the same two step processing as the forward loss received level data. A cross-correlation between the LFM received signal and the entire mathematical replica is performed in order to accurately estimate the return from the charge location, and then the sweeplets are used to isolate energy in selected frequency bands within the received signal. This allows for a much finer time resolution than that provided by the CW pulse. The RMS level of the correlator output is calculated over 1 ms intervals.

Figure 4.22 shows the backscattered LFM signal from phone 5 during event 1 after cross-correlating with the 62 kHz sweeplet. The pre-UNDEX data (where $T \leq 0$ [s]) shows the arrivals from the stationary objects. Since the matched filtering process re-references each received signal to the time when the 4kHz wide sweeplet was transmitted, $t = 0$ [s] corresponds to the time of transmission of the sweeplet center frequency. The LFM pulse sweeps from 5kHz to 65kHz in 30msec (at $\frac{2\text{kHz}}{[\text{ms}]}$), thus the 62kHz section of the pulse occurs about 29ms after the start of the ping, therefore the $t = 0$ [ms] is referencing 29 [ms] after the beginning of transmission of the LFM signal. The figures in this section show up to 150 [ms] after transmission of the LFM pulse.

Several portions of the plot are highlighted for emphasis: Two instances of electrical contamination are present in the receive signal. The persistent received signals in region (a) are the result of the second harmonic of the LFM transmit contamination in the vicinity of 30 kHz. The actual transmit contamination at 62 kHz is shown as the very strong arrival labeled (b), spanning several milliseconds around $t = 0$ [ms]. Energy backscattered from the pressure sensors and charge location are present within regions (c) and (d), respectively. Arrival from the metal cylinder (e) occurs a few milliseconds later because it is approximately 5 [m] from the charge location. The remainder of the signal is reverberation, (f). (g) highlights an effect of the circular FFT in MatLab, and is shown because the time of cut-off depends on frequency band center of the sweeplet. This effect (g) is the same effect shown for the LFM received signal in the forward-loss array (seen in Fig. 4.15), and should not be mistaken for a sharp decrease in reverberation level, (f).

Immediately following the UNDEX is a two second long band of no-received signal ($0 \leq T \leq 2$ [s]), followed by a short period of reverberation from the UNDEX, then by received acoustic data approximately 5 seconds after UNDEX. The charge is surrounded by a semicircle of pressure sensors on the side closest to the acoustic projector, and a metal cylinder on the other, and due to forces generated by the UNDEX, these objects are pushed away from the original charge location. They cannot be visually discerned from backscatter from the instrumentation and

bubbles for about 10 seconds after UNDEX, after which the pressure sensors (h) and metal cylinder (k) can be visually discerned. The pressure sensors experience a decrease in arrival time, indicating motion toward the projector and backscatter hydrophone array. The pressure sensors subsequently reach a maximum displacement at about 30 seconds before beginning to return to their original location. This motion can be seen in the post-UNDEX multibeam sonar measurements during the 2007 Quarry test (Fig. 4.28), discussed further in Sec. 4.3.3.

The metal cylinder is also displaced from its pre-UNDEX location, reaching a maximum displacement at about 45 seconds after UNDEX before returning to its original location. Backscatter from the UNDEX cloud containing bubbles and perhaps debris from the charge and its shell is visible centered at about 50 [ms], labeled (m). Scatter from the UNDEX cloud appears strongly in this 'window' that opens up between the displaced pressure sensors and metal cylinder. This scattering region from the UNDEX cloud is approximately 5 milliseconds wide lasting in excess of 200 seconds post-UNDEX and its effect decreases significantly with time post-UNDEX, which is expected since the scattering bubbles and debris will either rise, fall or disperse away from the UNDEX location.

Two anomalous regions of receive signal occur within this time record. The first is region (p), which has strong scattering properties immediately after UNDEX for up to 40 [ms] post-transmit. Although the magnitude and duration decrease with time, the signal is still present in excess of one minute after detonation. Although the cause of this scatter is unknown, the sudden onset at UNDEX suggests that this is an effect of the shock or pressure waves generated by detonation.

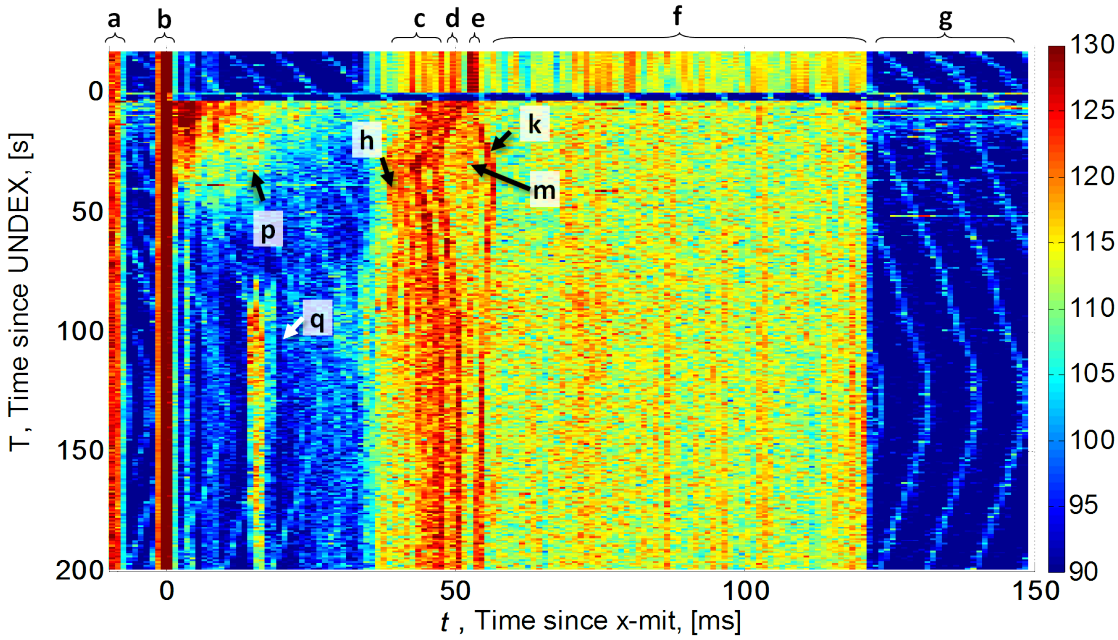

Fig. 4.22. Backscattered energy from the LFM pulse for the 62 kHz sweeplet during event 1 as recorded by hydrophone 5. See text for explanation of arrows marked (a)-(q). Color scale indicates matched filter output in dB.

This effect is discussed in further detail later.

The second anomalous received signal in this data begins at approximately $T = 75$ [s], and $t = 16$ [ms], labeled (q). These effects are not fully understood, but are present in the received signal for most of the hydrophones to some extent and during all UNDEX events. These artifacts are not introduced by processing. (q) appears near the same time within $\pm$ 1 milliseconds at all backscatter hydrophones. No physical object was known to be in the water that would cause scattering at this time, and its sudden appearance at 75 seconds after UNDEX seems inexplicable. The nearest boundary is the surface of the water, which is a 30.1 [m] total path, corresponding to a 20 [ms] travel time. It could perhaps be the surface bounce of another transmit frequency (or it's harmonic) bleeding through the matched filter for the 62 kHz bin. The consistency of arrival times suggests that the scatterer is relatively stationary with respect to the projector and backscatter hydrophone array.

Figures 4.24 through 4.27 are a small sample of the processed LFM backscatter data. In total, there are 30 frequency bands, for 9 hydrophones for 5 events; thus the data presented here is but a small portion of the possible analysis. Figures 4.24 and 4.25 show the 62 kHz frequency band sweeplet processed data for events 1 and 2, respectively. Each of these plots show characteristics of backscatter from event 1, phone 5 in Fig. 4.22. The relative level of received signals at each hydrophone corresponds well with that of the CW backscatter data (lowest in phone 13, higher in the bottom row). The direct-path arrival at phone 3 can also be seen in the outer hydrophones, such as ph 3. The direct-path arrival is expected about 4 ms after the transmit contamination (at $t = 0$, and $\frac{6.1[\mathrm{m}]}{1485\left[\frac{\mathrm{m}}{\mathrm{s}}\right]} \approx 4$ [ms]). This is an acoustic signal, since it does not persist through the UNDEX dropout ($0 \geq T < 5$ [s]); whereas electrical contamination is still present through the quiet region ($0 \geq t \leq 5$ [ms]).

The two anomalous scattering regions are present to some degree in all hydrophones. The scattering region that begins immediately after UNDEX ((p) in Fig. 4.22) is visible for several 10s of [ms] after transmit and is visible in all backscatter hydrophones at 62 kHz. One interesting characteristic of this phenomena is that it occurs only after the direct-path acoustic signal. This signal could be caused by scattering from small bubbles near the projector. Their appearance after the UNDEX could indicate that they were formed by the UNDEX shock and/or pressure waves. This effect is seen in all backscatter hydrophones to some extent during all events, but occurs primarily at high frequencies, suggesting only small bubbles or objects cause this effect. Cavitation is only one possible theory, as there is no hard evidence of what is causing this effect. The time scale of up to 60 seconds seems a very long time for cavitation induced bubbles to persist after UNDEX. This period of time is orders of magnitude longer than typical formation of a cavitation bubble and its subsequent collapse into a cavitation nucleus, however, cavitation bubbles formed by the shock wave may remain in the water [26].

This effect is also more visible for the hydrophones at 15.2 [m] depth, and highest at the central hydrophone, which could, in part, be due to the directivity of the Reson TC4032 hydrophones. Figure 4.23 shows the approximate response of these hydrophones in the vertical plane at 15 kHz, and in the horizontal plane at 100 kHz (reproduced from [23]). The hydrophones are fairly

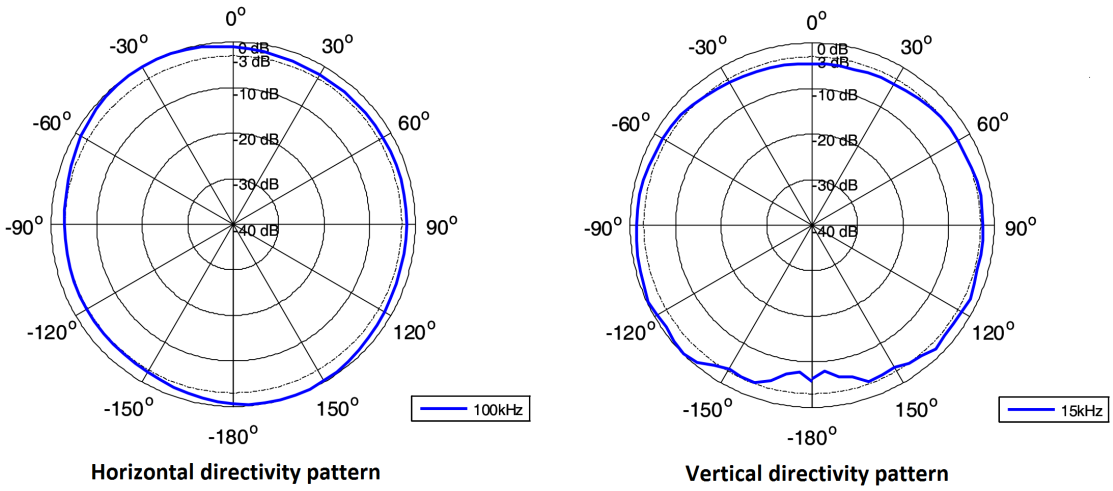

Fig. 4.23. Reson TC4032 hydrophone directivity pattern. Left: horizontal directivity of the hydrophone at 100 kHz, where 0° is an arbitrary location. Right: vertical directivity at 15 kHz, where 0° is in the direction of the bottom of the quarry. Reproduced from [23].

omnidirectional in the horizontal plane, and directional in the vertical. Since the beam pattern is not given for 62 kHz, we assume that the beam pattern varies linearly with frequency, thus since the beam width at 15 kHz is approximately 100°, then the beam width at 60 kHz would be approximately 25°.

The other occurrence of anomalous scattering is present for all phones at $t \approx 16$ [ms] beginning about 75 seconds after UNDEX at all phones, and is more visible at the lower hydrophones.

Another, completely separate electronic artifact is visible (for example) in phone 2, during the 'quiet' period introduced by the circular FFT ($t \geq 120$ [ms]) appearing as wavy near-vertical lines. This is likely a slightly variable electronic clock signal, and is not attributed to acoustic signals.

Scatter from the UNDEX cloud is visible in most of the phones, though more prominent in phone 5. The backscatter starts off fairly strong within a few seconds of UNDEX, then gradually diminishes into the background levels within 2 minutes. Scattering from the pressure sensors is strongest at the 18.3 [m] deep hydrophone, and visible through the entire time record. The metal cylinder can be seen primarily in phones 2, 3, and 5, but is not as strong of a scatterer and is not seen as moving significantly from its pre-UNDEX location.

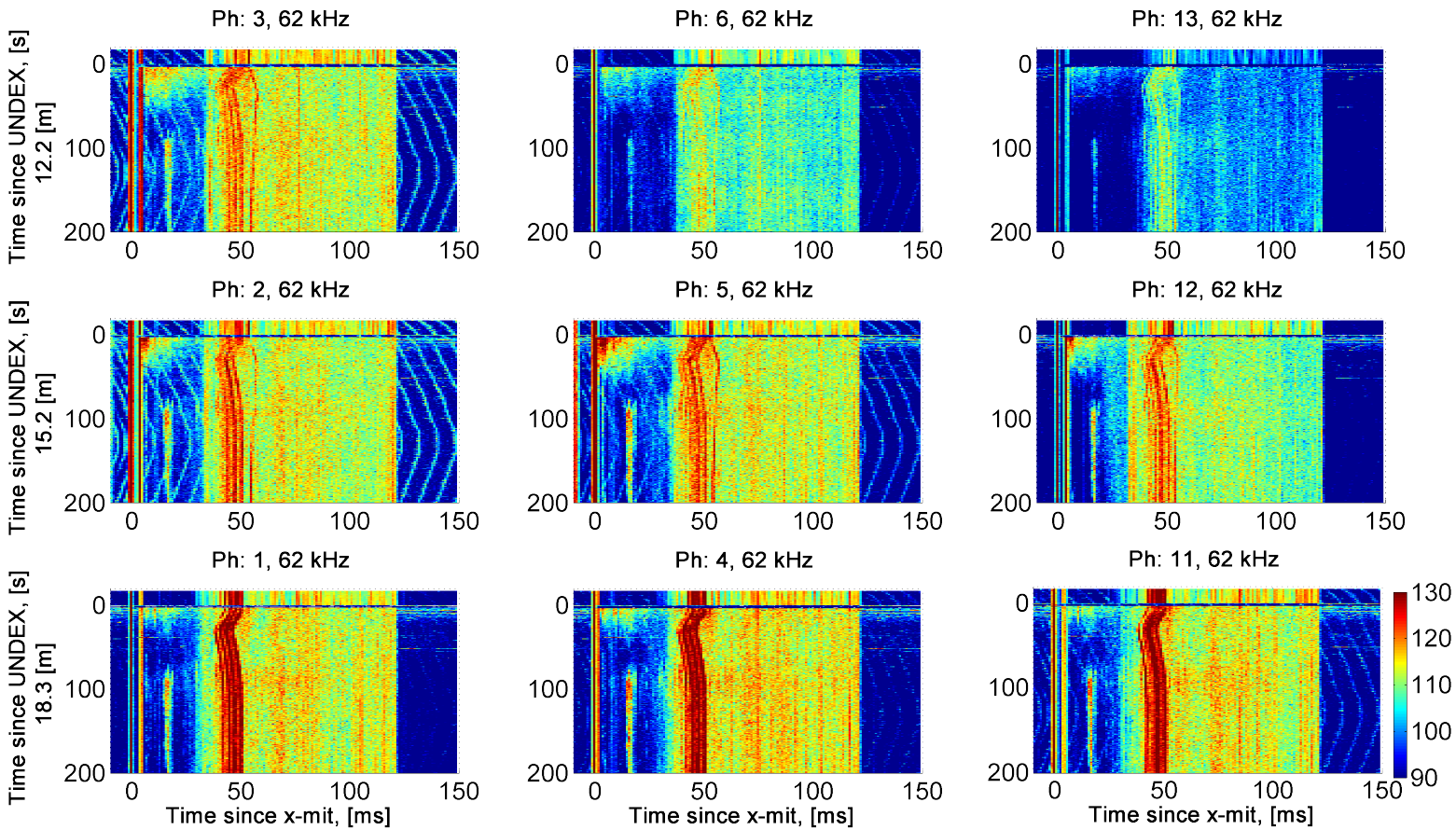

Fig. 4.24. Backscattered energy from the LFM pulse for Event 1 at 62 kHz, showing all backscatter receive hydrophones arranged according to their physical position in the water (see Fig. 4.3). The color scale indicates matched filter output for [90 130] dB.

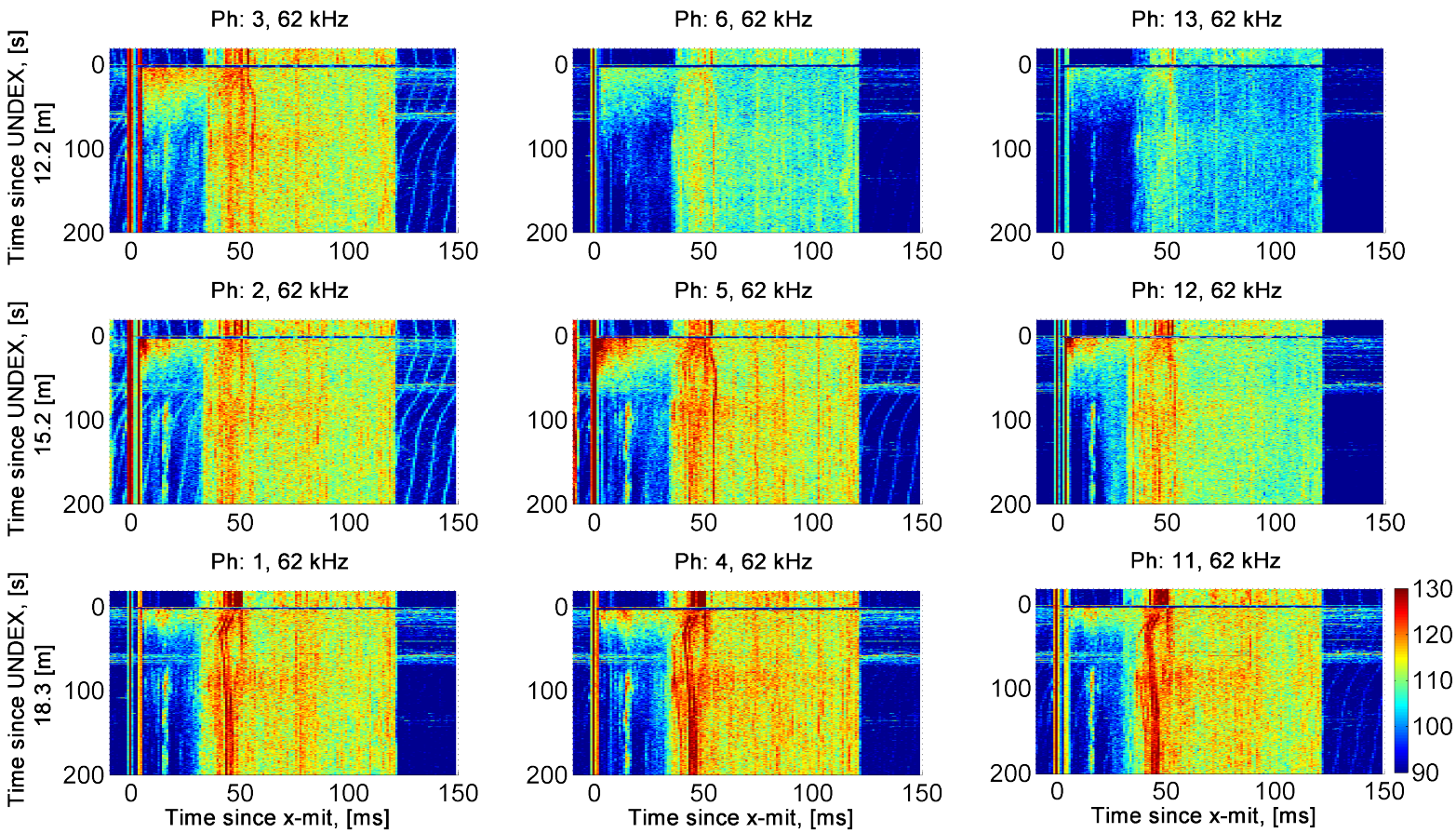

Fig. 4.25. Backscattered energy from the LFM pulse for Event 2 at 62 kHz, showing all backscatter receive hydrophones arranged according to their physical position in the water (see Fig. 4.3). The color scale indicates matched filter output for [90 130] dB.

Figures 4.26 and 4.27 show backscatter in several frequency bands for events 1 and 2, respectively, in order to illustrate the frequency-dependent effect of the UNDEX cloud. The sweeplet center frequency is shown in the title of each plot.

Figure 4.26 shows backscattered levels for event 1. Electronic contamination of the sweeplet center frequency occurs at t=0 [ms] in each plot, but a secondary contamination (labeled (a) in Fig. 4.22) can be seen shifting to a different time in each plot. The secondary contamination is due to transmit contamination of the LFM pulse near 40 kHz. The time series backscattered received signal for hydrophone 5, seen in Fig. 4.17, shows clipping at the ADC during transmit contamination for the LFM pulse, specifically around the 40 kHz section. The transmit contamination level at 40 kHz is so strong, it leaks into every sweeplet regardless of center frequency. The 40 kHz section of the LFM signal occurs approximately 18 [ms] into the 30 [ms] long pulse, and since the matched filtering process causes transmission of the sweeplet center frequency to be re-referenced to t =0 [ms], the secondary contamination appears at different times (t) for different sweeplet frequencies.

For 6 kHz (upper left plot, Event 1), the contamination is at approximately t=17 [ms]. The LFM pulse sweeps from 5 kHz to 65 kHz at a rate of 2 $\frac{\text{kHz}}{\text{ms}}$, so transmission of the 6 kHz region occurs about 0.5 [ms] after beginning of transmission; the 40 kHz region occurs approximately 18 [ms] after the beginning of transmission. Since 6 kHz is at $t = 0$ [ms], after 17 [ms] at a rate of 2 $\frac{\text{kHz}}{\text{ms}}$ (17 [ms]*2 $\frac{\text{kHz}}{\text{ms}}$), the contamination signal is 40 kHz. For 14 kHz, the contamination occurs at 13 [ms], so 14 kHz + (13 [ms] * 2 $\frac{\text{kHz}}{\text{ms}}$) = 40 kHz, et c. While this artifact is present in all frequencies, it does not interfere with detection of backscattered signal from the UNDEX cloud.

Also at 6 kHz (Event 1), the charge, pressure sensors, and metal cylinder are not separately visible; however, it is possible to see some scattering from the UNDEX location. At 6 kHz, $\lambda \approx$25 [cm], which is on the order of the metal cylinder diameter. There is little effect on the received signal at 6 kHz due to UNDEX. The largest contribution from UNDEX is noise and reverberation, lasting for about 50 seconds after detonation, which are fairly prominent horizontal lines of high received levels.

For 10 kHz (Event 1), more backscattered energy is visible, but it is still not possible to detect discrete arrivals for the charge, pressure sensors, and metal cylinder.

For 18 kHz (Event 1), the metal cylinder and pressure sensors can be differentiated, however it is difficult to determine the backscatter arrival of the charge shell. After UNDEX the metal cylinder can be seen moving out (larger t values) and returning to its original position. Backscatter from the pressure sensors and UNDEX cloud are not visible.

For 24 kHz (Event 1), background levels are higher than at lower frequencies. The metal cylinder, charge, and pressure sensor locations are visible (as a group) prior to UNDEX, but become indistinguishable after UNDEX. Their disappearance could be an effect of the attenuation within the UNDEX cloud at this frequency. At about $T = 100$ [s] an increase in backscattering level occurs, this is approximately the time of arrival from the pressure sensors, which is higher in level at higher frequencies. This could be due to the decrease in the level of attenuation caused

by UNDEX, or by the movement of the pressure sensors into a stronger portion of the projector's main lobe relative to the backscatter hydrophones.

For 40 kHz (Event 1), pre-UNDEX arrivals are strong, and separable for the pressure sensor, charge and metal cylinder locations. After UNDEX, the metal cylinder is well resolved, and can be seen moving out from its original position, having a maximum displacement at approximately $T = 60$ [s], and subsequently returning to its original position. The pressure sensors can be seen moving in (closer to the projector and backscatter array). Energy is detected in the expected region of the UNDEX cloud ($t_{hroiz} \approx 50$ [ms]), but is only slightly above the noise level, though it does show decay with time that is expected as the UNDEX cloud disperses and rises.

For 52 kHz (Event 1), the pre-UNDEX backscatter clearly shows steady, discrete arrivals for the pressure sensors, charge shell, and metal cylinder. After UNDEX, the scattering region is smeared for several seconds, after which the pressure sensors and metal cylinder clearly diverge, opening a 'window' in which backscatter from the UNDEX cloud is present, and lasting for several 10s of seconds. Backscatter from the cloud falls into the background noise level within about 100 seconds.

For 58 kHz (Event 1), the pre-UNDEX levels are consistent, and scattering from the metal cylinder and charge are visible. After UNDEX, the pressure sensors are clearly visible. Backscatter from the metal cylinder is almost too weak to be seen, while backscatter from the UNDEX cloud is visible for up to 80 seconds.

In general, as frequency increases, the metal cylinder, charge, and pressure sensors become more visible. At 52 kHz, scattering from the pressure sensors is dominant throughout UNDEX since the wavelength (≈ 2.8 [cm]), which is approximately the size of the pressure sensor capsules.

Scatter from the bubble cloud is visible within the 'window' that occurs between the pressure sensor and metal cylinder arrivals in the measurement time-record, but is often weaker than either of those two arrivals, diminishes with time, or is otherwise masked by elevated background reverberation levels.

The multi-frequency backscatter plot for event 2, phone 5 are presented in Figure 4.27. Many of the same characteristics of the backscatter are similar to Event 1 (Fig. 4.26), however several differences should be noted.

For 6 kHz (Event 2, Fig. 4.27) prior to UNDEX, there is noticeable backscatter from the region of the charge location, however individual scatterers are difficult to differentiate. Noise and reverberation from detonation appear as horizontal lines of strong received level, lasting for up to 75 seconds after UNDEX. The level and duration of this noise much stronger and longer lasting than for event 1.

At approximately T=75 [s], a strong broadband noise source is introduced, appearing as a strong horizontal band of energy lasting for about 10 seconds. This is most prominent at lower frequencies, however is present at all frequencies and is likely introduced by human activity.

The backscatter for 10, 18, and 24 kHz are not significantly different than for event 1, and do not show clear signs of the UNDEX cloud. The remainder of the frequencies for event 2 show a significant amount of backscatter from the UNDEX cloud, and at higher frequencies the received

signal is not masked by backscatter from the pressure sensors.

For 32 kHz (Event 2), backscatter from the UNDEX cloud is strong, and differentiable from the pressure sensors after $T \approx 20$ [s]. The metal cylinder is not clearly visible in this panel

For 40 kHz (Event 2), the UNDEX cloud is clearly visible, and can be seen decreasing in received level over time, until it recedes into the noise level at about $T \approx 80$ [s]. The metal cylinder also shows a decreased received level over this time, which could indicate either an increase in the attenuation within the bubble cloud, or movement of the cylinder out of the main lobe of the projector.

For 44 kHz (Event 2), the received level is largely in the background, however, a small region near $t = 50$ [ms] appears to be backscatter from the UNDEX cloud.

For 52 kHz (Event 2), there is little contamination from the metal cylinder or pressure sensors, leaving the UNDEX cloud distinctly visible. Backscatter level remains high for approximately 50 seconds before beginning to fade into the background noise.

For 58 kHz (Event 2), the UNDEX cloud is strongly visible, but has more contamination than at 52 kHz, as a result is difficult to discern the approximate boundaries of backscatter for the cloud for the first 40 [s] after UNDEX. After this time, the cloud remains strong for many 10s of seconds before receding into the noise level.

In general, the backscatter for event 2 (Fig. 4.25) does not appear as informative as for event 1 (Fig. 4.24). The metal cylinder is generally harder to locate, and most received levels are likely masked by elevated reverberation levels.

The two anomalous received signals are visible in both sets of data as well. The region in the top left ((P) in Fig. 4.22) is strongest at high frequencies, and decreases in intensity and duration with lower frequencies.

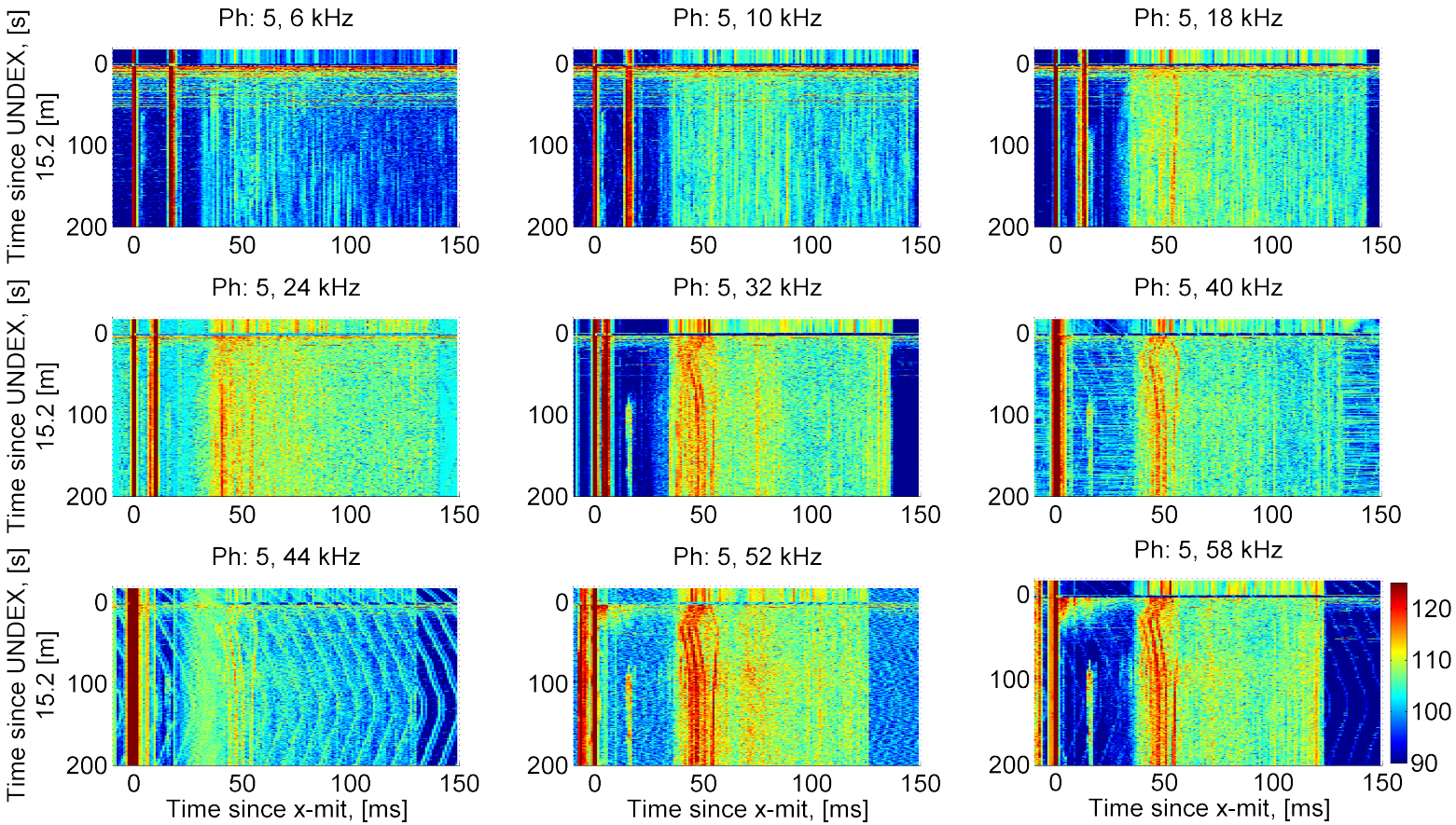

Fig. 4.26. Backscattered energy from the LFM pulse for Event 1, Phone 5 for several different frequency bins. The color scale indicates matched filter output for [90 125] dB.

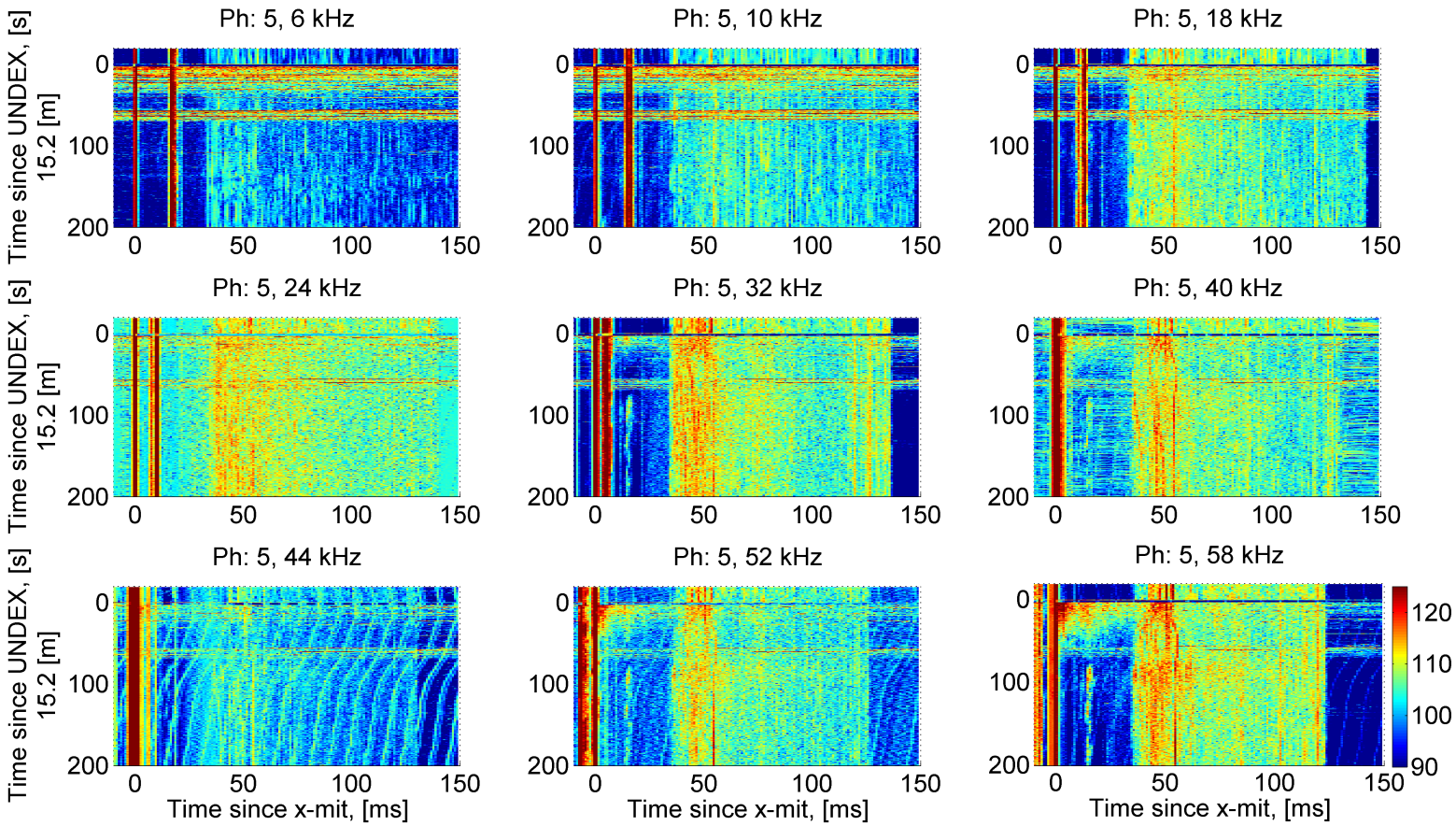

Fig. 4.27. Backscattered energy from the LFM pulse for Event 2, Phone 5 for several different frequency bins. The color scale indicates matched filter output for [90 125] dB.

4.3.3 Mutlibeam Sonar Data

This section is a brief detailing of the multibeam sonar measurements made during the quarry tests. A Reson SeaBat 7125 multibeam sonar operating at 400 kHz was used in the quarry test to image the region of the UNDEX.

This thesis presents and analyzes measurements made in May of 2008; however, a similar series of tests were made in September of 2007 at the same location, using a similar measurement geometry. The 2007 test resulted in a set of forward-loss attenuation and multibeam sonar measurements. The attenuation measurements from the 2007 quarry test will not be discussed, however the mutlibeam sonar measurements are presented here. In the Sept. 2007 measurement, the multibeam sonar was oriented to image a horizontal plane containing the UNDEX. In the 2008 measurement, the sonar was oriented to image the vertical plane containing the UNDEX.

Multibeam sonar images are presented here to indicate the apparent spatial and temporal properties of bubbles and debris in the water. A 400 kHz sonar will detect resonant bubbles ($a = 8$ [μm]), large bubbles result in geometric scattering, and various debris present in the water.

Figure 4.28 shows an image of the test geometry prior to detonation of the charge during the Sept. 2007 test. This image spans the horizontal plane containing the charge (labeled C), metal cylinder (M), pressure sensors (S) and acoustic projector (P). Strong scattering from the metal cylinder is the reason for the side-lobe leakage that is present at about 100 [ft.] from the origin.

Figure 4.29 shows a horizontal cross section of the UNDEX cloud approximately 5 seconds after detonation during the Sept. 2007 test. This image shows a significant amount of scatterers spread large distances from the (former) charge location. The metal cylinder is still quite visible in this image. Images for subsequent times (not presented) show that the metal cylinder moves out and then back.

Figure 4.30 shows multibeam sonar images from the 2008 quarry test, where the receive beams spanned the vertical plane of the UNDEX cloud. The measurement system was shaken significantly as a result of UNDEX, so this image has been rotated to show the surface of the water and bottom of the quarry as horizontal. The UNDEX location is shown at approximately 0 [ft.] depth in this figure. The left panel shows the UNDEX cloud approximately nine seconds after UNDEX. A large cloud of scattering objects are present around the UNDEX location, and in the water column as they rise to the top of the water column. The metal cylinder is visible at approximately 0 [ft.] depth and 100 [ft.] (30.4 [m]) range. Increased levels below the charge depth (¿0, downward) are likely due to strong scattering (side-lobe leakage) from the bubble layer near the surface.

The 'spoke' of high received level shown at 0 [ft.] depth across all ranges is either an artifact of the multibeam sonar system, a strong specular reflection from the quarry wall (not visible in Fig 4.30), or other signal saturation, and is not indicative of physical scattering objects.

The right panel of Fig. 4.30 shows the cloud approximately 180 seconds after UNDEX. The scattering objects have largely migrated toward the surface, appearing as a dense layer of strong

received level. The black line here shows the approximate surface of the water, since the thick bubble layer near the surface obscures its exact location. As multi-path increases, a mirror-image of the near-surface bubble layer appears above the water's surface. The metal cylinder remains visible (at about 0 [ft.] depth and 100 [ft.] range).

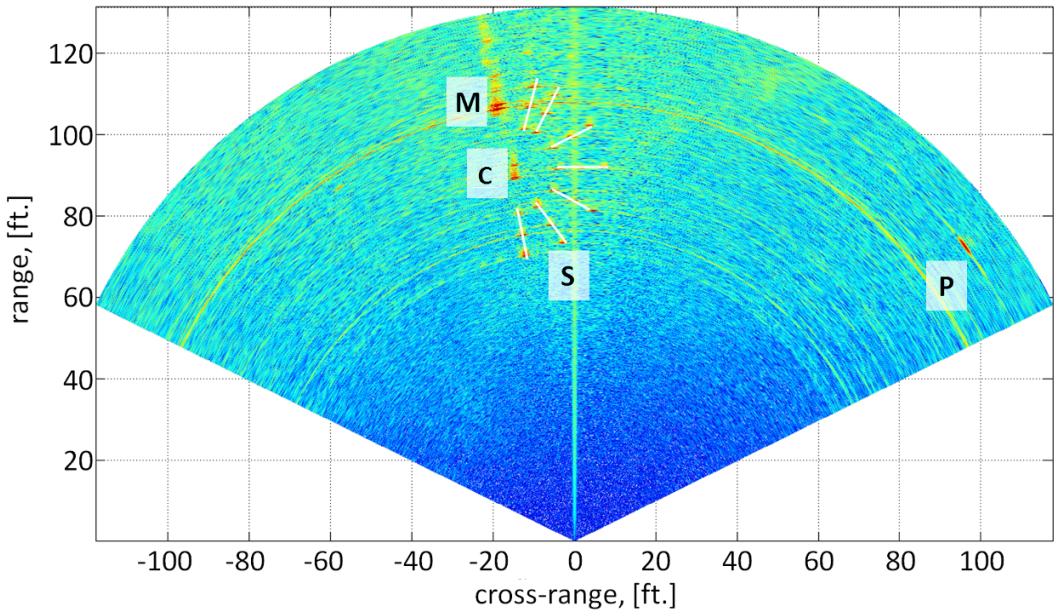

Fig. 4.28. Pre-UNDEX multibeam sonar image from 2007 quarry test showing the test geometry. The charge is labeled (C), metal cylinder (M), pressure sensor array (S), and acoustic projector (P). (Red indicates a strong arrival, blue indicates a weak arrival)

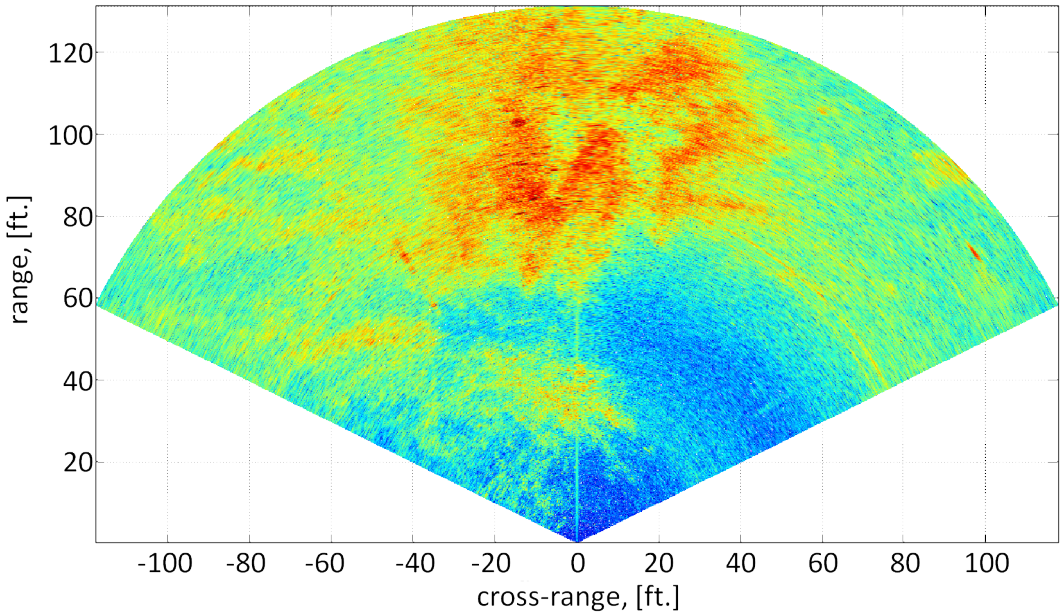

Fig. 4.29. Multibeam sonar image from 2007 quarry test showing the horizontal plane of the UNDEX cloud approximately 5 seconds after detonation. (red indicates a strong arrival, blue indicates a weak arrival)

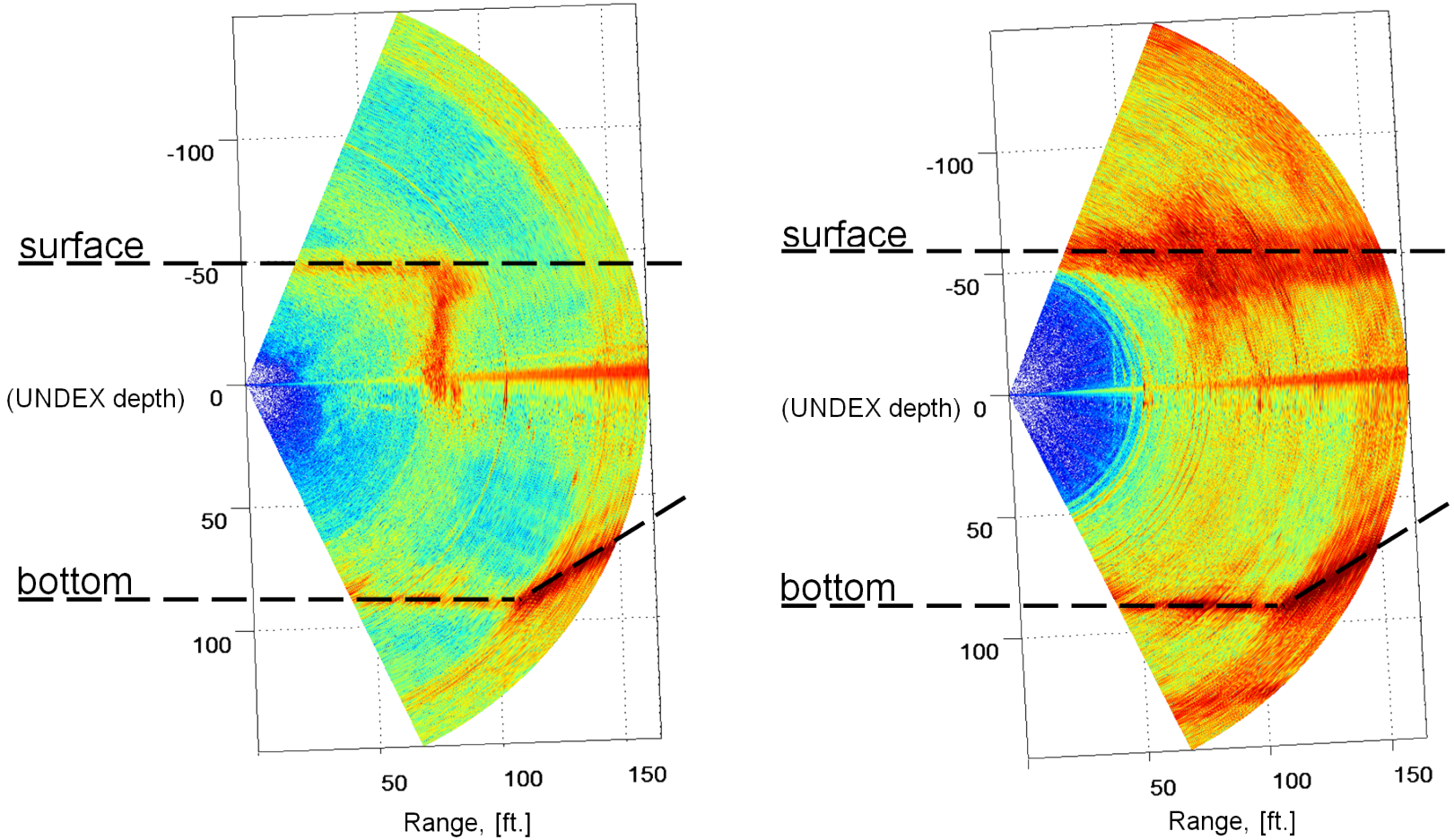

Fig. 4.30. Left: multibeam sonar image from 2008 quarry test showing the vertical plane of the UNDEX cloud approximately 9 seconds after detonation. Right: approximately 180 [s] after UNDEX. These images are slightly tilted to properly orient the water's surface and bottom of the quarry (black lines). (red indicates a strong arrival, blue indicates a weak arrival)

4.3.4 Hydrophone Response to UNDEX

The charge detonation generates a nonlinear, high-pressure shock wave propagating faster than the ambient sound speed in the water. It is important to observe how the hydrophones react to the shock wave, since the piezoelectric elements and electronics in the hydrophone may behave abnormally.

Figure 4.31 shows the RMS power in dB (//1 [V]) vs time for a period of nine seconds containing UNDEX. The six panels that comprise the left half of the figure show the response of a Reson hydrophone (# 8, 7.9 [m]), where the UNDEX occurs at approximately $t = 0$ [s]. The second panel is a continuation of the first panel, and the horizontal axis is the time since the UNDEX shock wave is detected, in seconds. The period of time from [-0.3 to 0] seconds shows the pre-UNDEX ambient level in the quarry. At approximately $t = 0$ the shock wave is detected, after which, the Reson hydrophone is insensitive for a few tens of milliseconds, and does not record any acoustic signal. The received signal returns shortly thereafter, but appears to be insensitive to acoustic pressure fluctuations, instead it shows an exponentially decreasing level. The hydrophone is not completely insensitive to pressure fluctuation during this period, since at approximately 0.38 and 0.72 seconds the pressure waves from the gas-globe oscillation are detected. Transmission of the signal begins approximately 0.9 [s] after UNDEX, and even though the hydrophone appears to be insensitive to acoustic signals, the electronic contamination is present after this time. Sensitivity to acoustic signals returns about 5 seconds after UNDEX;

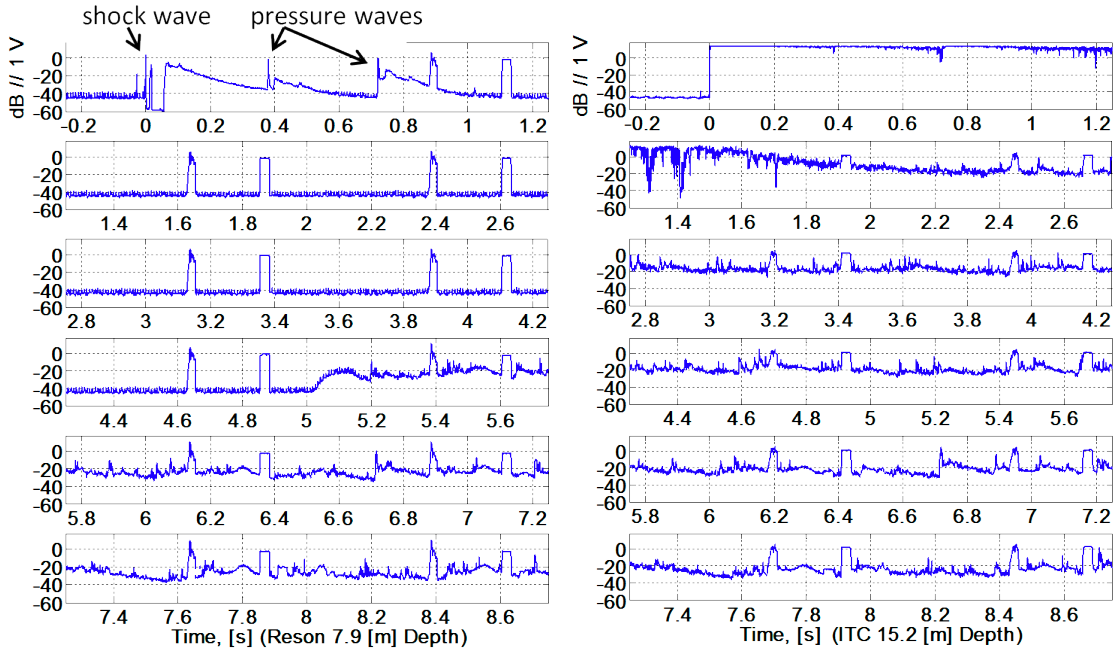

Fig. 4.31. RMS power for a Reson and ITC hydrophone during a nine second period containing the UNDEX shock wave for event 1. Left: 7.9 [m] deep Reson hydrophone (# 8), Right: 15.2 [m] deep ITC hydrophone (# 14).

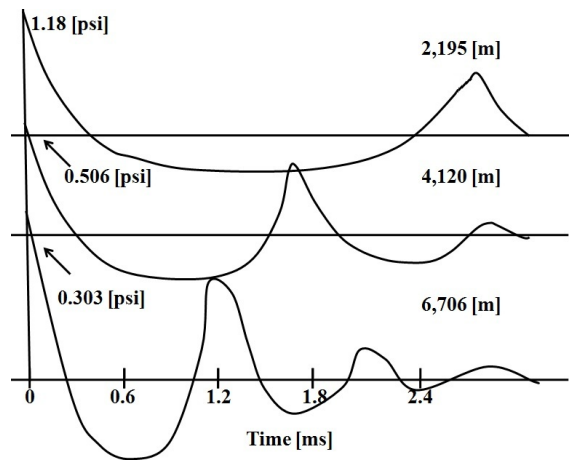

Fig. 4.32. Acoustic pressure signature of an UNDEX. 1 [lb.] charge was detonated at three depths, and recorded near the surface of the water, acoustic pressure reported in [psi]. (After [7])

however, the background noise levels remain elevated in comparison to pre-UNDEX levels for several 10s of seconds after detonation (Fig. 4.31 only shows a period of 8.6 [s] after UNDEX). The higher background noise levels are due to reverberation from the UNDEX.

Figure 4.32 presents the characteristic pressure signature seen at the water's surface from the detonation of a 1 [lb.] TNT charge detonated at three depths (7,200 [ft.], 14,500 [ft.], and 22,000 [ft.]) from [7]. As the depth of detonation increases, the period of oscillation of the gas-globe shortens. The initial shock wave has a steep rise in pressure, followed by a gradual decrease in pressure, eventually a rarefaction and then the second pressure wave. Depending on the depth and size of the charge, the subsequent pressure waves may be too low in magnitude to see. The shock wave, and two pressure waves with slowly decreasing tails can be seen in the hydrophone response for the Reson TC4032 phones (left panel of Fig. 4.31).

The period of oscillation of the gas globe is a function of charge weight and depth, and can be calculated by

$$T(w, z_c, \kappa) = \frac{\kappa w^{\frac{1}{3}}}{(z_c + 33)^{\frac{5}{6}}} \qquad [\mathrm{s}] \tag{4.1}$$

where κ is a proportionality constant (=4.36 for TNT), z_c is the charge depth in [ft.], w is the charge weight in [lbs] [6]. Eqn. 4.1 is the result of theoretical analysis. For the calibration detonations, 30 [lb.] of TNT-equivalent explosive was detonated at 50 [ft.] depth, thus Eqn. 4.1 yields $T = 0.34$ [s]. The RMS power shown in Fig. 4.31 shows arrivals from the shock wave and subsequent pressure waves at about 0, 0.38, and 0.72 [s], leading to an approximate period of 0.36 [s] (≈6% difference). The discrepancy could, in part be due to the explosive compound being PBXN-111 instead of TNT (for which we could not find κ, and approximated as TNT).

The right half of Fig. 4.31 shows the same nine second duration for the 15.2 [m] deep ITC hydrophone. The ITC hydrophone saturates in response to the shock wave. The level is clipped at the analog-to-digital converter for approximately 0.9 [s]. The hydrophone experiences a reduced

sensitivity to acoustic signals for approximately 1.5 [s]. The initial transmit at 0.9 [s] is masked by saturation levels, and acoustic signals are detected approximately 1.6 [s] after UNDEX. Elevated received background levels are also present for the ITC hydrophone lasting several seconds after UNDEX.

Post-UNDEX background levels remain elevated for up to fifteen seconds after sensitivity returns. This is likely due to elevated noise levels and reverberation from UNDEX. The reverberation is frequency dependent, and is seen clearly in the processed backscatter data that is discussed in Sec. 4.3.2. Noise and reverberation are present for in excess of 30 seconds

The reason for the discussion of the hydrophone response is to show how long the measurement system is compromised after the UNDEX. The system is affected for the first 6 or so seconds after UNDEX, spanning the first few transmitted pings, thus precautions must be taken to avoid conclusions based on these affected pings. The measurement system appears to return to normal operation by about 6 seconds after UNDEX.

4.4 Estimate of Attenuation Due to UNDEX

Acoustic attenuation caused by the UNDEX is estimated by first averaging the pre-UNDEX received levels to obtain an average value for the signal level before noise and signal loss are introduced by the explosion. This received level is then subtracted from the averaged pre-UNDEX level, resulting in an estimate of attenuation. In equation form this is,

$$Attenuation = < SPL_{\text{pre-UNDEX}} >_t - SPL_{\text{Rcv}} \tag{4.2}$$

where brackets indicates a time-averaged value, and attenuation is a positive value. The resulting estimate of attenuation is inherently corrected for spreading and other systematic losses since it depends on the difference between pre- and post-UNDEX received level. Attenuation estimates reported in the following sections are reported in dB. Note that earlier discussion regarding attenuation were for a given bubble population within a specified (normalized) volume, while here we present measurements of the cumulative attenuation due to bubbles and debris between the projector and the receive hydrophones, which have not yet been normalized to a unit distance[6].

4.4.1 CW Attenuation Estimate

Figures 4.33 and 4.34 show the CW attenuation estimate from the vertical and horizontal array, respectively. These plots show both events 1 and 2, in the same manner as the CW received levels (Figures 4.9 and 4.10). The characteristics of these plots are unchanged with respect to Figs. 4.9 and 4.10 since they are essentially shifted versions of the same data. Note that the units of attenuation here are dB whereas in Chs. 2 & 3 the units of attenuation were $\left[\frac{\text{dB}}{\text{m}}\right]$.

[6]The dimensional discrepancy between bubble populations in volume [m^3] and attenuation in $\left[\frac{\text{dB}}{\text{m}}\right]$ is discussed further in Ch. 6. Attenuation assumes propagation along a path, not through a volume with unit length.

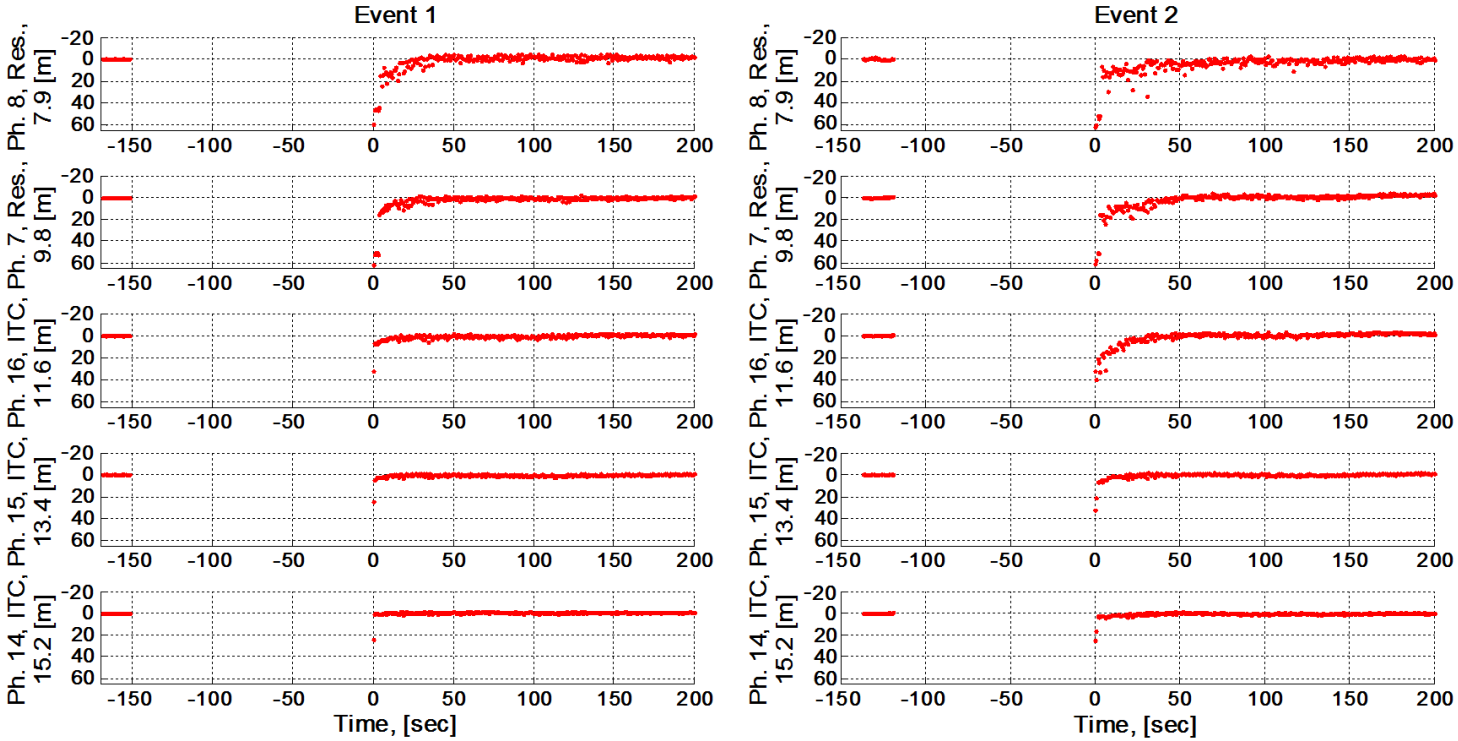

Fig. 4.33. Attenuation estimate for the vertical array during events 1 and 2. Positive values indicate signal attenuation.

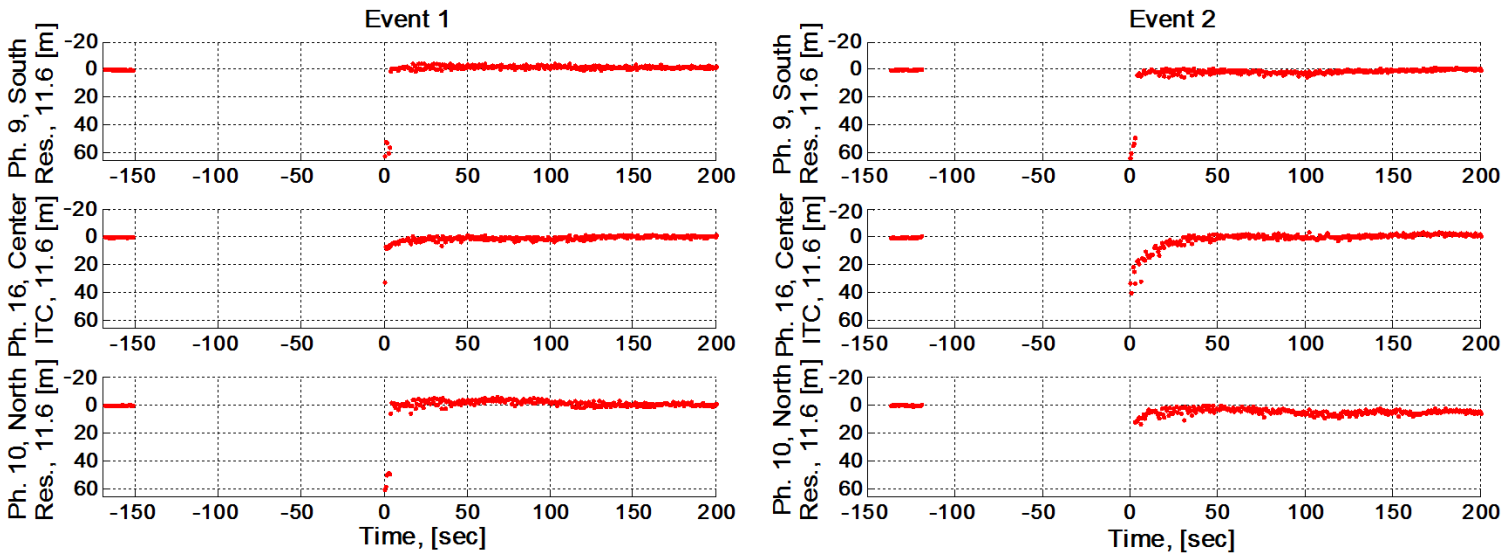

Fig. 4.34. Attenuation estimate for the horizontal array during events 1 and 2. Positive values indicate signal attenuation.

4.4.2 LFM Attenuation Estimate

Attenuation of the LFM pulse can be estimated in a similar fashion as the CW pulse. The pre-UNDEX levels are averaged for each frequency band, then the direct-path received level is subtracted from the averaged level for the entire time record on a per-frequency basis to arrive at an estimate of the attenuation due to the UNDEX cloud.

Figures 4.35 and 4.36 present the attenuation estimate for the LFM pulse during events 1 and 2, respectively. These figures show the frequency-time plots arranged according to their physical location in the forward loss array. 100 seconds of attenuation data are shown for each hydrophone as a compromise between duration and detail of the attenuation estimate immediately following UNDEX. The color scale for all panels is [-5 25] dB, positive values indicating attenuation.

For event 1, the outside phones (9 and 10) show almost no attenuation, even a slight signal level 'gain' between 40 and 60 kHz likely due to the motion of the projector. The vertical array shows several key characteristics about the UNDEX. Data from the shallowest hydrophone (7.9 [m]) is displayed in the top panel, and the deepest phone (15.2 [m]) in the bottom panel. Dependence on depth is clearly dominant, which agrees well with the attenuation estimated from the CW pulse. The deepest hydrophone shows up to 5 dB attenuation at higher frequencies lasting for only a few seconds, and almost no attenuation below 50 kHz. The 13.4 [m] deep hydrophone shows a slightly higher level of attenuation at all frequencies, but attenuation is still higher in magnitude and longer lasting at high frequencies. Recall that the first few seconds of data for both Reson and ITC hydrophones may not be representative of attenuation, rather the hydrophone's response to UNDEX (see Fig. 4.31), and this can be seen as an anomalously high region of attenuation (approximately 1-2 pings for ITC phones, and 6 for Reson phones). In general, the level and duration of attenuation decrease with depth.

The shallowest hydrophones show up to 25 dB of attenuation for a few seconds following UNDEX, and up to 10 dB of attenuation for 50 seconds at high frequencies. The attenuation at each hydrophone is strongly frequency dependent. All of the phones show the vertical striations that suggest motion of the projector or forward loss hydrophones (moving independently) about an equilibrium position for some many 10s of seconds after UNDEX. This effect is likely due to the 'seiching,' or sloshing of water within the quarry due to the UNDEX. The projector was mounted on a 15.2 [m] long section of PVC pipe, and water motion could cause it to rotate or translate, resulting in the projector's directivity pattern moving with respect to the forward loss array of hydrophones and possibly causing the received level to fluctuate several dB (*see:* Fig. 4.11).

Figure 4.36 shows the LFM attenuation estimate for event 2. The charge used in events 1 and 2 were the same size, however, in general the attenuation due to the UNDEX cloud is significantly higher than for event 1. The 15.2 [m] phone sees attenuation up to 5 dB at higher frequencies for up to 10 seconds, but much less for lower frequencies. The 7.9 [m] deep phone shows up to 25 dB of attenuation for up to 60 seconds for most frequencies. The UNDEX cloud has more of an effect at the outer phones of the horizontal array during event 2, which also experience up to

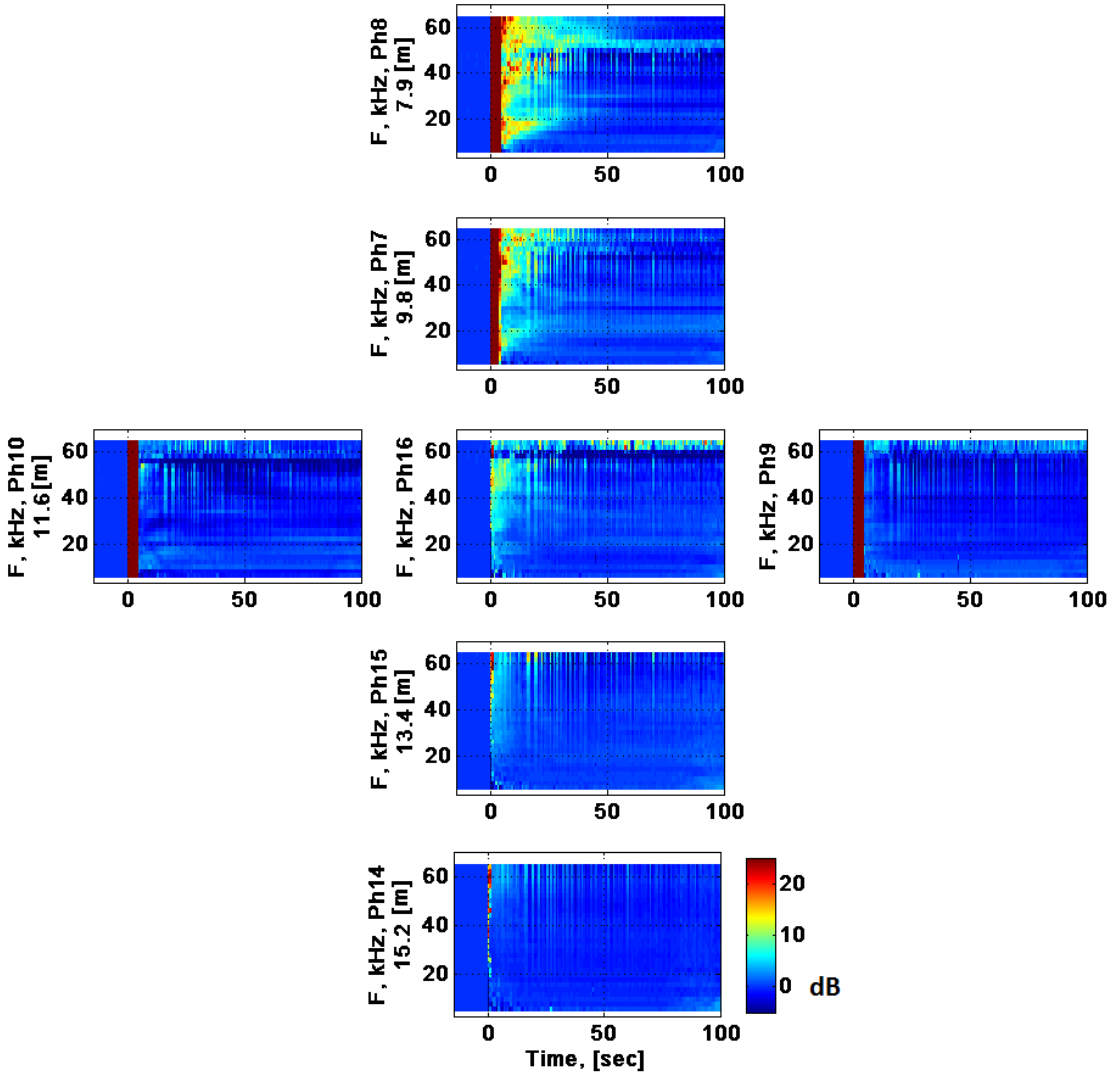

Fig. 4.35. Attenuation estimate for the forward loss array during Event 1. (color axis is [-5 25] dB for all phones, Reson: 7, 8, 9, 10, ITC: 14, 15, 16)

15 dB attenuation lasting up to 20 seconds, though only between 36 and 52 kHz.

While the charges for these two events were the same size, the attenuation measurements suggest that the UNDEX cloud for event 2 had a significantly larger effect on sound propagating through the region of UNDEX than for event 1. The reason for this discrepancy is not clear.

One reason for the complex time dependence clearly visible in the attenuation data (for both events) is the different velocities at which bubbles rise through the water column, passing through each hydrophone's field-of-view. Bubbles rise through the water column under the influence of buoyancy, and larger bubbles rise faster than smaller ones [24]. This effect is evident in two ways in this data. First is the 'spur' that is most visible in the 7.9 [m] deep phone at frequencies below 20 kHz in event 1 (Fig. 4.35), appearing as a (nearly) diagonal line lasting up to 25

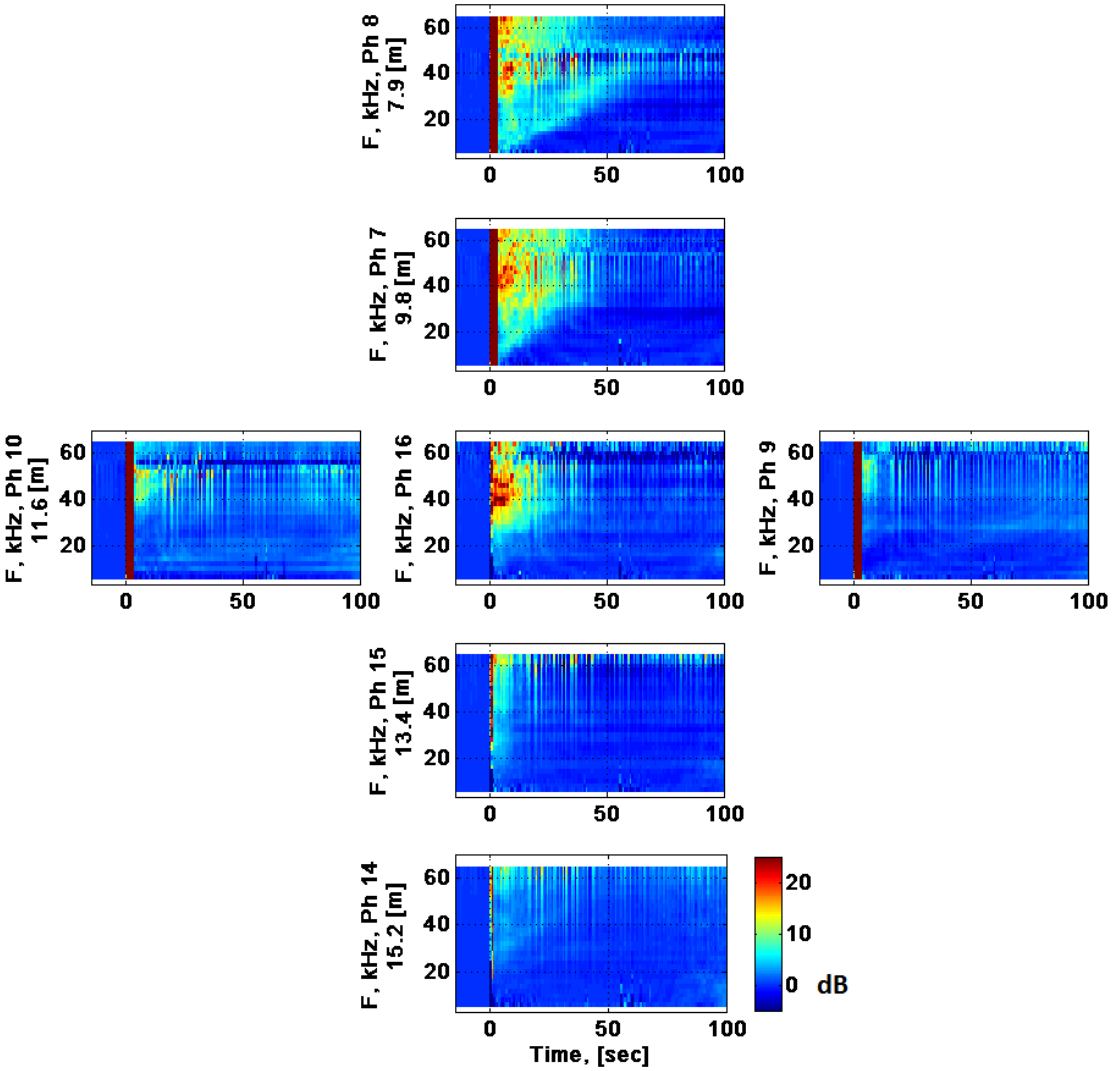

Fig. 4.36. Attenuation estimate for the forward loss array during Event 2. (color axis is [-5 25] dB for all phones, Reson: 7, 8, 9, 10, ITC: 14, 15, 16)

seconds. A simple model indicates that this is the result of the UNDEX injecting bubbles below the charge depth, after which they rise through the hydrophones' field of view. For a given depth, *e.g.* 15.2 [m], the larger bubbles will rise through the hydrophone's field of view (and attenuate lower frequencies) prior to the smaller bubbles (which attenuate at higher frequencies). This effect results in a characteristic slope of the 'spur', that flattens out at shallower hydrophones (since smaller bubbles require more time to reach a given depth). As bubbles rise in the water column, they expand as ambient pressure decreases, thus the bubbles should accelerate as they rise, however this effect is too difficult to distinguish in these attenuation measurements (it would appear as a bend in the spur). The spur effect becomes more prominent for the shallower hydrophones.

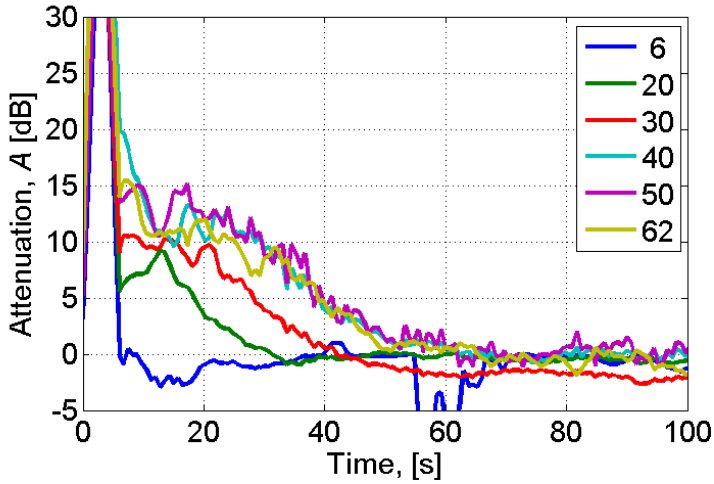

Fig. 4.37. Cumulative attenuation vs. time for event 2, phone 7 at several frequencies. A 4-point moving average filter has been applied to this data.

The second occurrence is most evident in the shallower phones, where the attenuation drops rather abruptly, again appearing along a nearly diagonal line (*e.g.,* in event 2, if we were to draw a line between 30 kHz at $t = 0$ [s] to approximately 50 kHz at $t = 50$ [s]). The gas-globe that rises through the water column is ejected from the surface of the water within a matter of seconds after UNDEX, leaving a large number of bubbles at the explosion depth and elsewhere and in the water column. As larger bubbles rise through the field of view for a given hydrophone, attenuation at the corresponding resonant frequency drops very quickly, this can be seen at 22 kHz in the 7.9 [m] deep hydrophone.

Figure 4.37 shows cumulative attenuation vs time for various frequencies for hydrophone 7 during event 2 after applying a 4-point moving average filter. The first 5 seconds of data are not representative of acoustic attenuation, and are the result of the hydrophones response to UNDEX. Note that for some frequencies the attenuation oscillates about a constant value before beginning an exponential-like decay in time (*e.g.*, 30, 50, and 62 kHz). The length of time that the attenuation remains 'high' (*i.e.* before beginning to decay) is clearly frequency dependent, suggesting that the decay rate is dependent on the rate at which bubbles rise through the field of view for a given hydrophone. After this period, received levels typically return to pre-UNDEX values (or 0 attenuation) within 30 seconds. This effect is visible in the attenuation vs. time data in Fig. 4.37, but is not a strong or consistent for all frequencies, thus is ignored. The sudden drop in attenuation for 6 kHz at about $t = 60$ [s] is due to the man-made noise that is also visible in the backscatter data (see: Fig. 4.27)

4.5 Signal-to-Noise Ratio

The time-series received signals shown in Fig. 4.7 showed clipping at the analog-to-digital converter, and while this was known to be an electronic artifact it prompted further investigation as to how much attenuation could be measured. The dynamic range of the measurement system determines how much attenuation can be measured, but is limited by the level of background noise present in the quarry (which dramatically increases after the UNDEX). Calculating the signal-to-noise ratio (SNR), as a function of time is the most appropriate method to validate the attenuation measurements presented in Sec. 4.4 (though the same information can be conveyed with dynamic range and attenuation measurements).

The method used to calculate the SNR was to use the received level in each frequency bin during signal transmit, and the ambient noise level immediately prior to transmit. The procedure for determining received level for the LFM pulse was presented in Sec. 4.3.1.2, and the results for phones 8 and 14 during event 2 were presented in Fig. 4.16. The ambient noise levels are averaged for a period of 30 [ms] prior to each ping (*i.e.* prior to the beginning of signal transmit to avoid the signal contamination seen in $0 \leq 0.03$ [s] in Fig. 4.7), and processed with the same procedure presented in Sec. 4.3.1.2. The SNR is then computed by

$$SNR = 20 \log_{10} \left(\frac{P_{signal}}{P_{noise}} \right) \qquad \text{dB}, \tag{4.3}$$

where P_{signal} and P_{noise} are the RMS acoustic pressure magnitudes for the signal and noise, respectively. The SNR is reported in dB.

The attenuation measurements presented in Sec. 4.4 involved comparing the pre- and post-UNDEX received level to estimate the difference in received level (being measured attenuation of received signal). SNR compares the acoustic received level of signal to noise within a window of 115 [ms] (30 [ms] ambient noise, followed by 50 [ms] of signal travel time, and then 30 [ms] of received signal). Provided that the ambient noise level does not change significantly over this period of time, the SNR tells us how much attenuation can be measured by the system without clipping. Whenever the SNR drops to zero or below, attenuation cannot be accurately reported by the receive system since $P_{noise} \geq P_{signal}$, and any attenuation reported during this time must be disregarded.

Figure 4.38 (on following page) presents the calculated SNR for all hydrophones during event 2, for the same time span as the attenuation measurement (Fig. 4.36). The Reson hydrophones (#s 7, 8, 9 and 10) show a strong reduction in SNR during the period of time that they were not sensitive to acoustic signal, and this period of time ($t \leq 5$ [s]) was omitted from analysis. After the hydrophones regain sensitivity, the SNR is strongly frequency dependent. In the regions of highest attenuation (approximately 40 kHz for phones 7 and 8) following UNDEX, $SNR \geq 20$ dB meaning that the attenuation reported within this region is well within the measurable range of the measurement system.

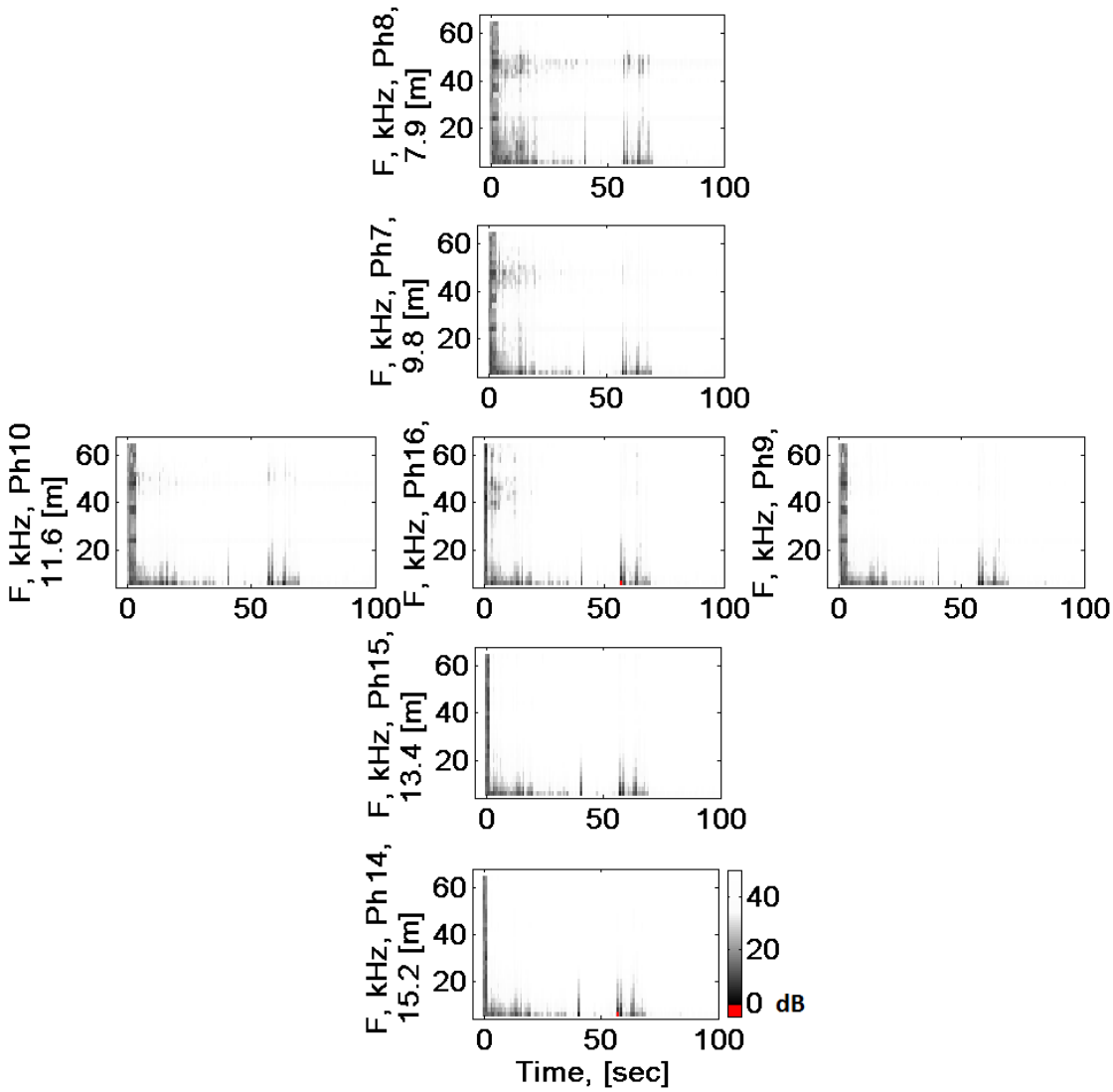

Fig. 4.38. Estimated signal-to-noise ratio for the attenuation measurements, presented as frequency vs. time for each hydrophone, arranged according to their physical location in the forward loss array. The color scale indicates dB of SNR, white indicating more than $SNR \geq$20 dB, gray indicating $0 < SNR \leq 20$ dB, and red indicating $SNR \leq 0$ (indicating no attenuation measured).

4.5.1 Comments

This chapter has presented a lengthy exploration of the measurement system, and intricacies of the processing of the received signals. However it has been included in order to build confidence in the attenuation estimates that were used to obtain bubble population estimates. It is paramount to obtain a good estimate of attenuation so that the resulting bubble model is a reasonable approximation to reality.

Chapter 5

Bubble Population Estimates

5.1 Introduction

This chapter discusses the application of bubble inversion techniques (discussed in Ch. 3) to the attenuation measurements presented in Sec. 4.4. Each of the following sections examine the challenges of applying the method to the measured attenuation and discusses the resultant bubble population estimates.

The attenuation measurement used for illustration in this chapter is taken from event 2. Figure 5.1 shows the attenuation estimate for forward loss phone 7 in event 2 (same as in Fig. 4.36), as well as attenuation vs. frequency for a ping that was transmitted approximately 5.25 seconds after UNDEX, which is after the hydrophones began reporting reliable data. The attenuation vs. frequency data have been smoothed using a 2-pt low-pass filter to reduce large jumps between adjacent points. The low-pass filtered attenuation in the right panel of Fig. 5.1 will be referred to

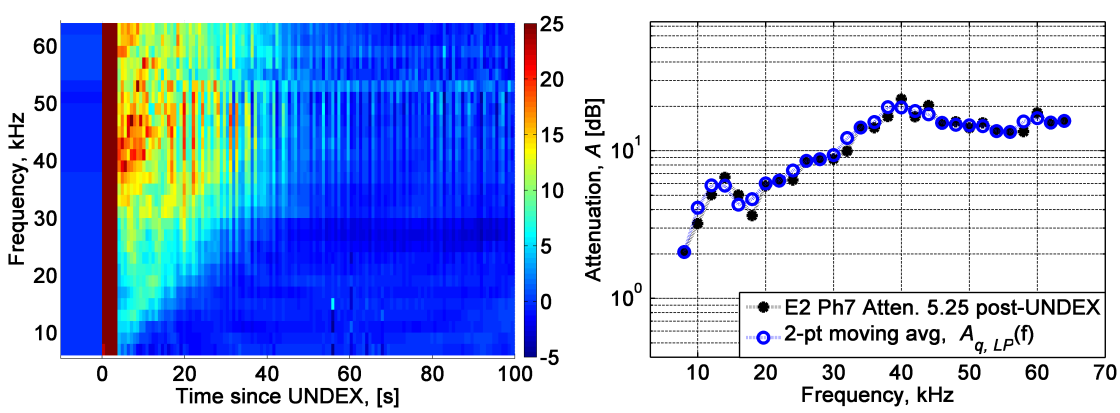

Fig. 5.1. Left: Attenuation in a frequency vs. time plot (same data presented in Fig. 4.36) for hydrophone 7 at 9.8 [m] depth. Right: Attenuation vs frequency for a ping occurring approximately 6 seconds after UNDEX. This data has been put through a 2-pt low-pass filter.

as $A_q(f)$ for the remainder of this chapter. Note that the units of attenuation are in dB instead of $\left[\frac{\text{dB}}{\text{m}}\right]$ as in Chs. 2 and 3. This discrepancy is addressed in Ch. 6.

5.2 Bubble Population Inversion Results

The following examples utilize a sample of the data that have been processed utilizing these methods, in order to show that these methods are valid when applied to real attenuation measurements.

5.2.1 Commander & McDonald Method

The Commander & McDonald method discussed in Ch. 3 was successfully applied to the attenuation measurements from the quarry presented in the previous chapter. However, a couple of compromises had to be made. The example populations in Ch. 3 (ψ_{tri} and ψ_{PL}) used knot radius spectrum with a constant da. However, for the range of frequencies at which attenuation was measured in the field experiment ($A_q(f)$), an evenly spaced knot radius regime would result in either a large number of knot radii (to properly resolve the smaller bubbles), or too few knot radii to sufficiently resolve both low- and high-frequency attenuation (after applying the formal theory, Eqn. 2.19). The compromise is to generate a knot radius spectrum that uses a combination of resonant radii and variably spaced knot radii that provides sufficient resolution in the small radius region of the spectrum without overpopulating the larger radius region. The resulting radius spectrum is shown in the left panel of Figure 5.2. Knot radii smaller than about 220 [μm] correspond to the frequencies at which attenuation was measured, and knot radii larger than 220 [μm] are spaced 15 [μm] apart (red $\circ$'s). This choice requires interpolation of the attenuation measurement, which assumes that the measured attenuation is a smooth and continuous function of frequency. The blue stems in this plot indicate radii corresponding to frequencies at

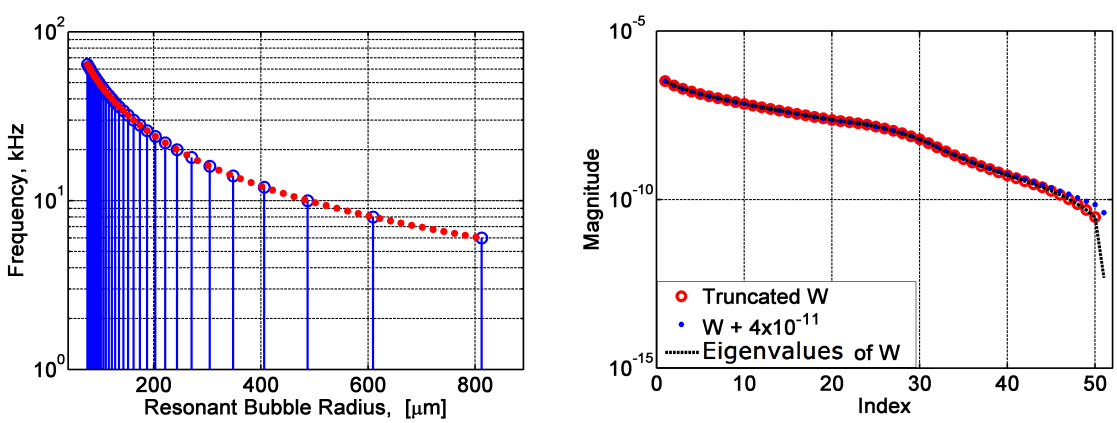

Fig. 5.2. Left: 'knot' radius spectrum chosen for this inversion. Note that spacing between adjacent 'knot' radii is not constant (variable da). Right: eigenvalues for the **K**-matrix (shown in Fig. 5.3). Black are the eigenvalues of **K**, red indicates adding 4×10^{-11} to all EVs, blue dots indicate truncation

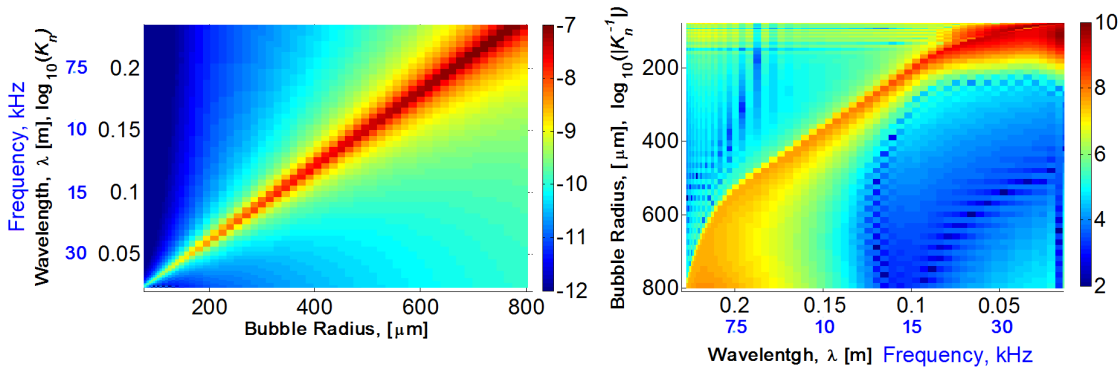

Fig. 5.3. Left: $\mathbf{K}_n$. Right: Inverse $\mathbf{K}_n$ matrix via EVD after adding $4{\times}10^{-11}$ to all eigenvalues, note the high level of variability for bubbles smaller than about 250 [μm]. Levels in both plots are shown as $\log_{10}(|\#|)$. Frequency in this figure is shown in kHz, and bubble radius in [μm].

which attenuation was measured.

The **K**-matrix can be formed by the method presented in Sec. 3.1.1 after determining the knot radii. Figure 5.3 presents the **K**-matrix generated from the knot radius spectrum (Fig. 5.2) and frequency span present in the measured attenuation (Fig. 5.1). Attempts to invert **K** directly (and multiply by the measured attenuation, $A_q(f)$) did not yield a reasonable bubble population, thus some form of regularization needed to be applied. Eigenvalue decomposition[1] (EVD) provides an alternative method for inversion (discussed in Sec. 3.1.1).

The right panel in Figure 5.2 presents the eigenvalues (EVs) for the **K**-matrix (from the diagonals of **W** in Eqn. 3.8), ordered according to magnitude (index 1 being the largest contribution, 51 being the smallest). The smallest eigenvalue is an outlier by almost an order of magnitude. In order to successfully invert the matrix, two methods have been applied: the first is to add a small number to all of the eigenvalues, which is equivalent to adding a small amount of noise to the entire **K**-matrix, thus easing inversion. The resulting eigenvalues are shown by blue dots in the right panel of Fig. 5.2. The second is to truncate the eigenvalues of **K**, effectively removing the contribution of the smallest eigenvalues of the **K**-matrix. The truncated eigenvalues are indicated by red circles in the figure.

The result of adding a small amount of noise to the **K**-matrix (in this case $4{\times}10^{-11}$, chosen arbitrarily) is shown in the left panel of Figure 5.3 (denoted $\mathbf{K}_n$), and its inverse is shown in the right panel (obtained by EVD, Eqn. 3.9). Both plots show $\log_{10}$ of the magnitude of $\mathbf{K_n}$ or $\mathbf{K}_n^{-1}$. The inverted matrix shows a large amount of variability for bubble radii smaller than about 250 [μm], and in the upper off-antidiagonal.

The resultant bubble population is shown in the left panel of Figure 5.4 by blue dots. The high level of variability in $\mathbf{K_n^{-1}}$ yields 'negative' bubble populations (red x's, shown as $|\psi_{SVD,n,invalid}|$), which are an unphysical representation of the bubble population, thus will be omitted in subsequent analysis. The units of ψ (for this chapter) are $\left[\frac{\#}{\mathrm{m}^2} \text{ in a } 1\ \mu\mathrm{m} \text{ bin}\right]$ instead

[1]For this example, **K** is square meaning that the EVD is used. The procedure is the same as presented for the SVD.

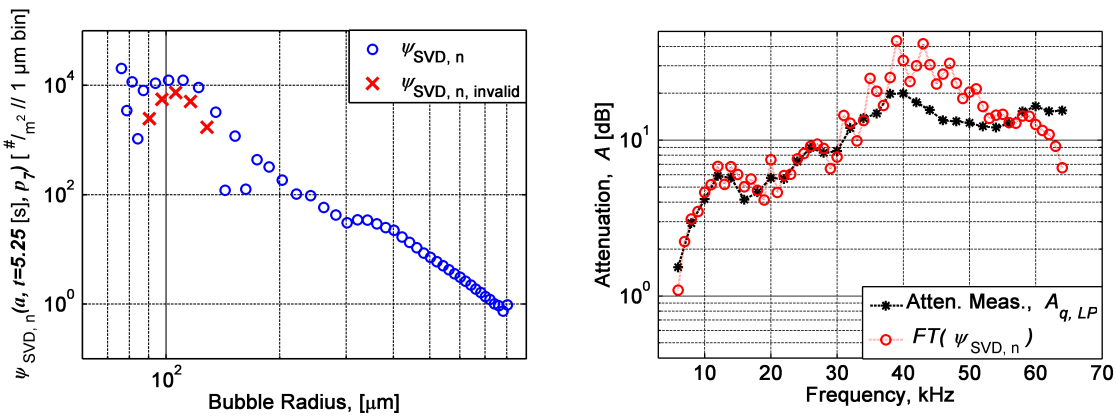

Fig. 5.4. Left: Bubble population as predicted by the Commander and McDonald method by adding noise to the **K**-matrix (denoted $\mathbf{K}_n$). The population estimate is shown in blue. Red 'x's represent negative bubble population estimates (shown as $|\psi_{invalid}|$), which are unphysical and disregarded. Right: The attenuation calculated from the bubble population in the left panel.

of $\left[\frac{\#}{\mathrm{m}^3} \text{ in a } 1\ \mu\text{m bin}\right]$ as the bubble populations presented in Chs. 2 and 3. Since the attenuation measurements have not yet been normalized to a 1 [m] range bin (as discussed in Ch. 5.1), the inverted bubble population accounts for the total number of bubbles between the acoustic projector and receive hydrophones. The bubble population presented in the left panel of Fig. 5.4 is expressed as

$$\psi_{\mathrm{SVD},n}(a,\ t\ =\ 5.25\ [\mathrm{s}],\ \mathbf{P}_7), \tag{5.1}$$

where $\mathbf{P}_i$ ($\mathbf{P}_7$ for hydrophone 7, in this case) is the path between the acoustic projector and receive hydrophone, indicating the total bubble population along $\mathbf{p}_i$. Further discussion of $\mathbf{p}_i$ is presented in Ch. 6.[2]

For bubbles smaller than about 200 [μm], adjacent radii show significant variability. For radii larger than 200 [μm] show a consistent power-law like trend. The 'consistency' for the larger bubble radii is, in part, due to the interpolation in attenuation performed primarily on the lower frequencies while generating the large bubble end of the knot radius spectrum (left panel of Fig. 5.2). The right panel of Fig. 5.4 presents the attenuation measured in the quarry (black *'s), as well as the attenuation predicted by applying the formal theory (Eqn. 3.12) to the bubble population presented in the left panel (blue ∘'s). The comparison agrees well below 35 kHz, but becomes more jagged and overestimates the attenuation between 35 and 55 kHz as a result of excluding the unphysical (negative) bubble population. The upper bound of attenuation is also underestimated for the reasons discussed in Sec. 3.1.1.

The second inversion method applied to the data shown in the right panel of Fig. 5.1 is to truncate the eigenvalues of the **K**-matrix such that the span of the EVs contain no large gaps and are smooth enough to allow for a suitable inverse (denoted by $\mathbf{K}_t$). For the EVs shown in the right panel of Fig. 5.2, the last EV is nearly an order of magnitude smaller than the

[2]The bubble population is denoted by (the more general) ψ_{SVD} even though in this example **K** is square, and the eigenvalue decomposition (EVD) is used.

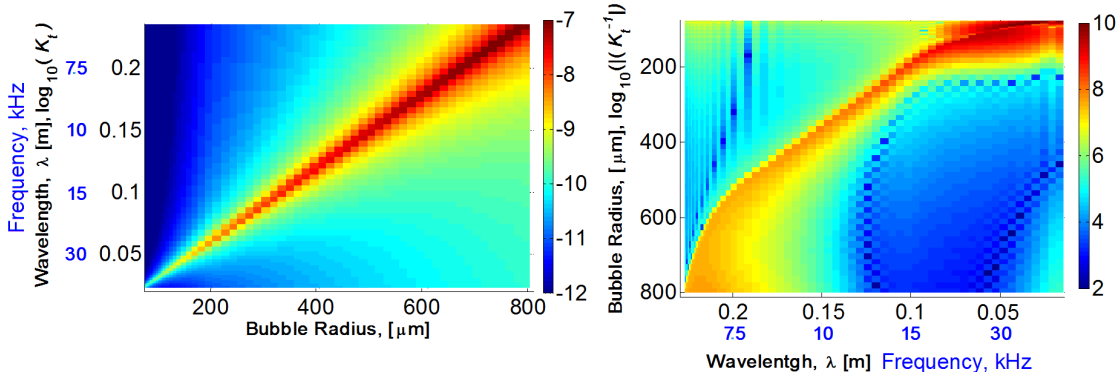

Fig. 5.5. Left: $\mathbf{K}_t$. Right: $\mathbf{K}_t^{-1}$. Levels in both plots are shown as $\log_{10}(\#)$. Frequency in this figure is shown in kHz, and bubble radius in [μm].

next-smallest EV. This large span of EVs hinders inversion, though the presence of only a single very small eigenvalue (or outlier) is specific to the ping chosen for this example (*see:* Fig. 5.1). Applying this method to other pings may require significant truncation of the eigenvalues as a result of the variable frequency span of the measured attenuation (some frequencies exhibit 'positive' attenuation, or 'gain', and must be ignored), thus the frequency spread (thus the span of knot radii) depend on the viability of the attenuation measurement. The compromise is to retain a large enough spread of inversion radii to sufficiently reproduce the measured attenuation. For the example in the right panel of Fig. 5.2, removing the last eigenvalue is sufficient to allow inversion. $\mathbf{K}_t$ and its corresponding inverse are shown in Figure 5.5. The difference between this K-matrix and that shown in Fig. 5.3 is small, however $\mathbf{K}_t^{-1}$ appears to have less variability for radii smaller than about 250 [μm], as well as the smaller scale variability surrounding the diagonal of the matrix.

The resulting bubble population estimate is shown in the left panel of Figure 5.6. This method

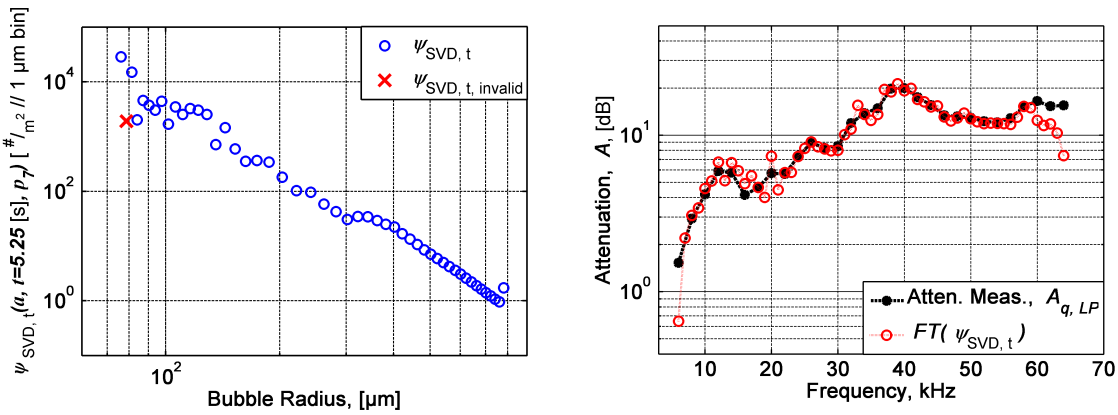

Fig. 5.6. Left: Bubble population as predicted by the Commander & McDonald Method by truncating the smallest EV of $\mathbf{K}_t$. The population estimate is shown in blue, red 'x's represent an estimated negative bubble population, which is unphysical and disregarded. Right: The attenuation as calculated from the bubble population in the left panel.

can also yield negative (unphysical) values for the bubble population, however there is only one such value for this ping. The smaller bubble radii show markedly less scatter for the EVD plus noise case, Fig. 5.4. The general trend of this bubble population could be characterized as a power-law dependent on radius (appears linear in log-log space). In the right panel of the figure, the attenuation measurement (black *'s) is compared to that predicted by applying the formal theory to the bubble population shown in the left panel (red ∘'s). The predicted attenuation matches better over the entire frequency range than when noise was added to the **K**-matrix ($\mathbf{K}_n$). The match is particularly good between 25 and 60 kHz, where the deviation is less than ± 2 dB. The same issues regarding boundary fall-off are present at both the low and high frequency bounds.

These were two methods that yielded the most appropriate bubble populations. While Commander & McDonald suggested a method to iteratively correct (primarily visually) the distribution by instituting a minimum curvature constraint (Eqn. 3.11) on the estimated bubble population, this method was time consuming and was not conducive to automation that consistently yielded results comparable to that in Fig. 5.6. The truncation method appeared to be the most stable, and most reliable at reproducing the measured attenuation from the quarry. For this reason, when referring to the Commander & McDonald method in the remainder of this thesis, the truncation procedure should be assumed unless otherwise stated.

5.2.2 Caruthers *et al.* Method

Applying the Caruthers method required little modification to the assumptions made previously in Sec. 3.2, and afforded more flexibility in terms of generating the knot radius spectrum. The knot radii could be spaced variably, however this was not required to yield bubble population estimates that sufficiently matched the measured attenuation. The example shown here uses radii corresponding to equal spacing in the frequency domain, which is logarithmic in the radius domain (see Appendix: A).

This method utilizes an iterative approach to obtain a bubble population. Following the steps detailed in section 3.2, the bubble population estimated by the first and second iterations for the data shown in Fig. 5.1 are shown in Figure 5.7. The left panel shows the two estimated bubble populations. Blue circles indicate the results of the first pass (ψ_{RBA}). They are largely hidden behind the red x's, which are the result of the second pass, or *corrective* iteration of this method (ψ_t'). The corresponding predictions of attenuation are shown in the right panel of the figure. The ripples in the high frequency attenuation, while not particularly large for this ping, are clearly reproduced more accurately by the first iteration. This method also suffers from notable departure near the high-frequency bound, which is detrimental to attenuation above 60 kHz

Overall, the Caruthers method produces smooth bubble population and attenuation curves that reproduce the measured attenuation to less than ±1 dB over most of the frequency range. This method does not require regularization of ill-conditioned matricies, therefore provides a consistently more stable result than Commander & McDonald.

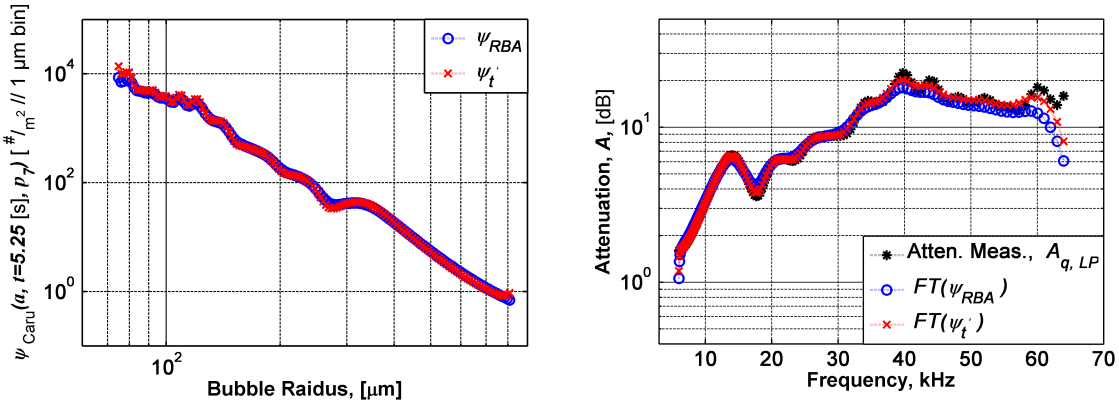

Fig. 5.7. Left: the estimated bubble populations via Caruthers *et al.* method applied to the attenuation data shown in Fig. 5.1. ψ_0 and ψ_t' are the bubble population estimate using RBA only, and the first iterative correction, respectively. Right: Attenuation as calculated by the bubble populations in the left panel of this figure.

5.2.2.1 Extrapolation of the Attenuation Data

As mentioned in the discussion of the inversion methods in Sec. 3.2.3.1, all of these methods produce a bubble population estimates that are unable to reproduce the limits of the attenuation (*i.e.* in the right panel of Fig. 5.7). One method used to resolve this departure was extrapolation of the attenuation.

Figure 5.8 shows the effect of extrapolating the attenuation data on the bubble population estimate. Only the high frequencies suffered from boundary underestimation in the bubble population estimates for this ping, the attenuation value at 64 kHz was held for an additional three points (66, 68 and 70 kHz). The bubble population estimates appear in the left panel of this figure, and include additional radii at the low end (by comparison to Fig. 5.7), which are neces-

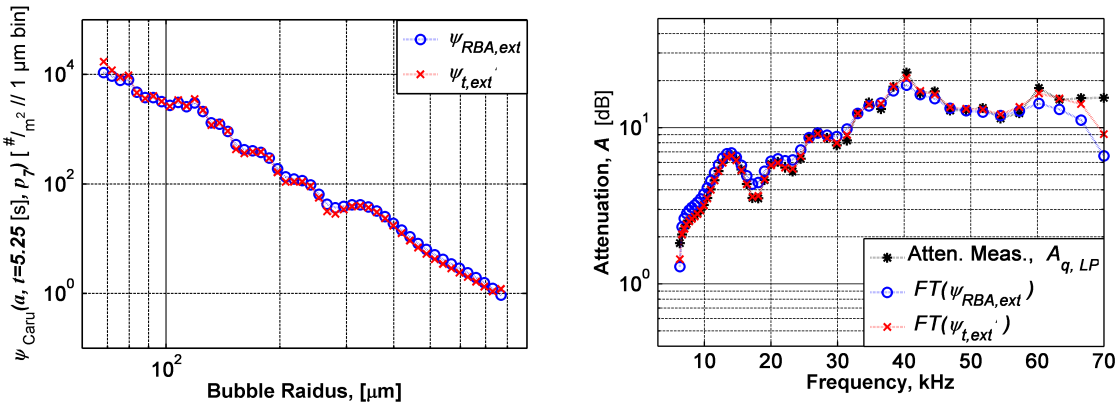

Fig. 5.8. Left: the estimated bubble populations via Caruthers *et al.* method. $\psi_{RBA,ext}$ and $\psi_{t,ext}'$ are the bubble population estimate using RBA only, and the first iterative correction, respectively. This result utilizes the extrapolation technique, in which the attenuation measured at 64 kHz is held constant out to 70 kHz. Right: Attenuation calculated with the bubble populations in the left panel of this figure.

sary to reproduce the attenuation curve up to 64 kHz. The improvement in attenuation estimate is visible in the right panel. Extrapolating the attenuation measurement does not 'cure' the high-frequency departure from the attenuation measurement, but it allows better reproduction of attenuation at the highest measurement frequencies, 64 kHz in this case. The additional radii introduced as a result of extrapolation must be included in further calculations if the high frequency bound is to be reproduced.

5.2.3 Czerski & Farmer Method

The third method applied to obtain a bubble population estimate from the attenuation measurement shown in Fig. 5.1 is the Czerski & Farmer (or 'sequence') method. The sequence method requires a similar set of assumptions as the Caruthers *et al.*, method since they both employ the RBA to compute the contribution of resonant bubbles to the total attenuation. However, the sequence method focuses on accounting for geometric scattering by large bubbles in order to better estimate the small bubble population.

Figure 5.9 presents the results of applying the sequence method. Again, the left panel shows the estimated bubble population, and the right panel compares the measured predicted attenuation by applying the formal theory to ψ_{seq}. This method agrees well with the measured attenuation, but still suffers from departure at the high frequencies. The sequence method performs very similarly to the first pass of the Caruthers method (or ψ_{RBA} from the Carutehrs method), but reproduces the attenuation at higher frequencies more accurately. Still, this method suffers from degraded performance at the bounds of the attenuation data.

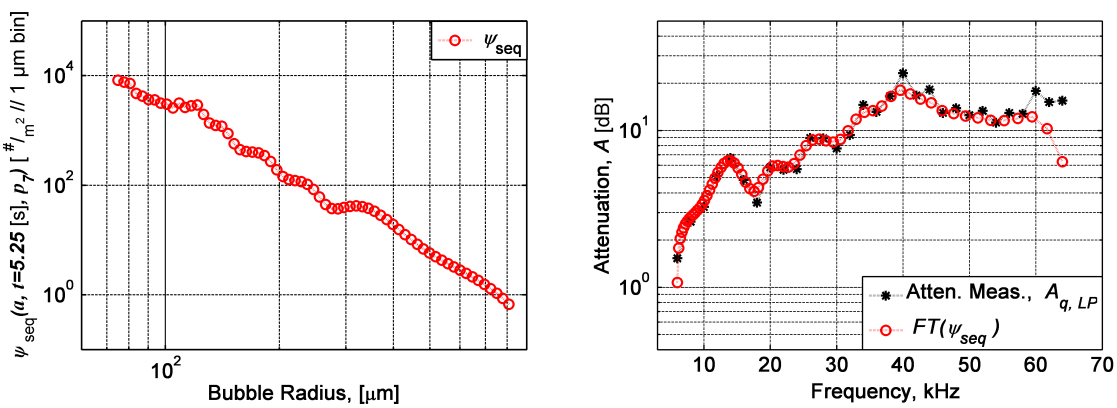

Fig. 5.9. Left: bubble population as estimated by the Sequence method. Right: Attenuation as calculated by the bubble population in the left panel of this figure (red ∘'s, and measured attenuation (black *'s).

5.2.4 Comments & Analysis of Inversion Algorithm Performance

All three of these methods provide reasonable estimates of the bubble population resulting from an underwater explosion. In this chapter, each method was applied to the same set of attenuation

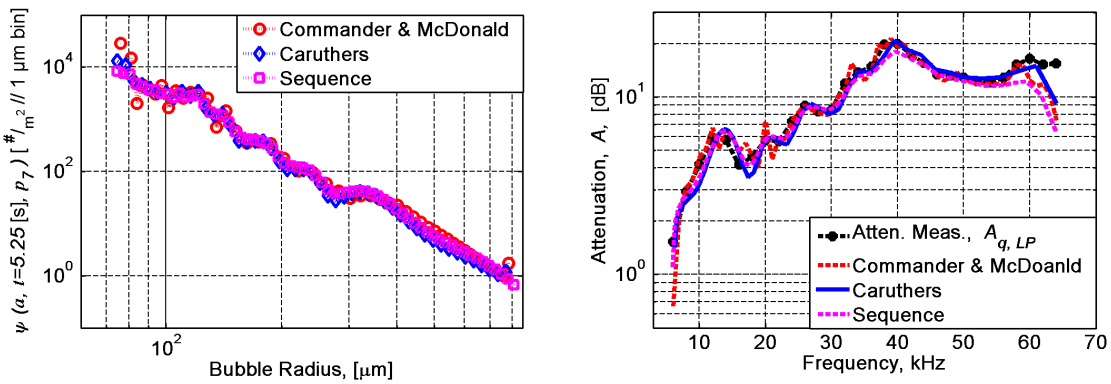

Fig. 5.10. The left panel shows a comparison of the three methods used for bubble population inversion. The right panel demonstrates the ability of these populations to reproduce the measurement of attenuation in the quarry.

measurements in order to directly compare their performance. The left panel of Figure 5.10 compares the bubble populations estimated via the Commander & McDonald method ($\psi_{SVD,t}$, red ○'s), the second pass of the Caruthers *et al.* method, ψ'_t (blue ◊'s), and the sequence method, ψ_{seq} (purple □'s). The right panel shows their corresponding attenuation calculated by applying the formal theory (Eqn. 3.12), as well as the attenuation measured in the quarry (black *'s).

While the Commander & McDonald method has considerably more scatter over the small bubble radii, all three bubble populations agree well. The results obtained using the Czerski and Caruthers methods are very close across the entire bubble spectrum, but as a result of the iterative process, the Caruthers method contains more ripples, resulting in better agreement with the measurement. All of the bubble populations show a strong trend toward a power-law relationship (depending on bubble radius a [μm]).

Attenuation calculated from all bubble population estimates agree well with the measured attenuation, and all methods suffer from some degree of boundary underestimation. As stated in Ch. 3, a technique of extrapolating the boundaries of the attenuation data alleviates this problem (for this ping, only the high frequency bound requires extrapolation), but requires assuming levels of attenuation at frequencies which were not measured. Also, this will add the effects of additional resonant and non-resonant bubbles, which will simultaneously increase the ability to reproduce the high frequency attenuation in the data, and possibly introduce error across the frequency band for which measurements are available.

Table 5.1 presents the RMS error and standard deviation (σ) between the attenuation measurements and that predicted using the three inversion methods. The error has been calculated by taking the difference between the smoothed attenuation measurement (the input to the inversion algorithms, Fig. 5.1) and the attenuation calculated by applying the formal theory to the inverted bubble populations. Since the density and location of the knot radii may not be consistent between the three methods, this is only calculated for the frequencies at which the attenuation was measured, for this case between 6 and 64 kHz in 2 kHz intervals.

Method:	RMS difference over meas. freqs, ± dB	Std. Deviation, σ
SVD, $FT(\psi_n)$	7.11	6.55
SVD, $FT(\psi_{trunc})$	1.72	1.66
Caruthers, $FT(\psi_{RBA})$	1.54	1.47
Caruthers, $FT(\psi'_t)$	0.90	0.86
Czerski Method, $FT(\psi_{seq})$	1.71	1.67

Table 5.1. Summary of the percent discrepancy and standard deviation for the three inversion methods applied to the attenuation data given in Fig. 5.1. SVD refers to the Commander & McDonald method.

The ping utilized in this chapter was chosen because it represented a well-behaved inversion. Not every ping is as easy to invert, and the statistics presented in table 5.1 may be uncharacteristic of the long-term performance of these inversion algorithms. Also, the statistics will vary with time due to the frequency-dependent attenuation decay and variability in level over time. Therefore, the most consistently performing algorithm is chosen for its overall agreement with the measured attenuation. Table 5.2 presents statistics averaged over a period of 7 seconds after the UNDEX for phone 7 during event 2 (same phone and event analyzed above). For this period of time, the trend is similar to the single-ping case, and in general, the Caruthers method provides the smallest RMS error and variance relative to the measured data.

Method:	RMS Error over All Freq., ± dB	Std. Deviation, σ
SVD, $FT(\psi_n)$	6.20	5.72
SVD, $FT(\psi_{trunc})$	2.04	1.99
Caruthers, $FT(\psi_{RBA})$	1.96	1.84
Caruthers, $FT(\psi'_t)$	1.24	1.24
Sequence Method, $FT(\psi_{seq})$	1.67	1.64

Table 5.2. Average error for five consecutive seconds of attenuation data for the same hydrophone used in this chapter (phone 7). The statistics in this table are representative of their overall performance of the three methods on data from various times, phones and events. SVD refers to the Commander & McDonald method.

5.3 Bubble Population Estimates for Event 2, All Forward Loss Hydrophones

In the previous section, the Caruthers method was shown to reproduce the measured attenuation with the least error and most consistently of the three methods applied to the data in Fig. 5.1. Figure 5.11 presents the estimated bubble population vs. time (since UNDEX) for all forward loss hydrophones for event 2 (event 1 not shown). These populations were calculated using the Caruthers *et al.* method[3]. The axes are of bubble radius (in [μm]) vs time, with color representing $\log_{10}(\psi'_t(a, t, \mathbf{P}_i))$ (see Eqn. 5.1 for notation). The four Reson hydrophones that

[3]The bubble populations in Fig. 5.11 were computed using the approach outlined in Sec. 3.2 and applied to the quarry attenuation measurements in Sec. 5.2.2, with one exception. Occasionally, the attenuation measured in the quarry drops below 0 dB due to the main lobe of the projector's motion relative to the forward loss array. Measured attenuation less than 0 is not indicative of attenuation from bubbles, thus the minimum value (or floor) of attenuation used to generate Fig. 5.11 was 0.01 dB.

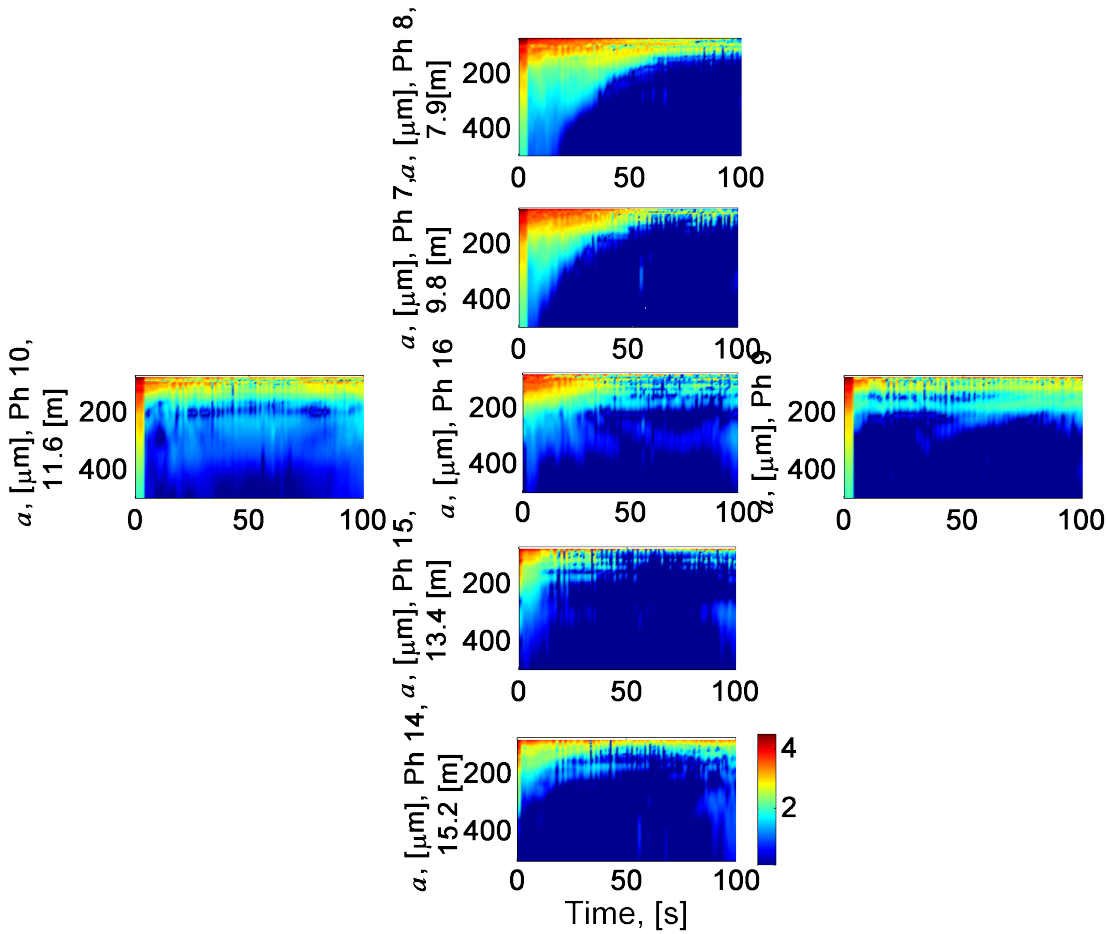

Fig. 5.11. Estimated bubble population for the first 100 seconds after UNDEX for all hydrophones during event 2. Bubble radius vs. time, color scale indicating $\log_{10}(\psi_t')$ of the number of bubbles. The units of these plots are $\left[\frac{\text{bubbles}}{\text{m}^2} \text{ in a 1 } \mu\text{m bin}\right]$

were insensitive for up to 5 seconds immediately following UNDEX (#s 7, 8, 9 and 10) show large bubble populations during this time, which are not a result of acoustic signal and should be ignored.

For the times shortly after UNDEX, the shallowest three hydrophones (7, 8 and 16) show the largest bubble populations, which agrees well with the attenuation measurements, since the same three hydrophones experience the highest magnitude and duration of attenuation. The 7.9 [m] deep phone experiences the longest presence of larger bubbles, with decreasing numbers of larger bubbles as depth increases. There are almost no bubbles larger than 300 [μm] present at 15.2 [m] depth. This is expected since large bubbles attenuate lower frequencies, and the lower hydrophones show almost no attenuation at lower frequencies (*see:* Fig. 4.36).

In general, the number of smaller bubbles show a strong dependence on depth (for a given time), which agrees well with the attenuation data, as the shallower hydrophones experience

a higher level and longer duration of attenuation at higher frequencies (at which smaller bubbles attenuate energy). The number of 100 [μm] bubbles ($f_R \approx 45$ kHz) appears to be highest in phones 7 and 16, which show the strongest attenuation at approximately 45 kHz ($\approx f_R(100[\mu\text{m}]$ at 9.8 [m] depth)).

The time dependence of these bubble populations largely follows that of the attenuation (discussed in Sec. 4.4). The outer phones (9 and 10) show a population of primarily smaller bubbles for a few 10s of seconds after UNDEX, with significant variability in time, which is consistent with the attenuation measurement for these phones. Phone 10 shows a high level of smaller and medium sized bubbles throughout the time record, however the attenuation measurement remains consistently low at all frequencies. This effect is likely caused by a slight change in the acoustic projector's pointing direction, rather than an increased, and long lasting population of bubbles of all sizes at this position.

Chapter 6

UNDEX Bubble Population Model

6.1 Introduction

This chapter addresses the development of the UNDEX bubble population model that reproduces the attenuation and backscatter observed in the UNDEX events. The following details the assumptions, simplifications, and compromises that were necessary to develop the model. All results in this chapter are derived from the bubble populations inverted from the measured attenuation during events 1 and 2 (Figs. 4.35 and 4.36, respectively), as well as multibeam sonar images of the UNDEX cloud (Sec. 4.3.3).

After the UNDEX bubble population model is presented, it is used to predict attenuation and backscatter from the modeled UNDEX bubble cloud, which are then compared to measurements made at the 2008 quarry test.

6.2 Model Development

Using the bubble population estimates for each hydrophone (Fig. 5.11), the spatial and temporal properties of the UNDEX bubble cloud can be characterized by a set of empirical equations. The following sections examine the UNDEX cloud's dependence on bubble size, the horizontal distribution of bubbles, the depth dependence, and how the bubble population changes over time. As these dependencies are discussed, a model equation is developed that accounts for all of these characteristics. The goal is to generate a 3-dimensional bubble cloud that ages with time similar to the bubble population inverted from the attenuation measurements.

Since this chapter addresses the spatial dependence of the UNDEX cloud, we now define a coordinate system centered at the charge location in order to streamline the following discussion. The origin is located at the surface of the water, above the charge. Depth, the z-axis, is positive downward and the backscatter array of hydrophones lie in a plane parallel to the $x - z$ plane of this coordinate system. Recalling the quarry test geometry (Fig. 4.2), the charge is located 15.2

[m] below the water's surface, thus its position is defined as $p_c = (x_c,\ y_c,\ z_c) = (0,\ 0, +15.2)$ [m]. The line passing through the origin and charge location (or the z-axis) will be referred to as the UNDEX axis. Each hydrophone position is given by p_i, where i corresponds to the hydrophone number. For example, the location of forward loss hydrophone 7 at 9.8 [m] depth is $\mathbf{P}_7 = (0, +38.1, +9.8)$ [m]. p_{F27} is the location of the acoustic projector (at $(0, -38.1, +15.2)$ [m]). A nonspecific coordinate in the geometry is denoted as $p = (x,\ y,\ z)$. This geometry is discussed further in Sec. 6.4.1.

In Eqn. 5.1, the notation $\mathbf{P}_i$ was introduced as the path between the acoustic projector and i^{th} receive hydrophone, which can now be written

$$\mathbf{P}_i = (\mathbf{x}_i, \mathbf{y}_i, \mathbf{z}_i), \tag{6.1}$$

to indicate the ensemble of vectors indicating positions along the path between the acoustic projector (p_{F27}) to the receive hydrophone p_i

6.2.1 Bubble Size Dependence

The bubble population estimates for the paths between the projector and the forward loss hydrophones, presented in Fig. 5.11, is exploited to model the bubble population spectrum. For each population estimate (vertical lines in Fig. 5.11), a two parameter power-law of the form

$$\psi(a, t, \mathbf{P}_i) = \psi_0(t, \mathbf{P}_i)\ a^{m(t, \mathbf{P}_i)}, \tag{6.2}$$

is applied to obtain a best-fit trendline. $\psi_0(t, \mathbf{P}_i)$ is an amplitude scalar for the number of bubbles, and $m(t, \mathbf{P}_i)$ is the slope of the population in log-log space. Both of these parameters depend on time and the source-to-receive hydrophone path ($\mathbf{P}_i$).

The left panel of Figure 6.1 shows an example of a power-law trendline (labeled ψ_{PL}, in red) for the ping presented and analyzed in Ch. 5 (phone 7, 5.25 [s] after event 2), as well as the individual inversion results (Commander & McDonald [the truncated SVD method, $\psi_{SVD,t}$], Caruthers [ψ_t'] and the sequence method [ψ_{seq}], shown with various black symbols in order to avoid distraction from the trend lines also shown in the plot.).

For the power-law fit shown in the left panel, $m(t = 5.25[\text{s}],\ \mathbf{P}_7) = -3.98$ and $\psi_0(t = 5.25\ [\text{s}],\ \mathbf{P}_7) = 6.1 \times 10^{11}\ \left[\frac{\text{bubbles}}{\text{m}^2} \text{ in a } 1\mu\text{m bin}\right]$. This bubble population estimate is defined over $70 \leq a \leq 860$ [μm]. For the remainder of this chapter, ψ_{PL} will be used to refer to the power-law fit shown in the left panel of Fig. 6.1.

The left panel also contains two published models for the bubble populations present under wind-generated breaking waves in seawater. The blue line is Trevorrow's model (2003), which utilizes an $\exp\left(\frac{-a[\mu\text{m}]}{34}\right)$ size dependence [2]. The line in green is from Hall's model, which is broken up into three radius regions, each with a different dependence on radius. Bubbles larger than about 50 [μm] in Hall's model (1989) have a power-law dependence of $a^{-4.5}$ [15]. The published models (Hall and Trevorrow) have been shifted vertically to match the magnitude of

the quarry bubble populations.

The power-law fit is able to capture the magnitude and general slope of the inverted bubble populations for the full range of bubble radii. Hall's model, shown in green, is steeper (has a more negative slope on a log-log scale) than ψ_{PL}. This results in either overestimating the number of bubbles with small radius, or underestimating the number of bubbles with large radius, compared to ψ_{PL} (though is dependent on scaling, which was arbitrary in this case). Trevorrow's model, shown in blue, has an exponential dependence on bubble radius, and thus cannot account for the population of larger bubbles compared to ψ_{PL}. However, as scaled in the figure, $\psi_{Trevorrow}$ appears to match the bubble population well for $70 \leq a \leq 300$ [μm]. In general, the slope of ψ_{PL} is reasonable compared with that of published in-water bubble populations under wind-generated breaking waves.

The right panel of Fig. 6.1 compares the attenuation measured in the quarry with that calculated by applying formal theory (Eqs. 2.14 and 2.21) to the bubble population models in the left panel. $FT(\psi_{PL})$, shown in red, is able to reproduce the general magnitude and frequency-dependent characteristics of the attenuation measured in the quarry, ($A_q(f)$, black). Attenuation calculated from Hall's model ($FT(\psi_{Hall})$) slightly underestimates $A_q(f)$ for frequencies below 15 kHz, and overestimates attenuation for frequencies above 40 kHz, often by more than a factor of two. Trevorrow's model ($FT(\psi_{Trevorrow})$, blue) underestimates $A_q(f)$ for low frequencies since the population does not contain many bubbles with larger radii. $FT(\psi_{Trevorrow})$ generally overestimates the attenuation for frequencies above 20 kHz, however exhibits a similar frequency-dependent curvature as the attenuation measurement.

Figure 6.2 shows $m(t, \mathbf{P}_i)$ of Eqn. 6.2 for the vertical array of hydrophones. Recall the first 5 seconds are unrepresentative of acoustic phenomena. The data shown in this figure are the result of a 7-point moving average filter, as the ping-to-ping slope changes rapidly. For the

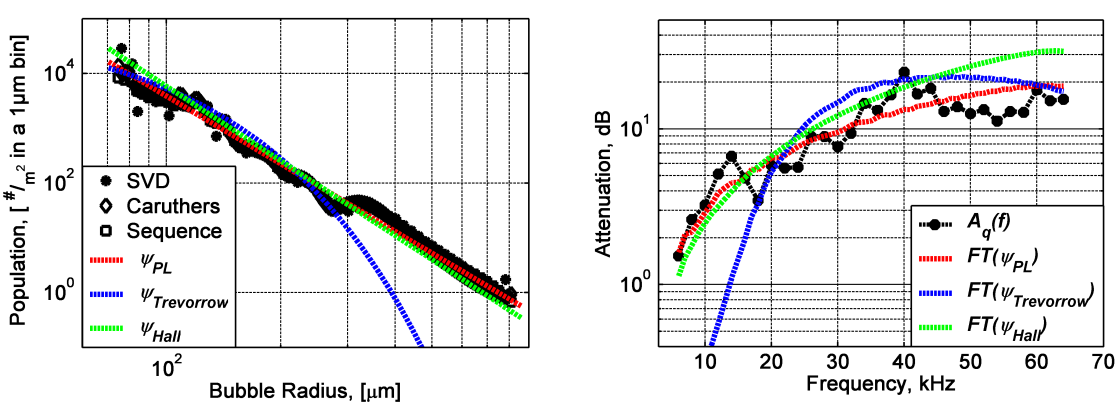

Fig. 6.1. Left: inverted bubble populations compared with other published in-water populations. Results of the inversion methods are indicated by various black symbols (*see:* Ch. 5), and a power law trendline in purple (phone 7, 5.25 [s] after event 2 UNDEX). Trevorrow [2](blue) and Hall [15](green) are published models for the bubble populations under wind-generated breaking waves. Right: a comparison of the attenuation computed for the model populations in the left panel. Attenuation measured in the quarry, $A_q(f)$ is also shown (for event 2, Phone 7, 5.25 [s] post-UNDEX).

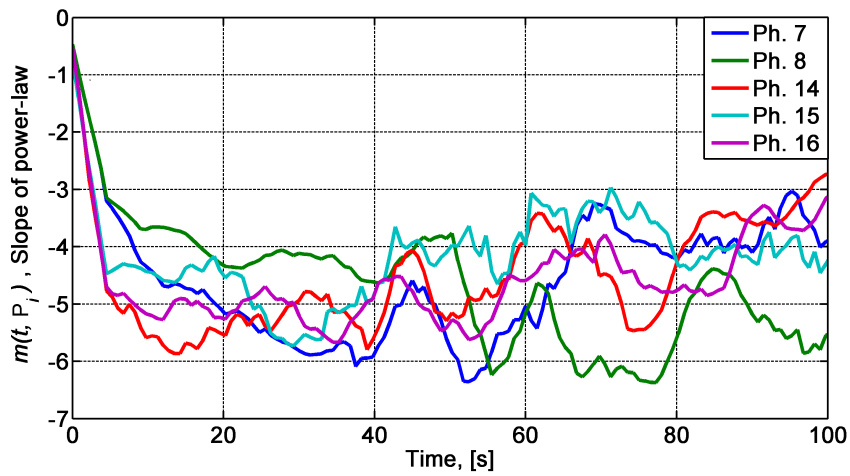

Fig. 6.2. Slope of the power-law fit to the bubble populations, $m(t, \mathbf{P}_i)$ in Eqn. 6.5 (data plotted after applying 7-pt low pass filter).

two shallowest hydrophones (7 and 8), the slope ($m(t, \mathbf{P}_i)$) consistently increases (becomes more negative) over $5 \leq t \leq 40$ [s]. As larger bubbles rise out of the scope of a given hydrophone, small bubbles linger, and the slope will steepen with time (*see:* Sec. 4.4.2). This is supported by the fast decay of attenuation at lower frequencies (at which large bubbles attenuate energy) seen in the forward loss attenuation measurements (Figs. 4.35 and 4.36). For $t \geq$40 [s]. In general, the characteristics of the bubble population are obviously not spatially or temporally stationary. The slope of the bubble population is highly variable ($-6 \leq m \leq -3$), but on average remains around -4.5. $m(t, \mathbf{P}_i)$ for the two outside hydrophones (9 and 10) are not shown in this figure.

For simplicity, the model presented here will employ a constant value of $m(t, \mathbf{P}_i)$ for all time and for all hydrophone positions. This value, $< m >_{t,\mathbf{P}_i} = -4.1$, was derived from the time-averaged slopes of the forward loss array (including bubble populations from the horizontal array, not shown). For the remainder of this chapter $< m >_{t,\mathbf{P}_i}$ will be shortened to m. The scalar used to account for the number of bubbles ($\psi_0(t, \mathbf{P}_i)$ in Eqn. 6.2) is further analyzed next.

6.2.2 Temporal Dependence of the UNDEX cloud

The bubble populations for the UNDEX cloud (Fig. 5.11) show a strong time-dependence caused, in part, by bubbles rising through the water column and bubble dissolution. Figure 6.3 shows the number of 100 [μm] bubbles for each hydrophone vs. time since UNDEX ($\psi_0(t, \mathbf{P}_i)$ in Eqn. 6.2). Also, a 3-pt moving average has been applied to this data. Recall that the first few pings occur when the hydrophones are insensitive to acoustic fluctuations, and the first useful ping is approximately 5.25 [s] after UNDEX. The three shallower phones in the vertical array (7, 8 and 16) all have a significantly larger bubble population than the deeper hydrophones (14 and 15), which is consistent with Fig. 5.11 and the attenuation measurement for event 2 (Fig. 4.36). The bubble population consistently decreases from 5.25 [s] until approximately 55 [s] after UNDEX, indicating that bubbles are rising, dissolving or otherwise dispersing out of the scope

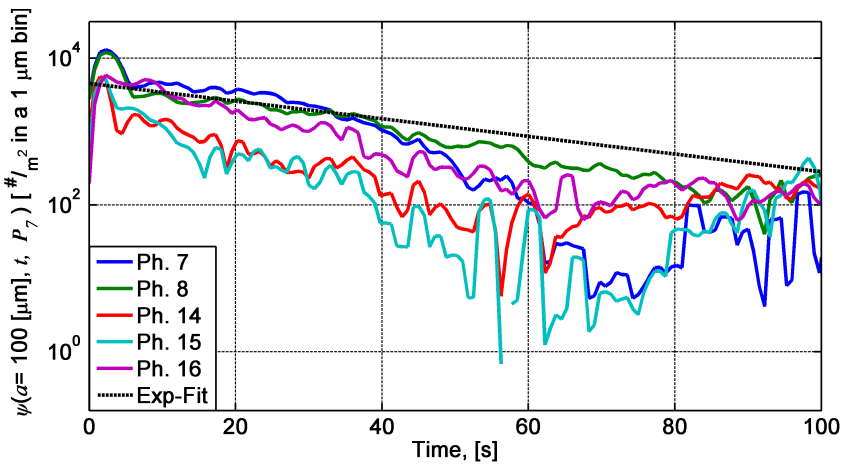

Fig. 6.3. Number of 100 [μm] bubbles ($\psi(a = 100[\mu\text{m}],\ t,\ \mathbf{P}_i)$) vs. time for the forward loss vertical array of hydrophones (data plotted after applying a 3-pt moving average). Each hydrophone plotted separately. Exponential fit shown as a black dashed line.

of the measurement hydrophones. For phone 7, $\psi(a = 100[\mu\text{m}],\ t,\ \mathbf{P}_7)$ changes slowly over $5.25 \leq t \leq 35$ [s] before decreasing more rapidly, which roughly agrees with the constant (or 'high') attenuation level in Fig. 4.37. However, this effect is not strong and is ignored.

The time dependence of the bubble cloud is approximated using an exponential decay in the number of bubbles as the cloud ages (resulting in an exponential-like decay in attenuation). The black dashed line in this plot indicates an exponential fit to the number of bubbles estimated from attenuation measured at the vertical array of hydrophones between $5 \leq t \leq 55$ [s]. The fit is an average of the slopes of the individual hydrophones. The time dependence fit is

$$\psi(t) \propto \exp\left(-\frac{t}{36.\ [\text{s}]}\right), \tag{6.3}$$

where t is time since UNDEX in seconds (for $t \geq 0$ [s]). Eqn. 6.3 indicates that the bubble population (for bubbles with radius of 100 [μm]) has an e-folding time (T_C) of 36.1 [s] over $5 \leq t \leq 55$ [s]. Eqn. 6.3 is used to age the bubble cloud by effectively reducing the number of bubbles present in the cloud in order to account for the physical mechanisms causing decay of the bubble cloud (bubble rise physics, currents, and dissolution).

6.2.3 Spatial Dependence of the UNDEX Cloud

During UNDEX, several mechanisms result in the horizontal and vertical displacement of bubbles for a considerable distance from the charge location. This can be seen from the bubble rising phenomenon as discussed in Sec. 4.4.2, from the horizontal extent of attenuation seen in the forward loss attenuation measurements, and from the multibeam sonar images that were collected in the 2007 and 2008 Quarry tests (*see:* Sec. 4.3.3). In order to extract a 3-dimensional bubble population model from this data, fitting must be done to the physical spread of bubbles within the region of the UNDEX. A two-step approach is used. The depth dependence of the bubble

cloud is obtained from the number of bubbles of various sizes along the paths to each vertical array element, and the distribution of bubbles in the horizontal plane of the UNDEX is obtained from the bubble population estimates for the forward loss horizontal array.

6.2.3.1 Depth Dependence of UNDEX Cloud

For each hydrophone in the vertical array, the number of bubbles of each size is averaged over a period of 6 seconds (following the drop-out induced by UNDEX, and extracted from Fig. 5.11), and used to determine the depth-dependence of the UNDEX cloud. Fig. 6.4 shows number of 100, 200, and 400 [μm] bubbles vs. water column depth (arithmetic mean between projector and receive hydrophone depths), as well as an exponential fit for each of the bubble sizes. This plot shows that, on average, the number of bubbles present in the UNDEX cloud decreases with depth. For the 100 [μm] bubbles, hydrophones located at 9.8 [m] and 11.6 [m] do not follow this trend exactly. In Fig. 4.36, these two hydrophone exhibit a higher level of attenuation near 40 kHz than the surrounding hydrophones.

The black dashed lines in Fig. 6.4 indicate exponential trendlines fit to the data, in the form of

$$\psi(t, \mathbf{P}_i) = \psi(t, \mathbf{x}_i, \mathbf{y}_i, \mathbf{z}_i) = \psi_0(t, \mathbf{x}_i, \mathbf{y}_i) \ \exp\left(-\frac{\mathbf{z}_i}{D_c}\right), \tag{6.4}$$

where D_c is the e-folding depth (see: Table 6.1), and $\mathbf{z}_i$ contains the depths in the water column for which we have measured data. The dependence on path $\mathbf{P}_i$ has been broken into its constituent components in order to separate dependence on depth from that of horizontal distance from the UNDEX axis. Table 6.1 presents the e-folding depth (D_c) for the bubble sizes shown in Fig. 6.4, as well as an R^2 value (correlation coefficient of the fit). For simplicity, the e-folding depth for 100 [μm] bubbles will be used in further development of the model.

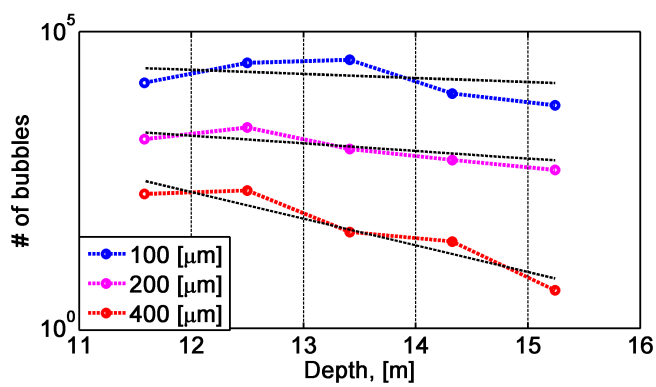

Fig. 6.4. Number of bubbles of three sizes (averaged over 6 pings following UNDEX, excluding first 5 sec.) vs depth at the charge location. An exponential fit for the 100 [μm] bubble curve is shown by the black dashed line.

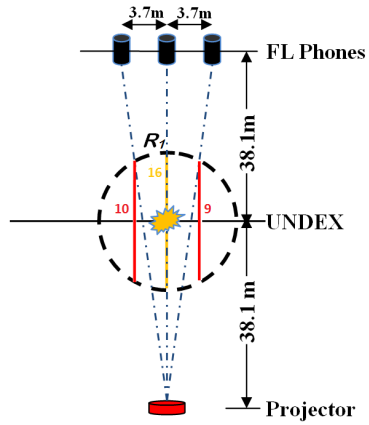

Fig. 6.5. The acoustic paths from the projector to the forward loss (FL) horizontal array of hydrophones. The dashed circle around the UNDEX represents the maximum extent of the bubble cloud (from multibeam sonar data). The acoustic projector is at 15.2 [m] Depth, and the FL horizontal array is comprised of three hydrophones at 11.6 [m] depth. (This figure is not shown to scale)

We define the depth dependence to be

$$\psi(a, t, \mathbf{x}_i, \mathbf{y}_i, z) \propto \exp\left(-\frac{z}{D_c}\right). \tag{6.5}$$

Since Eqn. 6.5 is general, it is valid not only at depths at which measurements were taken ($\mathbf{z}_i$), but can be used to extrapolate for any depth, z.

The attenuation and multibeam sonar data both provide evidence of a population of bubbles at, and below the charge depth (*i.e.* from attenuation spur seen in Fig. 4.36). The 2008 multibeam sonar images of the UNDEX cloud show that some bubbles have been injected a few meters below the charge depth (left panel of Fig. 4.30). Accordingly, the bubble population model due to an underwater explosion occurring at depth z_c should be truncated below $D_{\max}$, which is approximately 3 [m] below the charge depth (empirical limit derived from the multibeam sonar data, *see:* Sec. 4.3.3).

6.2.3.2 Horizontal Extent of UNDEX Bubble Cloud

As discussed previously, the attenuation measurements presented in Ch. 4 are for the entire acoustic ray path from the projector to the hydrophone. Figure 6.5 shows a plan view of the

	e-folding depth, [m]	R^2 of fit
100 [μm]	6.01	0.63
200 [μm]	3.38	0.71
400 [μm]	0.97	0.86

Table 6.1. e-folding depth for 100, 200 and 400 [μm] bubbles. These e-folding depths correspond to the exponential fits (black dashed lines) in Fig.6.4.

approximate ray paths between the projector and the horizontal array of hydrophones ($\mathbf{P}_i$). The dashed black circle indicates an estimate of the bubble cloud boundary taken from the multibeam sonar data, Fig. 4.29. The acoustic ray paths form three chords through the bubble cloud, each at an upward angle (from the projector (15.2 [m]) to the receive hydrophones (11.6 [m])).

Table 6.2 presents the average number of bubbles for these ray paths during the same 6 second period as shown in Fig. 6.4. The central phone consistently shows a larger population of bubbles with a radius of 100 [μm], and drops off unevenly toward either side.

Hydrophone Number & Location:	# of bubbles at 100 [μm]	200 [μm]	400 [μm]
South, Ph. 9 ($\psi(a = 100[\mu\text{m}],\ \mathbf{P}_9)$)	1478	30	1
Center, Ph. 16 ($\psi(a = 100[\mu\text{m}],\ \mathbf{P}_{16})$)	4170	131	6
North, Ph. 10 ($\psi(a = 100[\mu\text{m}],\ \mathbf{P}_{10})$)	2472	15	3

Table 6.2. Number of 100 [μm] bubbles for the horizontal array. This is bubble density integrated over the path between the projector and hydrophone array (or ($\psi(a = 100[\mu\text{m}],\ \mathbf{P}_i)$)), and assumes a depth of 13.4 [m] at the UNDEX axis.

A simplified geometry is used to obtain a 2-dimensional cross section of the bubble cloud over this region. We approximate all chords as being horizontal at the arithmetic mean depth between the projector and horizontal array of hydrophones (meaning constant z), and the two outer chords are displaced by 1.83 [m] (6 [ft.], shown as (9) and (10) in Fig. 6.5) from the central chord. A key assumption made to approximate the horizontal distribution of bubbles is that the explosion is, on average, omnidirectional; that is, it results in a spherical gas globe and ejects equal amounts of debris and bubbles in all directions[1]. Then, a 2-D Gaussian spatial dependence is assumed[2], and the bubble population model takes the form

$$\psi(a, t, x, y, z) = \psi_g(a, t, z)\ \exp\left(-\frac{\mathbf{r}(\mathbf{x}_i, \mathbf{y}_i)^2}{2\sigma_g(t, z)^2}\right), \tag{6.6}$$

where $\mathbf{r}(\mathbf{x_i}, \mathbf{y_i}) = \sqrt{(\mathbf{x}_i - x_c)^2 + (\mathbf{y}_i - y_c)^2}$ is the radial distance away from the UNDEX axis in [m], (x_c, y_c) are the coordinates of the UNDEX axis and $\sigma_g(t, z)$ is the standard deviation of the bubble density. A normalization constant in the formal definition of a Gaussian distribution, $\frac{1}{\sqrt{2\pi\sigma_g(t,z)^2}}$, is absorbed into the scaling factor $\psi_g(a, t, z)$ (modified from [28]).

The solution to Eqn. 6.6 is an inverse problem in which the number of bubbles along three acoustic ray paths between source to the receive hydrophones are known (calculated from measurements of attenuation, like that in the left panel of Fig. 6.1), and the variance ($\sigma_g(t, z)$) and the scaling factor ($\psi_g(a, t, z)$) are to be obtained.

Now, looking only at the distribution of bubbles in the horizontal plane (meaning fixed z), we define a general set of integrals that describe the total number of bubbles existing within a 1 [m] square rectangular tube along the acoustic ray path (or chord, labeled 1, 2, or 3 in Fig. 6.5)

[1] It turns out this is likely a poor assumption based on personal correspondence with Helen Czerski. However the effects of a non-omnidirectional explosion are not known in this data, thus the model is developed by assuming an omnidirectional charge. Webber has looked extensively at acoustic propagation through non-uniformly distributed bubble clouds [27].

[2] In general, the assumption of a Gaussian distribution is made since it seemed a reasonable visual approximation to the multibeam sonar data (Sec. 4.3.3), and appeared to be as appropriate as any other alternative.

as

$$\psi_i(a,t,\mathbf{x}_i,\mathbf{y}_i,z) = \psi_g(a,t,z)\int_{-\infty}^{\infty}\exp\left(-\frac{\mathbf{r}(\mathbf{x}_i,\mathbf{y}_i)}{2\sigma_g(t,\mathbf{z}_i)^2}\right)d\mathbf{y_i}. \tag{6.7}$$

where we have allowed the normalization factor to be absorbed by $\psi_g(a,t,z)$ (introduced to indicate the contribution due to only the Gaussian distribution). Eqn. 6.7 describes the 2-D spatial distribution of bubbles in the horizontal plane at 13.4 [m] depth (mean depth of projector and horizontal array of hydrophones). Since we have assumed circular symmetry (in the horizontal plane), rotating the chords about the UNDEX axis leads to the same result, thus x_i can be held constant during these integrals. This analysis will be done for bubbles with radii of 100 [μm], and approximately 5.25 [s] after UNDEX.

After defining the other two integrals along chords through the UNDEX cloud in a similar fashion ($\psi_{10}(a = 100[\mu\text{m}], t = 5.25[\text{s}], x_{10} = -1.83[\text{m}], \mathbf{y}_{10}, z = 13.4[\text{m}])$, and $\psi_9(a = 100[\mu\text{m}], t = 5.25[\text{s}], x_9 = -1.83[\text{m}], \mathbf{y}_9, z = 13.4[\text{m}])$), algebraic manipulation results in several terms requiring the integration of the Gaussian function ($\exp(-x^2)$), which has a well known property of

$$\int_{-\infty}^{\infty}\exp\left(-Cx^2\right)dx = \sqrt{\frac{\pi}{C}}, \tag{6.8}$$

and can be applied to Eqn. 6.7 in order to solve for $\psi_g(a,t,z)$ and $\sigma_g(t,z)$ [28]. This technique of estimating the horizontal distribution of bubbles results in an overdetermined system of equations (3 equations (chords), 2 unknowns ($\psi_g(a,t,z)$ and $\sigma_g(t,z)$). This results in two estimates of $\psi_g(a,t,z)$ and $\sigma_g(t,z)$, which are then averaged.

By exploiting the number of bubbles along each chord through this UNDEX cloud, we can solve the integral equations. Using $\psi(a = 100[\mu\text{m}],\ t = 5.25[\text{s}]\ \mathbf{P}_i)$ in Table 6.2, the most appropriate values of $\sigma_g(t,z)$ and $\psi_g(a,t,z)$ are given in Table 6.3. Note that $\psi_g(a,t,z)$ is given in $\left[\frac{\#\text{ of bubbles}}{\text{m}^3}\right]$, since this procedure normalizes the bubble population to a 1 [m] range.

	value
Standard Deviation, $\sigma_g(t = 5.25[\text{s}], z = 13.4\ [\text{m}])$	1.05 [m]
$\psi_g(a = 100[\mu\text{m}], t = 5.25[\text{s}], z = 13.4\ [\text{m}])$	$1.78 \times 10^3\ \left[\frac{\text{bubbles}}{\text{m}^3}\right]$

Table 6.3. Standard deviation [$\sigma_g(t = 5.25[\text{s}], z = 13.4\ [\text{m}])$] and magnitude scalar [$\psi_0(a = 100[\mu\text{m}], t = 5.25[\text{s}], z = 13.4\ [\text{m}])$] for the Gaussian distribution used in the bubble population model.

The values of ψ_g and σ_g given in Table 6.3 are used in Eqn. 6.7 to calculate the bubble population along the chords, which are then compared to the values in Table 6.2. The percent difference between the 100 [μm] bubble population estimate reported in Table 6.2 and the values calculated using Eqn. 6.7 with $a = 100[\mu\text{m}]$, $t = 5.25[\text{s}]$, $z = 13.4[\text{m}]$, and the values for σ_g and ψ_g given in Table 6.3, are presented in Table 6.4. The number of bubbles along the central chord (ψ_{16}) agrees well with the inverted bubble population, but due to the uneven decrease in the population for the outside hydrophones of the horizontal array, the outside chords show a 4.2 % discrepancy.

The values given in Table 6.3 represent the bubble population present in the horizontal plane at 13.4 [m] depth, given the assumptions made in the beginning of Sec. 6.2.3.2 (which

	% Error w.r.t. Power-Law Bubble Population
South chord, Ph. 9	-4.2%
Central chord, Ph. 16	$\ll 1\%$
North chord, Ph. 10	+4.2%

Table 6.4. Percent error between the inverted bubble population along a given chord through the UNDEX cloud shown in Fig. 6.5 and the calculated values based on the Gaussian model.

are: at approximately 5.25 [s] after UNDEX, parallel chords in the horizontal plane at mean depth between the 11.6 [m] deep hydrophone and the 15.2 [m] deep projector, time-averaged magnitude and slope of an assumed power-law bubble population, a 30 [lb.] PBXN-111 charge, and measurement geometry).

In order to simplify the model, only a single value will be used for $\sigma_g(t, z)$, which is given in Table 6.3, and will hereafter be referred to as σ_g. $\psi_g(a, t, z)$ is assumed to be at 13.4 [m] depth, and will be referred to as ψ_g. In order to obtain an estimate of the 3-D bubble population for this time after UNDEX, the depth dependence (Sec. 6.2.3.1) must be combined with the horizontal cross-section of the bubble population, which is now discussed.

6.3 UNDEX Model Equation

After having determined the general spatial and temporal characteristics of the bubble cloud, Eqns. 6.2 6.3, 6.4 and 6.6 are combined (multiplied) to obtain a general equation for the UNDEX bubble population,

$$\psi_U(a,\ t,\ x,\ y,\ z) = \begin{cases} \psi_0 \ \exp\left(-\frac{r(x,y)^2}{2{\sigma_g}^2} - \frac{z}{D_c} - \frac{t}{T_c}\right) a^m, & \text{where} \quad z \leq D_{\max} \\ 0, & \qquad\qquad\quad z > D_{\max} \end{cases} \tag{6.9}$$

where ψ_0 is the magnitude scalar for the Eqn. 6.9, in $\left[\frac{\text{\# of bubbles}}{\text{m}^3}\right]$,
$r(x, y) = \sqrt{(x - x_c)^2 + (y - y_c)^2}$ is the radial distance from the UNDEX axis
σ_g^2 is the variance of the 2-D Gaussian distribution of bubbles in the UNDEX cloud in [m] (Sec. 6.2.3.2),
z is the depth in [m],
D_c is the e-folding depth in [m] (Sec. 6.2.3.1),
t is time since UNDEX, in [s],
T_c is the e-folding time in [s] (Sec. 6.2.2),
a is the radius of a bubble in [μm],
m is the slope of the power-law factor for bubble radius (Sec. 6.2.1),
$D_{\max}$ is the maximum depth of the UNDEX cloud in [m] (Sec. 6.2.3.1).

Eqn. 6.9 can be used to compute the bubble population for any depth, time, or distance away from the charge. ψ_0 is a scalar that is derived from $\psi_g(a = 100[\mu\text{m}], t = 5.25[\text{s}], z = 13.4\ [\text{m}])$ (the number of bubbles at the center of the 2D Gaussian fit, Eqn. 6.7), the exponential depth dependence (Eqn. 6.5), and the time dependence (Eqn. 6.3). $D_{\max}$ is an empirical constant used to define the lower boundary of the UNDEX bubble cloud, determined from the multibeam sonar images from the 2008 test when the sonar was oriented to produce a vertical cross-section of the UNDEX cloud (left panel of Fig. 4.30). $D_{\max}$ is estimated to be 18 [m], as Fig. 4.30 shows bubbles up to about 3 [m] below the charge location after UNDEX.

Previously, the number of bubbles at the center of the (assumed Gaussian) horizontal cross section at 13.4 [m] depth $[\psi_g(a = 100[\mu\text{m}]t = 5.25[\text{s}], z = 13.4[\text{m}])]$ was determined to be $1.78 \times 10^3 \left[\frac{\text{bubbles}}{\text{m}^3}\right]$. This value was derived from an 6-second average starting approximately 5.25 [s] after UNDEX, and must be extrapolated to the time of UNDEX ($t = 0$ [s]) by employing the exponential time dependence (Eqn. 6.3). ψ_0 also needs to be extrapolated to the surface of the water ($z_i = 0$ [m]), and since these dependencies were derived for $a = 100$ [μm], must be extrapolated to the y-intercept of the left panel of Fig. 6.1 (meaning $\psi_{PL}(a = 0[\mu\text{m}])$ in Eqn. 6.2, but recall that ψ_{PL} is only defined for $70 \leq a \leq 860$ [μm] in Sec. 5.3).

The scalar ψ_0 is determined by evaluating Eqn. 6.9 for the conditions listed in the previous paragraph and along the UNDEX axis ($r = 0$ [m]), then slight algebraic manipulation yields

$$\begin{aligned}\psi_0 &= \left.\frac{\psi_0(t,z)}{a^m\ \exp\left(\frac{-r(x,y)^2}{\sigma_g^2} - \frac{z}{D_c} - \frac{t}{T_c}\right)}\right|_{r=0[\text{m}],t=5.25[\text{s}],z=13.4[\text{m}],\ a=100\ [\mu\text{m}]} \\ &= \frac{1.78\times10^3\left[\frac{\text{bubbles}}{\text{m}^3}\right]}{(100\ [\mu\text{m}])^{-4.1}\ \exp\left(-\frac{13.4\ [\text{m}]}{6.02\ [\text{m}]} - \frac{5.25\ [\text{s}]}{36.1\ [\text{s}]}\right)} = 2.31 \times 10^{12},\end{aligned} \tag{6.10}$$

where the units of ψ_0 are $\left[\frac{\text{bubbles}}{\text{m}^3}\right]$. After substitution of ψ_0 into Eqn. 6.9, all of the arguments become general $[(\mathbf{x}_i, \mathbf{y}_i, \mathbf{z}_i)$ become $(x, y, z)]$.

Note that the UNDEX bubble population model (Eqn. 6.9) does not explicitly depend on the charge properties (explosive material, weight), or location (primarily charge depth, z_c). However, the constants derived in the previous sections are inherently dependent on these parameters. The procedures presented in Sec. 6.2.3 explicitly determine the model constants for a set of bubble population estimates (like that presented in Fig. 5.11), where the charge weight, composition and UNDEX depth are as utilized in Events 1 and 2.

Table 6.5 presents a summary of the constants used in Eqn. 6.9 for a 13.6 [kg] (30 [lb.]) PBXN-111 charge detonated at 15.2 [m] depth in freshwater.

Constant:	Value:
ψ_0	2.31×10^{12} $\left[\frac{\text{bubbles}}{\text{m}^3}\right]$
m	4.1
T_c	36.1 [s]
σ_g	1.05 [m]
D_c	6.03 [m]
$D_{\max}$	18.2 [m]

Table 6.5. Summary of constants used in the bubble population model (Eqn. 6.9).

6.4 Verifying the UNDEX Bubble Population Model

This section is dedicated to evaluating the UNDEX bubble population model, and determining the validity of the simplifying assumptions made in the previous sections of this chapter. Since the characteristics of the bubble cloud were not spatially or temporally stationary, several blanket assumptions were made to create a simplistic model for the bubble population present in the water column after the gas-globe has been ejected from the surface of the water. The first method of verifying the model is to compute the attenuation resulting from this bubble population model, which is then compared to the attenuation measured in the quarry.

The second approach used to evaluate the model is to predict the backscatter from the UNDEX cloud, and to compare the estimated levels to those measured during the quarry. While the measurements of backscatter from the LFM pulse do not provide lend themselves to concrete conclusions about backscatter from the bubble cloud, this estimate will provide a 'ballpark' estimate of backscatter from the bubble cloud.

6.4.1 Predicting Forward Loss Attenuation via UNDEX Bubble Population Model

To compute the attenuation resulting from this bubble population model, we must utilize the generalized form of Eqn. 6.9 to generate a bubble cloud, which is comprised of a series of 1 [m^3] cells whose combined volume contains the UNDEX bubble cloud model. Figure 6.6 presents the simulation geometry, where the blue dots indicate the center of 1 [m^3] cells for which bubble populations are calculated, the acoustic projector is shown in red, and the hydrophone locations are denoted by black dots. The metal cylinder is shown (purple), but is not included in this analysis.

Figure 6.7 presents the results of evaluating Eqn. 6.9 (using the constants defined in Table 6.5) to produce horizontal and vertical cross sections of the UNDEX cloud at $t = 0$ [s]. These plots shows $\log_{10}(\psi_{\text{U}}(\text{a} = 100[\mu\text{m}],\ \text{t} = 0[\text{s}],\ \text{x},\ \text{y},\ \text{z})$. The left panel shows the horizontal cross section computed for a depth of 13.4 [m]. The 2-D Gaussian distribution is visible in this panel, as the population is highest in the center of the bubble cloud, and rapidly decreases along the radial in all directions. The right panel is a vertical cross section extending to 18 [m] depth. The bubble population shows a strong dependence on depth, and distance from the UNDEX axis (the left edge of this panel).

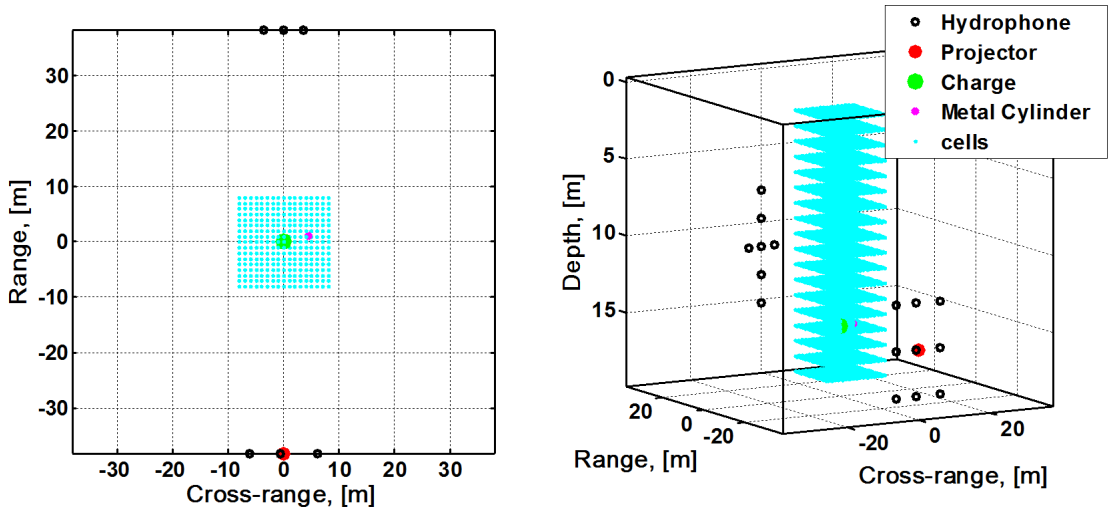

Fig. 6.6. Simulation of the quarry geometry. The acoustic projector, hydrophones, charge, and cells in which the bubble population are calculated are all shown in an plan view (left), and a 3-D plot (right).

Attenuation due to bubbles can be calculated for each cell (1 [m^3] bin) using the formal theory equation (Eqn. 2.19). Then, in order to directly compare the model to the measured data, the attenuation along the acoustic ray path between projector and receive hydrophone can be determined by integrating through the 3-D attenuation field on a 1 [m] basis using *interp3* in MatLab. This approach necessarily invokes the assumption of a continuous and smooth attenuation field (originally assumed in Sec 5.1). (*See:* Appendix B for the MatLab code used to compute the UNDEX bubble population model and corresponding attenuation.)

Figure 6.8 presents a comparison of the forward loss attenuation measurement during event

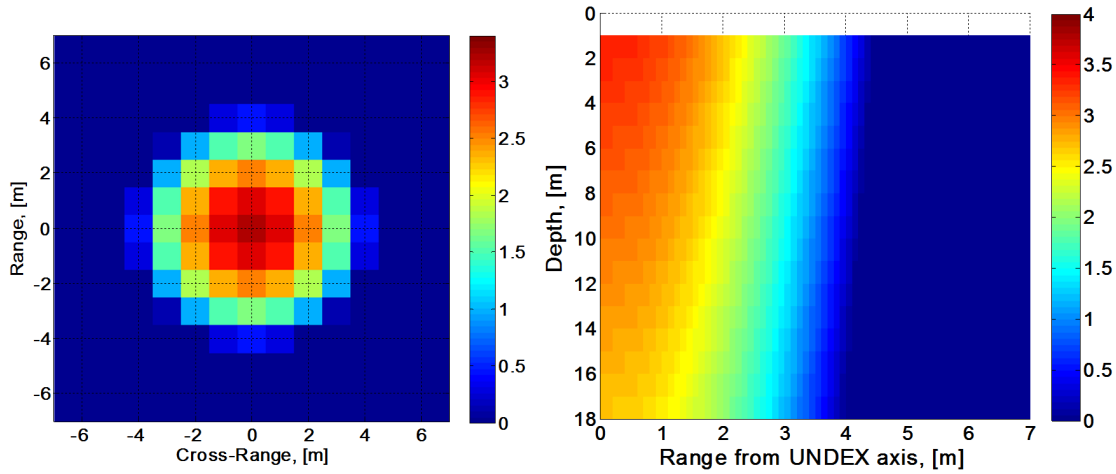

Fig. 6.7. Left: $\log_{10}$ of the bubble population model in a horizontal plane at the 13.4 [m] depth, immediately following UNDEX for bubbles with $a = 100$ [μm]. Right: same as left panel, except in a vertical plane through the UNDEX cloud (which is cylindrically symmetric).

2 (left, first presented in Fig. 4.36) with the attenuation calculated from the UNDEX bubble population model (right). The attenuation calculated using the Eqn. 6.9 (the UNDEX bubble population model) assumes the same charge size, composition, explosion depth and measurement geometry as the event 2, so these panels are directly comparable.

Visually, the model contains many characteristics that are similar to the event 2 attenuation measurement. The depth dependence is strong in both the level and duration of attenuation. The model tends to overestimate both duration and level of the attenuation at the lowest two hydrophone positions. Phone 8 shows approximately the same duration as the attenuation measurement, but overestimates the level and duration at frequencies above 50 kHz. The shallow hydrophones appear to have similar duration and level of attenuation immediately following UNDEX, however, the model again overestimates the attenuation at high frequencies. Phones 9 and 10 show some attenuation, but the model overestimates the duration, and underestimates the level compared to the measured attenuation.

Figure 6.9 compares the level of attenuation vs. frequency, and computed from the model for each of the forward loss hydrophones (except Ph 9). The RMS level of attenuation for the period of time prior to the onset of exponential-like decay (discussed for Fig. 4.37) on a per-frequency basis for the measured attenuation (black) and the model attenuation (red), these plots also include error bars indicating 1 standard deviation from the RMS value. In general, the UNDEX bubble population model produces attenuation measurements within a few dB of the measurement for phones 7, 8, and 16, over the majority of the frequency band investigated. For phones 14 and 15, the model overestimates the attenuation over most frequencies by up to 8 dB. Overestimation in the lower hydrophones is a result of the compromises made to obtain a simplified model whose dependence with depth was exponential in nature. The primary reason

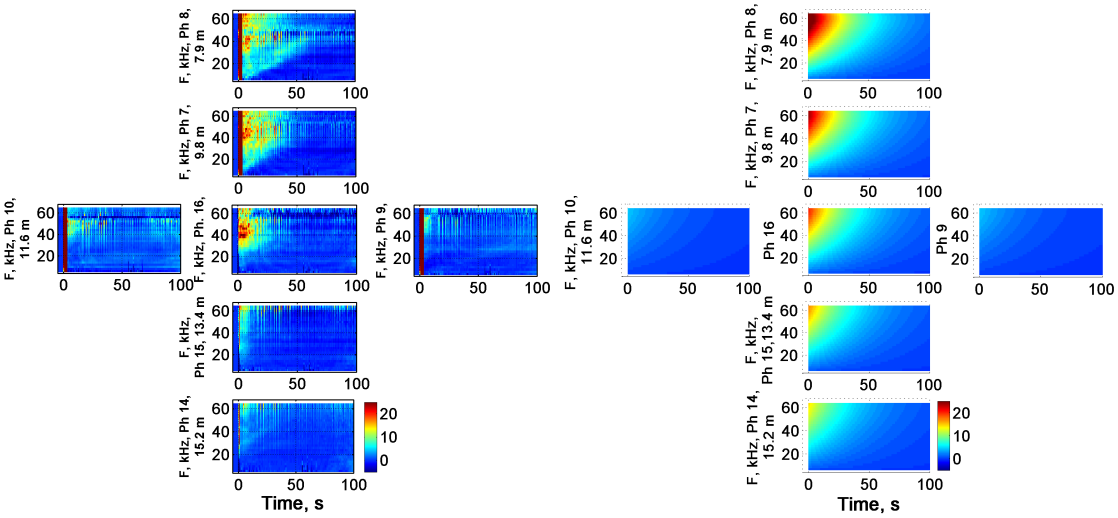

Fig. 6.8. Left: attenuation measurement for Event 2. Right: attenuation as calculated from the UNDEX bubble population model by applying the formal theory to the acoustic ray path between the projector location and the forward loss array.

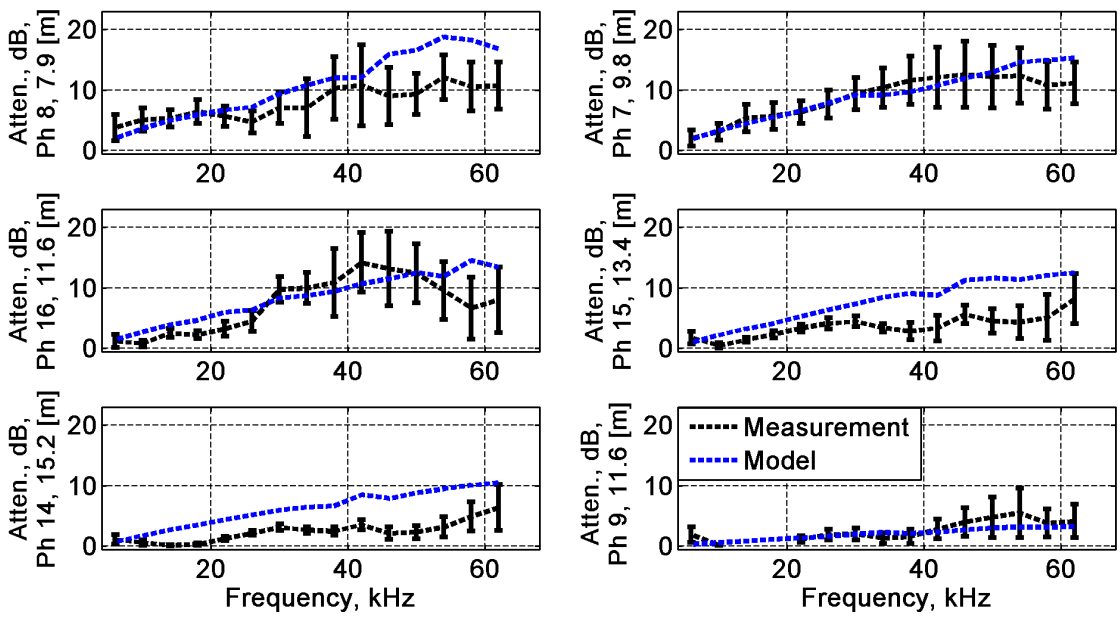

Fig. 6.9. Comparison of the mean and $\pm 1\sigma$ error bars for measured and modeled attenuation averaged over the period of time before exponential-like decay occurs. Refer to Fig. 4.2 for relative hydrophone depths.

for overestimation of high-frequency attenuation ($f > 50$ kHz) for most phones is the power-law dependence on bubble radius, resulting in more bubbles being present in the model than were present in the inverted bubble populations, on average (though is not visible in Fig. 6.1).

6.4.2 Calculating Backscatter from UNDEX Bubble Model

This section discusses how the bubble population model is used to calculate the energy backscattered to the region of the acoustic projector. This is the second method of verifying the UNDEX bubble population model. Backscattered energy predictions are compared to the backscatter measurement presented in Sec. 4.3.2.

For the following prediction of received backscatter levels, the location of hydrophone 5 is used (closest to projector). Each element in the simulated quarry geometry (Fig. 6.6) has a discrete round-trip arrival time for an acoustic wave emanating from the projector. Figure 6.10 shows the arrival times of scattering from each object in the measurement geometry as shown in Fig. 6.6. Return arrivals from the charge, and metal cylinder locations occur in the middle of the arrivals from the bubble population cells.

An estimate of backscatter is found by a rather involved computation accounting for the following considerations (among others):

- source level of acoustic projector (discussed in Fig. 4.11),
- frequency dependent source transmit voltage response and receive hydrophone sensitivity (Figs. 4.11 and 4.23),

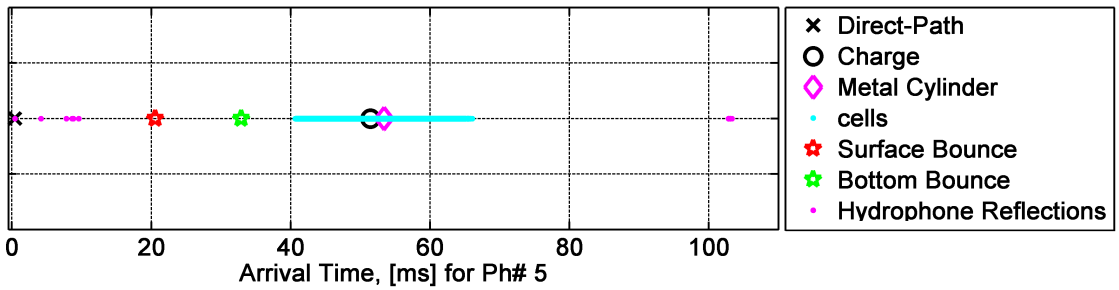

Fig. 6.10. Expected arrival times for scattering from each of the quarry model objects (*see:* Fig. 6.6) as seen by hydrophone 5, which is 0.6 [m] from projector at the same depth. This includes surface and bottom bounce-paths, as well as hydrophone reflections.

- transmission loss due to spherical spreading (Eqn. 2.1),
- scattering strength from the bubbles present in each volume element defined in the quarry geometry with respect to the position of the acoustic projector and hydrophones, follows from Eqn. 2.13
- attenuation of the acoustic wave through the bubble cloud before and after interaction with a given cell (1 [m^3] bins),
- summation of energy at the receive hydrophone locations (via RMS)
- 1 millisecond time resolution.

The backscatter measurements are compared to the model at 40, 54, and 62 kHz. For each frequency, three types of plots are shown.

The first result of the computed backscatter for the UNDEX model is shown in the right panel of Fig. 6.11. This example has been computed for 62 kHz, at the location of hydrophone 5. The left panel of this figure is the backscatter measurement at 62 kHz for phone 5, during event 2. Both plots of backscattered level are shown in dB //1μPa from prior to UNDEX until 200 seconds after UNDEX, and span the same range of received level ([90 130] dB). The backscatter measurement (left panel) shows a narrow time span of strong arrival from the UNDEX cloud (between about $49 \leq t_{horiz} \leq 56$ [ms]), however it is difficult to distinguish between bubble backscatter and backscatter from the pressure sensors, metal cylinder, possible debris in the water and/or ambient noise.

Backscatter calculated from the model (right panel) does not include scattering from the pressure sensors or metal cylinder that are present in the measured data. The model also does not exhibit the reverberation from the quarry walls or surface of the water, or from bubbles present between about $35 \leq t_{horiz} \leq 50$ [ms] in the measured data (discussed shortly).

A region of scattering centered at $t_{horiz} = 53$ [ms] in the model is due to UNDEX bubble cloud. A similar narrow interval of time around approximately 53 [ms] in the backscatter measurement shows a consistently elevated level for several 10s of seconds after UNDEX, and slowly reduces in level until it becomes indistinguishable from the pressure sensors or other reverberation. Receive levels (in dB) are similar between the model and measured data around $t_{horiz} = 53$

[ms], appearing within about 3-5 dB for the strongest arrivals during this period of time. The model suggests that this narrow region of elevated backscatter in the measured data is due to the bubble cloud. However, it is not possible to determine precise boundaries for backscatter due to the bubble cloud, as discussed in Sec. 4.3.2.

Figure 6.12 shows a direct comparison of the received level vs. time since signal transmit in milliseconds. The backscattered level is for a ping occurring approximately 70 seconds after UNDEX (black). The model result calculated for the corresponding time is shown in red. The ambient noise floor for the measured level is approximately 100 dB, and rises due to backscattered signal (likely from the quarry walls) between about 35 to 40 seconds. Discrete backscatter arrivals for the pressure sensors can be seen at approximately 40 [ms] and 44 [ms]. The backscatter from the bubble cloud is centered at approximately 52 [ms], and a strong arrival from the metal cylinder is at about 56 [ms]. The model predicts a maximum received level at approximately 53 [ms]. The predicted backscatter level is within about 6 dB of the measurement.

The predicted backscatter level in Fig. 6.12 is more broad than it appears in the right panel of Fig. 6.11 due to the color scale (the measurement and model are on the same color scale). This suggests that only the most dense portions of the model UNDEX bubble cloud are backscattering levels strong enough to match that of the measured data, possibly indicating that the horizontal distribution of bubbles is too concentrated near the center of the UNDEX cloud (seen in Fig. 6.7). This is supported by the 2007 multibeam sonar measurement in Fig. 4.29, where the horizontal extent of the UNDEX cloud is very large, and does not appear to be heavily concentrated at the former charge location (this could, in part, be due to the 400 kHz multibeam sonar, at which 6 [μm] bubbles are resonant).

Figure 6.11 compares the measured and modeled received level vs. time since UNDEX at a time corresponding to backscatter from the region very near the apparent center of the UNDEX cloud (region of highest backscattered level). This region of received level due to the UNDEX cloud occurs in ± 1 [ms] of t_{horiz}=53 milliseconds within the measured data (which appear as three vertical bands in the left panel of Fig. 6.11. Received levels from these times for the measured data are presented in Figure 6.13, where the black line is the RMS level of the three 1 [ms] bins (meaning t_{horiz} in 1 [ms] resolution), with the error bars showing 1 standard deviation. The measured level is maximum about ten seconds after UNDEX, and drops by about 10 dB over a period of 65 seconds. After about $t = 70$ [s] the received signal is dominated by backscatter from the pressure sensors, the metal cylinder or other reverberation (*e.g.*, quarry walls, surface).

The red line in Fig. 6.13 shows the RMS level of the same period of time calculated from the model. The model predicts a lower level for nearly the same region in time ($t_{horiz} = 52 \pm 1$ [ms]) is responsible for the largest contribution to the modeled backscatter. Immediately following UNDEX, the measured level is approximately 6 dB higher than the model. The prediction consistently decreases in level after $t = 0$ [s]. During the interval of time for which the measurement decreases ($5 \leq t \leq 65$ [s]), the backscatter level remains consistently higher than predicted by the model, but decreases faster than the model. This suggests that the model bubble population may not be decaying (or dispersing) as fast as the bubble cloud present during the measurement.

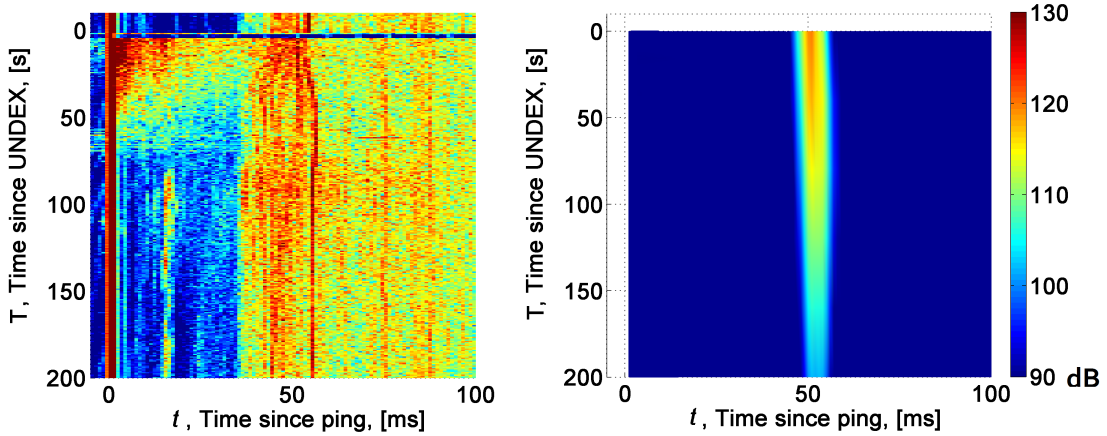

Fig. 6.11. Left: backscatter measurement for phone 5 during event 2, 62 kHz sweeplet center frequency (*see:* Sec. 4.3.2). Right: Estimate of acoustic backscatter from UNDEX bubble population model at 62 kHz.

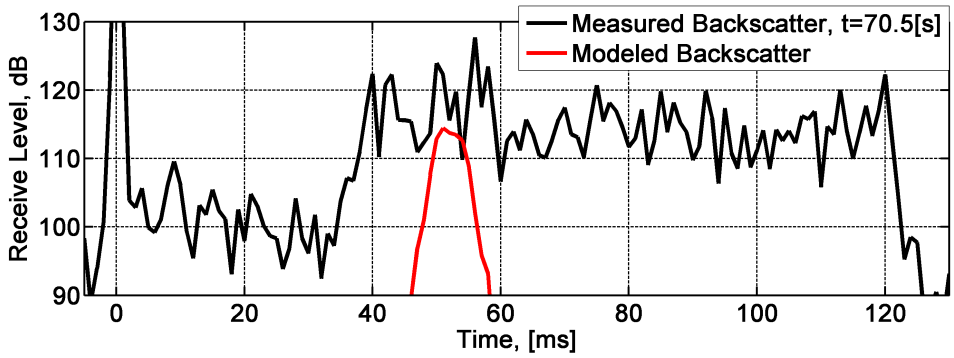

Fig. 6.12. Comparison of the backscatter measurement (black) and the prediction (red) using the model (Eqn. 6.9). The measured data is for hydrophone 5, at 62 kHz approximately 70 seconds after event 2.

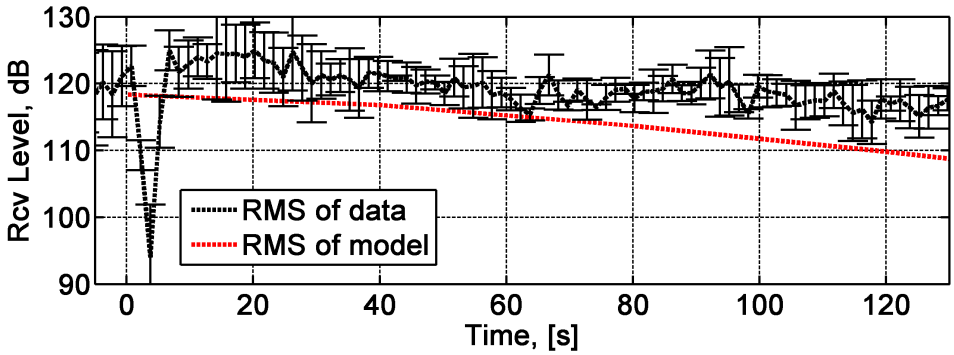

Fig. 6.13. RMS average in a 3 millisecond band during the region of maximum backscatter level due to the UNDEX cloud for the measured data at 62 kHz for event 2 (black) and calculated from the model (red).

Figures 6.14 through 6.19 demonstrate the model's ability to recreate the measured backscattered level at 40 kHz and 54 kHz, similar to the presentation of 62 kHz in Figs. 6.11 through 6.13. For 40 kHz, the left panel in Fig 6.14 shows the measured backscattered level at phone 5 for event 2. The backscatter for this frequency is lower in level than at 62 kHz, in part, due to the transmit voltage response of the acoustic projector. The pressure sensors and the metal cylinder are much less visible at this frequency, but a narrow region of elevated backscattered level due to bubble cloud is present at about $t_{horiz} = 53$ [ms]. The right panel in this figure shows the UNDEX model at 40 kHz. The predicted level appears to be several dB higher than the measurement over most of the time period shown.

Figure 6.15 confirms that the predicted level at 40 kHz is several dB higher than the measured level about 70 seconds after UNDEX. Again, the model predicts only a narrow interval of time for which the measured and predicted level of backscatter are comparable. Again, discrete arrivals from the pressure sensors and metal cylinder can be discerned in the received level, leading to an ambiguous arrival from the bubble cloud.

Figure 6.16 compares the RMS level of the 3 [ms] interval (when backscatter from the bubble cloud is highest) for both the measured and predicted levels. The predicted level is about 5 dB higher than the measurement at $t \approx 5$ [s]. The model consistently over-predicts the backscattered level at all later times. The model shows a slowly falling level, where the data shows a faster decline in received level that is overtaken by reverberation at about $t = 60$ milliseconds. After this time, the received no longer decays as a result of backscatter from the pressure sensors, metal cylinder and reverberation from the quarry walls or surface.

For 54 kHz, Fig. 6.17 compares the received backscatter level for hydrophone 5 during event 2 (left) to the model's prediction (right). The narrow region of backscatter near $t_{horiz} = 53$ [ms] can be discerned, and is well above the background level (noise, backscatter from the pressure sensors and metal cylinder). The model predicts a similar level of backscatter due to the UNDEX cloud around this time. After about $t_{vert} = 75$ [s], arrivals from the pressure sensors and metal cylinder begin to mask the bubble cloud ($t_{horiz} \approx 53$ [s]).

Figure 6.18 compares the measured and predicted levels for 54 kHz. Discrete arrivals for the pressure sensors are present at about 37 [ms] and 42 [ms]. In this figure, the bubble cloud could be responsible for scattering between $45 \leq t \leq 55$ [ms]. During this time, the predicted level peaks very near the measured level. Again, the model predicts only a narrow span of time within a few dB of the measurement.

Figure 6.19 compares the RMS level of the measured backscatter at 54 kHz to the predicted level for the narrow region around $t_{horiz} = 53$ [ms]. The agreement between the predicted and measured level is very good for this frequency. At about $t_{horiz} = 5$ [ms], the prediction matches the data within 1 dB. The model predicts the measured level within ± 3 dB for over two minutes following UNDEX. While this agreement is very good, Fig. 6.18 still suggests that the model is predicting too concentrated of a bubble cloud near the UNDEX axis.

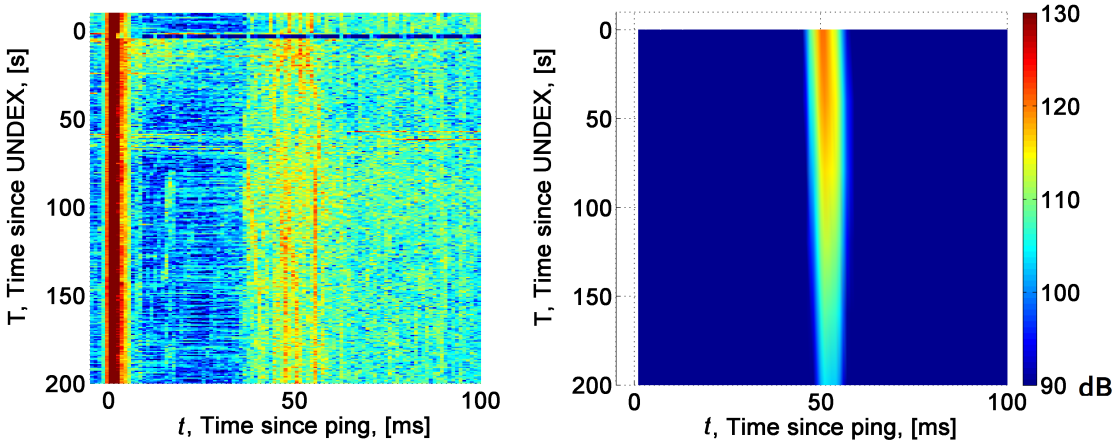

Fig. 6.14. Left: backscatter measurement for phone 5 during event 2, 40 kHz sweeplet center frequency (*see:* Sec. 4.3.2). Right: Estimate of acoustic backscatter from UNDEX bubble population model at 40 kHz.

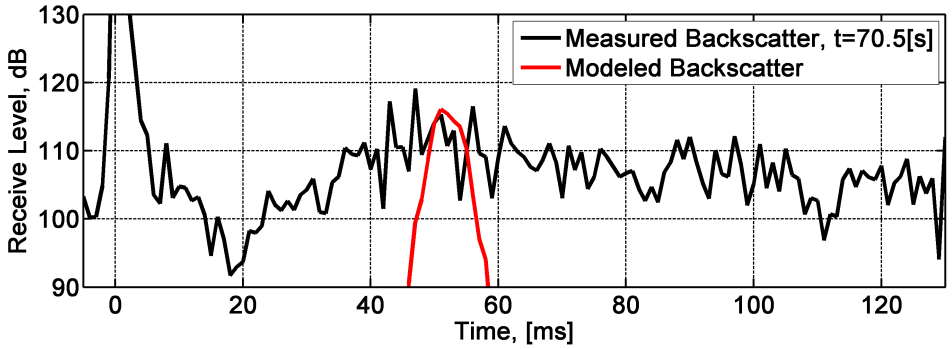

Fig. 6.15. Comparison of the backscatter measurement (black) and the prediction (red) using the model (Eqn. 6.9). The measured data is for hydrophone 5, at 40 kHz approximately 70 seconds after event 2.

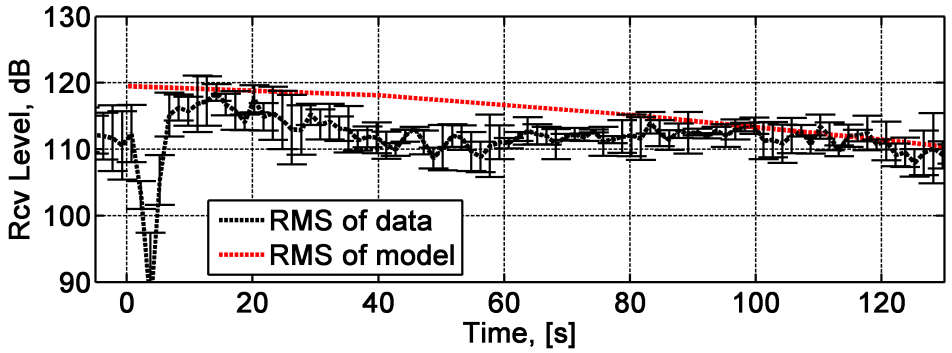

Fig. 6.16. RMS average in a 3 millisecond band during the region of maximum backscatter level due to the UNDEX cloud for the measured data at 40 kHz for event 2 (black) and calculated from the model (red).

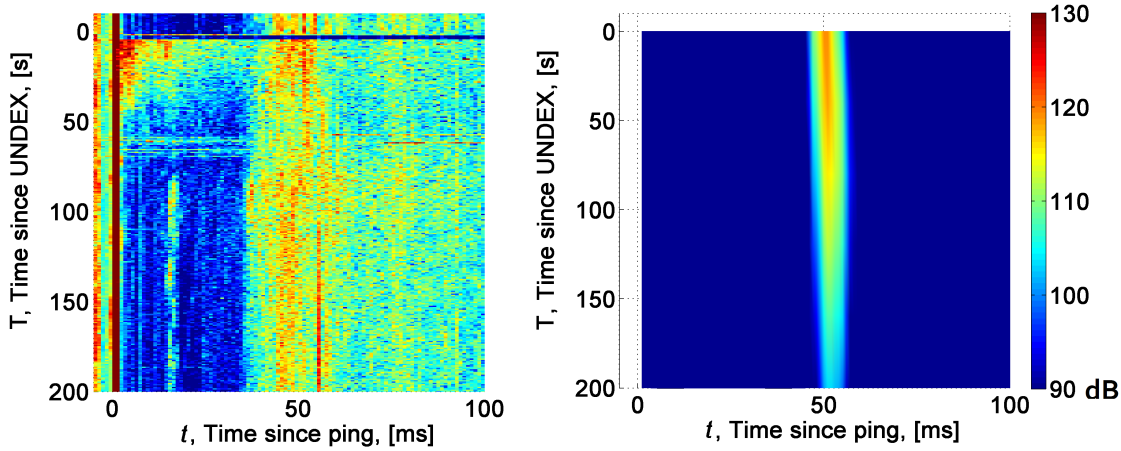

Fig. 6.17. Left: backscatter measurement for phone 5 during event 2, 54 kHz sweeplet center frequency (*see:* Sec. 4.3.2). Right: Estimate of acoustic backscatter from UNDEX bubble population model at 54 kHz.

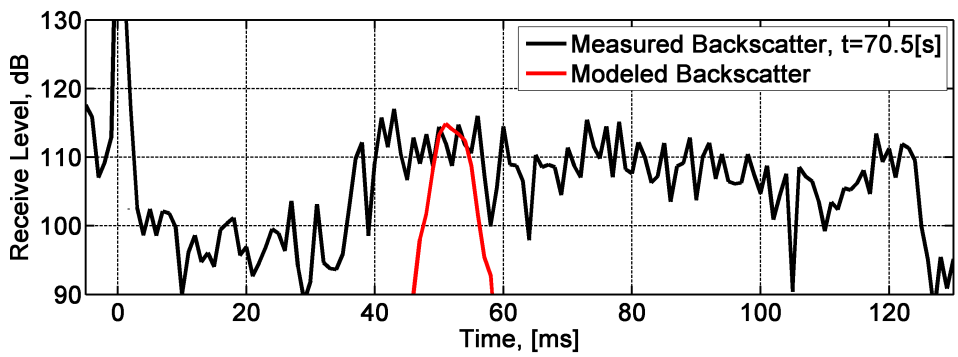

Fig. 6.18. Comparison of the backscatter measurement (black) and the prediction (red) using the model (Eqn. 6.9). The measured data is for hydrophone 5, at 54 kHz approximately 70 seconds after event 2.

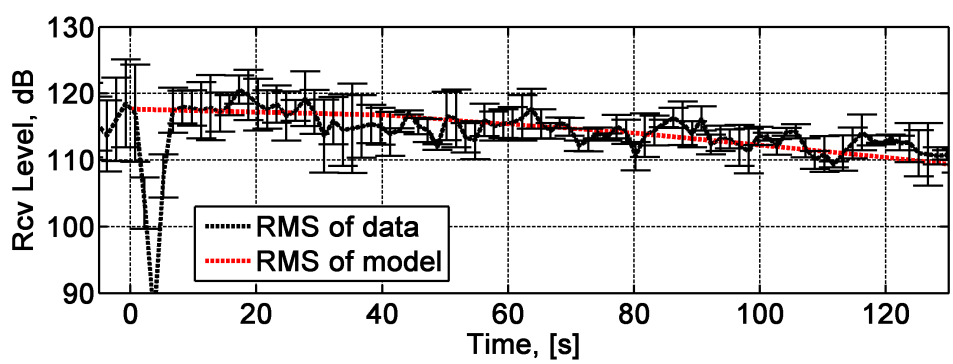

Fig. 6.19. RMS average in a 3 millisecond band during the region of maximum backscatter level due to the UNDEX cloud for the measured data at 54 kHz for event 2 (black) and calculated from the model (red).

The measured backscatter level for 40 kHz and 62 kHz decrease more quickly over a time interval of $5 \leq t \leq 60$ than is present for 54 kHz, which may suggest that the backscattered level near $t_{horiz} = 53$ [ms] is contaminated with scattering from objects other than the bubble cloud (*e.g.,* pressure sensors, metal cylinder, debris).

6.4.3 Comments

The UNDEX bubble population model ($\psi_{\mathrm{U}}(a,\ t,\ x,\ y,\ z)$, Eqn. 6.9) was empirically developed from the spatial and temporal characteristics of the forward loss attenuation measurements. Two methods for verifying the model consisted of comparing the predicted attenuation and backscatter to measurements made during the 2008 quarry test.

In general, the model shows a tendency to overestimate the level and duration of acoustic attenuation near the charge depth as a result of the simplifying assumptions such as exponential depth and time dependence (Secs. 6.2.3 and 6.2.2). A more complex dependence on depth, time and bubble size spectra would likely yield a better description of the UNDEX bubble population on depth.

The comparison of modeled vs. measured backscatter suggested that the UNDEX model could be too dense at the center of the bubble cloud, which results in the narrow time interval of predicted backscatter present in Figs. 6.12, 6.15, and 6.18. The backscatter comparison also suggests that the bubble cloud scatters more strongly for longer than that measured in the quarry, as seen by the discrepancy in the decay rate as discussed for Figs. 6.13 and 6.16. Due to the difficulty in differentiating backscatter from the bubble cloud from that of the pressure sensors, debris, or the metal cylinder, we claim that the model is not inconsistent with the measured data.

Chapter 7

Conclusions

7.1 Summary

This thesis examined the acoustic response of a bubble cloud generated by an underwater explosion in freshwater for frequencies between 5 kHz and 65 kHz. The acoustic attenuation resulting from this UNDEX bubble cloud was inverted to obtain an estimate of the bubble population present in the water. Characteristics of the inverted populations were used to develop a model that is capable of reproducing the general spatial, temporal and frequency-dependent properties of attenuation and backscatter measured in the 2008 quarry test.

In Chapter 2 the general acoustic theory was presented for the further understanding of this thesis. The effects of bubbles ensonified on- and off-resonance were explored to develop an intuition of how bubbles react in sound fields. Bubble resonance frequency, extinction cross section, and single and multiple bubble interaction were explored in depth, resulting in the ability to estimate the attenuation from a given bubble population spectrum.

Chapter 3 presented the three methods to invert acoustic attenuation data in order to obtain a bubble population estimate. Each of these methods has advantages and caveats that affect their performance on real data. The methods were demonstrated on example bubble populations. Potential caveats and regularization techniques were discussed for each method.

Chapter 4 presented data from the 2008 Quarry test, where two charges were detonated at a depth of 15.2 [m]. The techniques used to process the received signals was detailed, and yielded an estimate of the amount of energy attenuated by the UNDEX bubble cloud, and backscattered to the region near the acoustic projector. An investigation of the background levels (ambient noise and reverberation due to signal transmission and UNDEX) demonstrated that the measurement system was not compromised as a result of the shock or pressure waves from UNDEX.

Chapter 5 applied the inversion techniques developed in Ch. 3 to the attenuation measured in the 2008 quarry test (presented in Ch. 4). The Caruthers *et. al* method was shown to most consistently reproduce the measured attenuation to a desired tolerance. An estimate of the

spatial extent of the bubble population vs. time was presented for the second event.

Chapter 6 determined the inverted bubble populations dependence on bubble radius to be well characterized by a power-law, which was then compared to two published models of bubble populations under wind-generated breaking waves in saltwater. The spatial and time dependence of the UNDEX bubble cloud was discussed, and used to develop a model of the bubble population due to an UNDEX. The model was evaluated and compared to the measured acoustic attenuation through, and backscatter from the UNDEX bubble cloud for the second event.

7.2 Future Research

The development of the UNDEX bubble population model was presented in this thesis with several assumptions that limited its ability to reproduce the complex time, frequency and spatial dependence observed in the 2008 quarry measurements. The mathematical description of the physical phenomena was greatly simplified in this model. Many simplifications and generalizations were made in the development of the model that, if developed further, may improve agreement between the model's prediction and measurement data.

Further consideration of the spatial distribution of bubbles immediately following UNDEX would allow the incorporation of bubble rise physics that could potentially alleviate many the limitations imposed by using a two parameter description of the bubble population. Incorporating bubble rise velocity would likely improve the acoustic response of the UNDEX bubble cloud model at higher frequencies, allowing the bubble population to vary in time, and allow for a fluctuating bubble population that could reproduce the high level of attenuation at around 40 kHz, without overestimating the attenuation for frequencies above 50 kHz (*see:* Attenuation estimate for event 2, Fig. 4.36). The incorporation of bubble rise physics would also remove the exponential decay of the bubble population in time ($\exp(\frac{-t}{T_c})$ in Eq. 6.9)

The charge detonation was assumed to be omnidirectional, and the spatial distribution was assumed Gaussian. These assumptions may be unrepresentative of the true distribution of bubbles, but are limited by the resolution in the forward loss horizontal array of hydrophones. An increased resolution, and multiple arrays would greatly improve the spatial estimate of the bubble population.

The size and density of the UNDEX bubble cloud is also dependent on charge weight and explosion depth, neither of which were included in the development of the UNDEX bubble population model presented in Ch. 6. Future investigation of underwater explosions of various charge sizes, and occurring at various depths will provide a great insight into how the bubble cloud generated by an UNDEX depends on these additional dimensions.

Appendix A

Additional Information & Commentary

A.1 Introduction

This appendix addresses important topics not covered in the main text of the thesis. Some mathematical details and other information regarding transducers and testing procedure were omitted, and are now presented for clarification.

A.2 Additional Comments about Inversion Methods

A.2.1 Caruthers Mathematical Derivation Clarification

In the development of the Caruthers *et al.* method, a number of assumptions are made that provide a challenge in completing the math between Eq. 2.20 and Eq. 3.15. The assumptions and mathematical details are provided below to justify the claim that only bubbles near resonance contribute significantly to the attenuation.

First, Eq. 2.20 is reprinted below, where the assumption of operating at resonance has been made explicitly by incorporating only the resonant radius, a_R, population at that radius, $\psi(a_R)$, and bubble damping at resonance,δ_R. With these assumptions, the total extinction cross section per cubic meter is

$$S_e(f) = \int_0^\infty \left. \frac{4\,\pi\,a^2\,\frac{\delta}{\delta_r}\,\psi(a)\,da}{\left[\left(\frac{f_R}{f}\right)^2 - 1\right]^2 + \delta^2} \right|_R \approx \frac{4\,\pi\,a_R^2\,\psi(a_R)\,\delta_R}{\delta_{Rr}} \int_0^\infty \frac{da}{\left[\left(\frac{f_R}{f}\right)^2 - 1\right]^2 + {\delta_R}^2}, \tag{A.1}$$

where a_R (m) is the radius of the bubble that is resonant at frequency f. $\psi(a_R)$ is in $\left[\frac{\text{\# of bubbles}}{\text{m}^3}\right]$,

and $da = 1$ [m]. Then, focusing on the integral, and recalling that $\frac{f'_R}{f} = \frac{a_R}{a}$ according to Eqn. 2.2,

$$\int_0^\infty \frac{da}{\left[\left(\frac{a_R}{a}\right)^2 - 1\right]^2 + \delta_R^2}. \tag{A.2}$$

If $a_R \gg a$, the denominator of Eqn A.2 dominates and the integrand goes to 0. If $a_R \ll a$, the damping factor (δ) may dominate, and the response is strongly frequency dependent. The goal of this section is to prove that bubbles near resonance dominate the acoustic response of a bubble cloud for a particular frequency. We begin evaluating this integral by observing the effect of bubbles slightly larger than at resonance by some (positive) amount, ϵ (that is, $a = a_R + \epsilon$). If the difference between a and a_R is small, then

$$\frac{|a - a_R|}{a_R} = \frac{|\epsilon|}{a_R} \ll 1.$$

Then, by substitution,

$$\frac{a_R}{a} = \frac{a_R}{a_R + \epsilon} = \frac{1}{1 + \frac{\epsilon}{a_R}} \approx 1 - \frac{\epsilon}{a_R}$$

which can be substituted into the bracketed term in the denominator of the integrand in Eq. A.1,

$$\left[\left(\frac{a_R}{a}\right)^2 - 1\right]^2 \approx \left[\left(1 - \frac{\epsilon}{a_R}\right)^2 - 1\right]^2 = \left[1 - \frac{2\epsilon}{a_R} + \left(\frac{\epsilon}{a_R}\right)^2 - 1\right]^2 \approx \frac{4\epsilon^2}{a_R^2},$$

then, since the change in radius is ϵ, $da = d\epsilon$, the integral in A.2 becomes

$$\frac{1}{\delta_R^2} \int_0^\infty \frac{d\epsilon}{\frac{4\epsilon^2}{a_R^2 \delta_R^2} + 1}.$$

If we choose to perform integration by substitution, with a choice of $p = \frac{2\epsilon}{a_R \delta_R}$, which means $dp = \frac{2d\epsilon}{a_R \delta_R}$, the integration can be solved with a trigonometric property, and Eqn. A.2 becomes:

$$\frac{a_R}{2\delta_R} \int_0^\infty \frac{dp}{p^2 + 1} = \frac{\pi a_R}{4\delta_R}. \tag{A.3}$$

Since only values of $a \geq a_R$ were considered, we must multiply the solution to Eqn. A.3 by 2.

Then, substituting the solution back into Eqn. A.1, at resonance the total extinction cross section for bubbles per unit volume becomes

$$S_e(f)|_R = \frac{4\,\pi\, a_R^2\, \psi(a_R)\, \delta_R}{\delta_{Rr}} \int_0^\infty \frac{da}{\left[\left(\frac{f_R}{f}\right)^2 - 1\right]^2 + {\delta_R}^2} \approx \frac{2\,\pi^2 a_R^3\, \psi(a_R)}{\delta_{Rr}}, \tag{A.4}$$

where, a_R [m] is the radius of a bubble resonant at frequency f (in Hz). $\psi(a)$ is the bubble population in $\left[\frac{\#\text{ of bubbles}}{m^3}\right]$, and $da = 1$ [m]. Eqn. A.4 is equivalent to Eqn. 3.15, and further

development of the RBA is discussed in Sec. 3.2.

A.3 Comments on Quarry Measurements

The F27 acoustic projector was used to transmit a signal through the region of UNDEX during the 2007 and 2008 Quarry tests. This transducer as an output directivity pattern that is strongly frequency dependent, but is also dependent on the level of voltage used to drive the transducer.

Figure A.1 shows the transmit directivity pattern of the F27 at 40 kHz, 60 kHz and 80 kHz. The blue line indicates a measured directivity pattern, red lines indicating the −3dB beamwidth of the directivity pattern. The divisions within the plots are approximately 10 dB. While frequencies higher than 65 kHz were not used in the quarry test, the 80 kHz directivity pattern is included to show the strong frequency dependence of the output directivity pattern.

Table A.1 presents the −3dB beam width in degrees for the three frequencies shown in Fig. A.1.

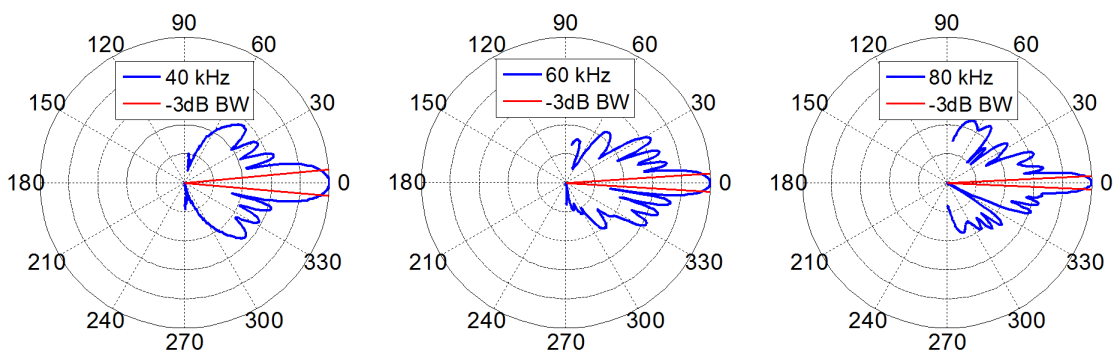

Fig. A.1. Directivity pattern for the F27 acoustic projector at 40, 60, and 80 kHz[21]. -3dB beam widths shown with red lines.

Frequency	Beam Width, Degrees
40 kHz	11
60 kHz	7.0
80 kHz	5.3

Table A.1. Beam width for the F27 acoustic projector at 40, 60, and 80 kHz.

Appendix B

MatLab Code

This appendix contains a sample of MatLab code used to evaluate the UNDEX bubble population model presented in Ch. 6. This appendix does not constitute an exhaustive collection of code used to evaluate the model. Rather an excerpt that demonstrates how the model was implemented and verified in Sec. 6.4.1.

B.1 UNDEX Bubble Population Model MatLab Code

This section presents the code used to generate the 3-D, time evolving bubble population model, essentially as presented in Eqn. 6.9.

```
function out = UNDEXbubDensityPL( W, D0, R, D, T, freq, S, T_c)
% Given an underwater detonation of a charge of known size and at known
%   depth, return the density of bubbles left behind by the explosion by size
%   (i.e. bubble radius) at a given depth and range from the site of the
%   explosion, and a given time after the explosion.  Note that the bubble
%   density is cylindrically symmetric.
% This version of the UNDEX bubble denisty model was designed for the
% charges in this thesis, to be included in F. Holt's MS thesis (fdh109@psu.edu).
% For information regarding the functions called in this code, see Appendix B.
%
%   N(a) =  UNDEXbubDensityPL( W, D0, R, D, T, freq, S, T_c);
%
% Inputs
%  W: charge size, not used in this code,       [kg]
%  D0: depth at which charge detonated,         [m]
%  R: range of the field point from the UNDEX   [m]
%  D: depth of the field point                  [m]     (Single value)
%  T: time in seconds since the UNDEX           [sec]   (column vector, easiest to
%                                       process all times at once, can be done o/w)
%  freq: sonar frequencies                      [Hz]    (row vector)
```

```
%  S: salinity (quary was freshwater 0.5)        ppt
%  T_c: water temperature,                       deg. C
%
%
% Outputs:
%  out.N - the density of bubbles (# / m^3 in 1  m bin) resulting from the
%          underwater explosion (UNDEX) as a function of radius a( m).
%  out.a - bubble radius spectrum, [\mum]
%  out.atten - attenuation of the cell's population, in dB/m

%  out.N_Var     - bubble population including random temporal variability
%  out.attenVar - attenuation for cells including random temporal variability
% Construct a simple model for the bubble density.
%     N(a) = N0 * exp( -Rcoef * R - Tcoef * t - Dcoef * D - Acoef * a);    2009 Jun
%     N(a) = N0 * a^{Acoef} * exp( -Rcoef * R - Tcoef * t_delay - Dcoef * D); 2010 Apr

% Written by F. Holt (fdh109@psu.edu / dryden@gmail.com)
% Last revised: 2010 Jun 11, Generated Rev.Cal for FHoltMSThesis
%

% Fred's Values as of 2010 Jun 11 (Power-Law dependence on bubble radius)
  % Introduce delay before exp. decay occurs:  (w.r.t. charge depth)
    D_max = D0 + 3;             % Fixed charge weight, not included in Rev.Cal
    D_tmp = D;
    D_tmp(D_tmp > D_max) = 0;


% Model Constants:
    Tcoef = 0.1658;     % e-folding time coefficient
    sigma_use = 1.05;   % Gaussian shape of the horiz. cross section
    Dcoef = 6.03;       % e-folding in depth (# of bubbles on central UNDEX axis,
                        %                     w.r.t charge depth)
    mean_slope = -4.1;  % slope of the power law dependence on bubble radius
    N0Highatsurface =2.31e12;    % Value for highest number of bubbles @ surface
                                 %  (becomes large at surface!)

    a = logspace(log10(70),log10(860),100);      % [ m] bubble radii

    N0 = N0Highatsurface * exp(-Dcoef*D - Tcoef * T  -R^2/(2*sigma_use^2));

    out.N = N0 * a.^mean_slope;  % Bubble Population [#/m^3 in 1 micron bin], Resultant
                                 % population (no temporal variability)
    out.a = a;                   % Output bubble radius tensor as well, in [\mum].

   % Calculate Attenuaiton for each bubble population: (Clay & Medwin Method, 1977)
     Atten = UWAtten(freq, a*1e-6, out.N, D, S, T_c);
     out.atten = Atten.atten;

%% Introduce random variability in time by varying the bubble population
  % This seciton is from the temporal variability from Cal charges, optional
```

```
    sigmaovermu = 0.1529;                % Std deviation from the mean  (found using RMS
                                         % variability for atten. data in time)
    [tmp ind] = min(abs(a - 118.5));     % Find radius closes to 40kHz @ 44' depth
                                         % (position of HA in atten. data)
    tmp_val = (out.N(:,ind) ./ (a(ind)^mean_slope));  % Number of bubbles of size 'ind'
                                         % (prev. line) at depth (to scale variability)
    nfreq = linspace(0, 2*pi*(1/.75)/2 ,floor(length(T)/2+1) ); % Frequencies
    powerfit = 48.9 * nfreq.^(-0.62);    % Via Population_Variability_Investigation.m
                                         % (RMS of all f for Ph8)
    powerfit(1) = 0;                     % Eliminate DC Component, also-(1/0) is undef.
    powerfit = [powerfit fliplr(powerfit(2:end))];
    if length(powerfit) ≠ length(T)     % Correct size of (powerfit) if numel(T) is even
        powerfit = powerfit(1:length(T));
    end

    PhaseSpectra = 2 * pi * (randn(size(powerfit)) - .5); % Introduce random phase
    Spect = powerfit .* exp( 1i * PhaseSpectra);
    Spectra = abs(ifft(Spect));
    Spectra = Spectra - mean(Spectra);  % Time variability
    Spectra = 3*Spectra / max(Spectra); % Limit fluctuation to 6*sigma
    out.N_var = (tmp_val + (tmp_val .* (Spectra'*sigmaovermu))) * a.^mean_slope ;
                                         % Employ STD Dev. as variability
   % Bubble Population including scaled variability

   % Calculate Attenuaiton for each bubble population: (Clay & Medwin Method)
     AttenV = UWAtten(freq, a*1e-6, out.N0_var, D, S, T_c);
     out.attenVar = AttenV.atten;

end
```

B.2 Verifying UNDEX Bubble Population Model by Computing Attenuation

This section presents a sample of MatLab code that utilizes the UNDEX bubble population model to compute the attenuation through the bubble cloud. The code executes a representation of the quarry geometry shown in Fig. 6.6, and computes the attenuation as presented in Fig. 6.8.

```
%% Plot_UNDEXBubble_Population_Calibration.m
% This script creates a similar type of plot for the attenuation for the forward loss
% vertical array during the UNDEX events.
clc; clear all; close all;

fName = 'Atten_Data.mat';
tmp_path = pwd;
```

```
cd ..
cd 'Inversion Routine MatLab Files'
disp('Loading Attenuation Data...');
load(fName) % Load saved Quarry attenuation data
disp('Attenuation Data Loaded.')
cd(tmp_path)

%% Constants needed for calculation
W = 13.5;                % charge size, [kg].
D0 = 50 * 12 * .0254;    % UNDEX depth, [m].
R = 0:1/10:15;           % range from the UNDEX to the field point
D = 1:D0+3;              % depth of the field point
T = 0;                   % time since UNDEX, [s].
T_c = 20;                % Temp, deg. C
Sal = 0.5;               % Salinity, ppt
a = logspace(log10(70),log10(860),100);  % [ m]



%% Plot frequency range attenuation
x = -8:1:8;     % [m], cross-range
y = -8:1:8;     % [m], range
    [¬, x0] = min(abs(x)); % find zeros of x and y
    [¬, y0] = min(abs(y));
t = 0:.75:200; % sec post UNDEX
freq = (6:2:64)*1e3;  % Investigation frequencies
d_int = [38 41 44 47 50]*.3048; % FL Atten. crossing depths with UNDEX location
d_int2 = 26:6:50;
d_near = [11 12 13 14 15]; % approx depth
Y = y + 125*.3048;
theta = atand( ((50*.3048)-d_int.')/(125*.3048) );
Y_int = Y.' * tand(theta.');


figure(10)
    plot(125*.3048,50*.3048-d_int,'kp'), hold on,
    plot(Y,Y_int,'ro'), hold off,
        xlim([0 250*.3048]),ylim([-10*.3048 50*.3048]), grid on,
        title('Postion of Calc. Atten. relative to Charge plane (x-z)'),
        legend('origianl','interp'),xlabel('Distance, [m]'),ylabel('Rise, [m]'),


% Plot the time-evolution of the attenuation from the UNDEX model
Den_Recalc = zeros(length(y),length(d_int),length(t),length(a));
Atten_Recalc = zeros(length(freq),length(y),size(Y_int,2),length(t));
disp('Calculating the population & attenuation in the Vertical Array...');
    for yy = 1:length(y)
        depth = Y_int(yy,:);
        for zz = (1:length(depth))
            z = D0 - depth(zz);    % Must Be 50'-depth, since the charge is located at
```

```
%  50' depth for comparison
            Range = sqrt(0 + y(yy)^2);

            Population = UNDEXbubDensityPL( W, D0, Range, z, t', freq, Sal, T_c);

            Den_Recalc(yy,zz,:,:) =  Population.N;
            Atten_Recalc(:,yy,zz,:) = Population.atten2;  % atten is w/o variability,
                                                          % attenVar is with
        end
    end

Den_Recalc2 = zeros(length(y),length(t),length(a));
Atten_Recalc2 = zeros(length(freq),length(y),length(t));
disp('Calculating the population & attenuation in the Horizontal Array...');
    for yy = 1:length(y)
        z = 44*.3048;   % The gaussian parameters were designed as chords thru 44'
                        % depth (avg @ undex axis)
        x = 6*.3048;    % constant - how the undex cloud was designed
        Range = sqrt(x^2 + y(yy)^2);

        Population = UNDEXbubDensityPL( W, D0, Range, z, t', freq, Sal, T_c);

        Den_Recalc2(yy,:,:) =  Population.N;
        Atten_Recalc2(:,yy,:) = Population.atten2;  % atten is w/o variability,
                                                    % attenVar is with

    end
    phones =  [7 8 9 10 14 15 16]; % Numeric order of virtual 'phone' locations
    position = [0 0 0 0 0 0 5 2 9 7 0 0 0 14 11 8]; % Virtual 'phone' location in plot



    d_tmp = 1:5;
    figure(11);clf;
    for Phind = 1:length(phones);
        phone2plot = phones(Phind);
        if phone2plot == 9 || phone2plot == 10
            pplot = squeeze(trapz(Atten_Recalc2,2));
             subplot(5,3,position(phone2plot)),
                    surf(t, freq/1e3, pplot,'EdgeColor','none'),
                          view(2),grid on,axis xy,
                    ylabel(['F, kHz, Ph ',num2str(phone2plot)],'fontsize',14,...
                          'fontweight','demi')   %colorbar('Location','SouthOutside'),
                    ylim([5 65]),xlim([-5 100]),caxis([-5 25]),%xlabel('Time, [sec]'),

        else
            pplot = squeeze(sum(Atten_Recalc,2));
            dd = [8 7 16 15 14];
            [val ind] = min(abs(dd - phone2plot));
             subplot(5,3,position(phone2plot)),
```

```
                surf(t, freq/1e3, squeeze(pplot(:,ind,:)),'EdgeColor','none'),
                      view(2), grid on, axis xy ,
                ylabel(['F, kHz, Ph ',num2str(dd(ind))],'fontsize',14,...
                      'fontweight','demi')  ,
                ylim([5 65]),xlim([-5 100]),caxis([-5 25]),

            if phone2plot == 14
                colorbar; xlabel('Time, sec','fontsize',14,'fontweight','demi'),
            end
        end;
    end

return
```

Bibliography

[1] Thorpe, S. A. (1982) "On the Clouds of Bubbles Formed by Breaking Wind-Waves in Deep Water, and Their Role in Air-Sea Gas Transfer," *Philosophical Transactions of the Royal Society of London. Series A, Mathematical and Physical Sciences*, **304**(1483), pp. 155–210.

[2] Trevorrow, M. V. (2003) "Measurements of near-surface bubble plumes in the open ocean with implications for high-frequency sonar performance," *The Journal of the Acoustical Society of America*, **114**(5), pp. 2672–2684.
URL `http://link.aip.org/link/?JAS/114/2672/1`

[3] Leighton, T. G. (1994) *The Acoustic Bubble*, Academic Press.

[4] National Defense Research Committee (1989) *Physics of Sound in the Sea*, Peninsula Publishing.

[5] Trevorrow, M. V., S. Vagle, and D. M. Farmer (1994) "Acoustical measurements of microbubbles within ship wakes," *The Journal of the Acoustical Society of America*, **95**(4), pp. 1922–1930.
URL `http://link.aip.org/link/?JAS/95/1922/1`

[6] Cole, R. H. (1945) *Underwater Explosions*, Princeton University Press.

[7] Urick, R. J. (1983) *Principles of Underwater Sound (3rd Edition)*, McGraw-Hill, Inc.

[8] Commander, K. W. and R. J. McDonald (1991) "Finite-element solution of the inverse problem in bubble swarm acoustics," *The Journal of the Acoustical Society of America*, **89**(2), pp. 592–597.
URL `http://link.aip.org/link/?JAS/89/592/1`

[9] Caruthers, J. W., P. A. Elmore, J. C. Novarini, and R. R. Goodman (1999) "An iterative approach for approximating bubble distributions from attenuation measurements," *The Journal of the Acoustical Society of America*, **106**(1), pp. 185–189.
URL `http://link.aip.org/link/?JAS/106/185/1`

[10] Czerski, H. and D. Farmer (2009) "Extending bubble measuremenets below 20 μm: in memory of Ralph Goodman's contributions." *The Journal of the Acoustical Society of America*, **125**(4), p. 2610.
URL `http://link.aip.org/link/?JAS/125/2610/5`

[11] Clay, C. S. and H. Medwin (1977) *Acoustical Oceanography: Principles and Applications*, michael e. mccormick and rameswar bhattacharryya ed., John Wiley & Sons, Inc., New York, NY, USA.

[12] Minnaert, M. (1933) "On musical air-bubbles and the sound of running water." *Philosophical Magazine*, **6**, pp. 235–238.

[13] Medwin, H. (1977) "Acoustical determinations of bubble-size spectra," *The Journal of the Acoustical Society of America*, **62**(4), pp. 1041–1044.
URL `http://link.aip.org/link/?JAS/62/1041/1`

[14] Commander, K. W. and A. Prosperetti (1989) "Linear pressure waves in bubbly liquids: Comparison between theory and experiments," *The Journal of the Acoustical Society of America*, **85**(2), pp. 732–746.
URL `http://link.aip.org/link/?JAS/85/732/1`

[15] Hall, M. V. (1989) "A comprehensive model of wind-generated bubbles in the ocean and predictions of the effects on sound propagation at frequencies up to 40 kHz," *The Journal of the Acoustical Society of America*, **86**(3), pp. 1103–1117.
URL `http://link.aip.org/link/?JAS/86/1103/1`

[16] Commander, K. and E. Moritz (1989) "Off-resonance contributions to acoustical bubble spectra," *The Journal of the Acoustical Society of America*, **85**(6), pp. 2665–2669.
URL `http://link.aip.org/link/?JAS/85/2665/1`

[17] Rajan, S. D., J. F. Lynch, and G. V. Frisk (1987) "Perturbative inversion methods for obtaining bottom geoacoustic parameters in shallow water," *The Journal of the Acoustical Society of America*, **82**(3), pp. 998–1017.
URL `http://link.aip.org/link/?JAS/82/998/1`

[18] Tikhonov, A. N. and V. Y. Arsenin (1977) *Solution of Ill-Posed Problems*, John Wiley & Sons, Inc.

[19] National Technical Systems, Inc. (2010), "National Technical Systems Engineering, Testing & Evaluation Services," .
URL `http://www.ntscorp.com/`

[20] Snay, H. G. (1957) *Naval Hydrodynamic Publ. 515: Hydrodynamics of Underwater Explosions*, National Academy of Sciences.

[21] Bobber, R. J. (1989) *Underwater Electroacoustic Measurements*, Peninsula Publishing, Los Altos, California.

[22] Intenational Transducer Corporation, i. (2010) *ITC Hydrophone 6080c Specification Sheet*.
URL `http://www.itc-transducers.com/`

[23] Reson, Inc. US (2010) *Hydrophone TC4032, Reson Specification Sheet*.
URL `http://www.reson.com/`

[24] Detsch, R. M. (1991) "Small Air Bubbles in Reagent Grade Water and Seawater, 1. Rise Velocities of 20- to 1000- m-Diameter Bubbles," *The Journal of Geophysical Research*, **96**(C5), pp. 8901–8906.

[25] Culver, R. L. (2008) "Test Plan for Underwater Explosion (UNDEX) Acoustic Measurements in Rustburg, VA., May 2008," .

[26] Brennen, C. E. (1995) *Cavitation and Bubble Dynamics*, Oxford University Press.

[27] Weber, T. C. (2006) *Acoustic Propagation Through Bubble Clouds*, Ph.D. thesis, The Pennsylvania State University.

[28] Papoulis, A. and S. U. Pillai (2002) *Probability, Random Variables, and Stochastic Processes*, fourth ed., McGraw-Hill, Inc.